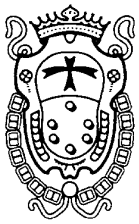

Scuola Normale Superiore di Pisa
Classe di Scienze

Tesi di Perfezionamento in Fisica

Young Stellar Populations in the Large Magellanic Cloud: surprises from *HST* observations

Relatori:
Prof. Giuseppe Bertin
Prof. Nino Panagia

Candidato:
Martino Romaniello

July 1998

Q: So, what's your sign?
A: Cancer.
Q: And what does it mean to be a Cancer?
A: I wish I knew.

Sir Martin Rees (to Claudia Dreifus)

Contents

Contents

List of Figures

List of Figures

List of Tables

Chapter 1

Summary

Since the 1920's, it has become common knowledge that our galaxy, the Milky Way, is not the only galaxy in the Universe. In those years Edwin Hubble discovered Cepheid stars, a particular type of variable stars that can be used as "standard candles", in the direction of the M31 "nebula". Today, although we know that Hubble had underestimated the distance to M31 approximately by a factor of two, his main conclusion still holds and, indeed, M31 is a galaxy on its own at about 700 kpc from the Sun (for comparison, the distance from the Sun to the center of our galaxy is about 8 kpc). Moreover, it is now clear that the Universe is made of billions and billions of galaxies. Galaxies are made of *stars and diffuse matter*, mainly hydrogen, but containing also heavier elements in atomic and molecular form. Therefore, the way a galaxy looks and evolves is the result of the interplay between these two different components.

The study of young stellar populations in diverse environments has an importance and bears consequences far beyond the direct goal of understanding the processes of star formation. In fact, the entire chemical and dynamical evolution of galaxies is dominated, or, at least, strongly influenced, by the formation of many generations of stars. The most massive ones enrich the surrounding medium of highly processed material and supply vast amounts of kinetic energy (both with their winds and, even more, with their ultimate explosions as Type II Supernovæ). Lower mass stars constitute one of the main sources of crucial elements, such as Carbon and Nitrogen (through stellar winds first, and a planetary nebula ejection later) in their individual evolution, and may be the main suppliers of the iron group elements if, in binary systems, they succeed to merge and explode as Type Ia Supernovæ.

On the other hand, to reach the frontiers of the Universe, one has to proceed by successive steps, each time losing part of the information and the detail, but gaining in generality and approaching the crucial phases of the early formation of galaxies. The obvious place where to start would be our Galaxy. However, since we are immersed in it, our vision of stellar systems is highly defective because of high galactic obscuration and because of the serious difficulty of measuring distances to individual stellar objects. Thus, one has to move out of the Galaxy and first go to the nearest, fair-sized galaxy, *i.e.* the Large Magellanic Cloud (LMC), where the stars are essentially all at the same distance, to within, say, 5-10% and our view is not severely obstructed by dust extinction. A few steps of roughly factors of ten would then take us to the beginning of the Universe quite readily.

1.1 Goals, methods, and results

The general purpose of this Thesis is to determine in detail some important properties of young stellar populations. This is achieved by devising two new methods to analyze the data. The first is a method that allows one to recover the intrinsic temperature and luminosity, as well as the reddening, for individual stars. The second is a procedure to infer directly the Star Formation Rate as a function of time and the underlying Initial Mass Function from the HR diagrams constructed for the observed fields. In particular, this will allow us to measure ages, mass functions, and spatial distributions of stellar populations in the neighbourhood of Supernova 1987A in the Large Magellanic Cloud and in a "parallel" field 120 pc away. We have observed these fields with the *Wide Field and Planetary Camera 2* on board the NASA-ESA *Hubble Space Telescope*. Its unprecedented spatial resolution is invaluable to resolve and carefully make the photometry of the stars in regions that, from the ground, would appear severely crowded.

The Colour-Magnitude diagram has been for many years the main tool used to study stellar populations. As the name suggests, it is a two dimensional plot in which the relation between colour and magnitude is displayed for the stars populating a given region of the sky. It requires only two photometric bands and, hence, it only uses a limited portion of the stellar spectrum. Moreover, there is no single combination of filters suitable for stars of every temperature, since the peak of the emitted light is shifted towards the ultraviolet as the star temperature increases. In this Thesis, we have developed a procedure, based on observations taken over a wide wavelength baseline, able to recover the intrinsic luminosities and temperatures, as well as reddening, of individual stars. At least one filter blueward of the Balmer jump is necessary to determine temperature and reddening simultaneously and we will use 6 bands for the field around SN1987A and 4 filters for the parallel one, covering a wavelength range from roughly 3000 to 9000 Å. The advantage of the method we have developed is twofold. *Firstly*, we can measure the interstellar reddening caused by the intervening dust along the line of sight to the stars and correct for it for each individual star. Hence, we can determine the distribution of the dust down to the smallest spatial

scales. This already leads to one surprising result: nearby stars are affected by significantly different amounts of extinction in an almost unpredictable manner. *Secondly*, by putting all the information together, the multi-band fit to theoretical stellar atmosphere models is found to provide an excellent determination of the intrinsic properties of the stars.

Once the stars are carefully placed in the HR diagram, we can evaluate their ages and masses to determine the star formation history of the regions considered. The location of the observed Zero Age Main Sequence is perfectly compatible with the distance to SN1987A of 51.4 ± 1.2 as measured by Panagia (1998, in *Views on Distance Indicators*, Società Astronomica Italiana, in press) from the rings around the Supernova itself. Also from the position of the observed Zero Age Main Sequence, we infer that the mean metallicity is $Z = 0.3 \cdot Z_{\odot}$.

Our fields contain massive stars as young as 3 Myr of age. Being extremely bright, they are easily recognized. On the other end of the mass spectrum, the low mass stars of this young age are still in the Pre-Main Sequence phase and share the same location in the HR diagram as the low mass stars belonging to the much older LMC field population. These latter are stars with ages in excess of a few hundred million years. We identify the Pre-Main Sequence stars by using their Hα and/or U-band excess when compared to the spectrum of a normal star of the same spectral type. As a consequence, we are able to recognize them only if these spectral features are strong enough and we can only place lower limits to their number.

Yet another surprise is that the *spatial distribution* of high ($M > 6$ $M_{\odot}$) and low ($M < 2$ $M_{\odot}$) mass stars belonging to the same young generation is remarkably different. In the field of SN1987A the massive stars are mainly concentrated in a cluster with a radius of 5 pc (the Supernova progenitor was a member of this cluster). The young low mass stars, on the other hand, are more uniformly distributed over the entire field. A similar behaviour is also seen in the parallel field. Here, however, there is no clear indication of a clump of massive stars. They are arranged in a linear structure pointing in the direction of the nearby association NGC 2050. In both regions we have observed, the LMC field population is uniformly distributed, as expected, and the average density of these stars is indistinguishable between the two fields.

An inspection of the HR diagrams immediately reveals that *the observations cannot be explained in terms of a single generation of stars.* Many episodes of star formation must have followed one another resulting in a complicated superposition of stars of different ages. In order to analyze this complex history of star formation, we have devised a method that directly assigns ages and masses to the stars in the HR diagram. The standard method usually adopted in the literature to analyze complex star formation histories consists in comparing a set of assumed models against the observed data and the least discrepant one among them is taken to be as representative of the actual history. The method we have devised (the "sieve"), instead, is direct in the sense that no model has to be imposed *a priori* and all the quantities of interest are derived directly from the data.

By applying the "sieve" to the HR diagram we have constructed for the stars in our

fields, we have determined the *star formation history* and found that it can be interpreted in terms of a uniform *Initial Mass Function*:

Star formation history: the Star Formation Rate is found to have monotonically increased, by a factor of at least 6, from the earliest times we can explore (roughly 8 Gyr ago) until the present epoch. The star formation activity is still very high at present. In particular, the region around SN1987A has experienced two episodes of star formation in the last 30 Myr and a relatively quiescent period of time between then and 100 Myr ago. One of these two peaks corresponds to a prominent population of roughly 12 Myr, *i.e.* coeval with Sk -69 202, the progenitor of SN1987A.

Besides the observed data, the main input in determining the star formation history is that of the theoretical evolutionary tracks. Thus it should be stressed that the detailed conclusions of our analysis may be model dependent, but the general picture is not.

Initial Mass Function: what we observe now is the result of the superposition of many generations of stars formed over the lifetime of the Large Magellanic Cloud. A pivotal assumption we are forced to make is that the Initial Mass Function is independent of the time and of the region in which the stars were formed. If this were not the case, there would be no way to reconstruct the mass distribution at formation from the Present Day Mass Function. This hypothesis needs to be tested in environments where the star formation history is simpler than in the regions we have studied. Here we can only determine the consequences if it is assumed to be true.

As far as the spatial homogeneity is concerned, we have already mentioned that we do find strong evidence that massive stars are more clustered than low mass ones. Nonetheless, if we average over a suitably large region (roughly 2000 pc^2 in the case of the field around SN1987A) we find that the concept of IMF between 1 and 7 $M_\odot$ is viable and the function is very well represented by a power-law. Its logarithmic slope has to be steeper than $\Gamma = -1.55$. Unfortunately, we can only place upper bounds on it because, as we have seen, it is only possible to place lower limits on the number of young, low mass stars. Again, these results are meaningful ONLY if the IMF is constant with time.

1.2 Outline of the Thesis

The Thesis is organized as follows:

Chapter 2: in the first part of the chapter we briefly introduce the basic concepts concerning the study of stellar populations.

In the second part, we examine the concept of Initial Mass Function, analyzing the conditions under which it is applicable. Examples of IMF determinations in various

astrophysical environments are reported, and three different theoretical approaches to the problem are briefly reviewed.

Chapter 3: here, we describe the instrument we have used to gather the data analyzed in this Thesis: the Wide Field and Planetary Camera 2 (WFPC2) on board the *Hubble Space Telescope*. The advantages of observing from space as opposed to the ground and the problems arising from dealing with an undersampled Point Spread Function (PSF) are illustrated by discussing a very simple model of the diffraction pattern that creates the image of a point-like source on the detector.

The filters we have used in our observations are briefly described and their choice motivated.

Chapter 4: this chapter is devoted to the problems and techniques related to optical data reduction and point source photometry. After the description of the standard pipeline needed to calibrate the raw data, we address the issues concerning the removal of cosmic rays.

We then compare the Colour-Magnitude diagrams produced with different photometry techniques. This comparison leads us to choose a simple *aperture photometry* method as the most suitable one to cope with the WFPC2 undersampled PSF.

Chapter 5: here, we first explain the reasons why the Colour-Magnitude diagrams are not the best way to study stellar populations, in particular the young ones. Then, we describe the procedure we have devised to recover the intrinsic properties of the stars. The requirements for this method to be applicable are discussed in detail and the advantages of applying it are shown.

Chapter 6: the technique derived in the previous chapter is applied here to the stars within 30 pc of Supernova 1987A. The presence of a substantial population of Pre-Main Sequence stars and its effects are discussed. In particular, the spatial distribution of young stars in different mass ranges is derived and the inhomogeneity that it discloses discussed.

Chapter 7: as in chapter 6, but on a "parallel" field 120 pc away from the one discussed there.

Chapter 8: the new technique we have devised to determine the stellar content of regions of complex star formation is presented and discussed. The technique is then applied to the stars in the field of SN1987A and in the parallel field 120 pc away from it.

Chapter 2

Introduction to the study of stellar populations

In this chapter, we shall introduce the general context in which this work is inserted.

2.1 The basics

Before discussing in details the purposes of our work, let us introduce a few fundamental astrophysical quantities.

2.1.1 Magnitude, colour and metallicity

The most direct way to gather information on stars is to measure the light that they emit. The most detailed information that one can possibly obtain on the photometric properties of a certain astronomical object is its spectrum (*spectroscopy*). Usually, this is given either as flux per unit of wavelength (f_λ, erg cm^{-2} s^{-1} Å^{-1}) or flux per unit of frequency (f_ν, erg cm^{-2} s^{-1} Hz^{-1}). Unfortunately, good spectroscopy requires a huge amount of observing time if one wants to observe a large number of stars, as needed to have a good statistics, and, in any case, it is not feasible in crowded regions.

On the other hand, for many purposes, it is not necessary to study the complete spectrum, but it is enough to measure the total amount of light received by a detector in a certain range of wavelengths (*photometry* or *imaging*). In order to do this, a filter is placed in front of the detector to select only certain wavelength intervals from the incoming radiation. In general terms, the more filters one uses, the more complete the information is.

Since the response of the human eye to light is roughly logarithmic and in order to approximately match the magnitude groups used by the ancient Greeks, the modern **magnitude scale** is defined as:

$$m_i \equiv -2.5 \log\left(\overline{f}_i\right) + ZP \tag{2.1}$$

where $\overline{f}_i$ is the average flux measured inside the passband "i" and ZP is the zeropoint of the system. With this strange definition, the higher is the flux, the smaller is the magnitude.

The **absolute magnitude** is defined as the magnitude that a star would have in a filter i, if placed at a distance of 10 pc from the Sun and is usually indicated with a capitol M to distinguish it from the *apparent magnitude* defined above. Their difference is called the **distance modulus** (DM$_i$):

$$\mathrm{DM}_i \equiv m_i - M_i \tag{2.2}$$

If the apparent magnitude is corrected for interstellar extinction (see section 2.1.4), that is different in different filters, hence the need for the index i, there is a one to one correspondence between DM and the distance D of the object:

$$\mathrm{DM}_0 \stackrel{\forall i}{=} \mathrm{DM}_i = -5 + 5 \cdot \log\left(\frac{D}{1pc}\right) \tag{2.3}$$

The standard photometric system, the so-called *Landolt system*, consists of 5 filters: Johnson's **U** [$\overline{\lambda}$=3650 Å, $\Delta\lambda$=680 Å], **B** [$\overline{\lambda}$=4400 Å, $\Delta\lambda$=980 Å] and **V** [$\overline{\lambda}$=5500 Å, $\Delta\lambda$=890 Å] and Cousin's **R** [$\overline{\lambda}$=7000 Å, $\Delta\lambda$=2200 Å] and **I** [$\overline{\lambda}$=9000 Å, $\Delta\lambda$=2400 Å] (see, for example, Zombeck, 1990, page 100). In any case, it is possible to use any passband one wants, as long as its response curve is well characterised. For example, one could want to use filters that do not include any lines in their passband or, on the other hand, filters that contain ONLY a certain line.

Modern optical detectors do not measure the energy of the incident photons, but actually count them. Therefore, the quantity that is measured is not the total energy in the passband, but the total number of photons through it. So, if N_γ is the number of photons detected per unit area and time, this corresponds to:

$$N_{\gamma,i} = \int P_i(\lambda)\, f_\lambda \,\frac{\lambda}{hc}\, d\lambda \tag{2.4}$$

where $P_i(\lambda)$ is the dimensionless throughput of the filter "i", the detector and the whole optical assembly together, i.e. the fraction of the detected photons over the incoming ones as a function of wavelength, f_λ is the spectrum of the source per unit wavelength defined above and the factor λ/hc converts the flux density from energy to number of photons. It is very important to stress that the response curve $P_i(\lambda)$ in equation (2.4) refers to the whole instrument one is using and not just to the filter, even if it is always referred to as "filter response". Of course, the spectral characteristics of the instrument itself must be very well measured in order to compare observations with theoretical predictions.

In order to obtain the average flux in equation (2.1), one has to divide $N_{\gamma,i}$ by the width of the filter:

$$\overline{f}_i \equiv \frac{N_{\gamma,i}}{\int P_i(\lambda)\,\frac{\lambda}{hc}\, d\lambda} \tag{2.5}$$

As it can be easily seen, $\overline{f}_i$ has the right dimensions of an energy density per unit wavelength. Equation (2.5) is the standard definition of $\overline{f}_i$ that enters in equation (2.1). However, let us notice here that, since the detector does not measure energy directly, it may seem more correct to use the average number of photons detected instead of the average energy. Of course, this easily done by substituting:

$$\overline{N}_{\gamma,i} = \frac{N_{\gamma,i}}{\int P(\lambda)\, d\lambda}$$

to $\overline{f}_i$ in equation (2.1). In any case, this corresponds just to a shift of the zeropoint of the magnitude scale.

Since it is very difficult to measure absolute fluxes, it is often preferred to refer the observed flux to that of a standard star, Vega (α Lyræ), an A0V star. In this magnitude

system (*VEGAMAG*), Vega has, by definition, magnitude 0 in all the passbands. Therefore, the zeropoint in equation (2.1) is not a constant, but depends on the filter used and it is just Vega's N_γ in the filter considered. As it can be easily seen, the denominator in equation (2.5) cancels out.

For the sake of completeness, we mention here that there is also another system (*STMAG*), in which Vega has magnitude 0 ONLY in the visual passband. In this system, ZP is a constant and its value is -21.10. In the following, we will always use VEGAMAG as the system for our magnitudes.

The difference of the magnitudes in two passbands is called **colour**:

$$c_{ij} \equiv m_i - m_j \tag{2.6}$$

Usually, the filter "*i*" is at shorter wavelengths than the filter "*j*". With this convention, together with the minus sign in the definition of magnitude in equation (2.1), the colours of two black bodies at temperature T_1 and $\mathrm{T}_2 > \mathrm{T}_1$ are such that:

$$c_{ij}(\mathrm{T}_2) < c_{ij}(\mathrm{T}_1)$$

Since real stellar spectra are not too different from black bodies, this is also true for stars. All in all, as a first approximation (*i.e.* neglecting the effects of interstellar absorption), the colour of a star is a measurement of its surface temperature. In the astrophysical jargon, the word "*blue*" is commonly used as a synonym for hot and "*red*" as a synonym for cold.

If the filters are the standard ones, B and V, for example, then it is customary to write:

$$c_{\mathrm{BV}} = \mathrm{B} - \mathrm{V}$$

Another quantity that is frequently used in astrophysics is the **metallicity** (**Z**), defined as:

$$\mathrm{Z} \equiv \frac{M_{heavy}}{M_{tot}} \tag{2.7}$$

where M_{heavy} is the mass in the form of all the elements heavier than ^{4}He and M_{tot} is the total mass, *i.e.* the mass in the form of hydrogen, helium and heavy elements. This one single number is usually used to summarise the chemical composition of a star, of a stellar population or of an astrophysical environment and the proportions among the various heavy elements are often assumed to be the same as those measured in the sun.

The chemical composition may also be expressed as the logarithm of Z in solar units:

$$\left[\frac{M}{H}\right] \equiv \log\left(\frac{Z}{Z_\odot}\right) \tag{2.8}$$

Astrophysical quantities are often expressed in solar units and we summarise their numerical values in Table 2.1 on the next page.

Quantity	Value
Mass ($M_\odot$)	$1.99 \cdot 10^{33}$ gr
Luminosity ($L_\odot$)	$3.90 \cdot 10^{33}$ erg s^{-1}
Temperature ($T_{eff,\odot}$)	5770 K
Radius ($R_\odot$)	$6.96 \cdot 10^{10}$ cm
Metallicity ($Z_\odot$)	0.02
Visual Magnitude	4.83 *mag*

Table 2.1: *Solar constants.*

2.1.2 Evolutionary tracks and stellar atmospheres

Once stars are formed, they evolve in time, both in luminosity and surface temperature, following the different nuclear reactions that provide the energy to balance the gravitational contraction. We recall that, in absence of rotation and magnetic fields, a stellar structure is described by 5 basic equations (see, for example, Castellani, 1985):

$$\begin{cases} \frac{dP(r)}{dr} = G \cdot \frac{M_r \cdot \rho(r)}{r^2} & \text{hydrostatic equilibrium} \\ \frac{dM_r}{dr} = 4\pi r^2 \rho & \text{continuity of the mass} \\ \frac{dT}{dr} = -\frac{3}{4ac} \cdot \frac{\kappa\rho}{T^3} \cdot \frac{L_r(r)}{4\pi r^2} & \text{energy transfer} \\ \frac{dL_r}{dr} = 4\pi r^2 \varepsilon \rho & \text{energy conservation} \\ P = P(\rho, T) & \text{equation of state} \end{cases} \tag{2.9}$$

Where P is the pressure, G is the gravitational constant, M_r is the mass enclosed in a sphere of radius r, ρ is the mass density, T is the temperature, a is the black body constant and L_r is the flux per unit surface and time through the surface of the sphere of radius r. All the physics is contained in three quantities: the total (radiative+conduction) opacity per unit mass $\boldsymbol{\kappa}$, the total rate of energy production per unit time and mass $\boldsymbol{\varepsilon}$ and the **equation of state**. As it can be seen, there are 5 equations and 5 unknowns (P, T, ρ, M_r and L_r), so the problem is well defined.

Given the mass of the star, its chemical composition and the input physics, that depends upon Z, the output of the stellar evolutionary computations is the temporal behaviour of the surface luminosity and of the radius and, hence, of the effective temperature, defined as the temperature that a black body of that luminosity and radius would have. Once solved, the equations (2.9) give the internal structure of a stellar model at a time t. From this, one can compute the nuclear reaction rates for the thermodynamical conditions of the matter and, from these, in turn, the new chemical composition inside the star and, hence, the new opacity and equation of state at a time $t+\Delta t$. Then, one can proceed to solve the 5 equations again, with these new conditions. Once this is done, one has computed a new model that is

the result of the temporal evolution of the previous one. Iterating this procedure, one can compute the time evolution of a star. Of course the chemical stratification of the first model computed must be known. For this reason, the first model is generally a pre-Main Sequence one in which the nuclear reactions are not yet active and convection is so efficient that the structure is chemically homogeneous. In Figure 2.1, taken from Chiosi et al. (1992), we show the evolutionary paths in the luminosity-temperature plane (the *Hertzsprung-Russell* or HR diagram) for models of 0.8, 5, 20 and 100 $M_\odot$. The locus of the Zero-Age main Sequence (ZAMS), *i.e.* where the hydrogen burning provides for the first time the entire luminosity of the star, is indicated as a dashed line.

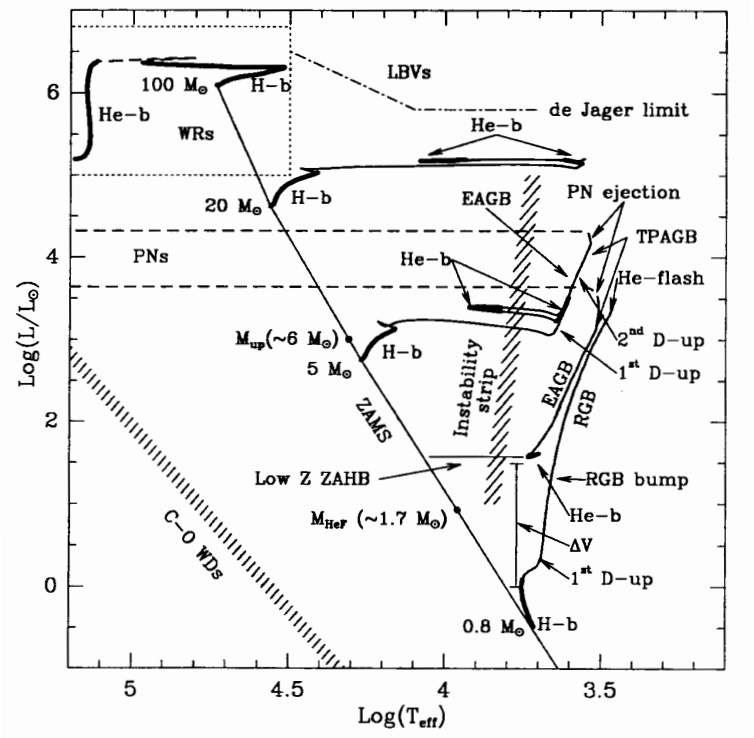

Figure 2.1: *The evolutionary paths in the HR diagram of model stars for $Z = 8 \cdot 10^{-3}$ from Chiosi et al. (1992). Thick lines indicate the stages of slow evolution, where the majority of stars are found.*

Stellar evolutionary times during hydrogen and helium burning phases from the models of Schaller et al. (1992), for masses between 0.8 and 120 $M_\odot$ and two chemical compositions, are reported in Table 2.2.

Stars are not black bodies, because the radiation that we see comes from layers at different temperatures, in the sense that the higher the opacity is, the more external and colder are the layers from which we receive the radiation. Therefore, in order to predict the observed fluxes in different passbands, we need a series of spectra, either theoretical or observed, for various combinations of temperature, surface gravity and chemical composition. Given the values of the luminosity and temperature from a theoretical model, the convolution of the spectrum of that temperature, normalized to the given total flux, with the response function of the instrument will provide the theoretical magnitudes and colours to be compared to

Initial	Z=0.02		Z=0.001	
mass ($M_\odot$)	H-burning	He-burning	H-burning	He-burning
120	2.5614	0.4145	2.7798	0.2836
60	3.4469	0.4233	3.7148	0.3602
20	8.1409	0.7885	9.3841	0.8350
12	16.0176	1.5689	18.1163	1.6049
5	94.4591	12.4288	88.2763	10.9212
3	352.503	86.1926	290.798	45.2332
2	1115.94	240.930	855.634	140.594
1.5	2694.65	—[a]	1842.74	—[a]
1	9961.73	—[a]	6263.59	—[a]
0.8	25027.88	—[a]	15029.5	—[a]

[a]Masses smaller than 1.7 $M_\odot$ were not followed through He-burning

Table 2.2: *Stellar lifetimes, in units of* 10^6 *yrs, during hydrogen and helium burning phases for Z=0.02 and Z=0.001 (from Schaller et al., 1992).*

photometric observations.

2.1.3 The chemical enrichment of the Interstellar Medium

In addition to being the source of a large fraction of the light that comes from galaxies, stars are the cauldrons in which heavy elements are produced out of the ones that were made in the primordial nucleosynthesis. This enrichment occurs both during the quiescent evolutionary phases and during the possible explosion of the star as Supernova. Stars, then, determine the **chemical evolution** of the universe as dictated by the evolution of the abundances of the different chemical elements. Supernovæ are divided in different classes depending on their spectral features (see Figure 2.2).

In a very schematic way, the production of heavy elements depends from the stellar mass in the following way (see, for example, Wheeler et al., 1989):

Very massive stars are expected to go through the pair formation ($\gamma \rightarrow e^+ + e^-$) instability, when their nucleus is still oxygen rich, on a time scale of a few million years. The production of C, Fe and r-process elements (*i.e.* far from the stability valley) is thought to be negligible. The Main Sequence mass lower bound for the pair formation process to occur is very uncertain, but it may be as low as 30 $M_\odot$.

Massive stars ($M \gtrsim 10\ M_\odot$) have e typical lifetime $\tau \lesssim 2 \cdot 10^7$ yr. They are thought to be a major source of oxygen and to contribute substantially to the production of the intermediate-mass elements, from neon to calcium, and to the r-process elements,

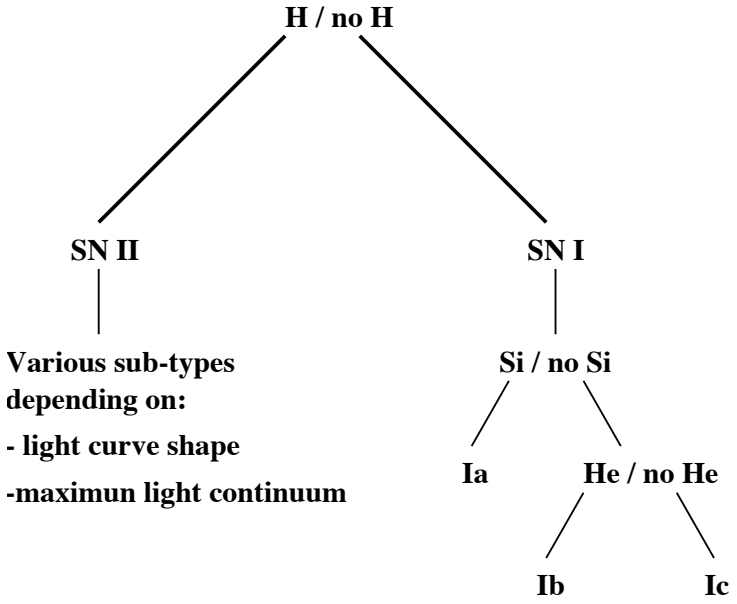

Figure 2.2: *Classification scheme for Supernovæ based on the early-time spectra and other features.*

synthesised both in the stages before and during the explosion as a Type II or Type Ib supernova. Very little production of iron, of the order of 0.075 $M_\odot$ in each event, is expected to come from this range of masses.

Intermediate mass stars These stars ($1 \leqslant M/M_\odot \leqslant 10$) die by ejecting their envelope and leaving the degenerate C/O core to cool as a white dwarf. In this process, they are expected to eject carbon, nitrogen and *s*-process elements, if iron-peak elements are present as "seeds", with typical timescales $\tau \geqslant 10^8 - 10^9$ yr.

Type Ia supernovæ are generally thought to come from a degenerate star in a binary system, accreting mass beyond the Chandrasekhar limit. Thus, the typical timescales are the same as those of the intermediate-mass star involved in the process. They are the major contributors to the abundance of the iron-group elements (about 0.7 $M_\odot$ of iron produced by every supernova), since the light curve is most likely powered by the decay of ^{56}Ni through ^{56}Co to, eventually, ^{56}Fe.

A crucial parameter to constrain the chemical history of a certain environment is the number of supernovæ that have exploded there. This is connected to a measurable quantity, *i.e.* the *mean supernova frequency* per unit luminosity of the host galaxy (ν) defined by:

$$\nu \equiv \frac{N_{SN}}{(\sum_n L_n) \cdot \Delta t} \tag{2.10}$$

where N_{SN} is the number of supernovæ that went off in a sample of galaxies during a monitoring time Δt and L_n is the luminosity of the nth galaxy in the sample. This supernova rate is usually expressed in **SNu**'s and 1 SNu is equal to one supernova per century per 10^{10} $L_\odot$ as deduced from B band measurements. This definition is usually preferred to the mean number of supernovæ per galaxy since the explosion rate depends on the galaxy type and on the host galaxy luminosity. A tentative estimate of the rates for the various types is given in Table 2.3 (see van den Bergh and Tammann, 1991).

	E	S0/a,Sa	Sab,Sb	Sbc-Sd	Sdm-Im
Type Ia	0.98 h^2	0.49 h^2	0.49 h^2	0.49 h^2	0.49 h^2
Type Ib	-	0.04 h^2	0.27 h^2	0.77 h^2	0.91 h^2
Type II	-	0.17 h^2	1.35 h^2	3.93 h^2	4.21 h^2
Total	0.98 h^2	0.70 h^2	2.11 h^2	5.19 h^2	5.61 h^2

Table 2.3: *Supernova frequencies in SNu in different types of galaxies (h is H_0 in units of 100 km s^{-1} Mpc^{-1} and comes from the luminosity in equation (2.10)).*

In Figure 2.3 we show a cartoon of the enrichment process caused by an instantaneous star forming process (the Simple Stellar Population defined in section 2.2.1) superimposed to a constant star formation rate.

2.1.4 The interstellar reddening

If dust is present along the line of sight to a certain object, the light reaching the observer will pass through it and interact with it. As a result, the intrinsic spectrum of the source will be modified in the process. In particular, the dust diffuses and absorbs the longer wavelengths less then the shorter ones and, therefore, a star may appear fainter and redder than it really is. This phenomenon is called *interstellar reddening* or *extinction* (see, for example, Whittet, 1992; Savage and Mathis, 1979).

Suppose that at a certain wavelength λ, the extinction *optical depth* integrated along the line of sight to a certain point source is $\tau(\lambda)$. Then, if $f^0(\lambda)$ is the intrinsic emission of the star at λ, the observed flux $f(\lambda)$ will be:

$$f(\lambda) = e^{-\tau} \cdot f^0(\lambda) \tag{2.11}$$

Astronomers usually express the fluxes in the magnitude scale defined by equation (2.1) on page 8 and, therefore, equation (2.11) is commonly written as:

$$m = m^0 + A(\lambda) \tag{2.12}$$

where $m = -2.5 \cdot \log(f(\lambda)) + ZP$ is the observed magnitude and m^0 is the intrinsic one. The quantity $A(\lambda)$ is usually referred to as *absorption coefficient*, even if it takes into account

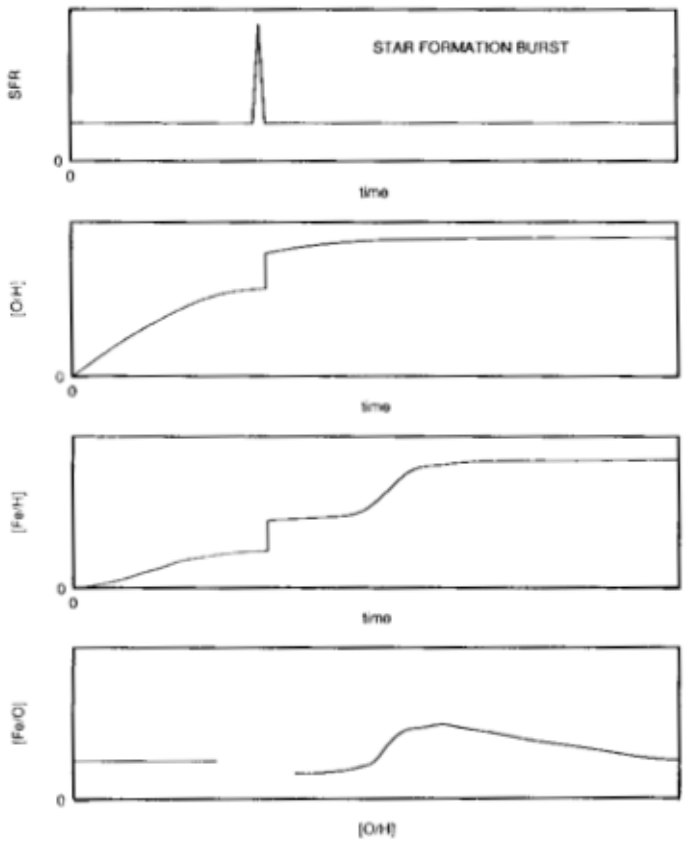

Figure 2.3: *Sketch of the time evolution of different chemical nuclei caused by an instantaneous burst of star formation superimposed to a constant star formation rate.*

both interstellar absorption and diffusion mechanisms. Its relation with τ follows naturally from the definition of magnitude:

$$A(\lambda) = 2.5 \cdot \log(e)\, \tau(\lambda) \tag{2.13}$$

Since extinction is wavelength-dependent, not only it causes the sources to be dimmer, but it also changes their colours. Given two wavelengths λ_i and λ_j, the observed colour c_{ij} is related to the intrinsic one c^0_{ij} by:

$$c_{ij} = c^0_{ij} + [A(\lambda_i) - A(\lambda_j)] = c^0_{ij} + E_{ij} \tag{2.14}$$

where E_{ij} is called the *colour excess*. Once again, if one is dealing with the standard passbands it is customary to write, for example, $E(\mathrm{B-V})$ instead of E_{BV}.

Interstellar absorption is proportional to the number of dust grains between the observer and the star multiplied by the cross section of the extinction process. To disentangle these two effects, is useful to normalise the reddening curve to a given value of the extinction, usually to $E(B-V) = 1$:

$$R(\lambda) \equiv \frac{A(\lambda)}{E(\mathrm{B}-\mathrm{V})} \tag{2.15}$$

In this way, $R(\lambda)$ only depends upon the properties of the dust grains along the line of sight and not on their amount. To increase confusion, A is often used in the literature to indicate both the total extinction, the one we have called A, and R. Given a reddening curve, *i.e.* $R(\lambda)$, equation (2.12) then becomes:

$$m = m^0 + R(\lambda) \cdot E(\mathrm{B}-\mathrm{V}) \tag{2.16}$$

In the definition of $R(\lambda)$, it is preferable to use the difference of the extinction in two bands, for example $E(\mathrm{B}-\mathrm{V})$, instead of an "absolute" extinction, such as $A(\mathrm{V})$, for example, because it is very difficult to measure this latter quantity. As a matter of fact, the zeropoint of the extinction curve is fixed through an extrapolation, requiring that:

$$A_\lambda \overset{\lambda\to\infty}{\longrightarrow} 0$$

because the small interstellar grains are unable to absorb and scatter radiation whose wavelength is much bigger that their size. In Figure 2.4 on the following page we show the galactic absorption curve from Mihalas and Binney (1981).

Curves like this are computed by comparing the energy distribution of a reddened star with that of a star of the same spectral type (*i.e.* with the same intrinsic spectrum), but not reddened. Apart from the peak at $\lambda = 2150$ Å, whose origin is still controversial (graphite, silicates etc.) the general trend is roughly:

$$R(\lambda) = \frac{A(\lambda)}{E(\mathrm{B}-\mathrm{V})} \sim \lambda^{-1} \tag{2.17}$$

Until now, we have examined the case of *monochromatic* observations. What happens when this is not the case, *i.e.* when a filter F of finite width is used? Formally, it is sufficient to substitute $A(\lambda)$ in equation (2.12) with an average value in the filter considered ($\overline{A}_F$). For the same reasons explained above, it is convenient to introduce the normalized average extinction coefficient $\overline{R}_F$:

$$\overline{R}_F \equiv \frac{\overline{A}_F}{E(\mathrm{B}-\mathrm{V})} \tag{2.18}$$

in terms of which the magnitude difference due to an amount of extinction $E(\mathrm{B}-\mathrm{V})$ in the filter F is:

$$\Delta m_F^{E(\mathrm{B}-\mathrm{V})} = m_F - m_F^0 = \overline{R}_F \cdot E(\mathrm{B}-\mathrm{V}) \tag{2.19}$$

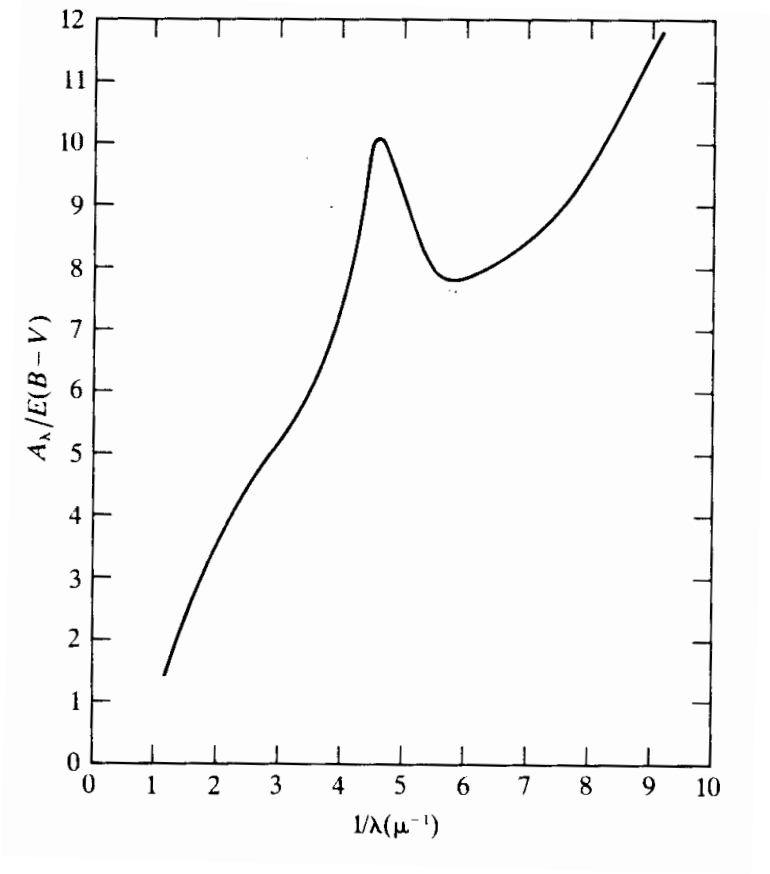

Figure 2.4: *Mean galactic interstellar absorption curve normalised to* $E(B-V)=1$.

Let us now write $\Delta m_F^{E(\mathrm{B-V})}$ explicitly for a given reddening law $R(\lambda)$, as usual normalized to unit $E(\mathrm{B-V})$. If $S^0(\lambda)$ and $S(\lambda)$ are the intrinsic and reddened spectra, respectively, and $F(\lambda)$ is the response curve of the filter:

$$\begin{aligned}\Delta m_F^{E(\mathrm{B-V})} &= -2.5\cdot\log\frac{\int F(\lambda)S(\lambda)\,\lambda\,d\lambda}{\int F(\lambda)S^0(\lambda)\,\lambda\,d\lambda}\\ &= -2.5\cdot\log\frac{\int F(\lambda)\left\{S^0(\lambda)\cdot 10^{-0.4[R(\lambda)\cdot E(\mathrm{B-V})]}\right\}\lambda\,d\lambda}{\int F(\lambda)S^0(\lambda)\,\lambda\,d\lambda}\end{aligned}$$

Which, combined with equation (2.19), leads to the explicit expression for $\overline{R}_F$ we are looking for:

$$\overline{R}_F = -\frac{2.5}{E(\mathrm{B-V})}\cdot\log\frac{\int 10^{-0.4[R(\lambda)\cdot E(\mathrm{B-V})]}\,F_i(\lambda)S^0(\lambda)\,\lambda\,d\lambda}{\int F_i(\lambda)S^0(\lambda)\,\lambda\,d\lambda} \tag{2.20}$$

Finally, since:

$$10^x \overset{x\to 0}{\longrightarrow} 1 + (\ln 10)\, x \quad \text{and} \quad \log(1+x) \overset{x\to 0}{\longrightarrow} (\log e)\, x$$

it is easy to compute the value of $\overline{R}_F$ in the limit of zero reddening:

$$\overline{R}_F \overset{E(\mathrm{B-V})\to 0}{\longrightarrow} \frac{\int R(\lambda)\, F_i(\lambda) S^0(\lambda)\, \lambda\, d\lambda}{\int F_i(\lambda) S^0(\lambda) \lambda\, d\lambda} \tag{2.21}$$

So, besides the natural dependence on the reddening curve $R(\lambda)$ and the filter response curve, the absorption coefficient also depends on the spectrum of the source and on $E(\mathrm{B-V})$. These last two are often neglected. On the contrary, as we will see in section 5.2.1, we have used the these formulæ to compute the absorption coefficients in the most accurate way possible.

In order to correct for the effects of reddening, one needs observations in at least three passbands, *i.e.* two colours, to distinguish between an intrinsically blue star reddened by dust and an intrinsically red one with no significant amount of dust along the line of sight. In some astrophysical environments, such as the galactic Globular Clusters, all the stars have the same reddening, since all the dust is in the foreground. In young, dust-rich regions, instead, the reddening may vary significantly from star to star because of the clumpiness of the interstellar material. Using an average absorption coefficient, then, can lead to an erroneous determination of the intrinsic temperature and luminosity of a star and, hence, of its evolutionary state.

2.2 The framework

To set the framework in which our research is inserted, let us begin with a few basic concepts and results on the way everything begins: the star formation process.

2.2.1 Star formation, Initial Mass Function and Present Day Mass Function

Clusters of young stars are always associated with the presence of dense nebulæ and interstellar dust clouds. Hence, they are thought to be formed by condensation from interstellar material (see, for example, the review article by Shu et al. 1987).

The simplest star formation history that one can imagine consists of a single burst out of a chemically homogeneous interstellar environment, with a negligible time extent as compared to the time scales of evolution of the stars that are generated. Such an event would produce, of course, stars all of the same chemical composition, since no chemical enrichment takes place during this instantaneous process. For rather obvious reasons the result of this process is

called a *Simple Stellar Population* (SSP). This is an important elementary tool of description, since, in general terms, every star formation history, no matter how complicated, can be regarded as the superposition of Simple Stellar Populations born at different times and with different metallicities.

The Simple Stellar Population is characterised by the so-called **Initial Mass Function** (**IMF**). This gives the number of stars of different masses formed. So, if N is the number of stars formed and M is their mass, the IMF (ζ) is defined as:

$$\zeta(M) \equiv \frac{dN}{dM} \equiv N_{tot} \cdot f(M) \tag{2.22}$$

where N_{tot} is the total number of stars formed and $f(M)$ is the fraction of them with masses between M and $M + dM$. Its integral is normalized to unity:

$$\int_{M_l}^{M_u} f(M)\, dM = 1 \tag{2.23}$$

where M_l and M_u are the lowest and highest masses formed, respectively.

As it can be seen from equation (2.22), $f(M)$ contains all of the information about the *shape* of the IMF and N_{tot} is just a scaling factor. For this reason, $f(M)$ itself is often referred to as IMF.

In the following, we will often express the IMF as the number of stars per unit *logarithmic* interval:

$$\xi(\log M) \equiv \frac{dN}{d\log M} \equiv N_{tot} \cdot F(\log M) \tag{2.24}$$

again, the information on the shape of the IMF is entirely contained in $F(\log M)$.

Of course, the number of stars in a given mass interval must be the same regardless of which function is used, $f(M)$ or $F(\log M)$. This implies that:

$$F(\log M)\, d\log M = f(M)\, dM$$

and, hence:

$$F(\log M) = \ln(10) \cdot M f(M) \tag{2.25}$$

The same relation links $\xi(\log M)$ to $\zeta(M)$.

Let us notice here that, in general, the mass function is not a directly measurable quantity, since it is very difficult to determine the masses of the stars. What is generally done, then, is to count the number of stars per unit magnitude in a certain passband m_i (*Luminosity Function*) and to convert this number to the desired one using a mass-magnitude relation, which can be either theoretical or empirical:

$$\zeta(M) = \frac{dN}{dm_i} \cdot \frac{dm_i}{dM} \tag{2.26}$$

Given a certain metallicity and as long as Main Sequence stars are considered, the mass-magnitude relation is a one-to-one correspondence.

In addition to the Simple Stellar Population, there is another ideal case in which it makes sense to talk about IMF: the case of a non instantaneous star formation during which, however, the mass dependence of the IMF remains constant with time. There is indeed *hope* that the might be a *universal function*, which would be independent of the specific conditions leading to star formation. In this case the IMF, or its shape, at least, might be the same in different galaxies.

Even under this assumption of a constant IMF, its reconstruction from the observed luminosity function requires significant non-trivial assumptions and modelling. Let us consider here an astrophysical environment in which stars have been forming over a period of time T_0, from $t = 0$ (the epoch at which the first stars were born) to $t = T_0$ (the present epoch, the one at which observations are made). What we see now, the *Present-Day Mass Function* (PDMF), is the superposition of the different generations of stars born all along the lifetime T_0 of the region considered. It does not reflect the frequency distribution of masses at birth because the Main Sequence lifetime is a function of the star's mass. Let us call this quantity $\tau(M)$. Stellar evolutionary models show that $\tau(M)$ is a decreasing function of mass, *i.e.* more massive stars have shorter Main Sequence lifetimes, as shown in Table 2.2 on page 13.

As a consequence, stars for which $\tau(M) \geqslant T_0$ did not have time to evolve and, for them, the PDMF counts all stars ever born. In fact, it is the time integral of the stars formed over the lifetime T_0. On the other hand, stars for which $\tau(M) < T_0$, depending on when they were born, may have had time to evolve and we only observe those which were born in the last $\tau(M)$ years.

Following the notation of Miller and Scalo (1979) and Scalo (1986), let us introduce the *Creation Function* C, such that $C(\log M, t) d\log M\, dt$ is the number of stars born per unit area in the galactic disk in the mass range $(\log M, \log M + d\log M)$ in the time interval $(t, t + dt)$. The Creation Function can be related to an observable quantity, the Present-Day Mass Function $\xi_{PD}(\log M)$. The PDMF, in turn, is defined so that $\xi_{PD}(\log M) d\log M$ gives the number of *observed* stars with masses between in the interval $(\log M, \log M + d\log M)$.

As we have already noticed, the stars for which $\boldsymbol{\tau(M) \geqslant T_0}$ are all on the Main Sequence at $t = T_0$ and so:

$$\xi_{PD}(\log M) = \int_0^{T_0} C(\log M, t)\, dt \quad \text{if} \quad \tau(M) \geqslant T_0 \tag{2.27}$$

On the other hand, if $\boldsymbol{\tau(M) < T_0}$, we only see those stars born between $T_0 - \tau(M)$ and the present epoch, since the ones which were born before that have already evolved:

$$\xi_{PD}(\log M) = \int_{T_0-\tau(M)}^{T_0} C(\log M, t)\, dt \quad \text{if} \quad \tau(M) < T_0 \tag{2.28}$$

It is important to notice that, if the star formation process ended at a time $T_1 < T_0$, all the stars with a lifetime $\tau(M) < T_0 - T_1$ have already evolved and:

$$\xi_{PD}(\log M) = 0 \quad \text{if} \quad \tau(M) < T_0 - T_1$$

As a consequence, there is a maximum mass (M_M) that can be probed, set by:

$$\tau(M_M) = T_0 - T_1 \tag{2.29}$$

In Globular Clusters, for example, whose age is typically greater than 12 Gyrs, only stars with masses smaller than roughly 0.8 $M_\odot$ are still on the Main Sequence.

In principle, equation (2.27) and (2.28) contain all the information needed. Unfortunately, though, they are of little practical use, because the Creation Function is unknown. However, these equations can be greatly simplified by assuming that the Creation Function is a *separable function* of mass and time and, then, it can be written in the following form:

$$C(\log M, t) = F(\log M) \cdot B(t) \tag{2.30}$$

where $F(\log M) d\log M$ is the fraction of stars formed with masses between $\log M$ and $\log M + d\log M$ and $B(t)dt$ is the number of stars born in time interval $(t, t+dt)$. In the literature $B(t)$ is often referred to as *stellar birthrate*. A related concept is the **Star Formation Rate** (SFR), defined as the total *mass* of the stars formed per unit time. Given the way we have chosen the origin of times, $B(t) = 0$ for $t < 0$. The normalization of $B(t)$ is such that the total number of stars ever formed in the region considered in the course of its lifetime is:

$$N_{tot} = \int_0^{T_0} B(t)\, dt \tag{2.31}$$

In general, we are only interested in the *shape* of the IMF and, hence, the normalization is arbitrary. A noticeable exception is the case of the field stars, *i.e.* stars in the Solar Neighbourhood, that we shall examine in section 2.2.2. The facts that stars of different masses can be observed to different limiting distances and the dependence of the disk scale height on the age, *i.e.* mass, require that the IMF be normalized per unit area of the disk.

In the case of the Simple Stellar Population described above, the star formation activity is limited to one single burst at $t = 0$, and $B(t) \sim \delta(0)$, where δ is Dirac's delta function.

On the existence and nature of the IMF

While the mathematical meaning of equation (2.30) is straightforward, its physical applicability is a more subtle matter. It often stated that it is just an assumption made for the sake of convenience and simplicity and its validity is assessed with various arguments. This approach was followed, for example, by Miller and Scalo (1979).

There is, however, an alternate approach, based on the stochastic nature of the star formation process. The argument, as extensively carried out in Scalo (1986), is as follows. Suppose we visualize the star formation process as stars forming individually at random positions in a given environment, for example the disk of our Galaxy. If the value M of the mass of a new-born star is a random value distributed according to some probability density $f(M)$, then one can think of each position as a realization of a stochastic time process $M(t)$ and the collection of stars as a statistical ensemble. If, then, this process is stationary in time and homogeneous in space, the definition of $f(M)$ is unambiguous: $f(M)dM$ is the fraction of stars at birth with masses between M and $M + dM$ in *any volume of space*. Of course, in order to recover the initial distribution, the observed number of stars in each mass interval needs to be corrected for the effects of the finite, mass dependent stellar life time.

However, stars are not formed independently of each other, but are observed to be born in groups. If this is the case, then, every cluster can be regarded as a realization of the star formation process and, as a consequence, of the IMF. Individual star forming regions will, then, have different IMFs, but the ensemble-average over a large number of them would still have a well defined statistical meaning.

The group can either remain bound or be disrupted and its members mixed with stars born in other groups. This latter scenario is the one of the Galactic disk, for example. In this case, the lower mass stars would have time during their Main Sequence evolution to move to large distances from their birth site. Massive stars, on the other hand, are short lived and are observed near where they were born. The situation, then, is very different from the simple case in which stars are born individually at random positions in the disk. Given a particular volume, the inferred IMF is a meaningful ensemble average only if the star formation process is indeed stationary in time and homogeneous in space. Any *systematic* variation with space or time would lead to an IMF determination that is only loosely related to the statistically correct ensemble average, may it be over the history of the disk, or a spatial mean at a given time.

Alternatively, one could determine the mass function in a large number of clusters of the *same age* and compute the IMF as their average. In this case, the IMF would be a spatial average at a particular time interval in the past. By comparing the results for clusters of different ages, it could be possible to estimate the time dependence of the IMF. In practice, though, there are limitations to the applicability of this method. For example, the higher mass probed in each cluster would depend upon its age. Also, the lower mass observed would depend on the distance of cluster from us: the farther away the cluster is, the fainter stars

of a given mass would appear. Also, as the observed region would look more crowded, a reliable photometry for faint stars would become more problematic. All in all, every cluster would give an insight only on a certain mass interval and combining them all together would again require the IMF to be stationary and homogeneous.

Let us conclude this digression by quoting Scalo (1986, page 8): *"the best we can do at present is to attempt an estimate of the IMF by assuming it to be constant in space and time, and then examine the nature of the fluctuations of this function among individual groups of stars, and search for evidence regarding systematic variations with position and time in our own and other galaxies"*.

Results for a separable Creation Function

Let us now go back to equation (2.30) and introduce the *relative birthrate* $b(t)$:

$$b(t) \equiv \frac{B(t)}{\langle B \rangle} \tag{2.32}$$

where $\langle B \rangle$ is the average birthrate over the history of the region:

$$\langle B \rangle = \frac{1}{T_0} \int_0^{T_0} B(t)\, dt$$

From equation (2.31), we can now write the total number of stars N_{tot} as:

$$N_{tot} = \langle B \rangle \cdot T_0 \tag{2.33}$$

By using equations (2.24), (2.32) and (2.33), equation (2.30) can be re-written as:

$$C(\log M, t) = F(\log M) \cdot \langle B \rangle \cdot b(t) = \frac{\xi(\log M)}{T_0} \cdot b(t)$$

and, using equation (2.27) and (2.28), we finally have a relation between the IMF (ξ) and the observable Present-Day Mass Function (ξ_{PD}):

$$\xi(\log M) = \begin{cases} \xi_{PD}(\log M) \cdot T_0 \cdot \left[\int_{T_0 - \tau(M)}^{T_0} b(t)\, dt \right]^{-1} & \text{if} \quad \tau(M) < T_0 \\ \xi_{PD}(\log M) & \text{if} \quad \tau(M) \geqslant T_0 \end{cases} \tag{2.34}$$

Of course, the first one of these equation only makes sense for $M \leqslant M_M$ (see equation (2.29)).

Let us notice here that for massive stars, *i.e.* the ones for which $\boldsymbol{\tau(M) \ll T_0}$, a Taylor expansion of $b(t)$ in the first equation leads to:

$$\xi(\log M) = \frac{\xi_{PD}(\log M)}{\tau(M)} \cdot \frac{T_0}{b(T_0)} \tag{2.35}$$

which means that the *shape* of the IMF of massive stars can be determined from the observed Present Day Mass Function and the knowledge of the Main Sequence lifetimes as a function of M. Its normalization is dictated by the ratio between the age of the region considered and $b(T_0)$, *i.e.* the ratio of the present birthrate to the average one in the past (see equation (2.32)). No detailed knowledge of the time dependence of b is necessary.

To summarize, once the evolved stars are rejected from the observed sample, the ingredients that enter the determination of the IMF are: the luminosity function, *i.e.* the number of stars observed per unit magnitude, the mass-magnitude relation to convert it to the observed mass function, the Main Sequence lifetimes and the Star Formation rate (see equation (2.34)). In addition, depending on the environment considered, further corrections may be needed to take into account dynamical effects, such as mass segregation in Globular Clusters, or the correlation between a star's age, and, hence, mass, and its height above the plane of the Galactic disk or selection effects (more luminous stars are visible out to greater distances).

Let us stress once more that equation (2.34) holds ONLY if the Creation Function is *separable*, *i.e.* if it can be separated into the product of a function of mass alone and a function of time alone (equation (2.30)). This is equivalent to requiring that the mass spectrum of the newly formed stars is independent of time. It is, perhaps, remarkable that no variations of the luminosity function with metallicity have been found for field stars in the Solar Neighbourhood (Hartwick et al., 1984), corroborating this hypothesis (see also Miller and Scalo, 1979). On the other hand, there are indications (Panagia, 1980; Lenzuni and Panagia, 1998) that the *upper limit cutoff* does depend on metallicity, in the sense that the higher the metallicity the lower the mass cutoff. This result is based on the fact that HII regions, *i.e.* regions in which the hydrogen is ionized, show less helium ionization as the metal content increases, disclosing the presence of fewer stars with surface temperature higher than the one required to ionize this element ($T_{eff} \geqslant 38,000$ K).

In conclusion:

- Only stars for which $\tau(M) \geqslant T_0$ are still on the main sequence today, regardless of when they were formed. For them, the IMF determination from the observed PDMF is straightforward using the second equation (2.34);
- The IMF for massive stars, the ones for which $\tau(M) \ll T_0$, can also be estimated fairly easily with equation (2.35);
- For intermediate mass stars, the ones with a lifetime comparable to T_0, the situation is much more difficult because a detailed knowledge of the star formation history is required, as shown by the first equation (2.34). A careful discussion of the influence of

the details of the birthrate dependence with time on the determination of IMF can be found in Miller and Scalo (1979).

In the case of the disk of the Galaxy, for example, $T_0 \simeq 10$ Gyrs and the threshold between evolved and non-evolved stars is at roughly 1 $M_\odot$. Equation (2.35) can be safely applied for stars more massive than roughly 2 $M_\odot$ (see Table 2.2).

2.2.2 IMF from the Solar Neighbourhood

In his pioneering work of 1955, Edwin Salpeter found that the IMF in the Solar Neighbourhood is well fitted by a *power law*:

$$f(M) \sim M^\alpha, \quad \alpha = -2.35 \tag{2.36}$$

for stars in the mass range $0.4 \leqslant M/M_\odot \leqslant 10$. A constant Star Formation Rate was used in the derivation.

Ever since Salpeter's seminal paper, the IMF has often been represented either as a single power law or as a superposition of power laws, each covering a different mass ranges. While α is commonly used to indicate the slope of the IMF expressed per unit linear mass, Γ is often used for the slope of the IMF expressed per unit logarithmic mass. From equation (2.25) on page 20, it follows that $\Gamma = \alpha + 1$.

More recent works seem to suggest that the IMF might be flatter then the Salpeter value at the lowest masses and steeper for $M/M_\odot > 10$. For example, the widely used, empirical IMF of Miller and Scalo (1979) is better represented by a log-normal form:

$$\log\left[\xi(\log M)\right] = a_0 - a_1 \cdot \log(M) - a_2 \cdot \left[\log(M)\right]^2 \tag{2.37}$$

The best fit to the data is achieved for a constant star formation over the past 12 Gyrs. The parameters in equation (2.37) are equal to: $a_0 = 1.53$, $a_1 = 0.96$, $a_2 = 0.47$. This corresponds to a law of the form (2.36) with an exponent that varies with mass: $\alpha = -1.4$ for $0.1 \leqslant M/M_\odot \leqslant 1$, $\alpha = -2.5$ for $1 < M/M_\odot \leqslant 10$ and $\alpha = -3.3$ for $M/M_\odot > 10$.

Changing the age of the disk does not seem to affect the slope of the IMF and, therefore, Miller and Scalo (1979) take it to be independent of the birthrate history.

In Figure 2.5, we show these two IMFs (Salpeter, 1955; Miller and Scalo, 1979) together with a third one (Rana, 1991), showing even more structure. As it can be seen, the general trend is the same for all of them, but the differences are not negligible.

As we have already noticed, the high-mass end of the Miller and Scalo (1979) Initial Mass Function is steeper than the extrapolation of the simple Salpeter power-law above 10 $M_\odot$. Scalo (1986) has computed a new IMF using *the same observational dataset* as Miller and Scalo (1979), but with updated stellar models, *i.e.* different Main Sequence lifetimes and mass-luminosity relation. The result, shown in Figure 2.6 on page 28, is that this

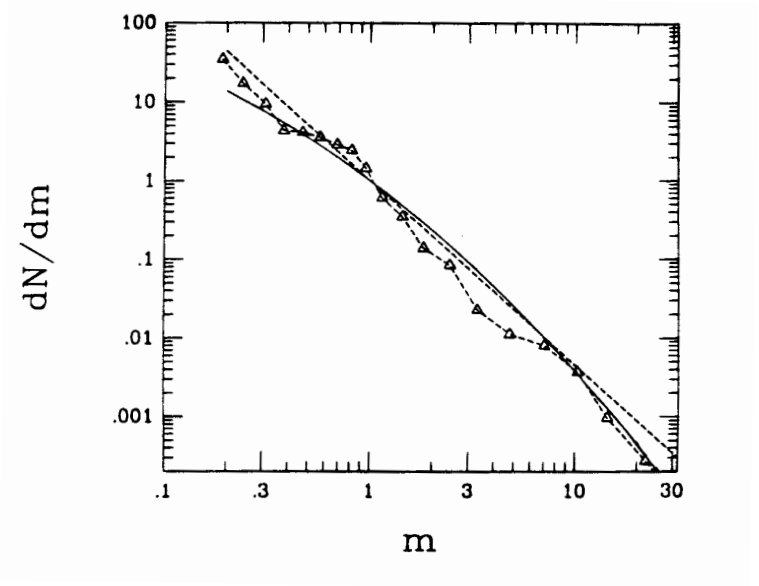

Figure 2.5: *Three different determinations of the IMF in the Solar Neighbourhood: power-law (Salpeter (1955), dashed curve), log-normal (Miller and Scalo (1979), solid curve) and Rana (1991)). All the distributions are normalised to unity at* $m = M/M_{\odot} = 1$.

discrepancy does not exist any more and that the high-mass end is compatible with a slope of $\Gamma = \alpha + 1 = -1.35$. Of course, the difference still remains for the lower masses, where a turn-over is present in the Miller and Scalo (1979) and Scalo (1986) mass functions, whereas the extrapolation of the Salpeter (1955) function goes on increasing.

The Miller and Scalo (1979) IMF is still widely used, despite the fact that John Scalo himself does not see any longer any evidence for a log-normal form for the Solar Neighbourhood IMF (Scalo, 1998).

2.2.3 IMF from the Globular Clusters

To avoid the difficulties described above concerning the star formation history, one may think of astrophysical environments in which the star formation process took place (almost) instantaneously. The most obvious candidates for this occurrence may seem to be the galactic Globular Clusters. Unfortunately, the use of Globular Clusters to determine the IMF is in practice limited by two factors.

Firstly, Globular Clusters are very old, older than 12 Gyr, and hence, by now, only stars with masses lower than, approximately, 0.8 $M_{\odot}$, are still on the Main Sequence. More massive stars have already evolved to their final fate of dark remnants or cooling White Dwarfs (WD). In principle, it would be possible to use the White Dwarf luminosity function to constrain the IMF for the WDs progenitors, but this requires very deep photometry to reach the portion of the cooling sequence influenced by the IMF. According to Brocato et al. (1998), at luminosities brighter than $M_V \simeq 15$, WD evolutionary times are short enough that the luminosity function only depends upon them and not on the WD progenitor's

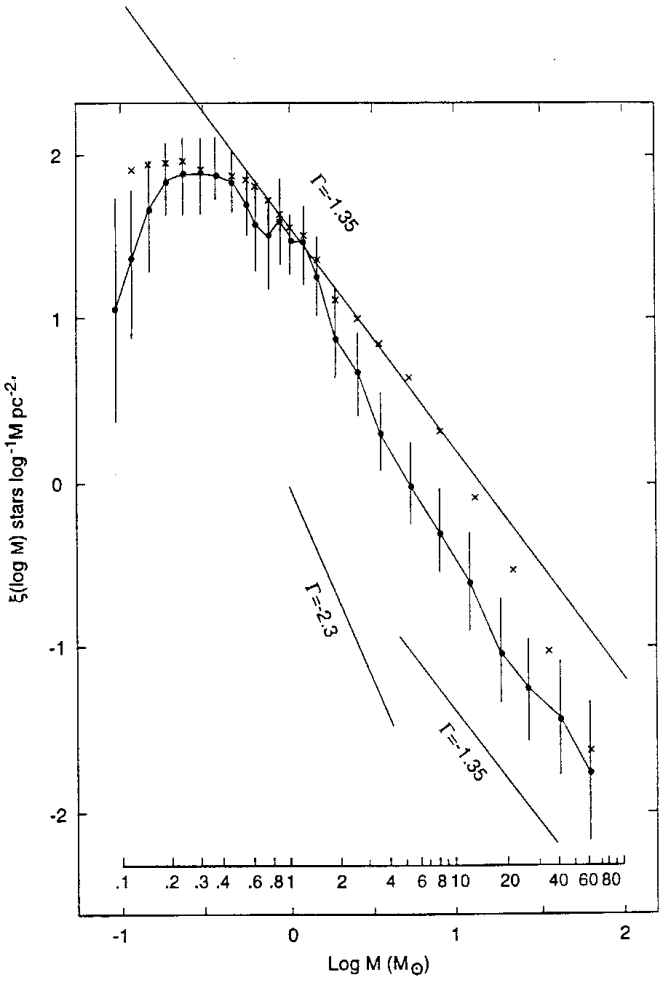

Figure 2.6: *Comparison of the Miller and Scalo (1979, crosses) and Scalo (1986, filled dots) IMFs. For reference, the Salpeter (1955) slope* ($\Gamma = \alpha + 1 = -1.35$) *and an approximation to the high mass end of the Miller and Scalo (1979) slope* ($\Gamma = -2.3$) *are also indicated as full lines.*

Initial Mass Function. Below this luminosity, instead, as the cooling times become longer, different IMFs lead to different expected numbers of WDs. In particular, given an age for the cluster, the flatter the IMF, the more low luminosity WDs are expected. Unfortunately, this effect may prove to be difficult to detect, even with *HST*. This is because an absolute magnitude of $M_V \simeq 15$ corresponds, for the closest Globular Clusters, to an apparent one of $m_V \simeq 27$. Good photometry for stars this faint is non trivial. In conclusion, mass function studies in Globular Clusters are restricted to stars that are currently on the Main Sequence, *i.e.* masses lower than, approximately, 0.8 $M_\odot$.

Furthermore, dynamical processes, both internal (mass segregation) and external (interactions with the Galaxy) result in variations of the mass spectrum with respect to the IMF. As it can be expected, dynamical computations based on multicomponent King models (Pryor et al., 1986), have shown that mass segregation causes the PDMF exponent (see equation (2.36)) to be larger than the true IMF one at large radii and smaller near the centre

of the cluster. However, it has been claimed (Richer and Fahlman, 1991), both from Fokker-Planck computations and from multi-mass King models, that the observed mass function for low mass stars "somewhere near" the half mass radius of the cluster should not be significantly different from the IMF. This very vague statement, which is only true in the absence of extensive tidal stripping, however, does not hold at all for masses of the order or greater than about 0.5 $M_\odot$. In any case, it is very difficult to disentangle the effects real variations in the IMF from those caused by dynamical processes.

A large body of ground-based observations (Richer et al., 1991) suggested that the low-mass end of the *luminosity* function is steeply rising leading to steep *mass* functions, possibly as steep as $\alpha = -2.7$ in the case of M13. This result, however, does not appear to be confirmed by recent, post-refurbishment *HST* observations. In fact, since the first detection with *HST* and subsequent study of the very end of the main sequence in the galactic Globular Cluster NGC 6397 by Paresce et al. (1995), there has been rising evidence for a sharp turnover in the luminosity function at $M_I \simeq 8.5$ where the number of stars starts decreasing: De Marchi and Paresce (1995a, M15), De Marchi and Paresce (1995b, 47 Tucanæ), Elson et al. (1995, ω Cen) and, again on NGC 6397, Cool et al. (1996); Mould et al. (1996). See also Piotto et al. (1997) for a comparison among 4 clusters: M15, M30, M92 and NGC 6397. The case of NGC 6397 is shown in Figure 2.7.

This discrepancy between ground and space-based results is probably due to the crowding of stars. This problem is much less severe from space than it is from the ground, because of the much better spatial resolution that is attained by avoiding the earth's atmosphere. As a matter of fact, little or no completeness corrections ($\sim 10\%$) are required for *HST* data, making the measurements much easier and reliable. This makes *HST* observations absolutely crucial when dealing with stellar statistics in order to minimise the effects of crowding, that can lead to bad measurements, and blending, *i.e.* two or more stars with an angular separation smaller than the resolution of the instrument that are detected as a single object.

Let us stress again here that, given an observed luminosity function, the corresponding mass function depends upon the adopted mass-luminosity relation following equation (2.26). This transformation is particularly difficult in this low-mass, low-metallicity regime (Elson et al., 1995). This causes the determination of the mass function to be very uncertain. In any case, mass functions rising as steeply as those found from the ground seem now unlikely.

2.2.4 IMF for Young Stellar Populations

To avoid the problems introduced by a complicated star formation history and by dynamical evolution as well as to be able to probe the massive portion of the IMF, we have chosen a different environment for our research: the Large Magellanic Cloud (LMC, an irregular galaxy, the closest companion of the Milky Way). We will return on the motivations for this choice later.

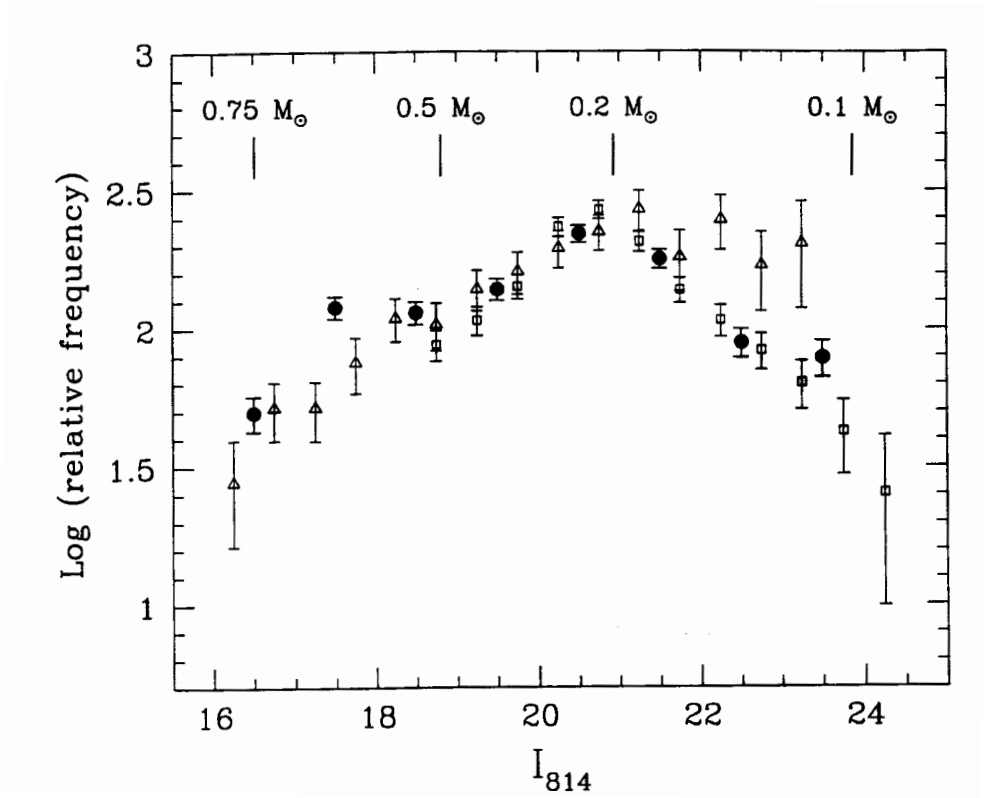

Figure 2.7: *Comparison of* HST *(Paresce et al. (1995, opens squares) and Cool et al. (1996, filled dots)) and ground-based (Richer et al., 1991, open triangles) I band luminosity functions for the galactic Globular Cluster NGC 6397. Marked masses are based on the mass-luminosity relation (D'Antona and Mazzitelli, 1996).*

As an example of an IMF determination in the LMC, let us consider R136, the centre of the the star cluster NGC 2070 in the HII region 30 Doradus in the Large Magellanic Cloud. An HII region is characterised by the presence of hydrogen ionized by the light coming from massive, *i.e.* hot and luminous, stars. Using the WFPC2 camera on board of the Hubble Space Telescope, Hunter et al. (1995, 1996) have studied the stellar population there using three broad band filters: B, V and I. Although they had to overcome some problems in calibrating the camera (the images were taken short after its deployment) they found that the Main Sequence Turn Off is very tight, indicating that the bulk of the stars are coeval. Furthermore, from the comparison with theoretical isochrones, they found that the average age is 3-4 Myr. The lower mass stars ($2< M/\mathrm{M}_\odot\ 4-5$), then, were formed in the same time period (1-5 Myr) as the high mass ones ($M \geqslant 25\ \mathrm{M}_\odot$). This is in contrast with theoretical models that predict that massive stars form last and stop further star formation (Lada, 1987). Some stars, however, may be as young as 1-2 Myr.

Since the time it takes for a star more massive than 2.25 $M_\odot$ to reach the *birthline*, *i.e.* the point at which it first becomes optically visible, is short (less than 0.6 Myr; Palla and Stahler, 1990), Hunter and collaborators do not expect a large population of invisible stars. On the other hand, since the cluster is so young, only stars more massive then, say, 25 $M_\odot$ have already exploded as Supernovæ. Therefore, to use their own words, "it is likely that most of the stars that have formed in R136 in the mass range of 2 to 15 $M_\odot$ are optically visible, and our census of the region, the present day mass function, is also a true *Initial* Mass Function".

Dividing the cluster in 5 radial bins, and assuming an average age of 4 Myr, they determined the IMF as a function of radius (Figure 2.8).

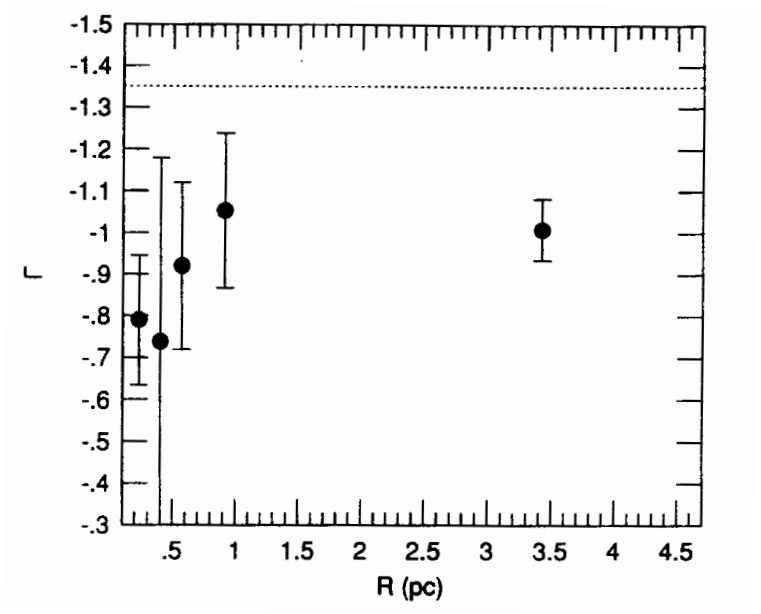

Figure 2.8: *PDMF slope in R136 for different radial bins.* $\Gamma = \alpha + 1$ *is the slope of the* $F(\log M)$*, see equation (2.25). As discussed in the text, the PDMF most likely coincides with the related IMF. The dashed line corresponds to the Salpeter (1955) slope.*

The smaller the distance from the centre, the larger is the minimum mass that can be probed, because of crowding and the incompleteness becomes too large to determine the IMF below about 2.8 $M_\odot$. As it can be seen in Figure 2.8, there may be a hint that the IMF is shallower at the centre than in the outskirts, but the errors are too big to conclude anything. If mass segregation is indeed in action in the mass range explored, its effects are smaller than detectable with this set of data. The overall slope in the region beyond 0.5 pc from the centre is $\Gamma = \alpha + 1 = -1.1 \pm 0.1$. For comparison, the classical Salpeter (1955) value is $\Gamma = -1.35$ and the Miller and Scalo (1979) one, in this mass range, is -1.5.

2.2.5 Overview of the IMF from resolved population

In the previous sections we have described a few examples of IMF determinations from resolved populations in different environments. Recently, Scalo (1998) has exhaustively

reviewed the subject. In particular, he has collected IMF slope determinations for 61 clusters in the Galaxy and in the Large Magellanic Cloud. The result is shown in Figure 2.9, where the power law index Γ is plotted against the average value of $\log(m) = \log(M/\mathrm{M}_\odot)$ for each determination. Error bars typically range from 0.1 to 0.4 in Γ.

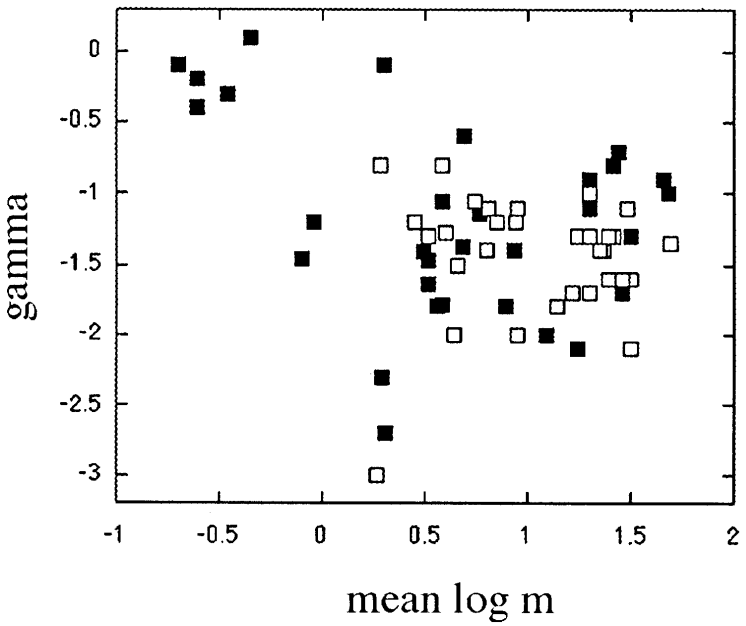

Figure 2.9: *IMF exponent Γ for 61 clusters in the Galaxy (filled symbols) and the Large Magellanic Cloud (open symbols) as a function of the average value of $\log(m) = \log(M/\mathrm{M}_\odot)$ as compiled by Scalo (1998).*

As it can be seen, the spread is quite large, in particular for $m = M/\mathrm{M}_\odot \gtrsim 1$, probably larger than a supporter of a universal IMF would like it to be. In fact, given the spread, there probably is no basis for adopting some average IMF.

An inspection of Figure 2.9 leads to two possible conclusion. It could be the case that *systematic* uncertainties among different determinations are so large that that the IMF cannot be yet estimated with any degree of confidence. Or, on the other hand, it could also be that the slope variations are real. If this is the case, though, the IMF variations do not seem to be strongly correlated with environmental parameters such as metallicity, density, galactocentric distance etc.

If the IMF variations are indeed real, than theoretical models should be able not only to predict an average IMF, but also a scatter similar to the observed one. For example, the model proposed by Elmegreen (1997), briefly described on page 38, can explain the scatter in Figure 2.9 simply as the result of different random realizations of the same system, in the sense that we have discussed in section 2.2.1.

As a concluding remark of his review, Scalo (1998), *if forced to choose an IMF for use in galactic evolution studies", suggests a three-segment power law form for it (which is not meant to be taken as implying that the IMF is a power law over any mass range):*

$$\Gamma = \begin{cases} -0.2 \pm 0.3 & \text{for} \quad 0.1 \leqslant M/\mathrm{M}_\odot < 1 \\ -1.7 \pm 0.5 & \text{for} \quad 1 \leqslant M/\mathrm{M}_\odot < 10 \\ -1.3 \pm 0.5 & \text{for} \quad 10 \leqslant M/\mathrm{M}_\odot < 100 \end{cases} \tag{2.38}$$

Here, the symbol $\pm$ is not the error on the quoted slope, but rather the rough range of slopes found in the literature. As we have discussed, it may be interpreted either as a measure of the observational uncertainties or as an indication of the real IMF variations, or both.

2.2.6 IMF from unresolved populations

In all of the examples we have discussed so far, the stellar content of a given region was determined by counting the individual stars, the evolutionary status and masses of which were derived from photometry and/or spectroscopy. Of course, this is the most direct and reliable way to determine the Present Day Mass Function and, ultimately, the IMF. Unfortunately, though, this is only feasible for the closest galaxies beyond the Milky Way. As a matter of fact, beyond a few Mpc the angular resolution attainable even with diffraction-limited observatories like *HST* is not high enough to resolve the individual stars. As an example, let us consider the case of the star clusters in NGC 1569, a galaxy at 2.5 Mpc. According to De Marchi et al. (1997), their typical angular size is of the order of $0''.1$, *i.e.* smaller than the resolution of the Wide Field detectors of the Wide Field and Planetary Camera on board *HST* (see section 3.1 for a brief description of this instrument). As a consequence, one has to rely only on the integrated light to probe the stellar content of these associations.

In the case of not-so-young stellar populations, the integrated spectrum in the optical depends very little on the slope of the IMF and is mostly affected by the age of the population itself, as we shall see in the case of the nuclear region of the spiral galaxy M51.

The optical colours of hot stars also suffer from a severe degeneracy at $\lambda > 3000$ Å. For example, the (U−B) and (B−V) colours are almost constant in the 40 to 100 $\mathrm{M}_\odot$ range (Massey et al., 1995). So, in the case of hot stars, *i.e.* young populations, it is necessary to access the UltraViolet (UV, roughly at 1500 Å) or, better still, far-UltraViolet (far-UV, shortward of the Lyman limit of 912 Å) regions of the spectrum.

These hot and young stars are generally still embedded in the gas and the dust from which they were born. The interstellar medium re-processes the stellar radiation by absorbing it and re-emitting it at longer wavelengths. The disadvantage of this is that, in the process, part of the flux is extracted from the beam reaching the observer and, thus, the source appears dimmer and, in the most extreme cases, might not be visible at all. On the other hand, however, this allows an analysis of the UV and far-UV photons from the stars via the nebular recombination lines and continuum flux re-processed to infrared wavelengths. Without going into the details, let us here review briefly the different diagnostic techniques

commonly used to infer the stellar content of a young region when it is not feasible to count directly the stars.

Some of the UV flux is absorbed and heats the dust grain to an equilibrium temperature of about 40 K and then is re-emitted peaking at roughly 60μm (Soifer et al., 1987), in the *far-InfraRed*. This simple picture can be complicated by the presence of an additional far-IR emission due to the heating by an old disk component. In any case, if the dominant component of the far-IR light is the UV radiation reprocessed, the Star Formation Rate (SFR) and luminosity at 60μm (L_{IR}) are related by:

$$SFR\,(10 \rightarrow 100\ \mathrm{M}_{\odot}) = 26 \cdot \frac{L_{IR}}{10^{11} L_{\odot}} \left(\mathrm{M}_{\odot}\ \mathrm{yr}^{-1}\right) \tag{2.39}$$

if the slope of the mass function is the Salpeter value between 10 and 100 $\mathrm{M}_{\odot}$ (Hunter et al., 1986). The far-IR flux is most sensitive to stars with masses around 10 $\mathrm{M}_{\odot}$ and Star Formation Rates derived for other mass ranges have to assume a given slope of the Mass Function.

Another method uses the *nebular emission lines*, *i.e.* the recombination lines or excited transitions generated in the interstellar medium are used to infer the spectrum of ionising photons. This, in turn, is used to model the stellar population that produces the photons. This method probes the content of stars with significant far-UV fluxes, that is hotter than about 30,000 K, corresponding to a Main Sequence mass larger than 20 $\mathrm{M}_{\odot}$. Even though the Hα[a] is the strongest hydrogen line, in case of strong extinction it is useful to use infrared lines (Paα, Brγ, HeI λ2.1μm) to minimise the effects of reddening (see section 2.1.4).

A more direct way to count massive stars is to use the UV lines generated in the their strong stellar winds. Photospheric far-UV photons are absorbed in the wind, thus transferring radiative into kinetic momentum with an efficiency η:

$$\eta = \frac{\dot{M} v_{\infty}}{\mathrm{L} c^{-1}} \tag{2.40}$$

where $\dot{M}$ is the mass-loss rate, v_{∞} is terminal wind velocity, L is the bolometric luminosity and c is the speed of light. The efficiency parameter η can be derived either from observations (Lamers and Leitherer, 1993) or from models (Puls et al., 1996). So, the line profiles contain information on the mass-loss and, hence, using equation (2.40) on the luminosity of the star. A stellar evolutionary model is then needed to tie the line profile to the stellar mass. Since the wavelength range of the photons driving the winds is the same as of those ionising the interstellar medium, these two methods probe the same mass interval.

[a]The hydrogen lines are divided in series according to the low level of the transition. The transitions to $n = 1$ are called the Lyman series, the ones to $n = 2$ the Balmer series, the ones to $n = 3$ the Paschen series and the ones to $n = 4$ the Bracket series. Within a series, the transition with $\Delta n = 1$ is labelled with the Greek letter α, the one with $\Delta n = 2$ with β etc. So, for example, Hα is the line corresponding to the $3 \rightarrow 2$ transition and has a wavelength of 6563 Å.

All in all, these methods are rather indirect and, in the words of Leitherer (1998), *"the willingness to believe in a variation or the universality of the IMF depends on the trust one has in stellar atmospheres and evolutionary models"*. In any case, always according to Leitherer (1998), there is little evidence for a significant influence of the environment on the IMF, at least in this high-mass range.

2.2.7 IMF: the theoretician's point of view

As we have thoroughly discussed, the very existence of an Initial Mass Function is questionable and what one really would like to know is the Creation Function. However, even *assuming* its existence, deriving it from first principles is an amazingly difficult task and, currently, there is no theory capable of doing it. Such a theory would have to take into account the role of turbulence in the star-forming molecular cloud, the interplay between gravity and magnetic fields, the possible rotation of the structure, the feedback of the outflows from the protostar on the material accreting onto it and so on. At the present time, the uncertainties on the basic physics are too big, but there are, nonetheless, various approaches to the problem dealing with our incomplete understanding of the most fundamental mechanisms.

Self regulating IMF

Let us begin this brief overview with a model in which a star itself determines its final mass through the action of stellar outflows (see, for example, Shu et al., 1987).

Following Adams and Fatuzzo (1996), this basic idea is implemented by separately evaluating:

- The spectrum of the initial conditions in the star-forming molecular cloud;
- The transformation between a given set of initial conditions and the final mass of the star. In this framework, the final mass of the star is determined by the condition that the stellar outflow is strong enough to reverse the material infall onto the star.

Let us start from the bottom and estimate the *Semi-Empirical Mass Function* (SEMF), *i.e.* the transformation between the initial conditions in the cloud and the mass of the newly formed star. Making a few assumptions on the characteristics of the stellar winds and of the infalling material, they derive the following relations linking the initial conditions in the cloud (a and Ω) to the mass of the star M. Their derivation is based on the estimate of qualitative behaviours of the different quantities involved:

$$\begin{cases} M/\mathrm{M}_\odot = 0.66 \left[\frac{\Lambda_3}{\eta}\right]^{1/3} a_{35}^3 \Omega_1^{-2/3} & M/\mathrm{M}_\odot \lesssim 3 \\ M/\mathrm{M}_\odot = 1.65\, \Lambda_3^{1/6} a_{35}^{11/6} \Omega_1^{-1/3} & 3 \lesssim M/\mathrm{M}_\odot \lesssim 10 \\ M/\mathrm{M}_\odot = 0.67\, \Lambda_3^{1/4} a_{35}^{11/4} \Omega_1^{-1/2} & 10 \lesssim M/\mathrm{M}_\odot \lesssim 100 \end{cases} \tag{2.41}$$

where a is the effective sound speed (taking into account the thermal, turbulent and magnetic field contributions) in units of 0.35 km s^{-1} and Ω is the angular velocity of the rotating material in units of km s^{-1} pc^{-1}. In presence of rotation, not all of the material falls all the way to the stellar surface, but the portion of it with high specific anguluar momentum collects in a circumstellar disk. All of the uncertain parameters in the calculations are encapsulated in the parameter Λ_3.

The dependence of the SEMF on the mass range derives from the different mass-luminosity relations appropriate in the different intervals. The stellar luminosity, in turn, enters the computations as a factor in determining the mass outflow. At low masses, the most important luminosity source comes from the infall of material and η in the first of the equations (2.41) is the fraction of the gravitational potential energy converted into photons. In the presence of rotation, one expects $\eta \simeq 0.5$. At higher masses, the dominant contribution comes from the star's own internal luminosity (deuterium burning, gravitational contraction, hydrogen burning) that scales as M^4 for $M \lesssim 10$ $\mathrm{M}_\odot$ and, for still higher masses, as M^2.

The next step would be to compute the initial conditions in the cloud from first principles. Unfortunately, no such theory exists and Adams and Fatuzzo explore their influence on the final stellar mass spectrum by considering two limiting cases:

- The effective sound speed is the only relevant parameter in determining the initial conditions;
- The initials conditions are set by an infinite number of independent variables.

These two case encompass the real situation that, necessarily, has to be somewhere in the middle.

In the first case the resulting IMF is a *power-law* of index $\Gamma \simeq -1.6$ at low masses and $\Gamma \simeq -2.1$ at high masses. The agreement with the Miller and Scalo (1979) is fair, but not exact. This models also predicts a star formation efficiency, defined as the ratio of the mass into stars to the total cloud mass, of 0.07. This number is at least of the same order of magnitude as the observed one (see, for example, Lada et al., 1993).

In the second case, the central limit theorem holds and the IMF approaches a *log-norm function*, *i.e.* it has the same shape of the Miller and Scalo (1979) one. In this case, then, the IMF can be written in the form:

$$\ln \xi \left(\ln M/\mathrm{M}_{\odot}\right) = A - \frac{1}{2 < \sigma >^2} \cdot \left[\ln\left(\frac{M}{M_c}\right)\right] \tag{2.42}$$

and the three parameters in the Miller and Scalo (1979) IMF (equation (2.37) on page 26) are related to the constant A, the characteristic mass M_c and the width $< \sigma >$ by:

$$\begin{cases} A & = & a_0 \ln(10) + \frac{a_1^2 \ln(10)}{4a_2} \simeq 4.65 \\ < \sigma >^2 & = & \frac{\ln(10)}{2a_2} \simeq 2.45 \\ \ln(M_c/\mathrm{M}_{\odot}) & = & -\frac{a_1 \ln(10)}{2a_2} \simeq -2.35 \end{cases} \tag{2.43}$$

Since the shape of the derived IMF is the same as the one of the Miller and Scalo (1979) one, Adams and Fatuzzo (1996) consider this model to be a reasonable approximation to the real case. As we have seen at the end of section 2.2.2, though, it is not clear at all that the Miller and Scalo (1979) IMF should be regarded as a good estimate of the the real one.

In any case, in the framework of this model, M_c is determined by the mean values of all the relevant variables and their widths combine to determine $< \sigma >$. Clearly, the model does not predict them and only a complete theory could. However, it is possible to estimate them from observations of the various physical parameters and compare them to the ones derived from the observed IMF listed in equations (2.43). A crude estimate gives $M_c \simeq 0.25$ $\mathrm{M}_{\odot}$ and $< \sigma > \simeq 1.8$. In the words of Adams and Fatuzzo (1996): "although these values are higher than the values required to fit the Miller-Scalo IMF, we consider the agreement to be quite good, given th crudeness of the calculation".

Finally, in the intermediate case in which the number of relevant parameters is finite, the exact form of the IMF depends on the distribution of the parameters themselves. When this distribution is taken to be *flat*, the resulting IMF converges rapidly to a log-norm form, whereas this convergence is much slower if the variable are distributed as power-laws and the IMF retains a power-law tail at high masses.

Merging-clumps model

Let us now briefly describe a model in which the *collisional interactions of cloud pieces* determine the mass distribution. The basic idea (Murray and Lin, 1996) is that thermal and dynamical instabilities cause the molecular cloud to fragment in cold and dense "cloudlets". These cloudlets fall into the centre of the parent cloud and, in the process, can merge and increase their mass. When the mass of a cloudlet exceeds the critical mass for gravitational instability (M_G) a star is born. The accretion process goes on until the UV flux from the newly formed star heats the surrounding material, sweeping it away.

As a natural consequence of the cloudlets falling to the centre of the cloud, a feature of these models is the presence of mass segregation right from the beginning, before two body

relaxation processes between stars come into play. This is in agreement with observations of Galactic open clusters (Jones and Stauffer, 1991).

Murray and Lin (1996) use a N-body scheme to model the evolution of the system. The cloudlets are seen as particles with a finite radius r_c, which may evolve as the result of mergers and gravitational contraction. Two particles merge if the distance of closest approach is smaller than the sum of their radii. Of course, the gravitational focusing is taken into account in computing the merging tree. If the mass of the merged cloudlet is smaller than M_G a new radius is computed as to conserve the volume of the original particles. If, however, the cloudlet's mass exceeds the threshold, it is assumed to undergo free-fall collapse on a short timescale compared to the dynamical one. This is consistent with the scenario of a self-similar growth of protostellar cores (see, for example, Shu et al., 1987).

Subsequent merging of a protostellar core (defined as having $r_c = 0$) with the remaining cloudlets are allowed until the UV flux of the protostar inhibits any further accretion. Let us notice here that neither the critical mass for gravitational collapse M_G nor the initial mass of the cloudlets M_i are computed from first principles. Rather, their ratio is given as an input parameter for the simulations. Also, the simulations do not take into account the three-body mergers and the possibility that tidal forces could dissipate enough energy to result in a merger of particles coming within as much as three radii of each other (Fabian et al., 1974). As a result, the merger cross section could be larger than the one used by Murray and Lin (1996), but the difference would be less than an order of magnitude.

The shape of the resulting IMF closely resembles a power-law and its slope is determined by the importance of the gravitational focusing in the encounters. If it is significant, then the protostars spend most of the time at low masses and only a few end up with a high mass. The IMF, hence, will be steep. Physically, this happens if the initial velocity dispersion is small and, hence, the system undergoes collapse. If however, gravitational focusing is not important and the encounter cross section is dominated by the geometrical size of the cloudlets, then the growth timescale increases with mass and the protostars spend less time at low mass. As a consequence, the IMF is flatter all the way up to the most massive star formed.

The slopes of IMF obtained by varying the initial conditions span quite a wide range from $\alpha \simeq -1.3$ to $\alpha \simeq -2.5$. The results are independent of the number of particles as long as the radii are changed to keep the initial filling factor of the cloudlets constant.

Sampling of a fractal cloud

To conclude this short overview, let us consider an approach in which the dominant assumption is on the *fractal geometry* of the star-forming cloud (Elmegreen, 1997). As we have seen, it is very difficult to model the details of the cloud evolution that ultimately determine the Initial Mass Function. The idea here is to renounce to follow it and just to assume that it results in a fractal structure (see, for example, Pfenniger, 1996). The fractal tree is than

randomly sampled to extract the newly born stars.

Let us consider a fractal cloud in which every piece contains, on average, N subpieces down to some minimum mass. The actual number of subpieces in every piece is drawn from a Poissonian distribution. The first thing to do is to find the number i of subpieces in each piece in a fractal cloud with H hierarchical levels. Then the occupancy index j is set to 1 for all of the pieces and subpieces and every piece is labelled with a value of the counter n. A flag of $j = 0$ indicates that a piece was chosen to become a star. Finally, the masses are assigned starting from the bottom level and adding these up to obtain the masses of the whole tree. Once the whole tree is set up this way, the random selection process can take place. The mass of the star formed is taken to be a fixed fraction of the mass of the piece in which it was formed.

As an example, let us compute the spectrum of a purely fractal cloud with $N = 2$ subpieces inside every piece and $H = 4$ levels of hierarchy. There is one cloud at the top ($h = 0$) with two clouds inside it at $h = 1$ and so on. Therefore, the total number of pieces is $1+2+4+8+16 = 31$ and, hence, the probability of extracting a cloud with $h = 1$ is $2/31$, with $h = 2$ is $4/31$ and, at the bottom of the hierarchy ($h = 4$), the probability is $16/31$. In general, the probability goes as N^h. Now, the mass of a piece at level h is the sum of the masses of the 2 subpieces inside it and so on until the bottom is reached in $H-h$ steps. As a result, the mass of a piece at h is N^{4-h}, in units of the mass of the pieces at the bottom level of the hierarchy. Let us notice here that going from a level to the next one, the logarithm of mass increases of $\log(N)$, a constant. So, the number of pieces at at certain level is inversely proportional to their masses and, since the probability of choosing a piece at a certain level is proportional to the number of pieces at that level, the resulting mass function scales as M^{-1} with constant *logarithmic* steps. So, the cloud mass function has $\alpha = -2$, independent of the fractal dimension.

There are two effects that make the *stellar* mass function different from the *cloud* mass function computed above. The first one is caused by the fact that once a cloud piece is converted into a star, the next selection is biased towards the same level of the tree. To illustrate this point, let us go back to the previous example and suppose that the first piece selected is one of the 4 ones at $h = 2$, *i.e.* it has mass of 4. The selected piece was made up of 2 subpieces with $h = 3$ and four subpieces with $h = 4$. So, the tree is left with $8 - 2 = 6$ pieces with $h = 3$ and $16 - 4 = 12$ pieces with $h = 4$. At $h = 2$, we are left with three out of the four original pieces. Let us consider what has happened to the $h = 1$ level. The branch that did not include the selected piece is not affected and its mass is still 8. This is the only piece left with this mass, since the other piece at the same level has now lost one of its subpieces pieces (the one the become a star) and its mass is now only 4. This last piece, consequently, does not belong to $h = 1$ any more, but to $h = 2$. To recapitulate, there is only one piece left at $h = 1$ and 4 pieces at $h = 2$ (the three left from prior to the formation of the star plus the one coming from $h = 1$). At the highest level ($h = 0$), there is still only one piece, but its mass is now 12 and not 16 as before. In the end, all of the levels have lost

members except for the one that gave birth to the star. This is the reason why this enhances its possibilities to give birth to another star. Since the most commonly chosen masses are the lower ones (they are more numerous) this mechanism biases the final mass distribution towards them.

The other effect that biases the IMF towards the lower masses is that stars are more likely to be formed where the gas is more dense, *i.e.* at low levels in the hierarchy. In order to take this effect into account, the sampling probability is not uniform, but is taken to scale as the square root of the density.

The selection of stars cannot apply to extremely small pieces because their self-gravity would not be high enough to make them collapse to form stars. To mimic this lower mass cutoff, the selected pieces are randomly discarded with a probability (P_f) that scales with mass. Elmegreen (1997) uses two different P_f, an exponential ($P_f = \exp(-M/M_J)$) and a Gaussian ($P_f = \exp(-(M/M_J)^2)$), where M_J is a fixed cutoff mass (the Jeans mass). The model does not include any of the physics required to compute M_J that is treated as a free parameter to explore its effects on the IMF.

When all of these effects are included, the resulting IMF is in excellent agreement with the observation with a medium-high mass tail of exponent $\alpha = -2.3$ and an exponential cutoff at low masses.

Bibliography

Adams, F.C. and Fatuzzo, M. 1996, *ApJ*, **464**, 256.

Brocato, E., Castellani, V., and Romaniello, M. 1998, *AA*. submitted to.

Castellani, V. *Astrofisica Stellare*. Zanichelli, Bologna, 1^{st} edition, 1985.

Chiosi, C., Bertelli, G., and Bressan, A. 1992, *ARAA*, **30**, 235.

Cool, A.M., Piotto, G., and King, I.R. 1996, *ApJ*, **468**, 655.

D'Antona, F. and Mazzitelli, I. 1996, *ApJ*, **456**, 329.

De Marchi, G., Clampin, M., Greggio, L., Leitherer, C., Nota, A., and Tosi, M. 1997, *ApJ*, **479**, L27.

De Marchi, G. and Paresce, F. 1995a, *AA*, **304**, 202.

De Marchi, G. and Paresce, F. 1995b, *AA*, **304**, 211.

Elmegreen, B.G. 1997, *ApJ*, **486**, 944.

Elson, R.A.W., Gilmore, G.F., Santiago, B.X., and Casertano, S. 1995, *AJ*, **110**, 682.

Fabian, A.C., Pringle, J.E., and Rees, M.J. 1974, *MNRAS*, **172**, 15.

Hartwick, F.D.A., Cowley, A.P., and Mould, J.R. 1984, *ApJ*, **286**, 269.

Hunter, D.A., Gillett, F.C., Gallagher, J.S. III, Rice, W.L., and Low, F.J. 1986, *ApJ*, **303**, 171.

Hunter, D.A., O'Neil, E.J., Lynds, R., Shaya, E.J., Groth, E.J., and Holtzman, J.A. 1996, *ApJ*, **459**, L27.

Hunter, D.A., Shaya, E.J., Holtzman, J.A., Light, R.M., O'Neil, E.J., and Lynds, R. 1995, *ApJ*, **448**, 179.

Jones, B.F. and Stauffer, J.R. 1991, *AJ*, **102**, 1080.

Lada, C.J. 1987, In *Star-Forming Regions*, M. Peimbert and J. Jugaku (Eds.), volume 115, Dordrecht. Reidel Pub. Co., p. 1.

Lada, E.A., Strom, K.M., and Myers, P.C. 1993, In *Protostars and planets III*, E. Levy and J. Lunine (Eds.), Tucson. University of Arizona Press, p. 245.

Lamers, H.J.G.L.M. and Leitherer, C. 1993, *ApJ*, **412**, 771.

Bibliography for chapter 2

Leitherer, C. 1998, In *The Stellar Initial Mass Function*, G. Gilmore and D. Howell (Eds.), volume 142 of *38th Herstmonceux Conference*, San Francisco. ASP Conference Series, p. 61.

Lenzuni, P and Panagia, N., 1998. in preparation.

Massey, P., Lang, C.C., Degioia-Eastwood, K., and Garmany, C.D. 1995, *ApJ*, **438**, 188.

Mihalas, D. and Binney, J. *Galactic Astronomy: Structure and Kinematics*. W.H. Freeman and Co., San Francisco, 2nd edition, 1981.

Miller, G.E. and Scalo, J.M. 1979, *ApJS*, **41**, 513.

Mould, J.R., Watson, A.M., Gallagher, J.S. III, Ballester, G.E., Burrows, C.J., Casertano, S., Clarke, J.T., Crisp, D., Griffiths, R.E., Hester, J.J., Hoessel, J.G., Holtzman, J.A., Scowen, P.A., Stapelfeldt, K.R., Trauger, J.T., and Westphal, J.A. 1996, *PASP*, **108**, 682.

Murray, S.D. and Lin, D.N.C. 1996, *ApJ*, **467**, 728.

Palla, F. and Stahler, S.W. 1990, *ApJ*, **360**, L47.

Panagia, N. 1980, In *Radio Recombination Lines*, P. A. Shaver (Ed.), Dordrecht. D. Reidel Pub. Co, p. 99.

Paresce, F., De Marchi, G., and Romaniello, M. 1995, *ApJ*, **440**, 216.

Pfenniger, D. 1996, In *New Extragalactic Perspectives in the New South Africa*, D.L. Block and J.M. Greenberg (Eds.), Dordrecht. Kluver, p. 439.

Piotto, G., Cool, A.M., and King, I.R. 1997, *AJ*, **113**, 1345.

Pryor, C., Smith, G.H., and McClure, R.D. 1986, *AJ*, **92**, 1358.

Puls, J., Kudritzki, R.P., Herrero, A., Pauldrach, A.W.A., Haser, S.M., Lennon, D.J., Gabler, R., Voels, S.A., Vilchez, J.M., Wachter, S., and Feldmeier, A. 1996, *AA*, **305**, 171.

Rana, N.C. 1991, *ARAA*, **29**, 129.

Richer, H.B. and Fahlman, G.G. 1991, In *The Formation and Evolution of Star Clusters*, K. Janes (Ed.), volume 13, Boston. ASP Conference Series, p. 120.

Richer, H.B., Fahlman, G.G., Buonanno, R., Fusi Pecci, F., Searle, L., and Thompson, I.B. 1991, *ApJ*, **381**, 147.

Salpeter, E.E. 1955, *ApJ*, **121**, 161.

Savage, B.D. and Mathis, J.S. 1979, *ARAA*, **17**, 73.

Bibliography for chapter 2

Scalo, J. 1998, In *The Stellar Initial Mass Function*, G. Gilmore and D. Howell (Eds.), volume 142 of *38th Herstmonceux Conference*, San Francisco. ASP Conference Series, p. 201.

Scalo, J.M. 1986, *Fundamentals of Cosmic Physics*, **11**, 1.

Schaller, G., Schaerer, D., Meynet, G., and Maeder, A. 1992, *AASS*, **96**, 269.

Shu, F.H., Adams, F.C., and Lizano, S. 1987, *ARAA*, **25**, 23.

Soifer, B.T., Sanders, D.B., Madore, B.F., Neugebauer, G.E., G. Danielson, Elias, J.H., Lonsdale, C.J., and Rice, W.L. 1987, *ApJ*, **320**, 238.

van den Bergh, S. and Tammann, G.A. 1991, *ARAA*, **29**, 363.

Wheeler, J.C., Sneden, C., and Truran, J.W. 1989, *ARAA*, **27**, 279.

Whittet, D.C.B. 1992, In *Dust in the galactic environment*, Bristol. Techno House.

Zombeck, M.V. *Handbook of Space Astronomy and Astrophysics.* Cambridge University Press, Cambridge, New York, 2nd edition, 1990.

Chapter 3

Instrument (WFPC2) and observations

Now that we know what we are looking for and why we are doing it, we have to ask ourselves what data are the most suitable for the task and with which instrument we can obtain them.

3.1 The instrument

The best present instrument to accomplish our goals is the **Wide Field and Planetary Camera 2** (WFPC2) on board of the NASA-ESA satellite **Hubble Space Telescope** (*HST*). The instrument is fully described in Biretta et al. (1996).

The WFPC2 field of view, shown in Figure 3.1 on the following page, is divided into four cameras by a four-faceted pyramid mirror near the *HST* focal plane. Each camera contains a CCD detector of 800 pixels on a side and the four of them are arranged side by side to form a square of 1600x1600 pixels^2.

The cameras have different focal ratios, and hence, different spatial resolution and field of view. The first one, the *Planetary Camera* (PC), has a field of view of $35'' \times 35''$ with

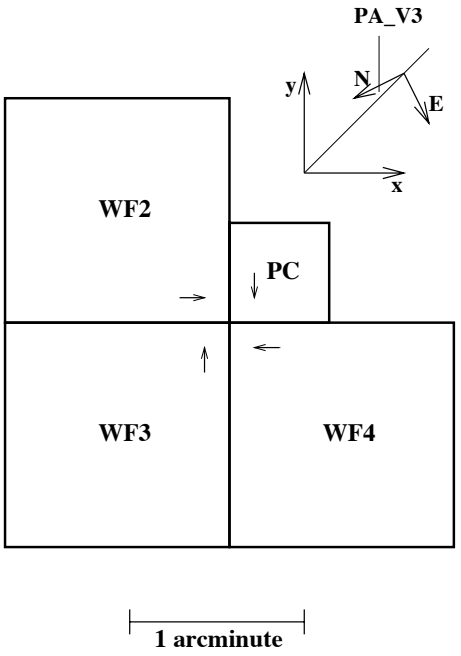

Figure 3.1: *WFPC2 Field-of-View projected on the Sky. The read out direction is marked with arrows near the start of the first row in each CCD.*

a scale of 46 milliarcsec/pixel. The other three of them, the *Wide Field Camera* (WF2-4), are arranged to form the shape of an L and cover a total area of $2'.5 \times 2'.5$ with a scale of 100 milliarcsec/pixel. To complete the explanation of its name, the number "2" in WFPC2 indicates that this is the second instrument of this kind that has flown on *HST*. The first one was replaced during the First Servicing Mission in December 1993 to correct for the spherical aberration of the primary *HST* mirror. Typically, 10 minutes of integration are enough to reach the 25^{th} magnitude in the V band for a point source with a signal to noise ratio of 5.

In ground-based observations, the bidimensional pattern of light produced by a point source on the detector (PSF) is caused mainly by the earth's atmospheric turbulence. The resulting PSF has a Gaussian shape, the width of which strongly depends on the telescope site and also on construction details such as the dome design etc. Moreover, it is time-dependent, as the atmospheric conditions change. Above the atmosphere, instead, the PSF is determined mostly by diffraction through the finite aperture of the telescope. Let us discuss this case in some detail.

3.1.1 Diffraction limited Point Spread Function

By definition, the *Point Spread Function* (PSF) is the image of a point-like source on the detector. This concept is particularly important, since, for any practical purpose, *a star is a point-like source*. To convince ourselves of this, it is enough to notice that the apparent angular diameter (δ, in seconds of arc) of a star of radius r at a distance d is:

$$\delta = 0''.009 \cdot \frac{r(\mathrm{R}_\odot)}{d(\mathrm{pc})}$$

Hence, already at a distance of one parsec, a typical star the radius of the Sun would have an angular diameter smaller than the resolution of *HST*, that is of the order of $0''.05$, as we will see shortly.

On the other hand, the way an *extended source* is going to look on the detector is just the convolution of its intrinsic brightness profile and the Point Spread Function of the instrument. All in all, a good characterization of the PSF is a very important step in obtaining good astronomic data.

So, let us consider the light a from point-like source as seen through a telescope outside of the earth's atmosphere, so as to avoid the effects of its turbulence on the incoming light. This is the situation of any space-based observatory and, in particular, of *HST*. Since the aperture of the telescope is of finite size, the incident light from the source will produce a diffraction pattern.

Let us consider the ideal case of a prefect optical system with an entrance radius a (primary mirror) and let ε be the fraction of the aperture radius obscured by other optical elements such as the secondary mirror, the optical parts to reduce the scattered light (*baffles*) etc. In the case of *HST*, for example, $a = 1.2$ m and $\varepsilon = 0.33$, bigger than the one that would be caused by the secondary mirror alone, the radius of which is only 15.4 cm. Following the notation of Schroeder (1987), in Figure 3.2 we show the exit pupil of the system with a spherical wavefront **W** of radius of curvature **R** emerging from it.

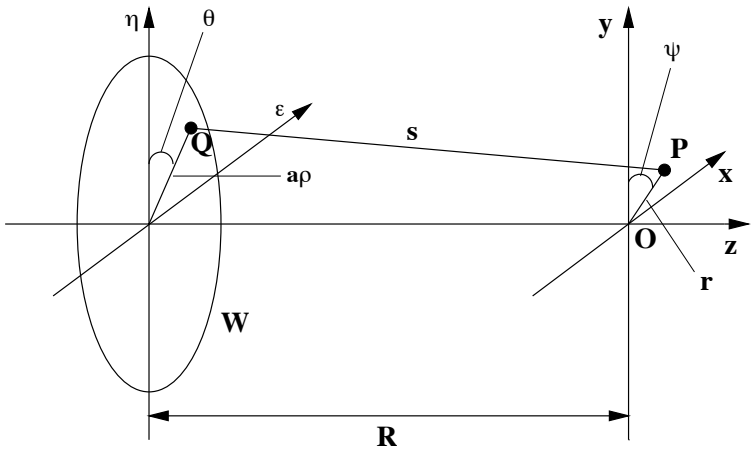

Figure 3.2: *Coordinate frames at exit pupil (η, ξ, ζ) and image surface (x, y, z) of the optical system.*

Relative to the origin O, the coordinates of an arbitrary point Q on the wavefront and of the point P on the image surface are:

$$\begin{cases} \xi = a\rho\sin(\theta) & x = r\sin(\psi) \\ \eta = a\rho\cos(\theta) & y = r\cos(\psi) \\ \zeta = -\sqrt{R^2 - a^2\rho^2} \end{cases}$$

According to Huygens' principle the amplitude of the field U at point P is the sum of all of the contributions dU from each area dS on W. Assuming that the distances z, r and a are small compared to R and that the incoming light is monochromatic at wavelength λ, this translates into:

$$U(P) = A \int\int_W \exp\left[ik(s - R)\right]\, dS \tag{3.1}$$

where $k = 2\pi/\lambda$, s is the distance from Q to P and A is just a constant proportional to the amplitude of the fields in Q (see Figure 3.2). Hence, from a mathematical point of view, $U(P)$ is just the Fourier transform of the entrance pupil. Since all the waves are in phase at O, the amplitude U has a maximum there.

Let us now define the two dimensionless variables u and v:

$$u \equiv \tfrac{2\pi}{\lambda}\left(\tfrac{a}{R}\right)^2 z \quad \text{and} \quad v \equiv \tfrac{2\pi}{\lambda}\left(\tfrac{a}{R}\right) r \tag{3.2}$$

in terms of which, with a little bit of algebra, the difference in optical path in equation (3.1) is:

$$k(s - R) = -v\rho\cos\left(\theta - \psi\right) - \frac{u\rho^2}{2} + u\left(\frac{R}{a}\right)^2$$

If we want to evaluate the amplitude only in the paraxial focal plane, we can set $u = 0$ and equation (3.1) becomes:

$$U(P) = A \int_0^{2\pi} \int_\varepsilon^1 \exp\left[-iv\rho\cos(\theta - \psi)\right] \rho\, d\rho\, d\theta \tag{3.3}$$

Since the system is symmetric about the z axis, $U(P)$ is independent of ψ and we can choose any convenient value for it, for example $\psi = \pi$. Integration of equation (3.3) then gives:

$$U(P) = \pi A \left[\frac{2J_1(v)}{v} - \varepsilon^2 \frac{2J_1(\varepsilon v)}{\varepsilon v}\right] \tag{3.4}$$

where J_1 is a Bessel function of order one. $U(O) = \pi A(1 - \varepsilon^2)$ since:

$$\lim_{x\to 0} \frac{2J_1(x)}{x} = 1$$

We are finally ready to compute $i(P)$, the PSF at point P:

$$i(P) \equiv \frac{|U(P)|^2}{|U(0)|^2} = \frac{1}{(1-\varepsilon^2)^2}\left[\frac{2J_1(v)}{v} - \varepsilon^2 \frac{2J_1(\varepsilon v)}{\varepsilon v}\right]^2 \tag{3.5}$$

The PSF of equation (3.5) is graphically shown in Figure 3.3 for the obscuration value appropriate for *HST* and for the extreme case of no obscuration at all.

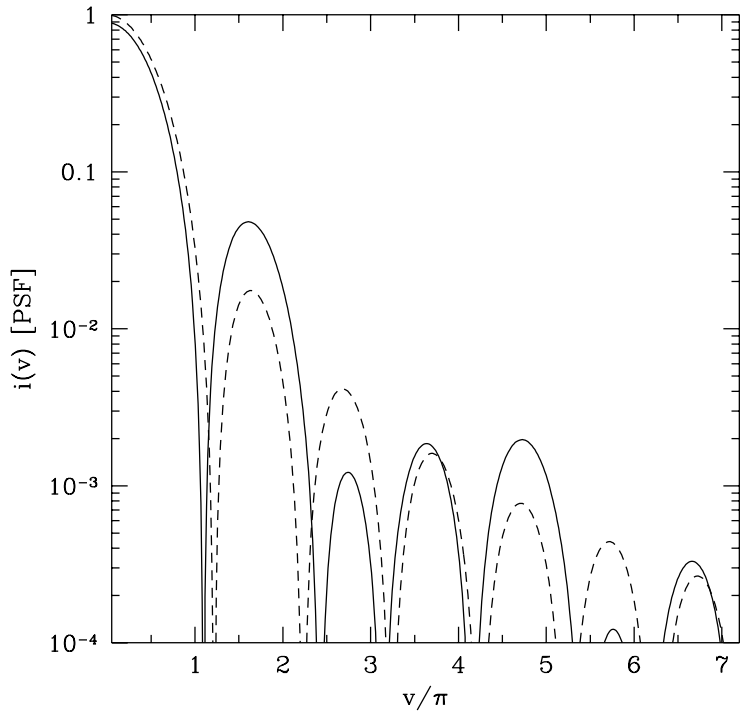

Figure 3.3: *PSF of a perfect image from equation (3.5) for the obscuration ratio of* HST *($\varepsilon = 0.33$, solid line) and for the extreme case of no obscuration ($\varepsilon = 0$, dashed line).*

So, the pattern of the PSF consists of a central bright disk, called **Airy disk**, surrounded by concentric dark and bright disks. For $\varepsilon = 0$ the intensity of the secondary peaks decreases with increasing v, *i.e.* radial distance from the center, whereas for $\varepsilon > 0$ it varies in a cyclic manner, depending on the actual value of the obscuration.

From equation (3.5), the angular radius in seconds of arc of the $i-th$ zero in the PSF is given by:

$$\alpha''_{i,0} = 2.06 \cdot 10^{-5}\, \overline{\alpha}_i\, \frac{\lambda(\text{Å})}{D(\text{m})} \tag{3.6}$$

where λ is the wavelength of the incoming light, $D = 2a$ is the diameter of the telescope aperture and the coefficients $\overline{\alpha}_i$ for the first three zeros are given in Table (3.1) for a few values of the obscuration around the value appropriate for *HST*.

ε	$\overline{\alpha}_1$	$\overline{\alpha}_2$	$\overline{\alpha}_3$
0.00	1.220	2.233	3.238
0.10	1.205	2.269	3.182
0.20	1.167	2.357	3.087
0.33	**1.098**	**2.424**	**3.137**
0.40	1.058	2.388	3.300

Table 3.1: *Radii of the dark rings for different obscurations ε (see equation (3.6)). Highlighted in boldface are the values for* HST.

The radius of the first Airy disk decreases as the obscuration increases, whereas the radius of the second one has a peak for $\varepsilon \simeq 0.3$. On the other hand, the radius at which the PSF has half of the peak value is remarkably constant with changing obscuration:

$$\mathrm{FWHM}''_{(\mathrm{PSF})} = 2.06 \cdot 10^{-5} \, \frac{\lambda(\text{Å})}{D(\mathrm{m})} \tag{3.7}$$

Please notice the the quantity in equation (3.7) is a *diameter* and the quantity in equation (3.6) is a *radius*. In the case of *HST*, the FWHM at 5500 Å would be $0''.047$.

Another important quantity is the *encircled energy* (EE), defined as the fraction of energy falling inside a certain dimensionless radius v:

$$EE(v) \equiv \frac{1}{E} \int_0^{2\pi} \int_0^v i(x) x \, dx \, d\psi \tag{3.8}$$

where i, as usual, is given by equation (3.5). In Table 3.2, we report the encircled energies for the same parameters of Table 3.1. As it can be seen from Table 3.2, the effect of obscuration is to transfer energy from the central disks to the wings of the PSF.

ε	EE_1	EE_2	EE_3
0.00	0.838	0.910	0.938
0.10	0.818	0.906	0.925
0.20	0.746	0.900	0.908
0.33	**0.654**	**0.898**	**0.904**
0.40	0.584	0.885	0.903

Table 3.2: *Encircled energy within the first three Airy rings for different values of the obscuration ε. Highlighted in boldface are the values for* HST.

So far we have computed the PSF in the idealized case of perfect optical system, *i.e.* in the case in which the wavefront emerging from the pupil is perfectly spherical. In real telescopes various defects concur in producing departures from this ideal case and they have to be taken into fully account to characterise the actual PSF. In the case of the instruments

on board *HST*, a software package was developed (TINYTIM; Krist and Hook, 1997) to fully model the behaviour of the optical system of the telescope.

Another important effect that causes the real PSF to deviate from the idealized one is the sampling by the detector. Since every detector has a finite pixel size, the PSF resulting from the optical path is binned in the detector pixels. This binned pattern is the PSF that is actually observed. Of course, the smaller the pixel size compared to the characteristic size of the PSF, for example the FWHM, the more similar the final PSF will be to the pattern resulting from the optical assembly of the telescope. In the case of WFPC2 the effect of the binning is very important, since the pixel size is of the order of (in the the PC chip) or even bigger than (in the three WF chips) the PSF resulting from the optics alone.

To quantify this effect, we have generated a number of synthetic PSFs with the TINYTIM software mentioned above and binned them with different pixel sizes. In Table 3.3, we report the FWHM of the resulting PSFs. For comparison, the FWHM at 5400 Å from diffraction alone from equation (3.7) would be $0''.046$.

Camera	Oversampling Factor	Effective Pixel size ($''$)	Filter	FWHM (pixels)	FWHM ($''$)
PC	1	0.0455	F555W[a]	1.19	0.054
PC	1	0.0455	Mono[b]	1.18	0.054
PC	2	0.0228	F555W	1.95	0.044
PC	5	0.0091	F555W	4.71	0.043
WF3	1	0.0996	F555W	1.31	0.130

[a]WFPC2 filter centered at 5400 Å and roughly 1300 Å wide. It corresponds to the Johnson V filter.
[b]Monochromatic bandpass at 5400 Å. It is not an actual WFPC2 filter.

Table 3.3: *FWHM of the PSF at 5400 Å (generated with the* TINYTIM *code) sampled with different pixel sizes.*

As it appears from Table 3.3, the effect of undersampling on the effective spatial resolution is very strong. One way to make things better is to take a series of exposures shifted by a fraction of a pixel from one another (*dithering*). By doing so and subsequently reconstructing the image, one effectively oversamples the PSF with respect to the original pixel size. This technique has been used in several WFPC2 projects and, most notably, in the Hubble Deep Field campaign where the highest possible angular resolution was required to distinguish between stars and galaxies at faint magnitudes and to characterise the morphology of galaxies.

In Figure 3.4, we show images of the TINYTIM model PSFs for the monochromatic filter at 5400 Å and for the WFPC2 F555W filter, which is centred at the same wavelength. The spider diffraction spikes that appear in both images are produced by the supports of the secondary mirror. Also, the Airy rings are clearly visible in the monochromatic image, but,

since their position depends upon wavelength, they are smeared in the broad band one. As it can be seen in Table 3.3, the FWHM of the central peak does not change significantly between them.

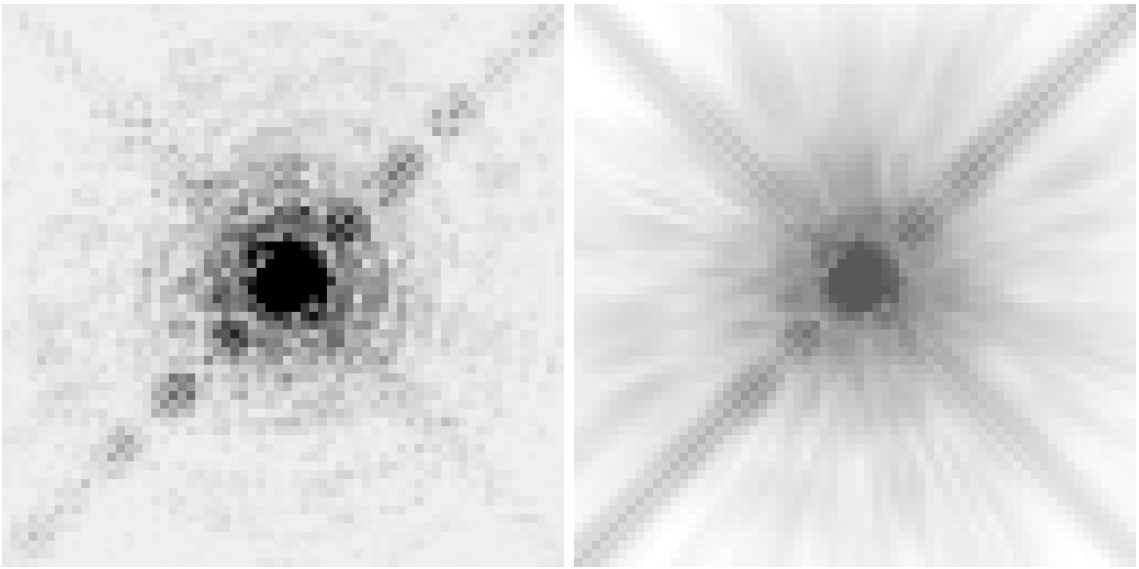

Figure 3.4: `TINYTIM` *model PSFs for a monochromatic filter at 5400 Å (left panel) and for the WFPC2 F555W filter (right panel). Both images are 64 PC pixels on a side, corresponding to 2″.915. The intensity stretch is logarithmic to enhance the fainter features.*

In all of the cases of Table 3.3, the PSF was built to have its centre in the centre of a pixel. However, if the PSF is not well sampled, as in the case of WFPC2, its characteristics also depend strongly on where its centre is compared to the centre of the pixel. For example, the fraction of light in the central pixel is 21% if the centre of the PSF falls in the centre of the pixel and only 11% if it falls on a corner (Biretta et al., 1996).

All in all, the *worst* angular resolution attainable with WFPC2 is of the order of 0″.15, which is several times better than the best resolution possible from the ground at these wavelengths with single dish telescopes. This has two main advantages. Firstly, it is possible to separate objects that, otherwise, would be blended together: the fields that we will consider in this work are only moderately crowded when observed with *HST*. Secondly, one can detect fainter objects, since their light is spread over very few pixels and, therefore, it is easier to achieve a good signal to noise ratio.

3.1.2 The detector

As already mentioned, the WFPC2 detector consists of four CCD sensors. They were built by Loral in 1991 and each of them is an array of 800x800pixels, the physical size of which is

15x15μm^2.

The CCDs are *front illuminated*, *i.e.* the light passes through the polysilicon gate structure overlying the 10μm thick active silicon layer. Because of its construction, the CCD surface is flat, thus reducing the astrometric uncertainties to about 1/10 of a pixel. On the other hand, however, due to absorption of the incoming light in the polysilicon structure, the front illumination lowers the *Detector Quantum Efficiency* (DQE), *i.e.* the number of photons revealed over the total number that reach the detector.

Every photon that is revealed by WFPC2 produces, on average, one electron that is trapped in the potential well of the pixel that was hit, or in one of the neighbouring pixels according to the Pixel Response Function K, *i.e.* the probability that a photon detected in a certain pixel produces an electron in a neighbouring pixel, of Table 3.4.

$$K = \begin{bmatrix} 0.0125 & 0.0500 & 0.0125 \\ 0.0500 & 0.7500 & 0.0500 \\ 0.0125 & 0.0500 & 0.0125 \end{bmatrix}$$

Table 3.4: *WFPC Pixel Response Function.*

At the end of an exposure all these wells are read and the data are transformed in digital form by an *Analog to Digital Converter* that packs the electrons in groups (Data Number, DN). The ratio between DNs and electrons is called *gain* and, for WFPC2, can have the values of 7 or 14 e$^-$/DN. This last setting is called *gain 15* for historical reasons and severely undersamples the CCD read out noise, that is of the order of 5 electrons per pixel (RMS).

The physical depth of the potential wells is of about 90,000 e$^-$ meaning that, when this threshold is passed, the electrons tend to drift to nearby pixels. The problem, however, is that at the time of the WFPC2 launch there were no flight-qualified ADCs working with more than 12 bits and, hence, the one that WFPC2 uses saturates at 4095 counts, *i.e.* much less than the physical depth of the potential well. This means that a saturated pixel can contain any number of electrons between (4095·gain) and the physical depth of the well. The saturated pixels are marked with a given flag (the number "8") and there are procedures to recover at least some of the information, as we will see later.

The intrinsic sensitivity of the CCDs drops below 4800 Å. To extend the detector capabilities below this threshold, the front surfaces of the CCDs are coated with a Lumogen phosphor that absorbs the photons shortward of 4800 Å and re-emits them in the 5100-5800 Å range and, eventually, these photons are detected by the CCD. This same coating acts as anti-reflection material, thus enhancing the quantum efficiency of the detector.

Just as an illustration of the characteristics of WFPC2, in Figure 3.5 we show quantum efficiency of the detector. This is the efficiency of the detector alone. To obtain the fraction of photons revealed with respect to the number of photons coming from the source, it is necessary to multiply this number by the throughput of the rest of the optical assembly and the filter used. The result is of the order of 10% in the visible and near infrared, while it

drops to the order of the percent, or even less, in the ultraviolet.

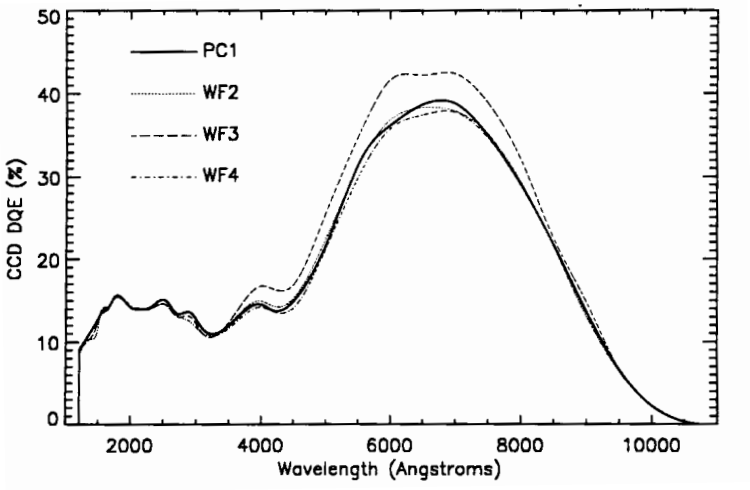

Figure 3.5: *Detector Quantum Efficiency of the 4 WFPC2 chips. The DQE is roughly 35% at 6000 Å and it drops sharply in the ultraviolet (15% at 2500 Å).*

3.2 Observing strategy and filter choice

It is easy to show that, in order to obtain both the reddening and the intrinsic temperature of a star from photometry, one needs observations at least at three wavelengths and the more bands one has, with the longest possible wavelength baseline, the better it is. Our observing strategy, then, is to have a number of broad filters in order to reconstruct at least the shape of the spectrum even if, of course, at very, very low resolution. We call this technique **Broad Band Spectroscopy**.

We decided to choose one filter immediately blueward and one filter immediately redward of the Balmer jump[a] to measure its magnitude. Since it is located at about 3650 Å, we chose WFPC2 filters similar to the Johnson U and B bands. In the earlier observations, we chose **F336W** [$\overline{\lambda}$=3342 Å, $\Delta\lambda$=381 Å] and **F439W** [$\overline{\lambda}$=4300 Å, $\Delta\lambda$=473 Å], but then we preferred to use **F300W** [$\overline{\lambda}$=2943 Å, $\Delta\lambda$=736 Å] and **F450W** [$\overline{\lambda}$=4519 Å, $\Delta\lambda$=957 Å] since they are wider and, hence, allow us to reach the same signal to noise ratio with shorter exposures. We also used a filter close to the classic Johnson V filter, since it usually takes very a short integration to reach a good signal to noise ratio for stars of all spectral types. Again, we started by using the **F555W** [$\overline{\lambda}$=5398 Å, $\Delta\lambda$=1226 Å], but then, for the same reason as before, we moved to the **F606W** [$\overline{\lambda}$=5935 Å, $\Delta\lambda$=1497 Å]. The red boundary achievable with WFPC2 is approximately 10500 Å. and, as our redder photometric point, we chose the

[a]The Balmer jump is the discontinuity in a spectrum due to the fact that photons shortward of 3646 Å have enough energy to ionise hydrogen atoms that are in the n=2 state. This additional source of opacity, corresponding to a bound-free transition, causes a diminution of the flux escaping the star at wavelengths shorter than 3650 Å.

F814W [$\overline{\lambda}$=7921 Å, $\Delta\lambda$=1489 Å] filter, which is very similar to the Cousin I band. We have occasionally used the **F255W** [$\overline{\lambda}$=2586 Å, $\Delta\lambda$=393 Å], which is especially useful for hot stars, but there the sensitivity really drops dramatically (0.5% at the peak), so that really long exposures are necessary. The throughput curves of these filters are shown in Figure 3.6.

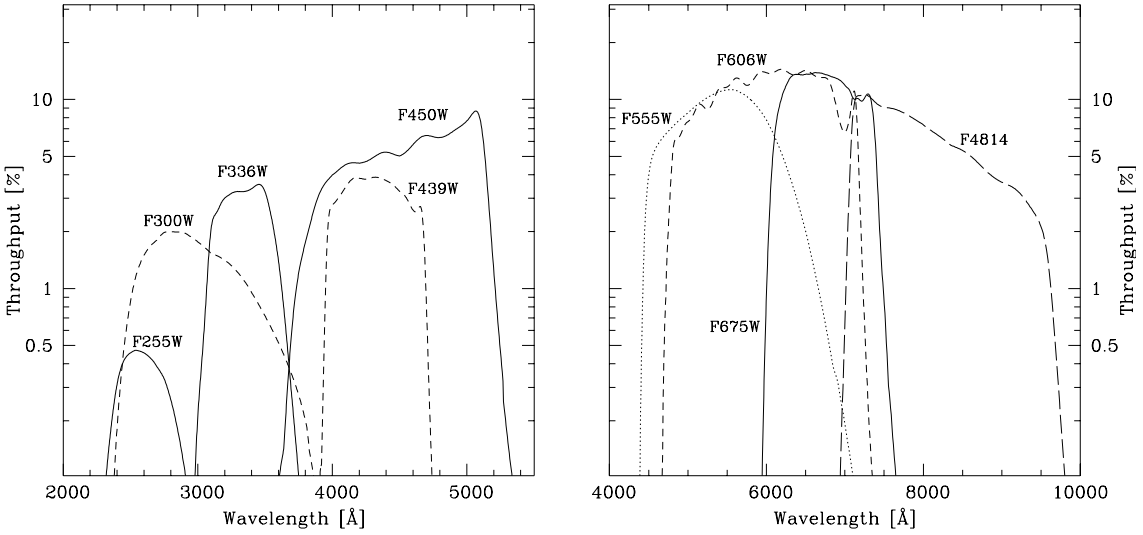

Figure 3.6: *Throughput of the WFPC2 broad band filters we have used. The "blue" filters are shown in the left panel, the "red" ones in the right panel.*

In addition to broad band filters, we want also to use narrow band filters to gain information on some crucial spectral features. This is useful to study both the *InterStellar Medium* (ISM) and peculiar stars that show emission lines. Most notably, we will use the comparison between a narrow filter centred on Hα (**F656N** [$\overline{\lambda}$=6563.7 Å, $\Delta\lambda$=21.4 Å]) and a broad band one bracketing it (the **F675W** [$\overline{\lambda}$=6696 Å, $\Delta\lambda$=866 Å], nearly a Cousin R filter) to identify stars that have an Hα excess. As we will see in more detail further on, this allows us to have a very detailed insight on the youngest generations of stars. The Hα filter together with the [OIII] one (**F502N** [$\overline{\lambda}$=5012.2 Å, $\Delta\lambda$=26.8 Å]) will be used to study the diffuse matter. In particular, the strength of [OIII] is used to distinguish high excitation HII regions (strong [OIII], which requires early O type stars, *i.e.* stars younger than 3-4 Myr) from low excitation ones (weaker [OIII], requiring late O or early B type stars, *i.e.* ages up to about 10 Myr).

For the full description and throughput curves of the WFPC2 filters see Biretta et al. (1996).

Bibliography

Biretta, J.A., Burrows, C., Holtzman, J., Heyer, I., Stevens, M., Bagget, S., Casertano, S., Clampin, M., Fruchter, A., Ferguson, H., Griffiths, R., Krist, J., Noll, K., O'Dea, C., Stiavelli, M., Suchkov, A., Surdej, J., and Whitmore, B. *WFPC2 Instrument Handbook Version 4.0.* STScI, Baltimore, 1996.

Krist, J. and Hook, R. *The Tiny Tim User's Guide Version 4.4*, 1997. http://scivax.stsci.edu/~krist/tinytim.html.

Schroeder, D.J. *Astronomical Optics.* Academic Press, Inc., San Diego, 1987.

Chapter 4

Data Reduction

An important part of the present work is devoted to measuring the flux of the stars in our fields in different passbands, *i.e.* doing *photometry*. It is absolutely crucial for any further interpretation of the data that the photometry be performed with the highest accuracy possible, taking into account all of the possible instrumental effects in order to minimize the final scatter in the data. In this chapter, we shall address the different issues concerning the *data reduction*, from the calibration of the raw data down-linked from the telescope to the different techniques for actually measuring stellar fluxes in the calibrated images.

Most of the data reduction and image processing was performed using the `Image Reduction and Analysis Facility` (`IRAF`) software. It is a product of the National Optical Astronomy Observatories and the reader should refer to the `IRAF` WWW Home-page for the software latest release and `IRAF`-related documentation:

`http://iraf.noao.edu/iraf-homepage.html`

In the following, we shall indicate `IRAF` tasks in ***boldface italics*** and their parameters in *underlined slanted*.

4.1 The WFPC2 Calibration

The Wide Field an Planetary Camera 2 (WFPC2) is really a wonderful instrument whose unprecedented capabilities have opened new, unexplored fields in astrophysical research. However, one of the things that make it so special, *i.e.* being above the earth's atmosphere on board of *HST*, can sometimes be a problem as far as its calibration is concerned. Any ground-based camera can be inspected directly at any time and its performances can be measured in a laboratory under controlled conditions. Of course, this is not possible for WFPC2 and the calibration has to rely on pre-launch tests and a continuous monitoring of its on-orbit performance, without being able to physically access the camera. Everything that one can ever want to know about WFPC2 and its calibration is probably in the *Wide Field and Planetary Camera 2 Instrument Handbook* (Biretta et al., 1996, is the current version at the time of writing) or in the *HST Data Handbook* (Voit, 1997). In any case, the reader should alway check the WFPC2 WWW page for the latest editions of the manuals, as well as for the Science Reports with the most up-to-date information on the instrument. The address is:

`http://www.stsci.edu/ftp/instrument_news/WFPC2/wfpc2_top.html`

Once a set of WFPC2 observations has been executed and down-linked to the ground, it is processed at the *Space Telescope Science Institute* (STScI) in Baltimore, MD (USA) through the *Post Observation Data Processing System* (PODPS, usually referred to as the *the pipeline*), where it is processed and calibrated. The calibration steps needed for a WFPC2 frame are in principle the same as those for any ground-based observation. The only difference is that single observers cannot take care of their own calibration files, but they have to be provided by the Instrument Team. In every *HST* cycle there are a number of calibration programs devoted to monitoring the behaviour of the camera, obtaining the best calibration data as a function of time and improving the overall photometric accuracy. The full calibration proposals are available through the Wold Wide Web at:

`http://presto.stsci.edu/public/propinfo.html`.

The calibration steps routinely performed on WFPC2 data are the following:

1. Flag static bad pixels;

2. Do analog-to-digital (A/D) correction;
3. Subtract the bias level;
4. Subtract the bias image;
5. Subtract the dark frames for exposures longer than 10 seconds;
6. Multiply by the inverse flat-field;
7. Apply shutter shading correction for exposures shorter than 10 seconds. This is never the case in our frames;
8. Calculate photometry keywords;
9. Calculate histograms from the raw and calibrated data;
10. Generate the science Data Quality File (DQF).

The files needed for the calibration, as well as the raw and the calibrated data are stored in an archive at STScI. Unsurprisingly, the URL for it is: `http://archive.stsci.edu`.

4.1.1 The Calibration Pipeline

Let us now review each of the calibration steps in some detail.

Static Mask

In this step the known bad pixels that do not change with time are flagged in the the output Data Quality File. The science data are not changed in any way and it is up to the observer to decide what to do with them. We will come back to this point later.

A/D correction

As we have already mentioned in section 3.1.2, the charge collected in each pixel at the end of an exposure is converted to a *Data Number* (DN, or simply counts). Two settings are allowed: 7 or 14 e^-/DN. The conversion is performed by comparing the observed charge to a reference. Since the device is not perfect, some values appear more often than they should and this can be accounted for in a statistical way. In the case of WFPC2, the converter is well behaved and the correction is small.

Global Bias Level Removal

In order to keep the A/D level above zero, the charges produced in the pixels by the incoming photons sit on a pedestal: the *bias* level. Of course, it has to be removed before the scientific measurements can be carried out. The mean value of the bias present during a certain integration is determined from the so called *overscan*, *i.e.* a few columns of the CCD that do not view the sky.

It was realized soon after launch that even and odd numbered columns show different bias levels. As a consequence, a value is derived separately from the odd and even columns of the overscan region. This is particularly important in reducing the final error in the cases in which the source is not bright enough to dominate the error budget with its Poissonian noise.

Bias Image Subtraction

The value of the bias level can, of course, vary with position across the chip. Hence, once the global level is removed from the image, a bias image is subtracted to correct for any position dependent pattern. This image is the result of many zero-length exposures, corrected for A/D imperfections and with the global bias level removed. They need to be zero-length exposures, so that the dark current is negligible (see next step).

The bad pixels in the quality files of the bias exposures are marked in the final data quality file.

Dark Image Subtraction

An electrical current is present in the CCD even when it is not illuminated. This *dark current* is caused by thermally excited electrons in the CCD and from the *dark glow* from the flat fielding lens bombarded by cosmic rays. While the first component is relatively stable between observations, the second is found to be correlated with the observed cosmic ray flux. Moreover, it is not spatially uniform, but shows a characteristic edge drop of about 50%, due to the geometry of the CCD windows. The typical value of the electronic dark current is of 0.001 $e^{-}s^{-1}$ and the dark glow is comparable in the WF2 chip and grows to 0.005 $e^{-}s^{-1}$ in the PC chip, where it is the main component of the dark background.

The dark reference files are generated from ten or more individual dark frames, *i.e.* long exposures with the shutter closed, that have been individually corrected for A/D anomalies and global and local bias. The resulting dark frame is scaled to the exposure time of the scientific observation and subtracted from it.

Dark frames are also used in dealing with *warm pixels*, *i.e.* pixels with dark currents several times larger than the mean. They are a few thousands per chip and are thought to originate as a consequence of on-orbit bombardment of heavy nuclei. To repair warm pixels

a monthly decontamination is run by warming up the instrument to a temperature of about 22 C. Since their number, position and value vary with time, dark frames as temporally near as possible to the actual observation are needed. However, this is usually not possible in the standard pipeline, since the dark frames too require some processing and usually become available a week or two later than the observation itself. As a consequence, the dark frames actually used in the standard pipeline are perfectly adequate to cope with the dark current and glow, but the warm pixels need to be treated separately. We will come back to this point later when describing the Post-Pipeline calibration in section 4.1.3.

The dark image is accompanied by its own Data Quality File.

Flat-fielding

The number of electrons produced by a given incoming flux through a certain filter in a pixel depends on the quantum efficiency of that particular pixel and on any eventual vignetting of the field of view caused by the telescope and camera optics. To correct for these inhomogeneities, the image is divided by a flat-field image, *i.e.* an image resulting from the uniform illumination of the camera.

In the case of WFPC2, the flat-field large scale structure is determined from on orbit data, obtained both with an internal lamp and using the sunlit earth as uniform source. The small scale variations in pixel response are inferred from data taken before launch. A combination of these two sets is used in determining the global flat-field reference frames used for calibration.

WFPC2 flat-fields are defined so that a source of constant brightness produces the same count rate per pixel across the image. However, geometric distortion causes the effective sky area seen by a given pixel to change with the position of the pixel on the chip. Given the way the flat-field are defined, surface photometry is totally unaffected by this effect, but point-source photometry is affected at a 1 to 2% level near the edges of the chip.

The flat-field image too has an associated Data Quality File that is used in creating the final one.

Shutter Shading Correction

In short exposures, the illumination of the field is uneven because of the finite flight time of the shutter blades. All exposures shorter then 10 seconds are corrected for this effect, but is never the case in any of our images.

Creation of Photometry Keywords

A series of photometry keywords are created using the IRAF-STSDAS[a] ***synphot*** package to provide the observer with the conversion factors from calibrated counts to flux and magnitude. The most up-to-date throughput tables available for the appropriate observing mode and filters are used.

Histogram Creation

Histograms of the raw data, the A/D corrected data and of the final calibrated data are created and stored in a multigroup three-line image. For example, the histogram of the final data for the WF3 camera will be stored in the third row of the third group on the histogram image. The default pipeline setting is to not produce this image.

Data Quality File Creation

Finally, the pipeline will generate the calibrated science Data Quality File (DQF) by combining the raw DQF with the static pixel mask and the DQFs for the bias, dark and flat-field reference images. A list of the flags currently used in the WFPC2 DQFs is reported in Table 4.1.

Flag Value	Description
0	Good pixel.
1	Part of a packet corrupted during transmission.
2	Calibration file defect.
8	A/D converter saturation[a].
32	Bad pixel that does not fall in the above categories.
256	Pixel lying above a charge trap and might be affected by it.
512	Unrepaired warm pixel.
1024	Repaired warm pixel.

[a]4095 DN in the raw image.

Table 4.1: *WFPC2 data Quality File flag values.*

[a]STSDAS, the Space Telescope Science Data Analysis System, is a software package running under IRAF for calibrating and analyzing data from the *Hubble Space Telescope*.

Regarding the saturation, the ADC works with 12 bits and, hence, saturates at 4095 DN and this is when a pixel is labelled. However, the actual value in the science image can be much lower than this due to bias subtraction and flat fielding. As a rule of thumb, any pixel in the science image with more than 3,500 DN is very likely to be saturated. Of course, one should always check in the calibrated DQF if this is really the case or not.

It is very important to bear in mind that the bad pixels flagged in the Data Quality File are not automatically fixed in the final science file during the calibration pipeline and it is left to the observer decide what to do with them.

File names

Each WFPC2 exposure is obtained as four images, one for each CCD chip. The raw images are INTEGER, and the calibrated ones are REAL, in virtue of the division by the flat-field file. An INTEGER WFPC2 image, such as the raw one or the DQFs, occupies roughly 5 MB of space, whereas a REAL one needs roughly 10 MB.

The name of an image is made of two parts: a rootname that identifies the dataset and a suffix that identifies its content. In Table 4.2, we report the suffixes of the most common files. Currently, the files are stored in the archive in FITS format (hence the final letter "f" in the suffix). The name of a file retrieve from the *HST* archive is in the form: **root-name_suffix**.fits.

Suffix	File content
d0f	Raw science data.
q0f	DQF for raw science data.
r0f	Static mask.
r1f	A/D correction.
r2f, b2f	Bias frame.
r3f, b3f	Dark frame.
r4f, d4f	Flat-field.
r5f	Shutter shading.
c0f	**Calibrated science data.**
c1f	**DQF for calibrated science data.**

Table 4.2: *Suffixes for various WFPC2 file types. The b*f files are the DQFs for the calibration images.*

In order to be processed with `IRAF`, the images have to be converted to the so-called *GEIS* (Generic Edited Information Set) format with the `STSDAS` task ***strfits***. In this format each image is composed by two files. An ASCII *header file* whose suffix ends with the letter "h" and a binary *data file* ending with the letter "d". So, for example, in GEIS format the science calibrated data file name will be something like: **rootname.c0h** for the header part, and **rootname.c0d** for the data part.

4.1.2 Recalibration?

As mentioned earlier, the *Space Telescope Science Institute* automatically runs all of the observations through the standard calibration pipeline using the most up-to-date reference files available *at the time of processing*. As we have discussed in the case of the Dark Image Subtraction, it is possible that the files used were not the best possible ones, hence the need to recalibrate the data.

In case one wants to recalibrate the data, the very same software used in the WFPC2 pipeline is made available to the general user as the `STSDAS` task ***calwp2***. Its use is very straightforward: everything that one needs to do is retrieve the appropriate calibration files from the archive, set the appropriate flag to "PERFORM" for the steps of the calibration process that need to be performed and let ***calwp2*** do its job. Let us notice here that all the calibration pipeline has to be repeated in order to change even one single reference file.

As far as the observations that will be discussed in this work are concerned, the standard calibration pipeline proved to be perfectly adequate in all cases, but one, for which we had to rerun it with updated files. In this case, we had retrieved from the archive Hα images centered on Supernova 1987A that were taken on February the 3$^{\rm rd}$ 1994, not even two months after WFPC2 was launched. The reference files used in the pipeline were necessarily mainly based on pre-launch data and were absolutely not suitable for our purposes, *i.e.* the estimate of Hα equivalent width from the comparison of these Hα images with R-band ones taken two years later. Actually, even the suggested dark files were not perfectly adequate and we had to generate a more suitable dark from single images taken around the actual date of the science observation. This greatly reduced the contamination from warm pixels.

4.1.3 The Post-Pipeline Calibration

At this stage, after the calibration steps described above were performed either by STScI or by us, we should be handling data that are as good as they can be, since all of the best current knowledge of the instrument was used in calibrating them. However, they are not quite ready for science yet and they can, and have to, be still improved in two respects: removal of *warm pixels* and *cosmic rays*. Let us see how it is possible to solve these two last calibration problems.

Warm Pixels Correction

As already mentioned before, warm pixels are pixels with a dark current several sigmas above the mean, probably caused by the bombardment by heavy nuclei. If the scientific goal is limited to a morphological study of well resolved objects, then one probably should not worry too much about them, since they are easily recognizable. However, if the goal is accurate photometry, as in our case, then warm pixel can easily be mistaken for cores of

faint stars or fall in the aperture used to measure the flux. In any case, it is advisable to correct them before the actual scientific measurements are carried out.

Given their nature, warm pixels are easily identified in dark frames. However, as explained before, their population varies with time and the standard dark correction fails to deal with them adequately. Even dark frames taken within one day of the observation will contain some warm pixels that have varied significantly from those in the observation.

As a part of the routine calibration plans, several WFPC2 dark frames are taken every week. In principle, one should retrieve the dark files taken at the time of observation, process them and subtract them from the raw data to correct the warm pixels. Luckily, though, an `STSDAS` task called ***warmpix*** was developed to do this for you.

The information about the warm pixels in each dark exposure taken are stored in tables that can be used as input for the ***warmpix*** task. Each table typically spans a period of one month between decontaminations. They can be retrieved, in `IRAF` table format, from the WFPC2 WWW page at:

`http://www.stsci.edu/ftp/instrument_news/WFPC2/wfpc2_warmpix.html`.

In detail, the ***warmpix*** task will do the following:

1. If a pixel has a high (***warmpix*** parameter *rej_thresh*) or highly variable (parameter *var_thresh*) dark counts, *i.e.* it is a *hot pixel*, it cannot be fixed. Its value is left unchanged or set to a constant user provided value. The corresponding pixel is marked in the DQF with "512";

2. If a pixel has a moderate dark count (parameter *fix_thresh*), its value can be fixed. A dark value is computed by interpolating between two epochs that encompass the observation. The corresponding pixel is marked in the DQF with the value "1024" (see Table 4.1 on page 62);

3. If a pixel has a normal dark count (below *fix_thresh*), its value and its data quality pixel are left unchanged.

The dark and flat-field reference files used in the calibration and specified in the header of the science image, should be available to the task. This is because the pixel needs to be multiplied by the same flat-field value used in the calibration before the dark value can be corrected. Once this is done, the pixels has to be divided again by the same flat-field value.

Typically, this procedure fixes 90 to 95% of the warm pixels.

Cosmic Ray Removal

WFPC2 images typically contain a large number of *cosmic ray events*. When a cosmic ray or a proton from earth's radiation belt hit one of the CCDs, they deposit a non negligible

fraction of energy in it. The average rate of hits is about 1.8 events s^{-1} per chip, with a variation of about 60% peak to peak depending on geomagnetic latitude and position with respect to the South Atlantic Anomaly. An event affects on average 6 pixels. In Figure 4.1 we show a 200x200 pixels portion of a PC chip after a 1400 seconds exposure. A lot of cosmic ray hits are clearly visible: the one in the top left corner is particularly energetic. Four real point like-sources are marked with circles. Needless to say, you want to get rid of the cosmic rays before performing your scientific measurements.

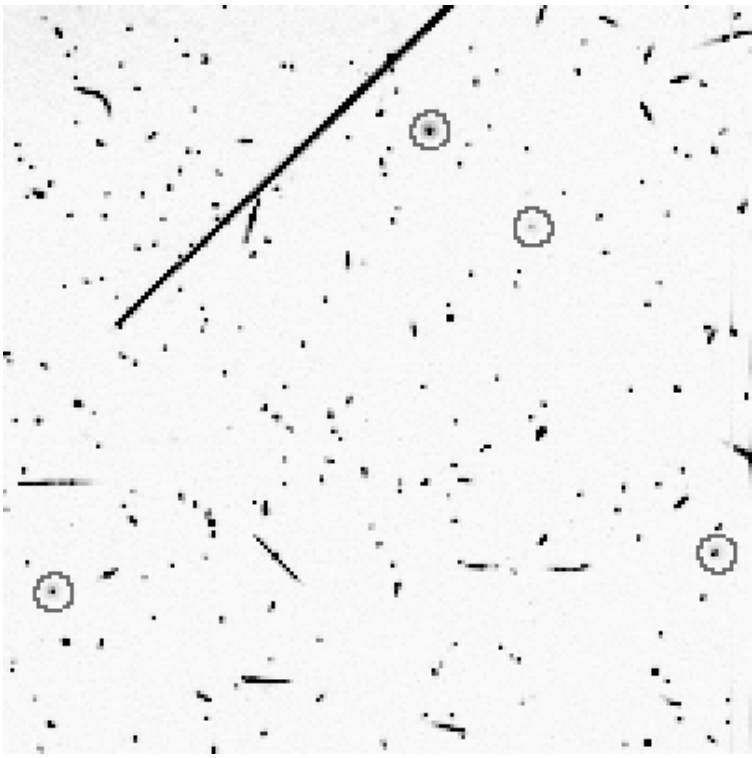

Figure 4.1: *Cosmic ray hits on a 200x200 pixels portion of the PC chip. The exposure time is 1400 seconds. Four real point like-objects are circled.*

Since cosmic ray hits are an intrinsically random process, it is unlikely that the same pixel is hit in two different exposures. Hence, the best way to get rid of them is to take at least two exposures with the same pointing in each filter and compare these two images rejecting the pixels that are not statistically in agreement. This technique is especially advisable if the PSF of your instrument is undersampled, like in the WFPC2 case, thus making it very difficult to differentiate stars from cosmic rays from a single exposure. In fact, exposures longer than 600 seconds are split by default for cosmic ray removal. We have always taken at least two exposures at each pointing in each filter to remove the cosmic rays cleanly.

We have used the `STSDAS` ***crrej*** task to identify and remove the cosmic rays from our images. This task produces an image corresponding to the *sum* of the input images exposure times. The basic idea is very simple: if corresponding pixels in different images are not affected by cosmic rays, then their values should lie a reasonable number of standard

deviations from each other. So, given a certain number of exposures all at the same pointing and with the same filters, the task builds an initial guess (zeroth-order image) by either taking the minimum or the mean value in each pixel among the input images. Then, for every pixel in every input image an estimate of the error is computed. This error (σ) is made up of three terms:

- A *constant term*: this is the Gaussian read-out noise of the detector;
- A term proportional to the *square root of the counts*: obviously, this is the Poissonian statistical error;
- A term proportional to the *number of counts*: this is crucial in case the telescope pointing has changed by a fraction of a pixel between exposures. Since the PSF is undersampled, even a small shift in pointing will cause a measurable difference in the counts in the core of a star. This additional noise term takes into account this effect.

The gain setting has also to be specified in order to compute the errors properly.

Now, every pixel in every input image, scaled by the exposure time, is compared with the corresponding pixel in the zeroth-order image. A given pixel in a certain image is considered to be "good" if it lies within a given number of σ from the initial guess value, "bad" otherwise. For pixels free from cosmic rays, the final value is simply the sum of all input pixel values. For pixels having one or more cosmic rays in their input stacks, the final value is the sum of the good pixels, scaled to the total exposure time of *all* input images. If all of the pixels in a stack are bad, then there is nothing one could do and that pixel given a user specified value and it is marked in the Data Quality File. The task makes it possible to propagate the rejection, that is to specify a lower error threshold in pixels adjacent to one that was identified as hit by a cosmic ray.

The lower the error threshold is set, the more cosmic rays are positively identified and removed. On the other hand, if the threshold is too low also a certain number of good pixels are going to be rejected just because, on pure statistical grounds, they happen to lie several standard deviations away from the true value they should have. What is the right threshold to choose, then? The answer to this dilemma is *iteration*, of course. The image produced thus far can be regarded as first-order cosmic ray free and the whole procedure can be iterated, lowering the rejection threshold, until a satisfactory result is achieved. Beside allowing the solution to reach an equilibrium, iterating the rejection procedure allows for the rejection to propagate to adjacent pixels.

After a few trials, we have found that it was enough to iterate three times with an error threshold of $\sigma = 8, 6, 5$ for the three iterations, respectively. As an example, in Figure 4.2 on the next page we show the same portion of the PC chip of Figure 4.1 after cosmic ray removal. As it can be seen, the cosmic rays have been removed quite effectively. In this particular case, the input images were 4, all with the same exposure time of 1400 seconds.

Hence, the output corresponds to a total integration time of 5600 seconds. In order to more or less match the contrast of Figure 4.1, and for illustration purposes only, the actual counts in the image in Figure 4.2 were divided by 4.

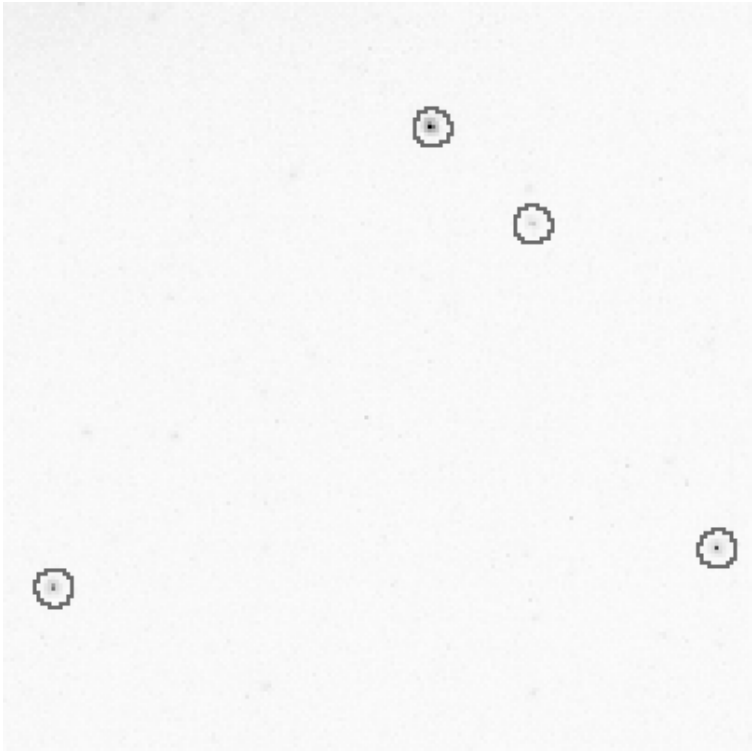

Figure 4.2: *The same portion of the PC chip of Figure 4.1 on page 66 after* ***crrej*** *was used to remove the cosmic ray hits. The same point-like objects of Figure 4.1 are circled.*

The Charge Transfer Efficiency problem

The WFPC2 CCDs have a small, but significant charge transfer efficiency problem which causes some signal to be lost when charge is transferred down the chip during read-out. This has the effect of making objects at higher row number, for which more charge transfers, appear fainter then they should. This effect depends on the CCD temperature and was greatly reduced when the temperature was lowered from -76 C to -88 C on April, 23^{rd} 1994. Unfortunately, at the time of writing the problem is neither well understood, nor well characterised.

In any case, we have not applied any correction for it since the background in our images is always fairly high, as discussed in Holtzman et al. (1995a).

4.2 Point Source Photometry

Now that the images are properly calibrated, we are finally ready to carry out our scientific measurements. What we want to do is to measure the fluxes from the stars in our frames. As we have discussed in section 3.1.1, stars appear on the detector as point-like sources with their characteristic Point Spread Function (PSF).

There are two methods to measure the fluxes from a point-like source: *aperture photometry* and *PSF fitting*. We will describe them shortly. However, before coming to measure any fluxes, we have to identify the stars in the field.

4.2.1 Finding stars

Given a series of exposures of the same field in different filters, we search and identify the stars once and for all in the deepest of them, usually the F555W. Of course, not all of the stars identified in this way will be well exposed also in all of the other filters. Actually, it easily foreseeable that most of them would not even be detectable in the bluer filters, where both the WFPC2 sensitivity and the intrinsic emission of the numerous red stars drop dramatically.

We have used the `IRAF` task ***daofind*** to identify the stars in our frames. For every pixel (i_0, j_0) in the input image, the task will compute the peak value (H_{i_0,j_0}) of the best-fitting Gaussian of specified FWHM (*fwhmpsf*) and ellipticity (*ratio*) centered on it. The fit is performed using the pixels in a sub-raster of width *nsigma*, expressed in units of *fwhmpsf*. If a star is indeed centered in that pixel, the central height of the fitted Gaussian will be proportional to the brightness of the star. If, on the other hand, no star is there, the fit will be very poor and the central height of the best-fitting Gaussian will be near zero. The user is asked to supply a threshold value above which the pixel will be considered as the centre of a star.

Let us consider a certain pixel (i_0, j_0) in the input image and the pixels (i, j) in the sub-raster surrounding it. If G is the Gaussian of unit height and given FWHM and ellipticity:

$$G\left(\Delta i, \Delta j; \sigma_i, \sigma_j\right) = \exp\left[-\left(\frac{\Delta i^2}{2\sigma_i^2} + \frac{\Delta j^2}{2\sigma_j^2}\right)\right] \tag{4.1}$$

where $\sigma_j = ratio \cdot \sigma_i$, $\Delta i = i - i_0$ and $\Delta j = j - j_0$, the fitting procedure described above is equivalent to convolving the input image (D_{ij}) with an appropriate truncated lowered Gaussian W (see Stetson, 1987):

$$H_{i_0,j_0} = \sum_{ij} \left(W_{i-i_0,j-j_0} \cdot D_{ij}\right) \tag{4.2}$$

where the convolution kernel W is related to the Gaussian function in equation (4.1) by:

$$W_{\Delta i,\Delta j} = \frac{G\left(\Delta i, \Delta j; \sigma_i, \sigma_j\right) - \left(\sum G\right)/n}{\sum G^2 - \left(\sum G\right)^2/n} \tag{4.3}$$

where n is the number of pixels in the sub-raster. Note that $\sum W = 0$.

The ***daofind*** task identifies the significant peaks in the convolved image performing the following steps:

1. Read the input parameters. The most important ones are *fwhmpsf*, *datamin*, *datamax*, *sigma* and *threshold*;
2. Compute a Gaussian kernel W of equation (4.3) to be convolved with the input image;
3. Reject the pixels outside the [*datamin*,*datamax*] interval and convolve the image with the Gaussian kernel. As said, this is equivalent to fitting a Gaussian with FWHM *fwhmpsf* at each point in the input image. Obviously, *fwhmpsf* has to be approximately equal to the FWHM of the actual PSF;
4. Search for local maxima in the convolved image H whose amplitude exceeds the specified *sigma*·*threshold*, where *sigma* is the standard deviation of the background. We usually set *threshold*=5;
5. For every maximum detected in the convolved image, various quantities are computed:
   - x and y centres with 1D Gaussian fits to the light profiles in x and y respectively;
   - The shape indicator *sharpness*:

     $$sharpness \equiv \frac{D_{i_0,j_0} - < D_{ij} >}{H_{i_0,j_0}}$$

     where $< D_{ij} >$ is the mean value in the sub-raster excluding (i_0, j_0). Hot pixels typically have values much greater than 1, and cold pixels of roughly 0. After a few tests, we have chosen to keep the default values of 0.2 and 1 as lower and upper threshold for the *sharpness*, respectively.
   - Another shape indicator, called *roundness*, designed to reject the fake detections along the bleeding directions of heavily saturated stars. It is defined as:

     $$roundness \equiv 2 \cdot \frac{h_i - h_j}{h_i + h_j}$$

     where h_i and h_j are the peak intensities of the 1D fitting Gaussian along the rows and columns, respectively. A perfectly round object will have a *roundness* of 0, one which is elongated in the x direction will have a negative *roundness* and a positive value will indicate an object elongated in the y direction. The *roundness*

was introduced to reject bad columns and rows and does not select efficiently against objects which are elongated in a direction inclined with respect to the rows and columns of the detector, such as, for example, an edge-on spiral galaxy. In this case too, we have found that the default values for rejection of 1 and -1 worked well.

- An estimate of the magnitude relative to the detection threshold. We have never used it.

6. Reject the local maxima whose centres are outside the image or whose value of *sharpness* or *roundness* fall outside of the specified boundaries;

7. Number the accepted local maxima (point-like objects) and write an output list with the quantities computed above.

Once ***daofind*** has completed its job, it is advisable to check visually on the original image the stars that it has identified. This can be done, for example by marking their positions on the image using a task like ***tvmark***. Most likely, ***daofind*** did do a good job, with the most noticeable exception of finding stars all along the diffraction spikes of very well exposed stars. These are caused by the supports of the secondary mirror and are oriented at 45 and 135 degrees with respect to the columns. Given the way it is defined, the *roundness* criterion does not reject them. We found that the easiest and simplest thing to do to get rid of these fake detections is probably to remove them by hand from the list and this is what we have decided to do. However, it is also possible to do it automatically by defining a *diagonal roundness* and tune the allowed values for it using a stars identified by eye (see, for example, Cool and King, 1995).

Next and final step, we perform a preliminary aperture photometry on the objects in this "cleaned" list on the image we had used to identify them, using the very same parameters that will be used for the final photometry (see section 4.2.5). The results are used to further select only the stars that have no errors during the photometry, *i.e.* during the centering, sky subtraction and the photometry itself, and that have a photometric error smaller than 0.2 *mag*. Also, we reject the objects that, due to recentering, have merged with others or are too close to the image edges.

Since saturated stars need to be treated in a different way from the other stars, we make a separate list with those that are saturated in at least one filter. A saturated star is easily recognizable by the appropriate flag ("8") in the Data Quality File (see Table 4.1).

To recapitulate, the final list of stars is the result of the following steps:

1. We use the ***daofind*** `IRAF` task to identify the candidate stars with a peak intensity $5 \cdot \sigma$ above the background level in the deepest image;

2. The obviously false detection along the spiders and bleeding columns of the saturated stars are rejected after a visual inspection;

3. We perform aperture photometry on the remaining stars in the filter used for the first identification and keep only those with a photometric error smaller than 0.2 *mag*. This is the final list for the field;

4. We create an auxiliary list with only the stars saturated in at least one filter. It will be used to treat them properly.

4.2.2 Aperture Photometry

Aperture photometry is point-source photometry in its simplest form. It consists in measuring the flux of a star inside a given aperture, usually circular. The flux inside the aperture is the sum of the fraction of star's PSF falling into it and of the diffuse emission projected onto the star, the so-called "sky". Of course, the sky value needs to be evaluated and subtracted from the total flux in the aperture to compute the flux from the star alone. Once this is done, the only further information needed is the fraction of the total flux that falls in the photometry aperture, *i.e.* the *aperture correction*. This can be computed, for example, from the growth curve[a] of bright, isolated stars in the field, should they exist. Very simple and very convenient, indeed. Aperture photometry is also the first-order flux estimate used in PSF fitting.

There is an `IRAF` task to perform aperture photometry: ***phot***. Schematically, this how it works:

1. Read in the input image, coordinate list and task parameters;

2. Read the coordinates from the input list and compute new centers. We have used a centering box (*cbox*) of 3 pixels on a side around the input value to compute the centroids in the x and y directions. The centroid algorithm simply consists in projecting the intensity distribution inside the centering box along the two axis and compute the means of the two projections as the x and y coordinates of the centre. The root mean square deviations in the two directions give an estimate of the uncertainty in the position of the centre. If the centering was error free, the flag "cier" is set to zero, otherwise it is set to a value indicating the type of problem encountered;

3. Compute the value of the sky emission that is superposed to the flux from the star. The sky value is estimated as the mode[b] of the intensity distribution in an annulus of radius *annulus* and width *dannulus*. An Optimal Filtering Technique is used to find the mode efficiently. It is preferable to use the mode instead of the mean, since it is almost totally insensitive to isolated pixels with very high or low values. The standard

[a] The *growth curve* is just the encircled energy defined in equation (3.8) on page 50 as a function of radial distance from the centre of the star.

[b] The *mode* of a distribution is the value corresponding to its peak, *i.e.* the most probable value.

deviation around the sky value is also computed and will be used as an ingredient to compute the error on the photometry. Also in this case, if the procedure was error free, the flag "sier" is set to zero, otherwise it is set to a value indicating the type of problem encountered;

4. Measure the integrated flux inside the photometry aperture of radius *apertures*. If a pixels falls only partially inside the aperture, only the appropriate fraction of its flux is used in the integral. The flag "pier" is used to signal any problem in measuring the flux;

5. Write all of the quantities computed above and various derived ones to the output file.

After trying both aperture photometry and PSF fitting, we have decided that this latter technique did not provide a substantial advantage and we decided to opt for the first one. The parameters we have used in the photometry are described in section 4.2.5.

4.2.3 PSF Fitting

Aperture photometry only uses the total number of counts inside a give radius from the centre of a star. The idea behind the PSF fitting technique is to use a PSF image to fit all of the stars in the field. It can either be constructed from a few relatively isolated and well exposed stars in the field or from any other reliable source. During the fit, the contribution of every pixel to the total sum is weighed in proportion to the Point Spread Function with other weights that take into account different sources of errors: flat-field errors, errors introduced when interpolating etc.

The PSF fitting technique was introduced to perform accurate photometry in very crowded regions, where the apertures might overlap and, obviously, aperture photometry fails. We will now briefly describe the PSF fitting method as implemented in the `IRAF/DAOPHOT` package. The basic algorithm and philosophy can be found in Stetson (1987, 1992). As a curiosity, the prefix "**DAO**" stands for the **D**ominion **A**strophysical **O**bservatory in Victoria, BC (Canada) where the software wad developed.

PSF fitting certainly is more involved than the simple aperture photometry, that is actually just a component of it, but, in principle, is pretty straightforward.

The PSF that is built is *psfrad* pixels on a side and consists of different parts: an analytic function and one or more lookup tables of residuals from it. Only the pixels within *fitrad* pixels from the centre are used in computing the analytical part.

An *analytic PSF* has the advantage that it can be integrated numerically over the area of a pixel, thus minimizing the effects of the finite pixel size in a undersampled PSF. The main disadvantages are that numerical integration of an arbitrary function can be quite time consuming and that many more parameters than one would want to use might be required to carefully reproduce the PSF. On the other hand, an *empirical PSF* can be integrated much

more efficiently and it avoids entirely the need for parameters in the fit. Unfortunately, though, it behaves very poorly if the original PSF is undersampled. A combination of the two is, therefore, needed.

What should we take for the two parameters that define the characteristic dimensions of the PSF? Well, *psfrad* should be maybe 1 pixel larger than the radius at which the brightest star of interest disappears in the background and *fitrad* should roughly match the FWHM of the PSF. It any case, it should be large enough to contain a fair number of pixels and, for WFPC2 images, 3 pixels is probably a good choice. It is not possible to give strict rules on how to set them and the only thing to do is trying different combinations until a satisfactory final result is obtained.

Let us now see in some detail the different steps involved in building a good PSF:

1. Run the ***daofind*** task described above to identify the stars;

2. Run ***phot*** task to perform aperture photometry on them. This will be used as first-order photometry in the actual fit;

3. Select the candidates from which to build the PSF among the stars identified by ***daofind***. Building a good PSF is the crucial step in the whole process and the greatest care should be used here.

   A good PSF star should be bright, with no other stars contributing any light within *fitrad* from its center, it should be the brightest in its neighbourhood and, obviously, it does not have to have bad rows, columns or even pixels around it. Since these requirements are quite difficult to meet in a crowded field, it is very likely that a bit of iteration is necessary to build a good PSF.

   We can use the ***pstselect*** task to select the zeroth-order candidates. All it does is to take the output from ***phot*** and select the brightest *maxnpsf* stars which are not saturated, more than *fitrad* pixels from the edges of the image, have no bed pixels within *fitrad* pixels and have no *brighter* neighbors within (*psfrad*+*fitrad*+2) pixels. Just about exactly what we were looking for;

4. At this point, one should visually check the vicinities of the stars selected as PSF candidates to see if there are stars that ***daofind*** has missed. If this is the case, then they should be added to the output ***phot*** file by running this task interactively on them;

5. We are ready to estimate the PSF for the first iteration. The ***psf*** task accepts as input an image and a list of stars in it and builds a PSF out of them. It is better to run this task interactively to delete from the input candidate list stars that might look suspicious, such as those with too close neighbours, or do not really look circular etc. When run interactively, the task allows to make mesh, contour and radial plots

in a region (*psfrad*+*fitrad*) pixels around the candidate star to carefully check its environment.

At the time of writing, the analytical component of the PSF can be chosen among a Moffat function, a Gaussian, a Lorentzian or a combination of these last two, *i.e.* a Gaussian core and Lorentzian wings. Usually, a Gaussian is the best choice for a well sampled ground-based image and a Lorentzian is to be preferred for *HST* observations. There is an option to try them all and pick the one with the smallest scatter.

The ***psf*** task also identifies as the *neighbors* of a candidate star the stars within (*psfrad*+2·*fitrad* +1) pixels from it and as *friends* to the neighbours the stars within (2·*fitrad*) pixels from them. The PSF star, its neighbours and their friends are called the *group* associated with the star. We shall see a bit further on why this grouping is done.

The PSF image is written to a file with the "psf" extension and the candidate PSF stars are saved in a ".psg" file, together with all of the information about their neighbours and their friends;

6. Let us now fit the stars in each group defined above with the PSF we have computed thus far. The task ***nstar*** will do it for us.

   To help prevent the bumps in the initial PSF from interfering with the profile fits in ***nstar***, it may be necessary to temporarily set *psfrad* to a lower value than before. A good guess is one pixel more than the separation of the nearest neighbour to a PSF star.

   The output file will have the "nst" extension;

7. Just to make sure that we are not missing something, what we want to do now is to subtract the stars in the "psg" file from the input image. This is to check and make sure that there are not any faint, still undetected stars around them. If these stars are indeed present, we have to add them to the list;

8. As we have already discussed, we do not want stars anywhere near a candidate PSF star. What we want to do now, then, is to remove all of them from the original input image before computing the next order PSF. This is what the friends and neighbours defined by ***psf*** are for. In order to do this, we take the ***nstar*** output file ("nst") from the step 6 and edit it to delete the PSF candidates and leave just their neighbours and their friends, *i.e.* the stars we want to subtract from the original image. Once this is done, we can run the ***substar*** task on this edited "nst" file. The output of ***substar*** is a subtracted image with the "sub" extension;

9. We can now compute the second-order PSF by running ***psf*** on the image from which we have subtracted the neighbours and their friends, *i.e.* the "sub" image from 8. At

this point we can restore *psfrad* to its original value. Once again, it is better to run this task interactively to look at the stars before actually accepting them to build the PSF;

10. Rerun ***nstar*** on the *original* image with the output ".psg" file from the previous step as input stellar photometry file and the newly computed PSF image;

11. If any neighbours stars are still visible, repeat the steps from 8 to 10 until a satisfactory removal is achieved. The main thing to remember here is that every time through the the loop the PSF is computed with ***psf*** from an image in which the neighbours and their friends, but not the PSF stars have been subtracted out. On the other hand, ***nstar*** and ***substar*** have to be run on the *original* image, the one with all the stars still in it.

Once a good PSF is finally built, we can move on and fit it to all of the stars, the ones that were originally identified by ***daofind*** in step 1 and all those that were added later (steps 4 and 7). Ideally, all of the stars in the frame should be fitted simultaneously to take into account their mutual influences. Although theoretically feasible, it would be very time consuming. In fact, to determine two centroids and the brightness scale factor for each of the N stars, this approach would require the simultaneous solution of at $3N$ equations. Solving for additional parameters, such as the brightness of the sky, for example, would involve an even larger number of unknowns.

The computation time can be greatly reduced if the problem can be broken up in independent problems each involving only a fraction of the total stars. As the name suggest, the ***group*** task groups together stars that should be fitted simultaneously. The algorithm works in the following manner. If two stars are within a distance of (*psfrad*+*fitrad*+1) pixels, the PSF of the brighter is evaluated at a distance of (*fitrad*+1) pixels from the fainter. If this value is larger than *critsnratio*, than the two stars are assigned to the same group, since the brighter star affects non negligibly to the photometry of the fainter one. A value of *critsnratio* of the order of 1 should work properly in most cases.

The task ***allstar*** fits all of the stars in the frame and subtracts them from the image. We can now use ***daofind*** on the subtracted image to see if there are any faint stars that were invisible previously and perform the photometry on them too.

One important thing to remember is that, even though the entire PSF is fitted to every star, the flux is computed only in the aperture used in the preliminary aperture photometry of step 2. Hence, it is still necessary to compute *aperture corrections*, just as in the aperture photometry case.

4.2.4 Photometry on saturated stars

As we have repeatedly pointed out, the WFPC2 Analog to Digital Converter (ADC) is a 12 bit device and, hence the biggest number it can handle is $2^{12}-1 = 4095$. If a bigger signal is stored in a pixel, the ADC is said to be *saturated* and the remaining electrons are lost. The problem is that a WFPC2 pixel can contain roughly 90,000 electrons (see section 3.1.2). This means that all of the electrons between 4095·*gain* and the full well capacity of a saturated pixel are simply lost. For the *gain*=7 setting this is a factor of more than 3.

In order to avoid the saturation problems, it is certainly a wise idea to take at least one short exposure in every filter, the length of which will be determined by the brightest star in that filter that is expected to be found in the field. However, this is not always possible or, maybe, it turns out that, in a particular field, there was a star brighter than expected. Given the uncertainty on saturated star photometry, one could just disregard them and study only the "well behaved" ones. In our case, this would be a great loss of information, since the saturated stars are generally the more massive and, hence, younger ones. Since we do not want to miss what they can teach us, it is certainly well worth it to try to find ways to recover good photometric information for them. Let us see how we did it.

When the full well capacity of a pixel is reached, any further electron produced there cannot any longer be stored in the pixel and will drift to a neighbouring one along the read-out column. Clearly, if all of the ADC saturated pixels have reached their full well capacity, then no charge is lost: it has simply been relocated to somewhere else. This condition is nearly met in heavily saturated stars. Let us consider the case of a star so bright that its central n pixels are not only ADC saturated, but have also completely filled their potential wells. They will be marked in the Data Quality File as ADC saturated and the excess electrons will have bled to neighbouring pixels. More specifically, they will be stored in the next available pixel that has not reached its full capacity. The only charge that is actually lost, of course, is the one in excess of the ADC saturation value stored in pixels that are ADC saturated, but did not fill the potential well. If n is big enough, the fraction of charge lost is going to be small compared to the total and one can safely assume that all of the ADC saturated pixels have also reached the full well capacity. Under this assumption, one can substitute the actual number of DNs recorded in the image[a] with the one corresponding to the filled well.

This idea is behind the method described in Gilliland (1994). In this work, stars in the Galactic open cluster M67 were used to derive an effective full well capacity for the different WFPC2 chips. This is done by comparing short exposures, in which a certain star is well exposed but not saturated, to long exposures, in which the star is saturated. The full-well depth per pixel can then be derived as the multiplicative term required to maintain a linear scaling of total counts with the exposure time. A total of 30 images were used to derive the

[a]Because of dark frame subtraction and flat-fielding, this value is going to vary from pixel to pixel and will be substantially lower than 4095 (see section 4.1).

effective full-well depth of a pixel in *electrons*:

$$\mathrm{FW}_e = \mathrm{FW} + n_s \cdot \mathrm{FWS} \tag{4.4}$$

where n_s is the number of saturated pixels and the coefficients FW and FWS are listed in Table 4.3 for the four WFPC2 chips. If charges were perfectly conserved, FW_e would be independent on n_s. The dependence on it, however, is very mild.

Chip	FW	FWS
PC	79321	98.7
WF2	92092	32.5
WF3	81682	118.0
WF4	89516	50.7

Table 4.3: *Coefficients for equation (4.4).*

From what we have discussed above, we can substitute the counts in the saturated pixels with their effective full-well capacity. So, let DN_{tot} be the total number of counts inside an aperture that encloses *all of the saturated pixels* and, of course, also some that are not saturated. If n_s is the number of saturated pixels inside it and DN_{sat} are the counts in them, then the number of counts (DN) that we should use in measuring the flux is given by:

$$\mathrm{DN} = \mathrm{DN}_{tot} - \mathrm{DN}_{sat} + \frac{\mathrm{FW}_e \cdot n_s}{gain} \tag{4.5}$$

An aperture correction corresponding to the radius used to compute DN_{tot} needs to be applied to DN to have the total flux. According to Gilliland (1994), in the best cases it is even possible to reach a photometric accuracy as good as 2% with this technique.

We have checked the reliability of this method using a few stars near Supernova 1987A for which independent ground-based measurements were available. The first one is **Star 2**, one of the two bright stars projected close to the Supernova. The angular separation from the Supernova is just $2''.91$ at a position angle of 318°, as measured in our images (see also Sonneborn et al., 1997). Star 2 is heavily saturated in our images (n_s=22 pixels) and, applying the method described above, we find $m(\mathrm{F555W})_{\mathrm{WFPC2}} = 14.99$. Given its colours (*e.g.* B−V$\simeq -0.05$), the transformation term to standard V magnitude is negligible (Holtzman et al., 1995a). This is in excellent agreement both with the value of V= 14.96 ± 0.04 of Walker and Suntzeff (1990) (see their note added in press, not the value in their Table 4) and with the value of V=15.03 found by Walborn et al. (1993).

Scuderi et al. (1996) have obtained a spectrum for Star 2 with the *HST* Faint Object Spectrograph (FOS) before COSTAR was deployed to correct the spherical aberration of the primary mirror. We have convolved it with the response curve of the F555W WFPC2 filter[a] to compute its magnitude through this filter and found $m(\mathrm{F555W})_{\mathrm{FOS}} = 15.25$. Due to the

[a]The convolution was performed using the ***synphot*** synthetic photometry package.

aberration and pointing problems, only a fraction of the stellar flux fell within the adopted FOS aperture (B-3, 0″.83 in diameter). Since no other information was available, Scuderi et al. (1996) computed a mean correction, independent of wavelength, needed to recover the entire flux using the ground-based photometry by Walborn et al. (1993). The correction turned out to be of -0.29 *mag* and, given the way it was computed, the corrected FOS magnitudes are bound to agree with the photometry of Walborn et al. (1993). Unfortunately, hence, we cannot use the FOS spectrum as yet another independent check of our photometry.

We cannot use **Star 3**, the other companion to Supernova 1987A (the separation from SN1987A is 1″.63 at a position angle of 118°), for this kind of comparison, because it is known to be a systematic, long term variable. According to Walborn et al. (1993), the amplitude of its variations is of the order of 0.3 *mag*.

Another star on which we tested the method is one of the Local Standard stars reported in Walker and Suntzeff (1990), namely **S6** in their Table 3. Walker and Suntzeff (1990) find $m(\mathrm{V}) = 13.96 \pm 0.02$ to be compared to our value of $m(\mathrm{F555W}) = 14.01$, which corresponds to $m(\mathrm{V}) = 13.98$ once the the transformation from F555W to the Johnson V filter of Holtzman et al. (1995a) are applied. As it can be seen, the agreement is almost perfect.

Unfortunately, the agreement is not alway this good. In the case of the Local Standard star **S1**, Walker and Suntzeff (1990) find $m(\mathrm{V}) = 14.46 \pm 0.02$, and our method gives $m(\mathrm{F555W}) = 14.55$ and, once again, the colour term to transform to standard V magnitude is negligible. Overall, we reckon that 10% is a reasonable estimate of the uncertainty associated with the "desaturation" procedure described above.

Since it is very difficult to evaluate the error on the flux recovered with this technique, we have arbitrarily assigned an error of 0.032 *mag* to all of the stars treated this way.

As we have mentioned earlier, the Gilliland (1994) technique assumes that the whole potential well of an ADC saturated pixel if actually filled. This is a good approximation when a large number of pixels are ADC saturated, but it surely breaks down when this is not the case and using it would lead to overestimate the flux. In the case in which only a few pixels were saturated, we have excluded them altogether from the photometry and we have measured the flux in an annulus around the saturated stellar core. Its inner radius is the one of the smallest circle that contains all of the saturated pixels and we have taken its width to be 2 pixels. To obtain the total flux, it will be enough to compute the appropriate fraction of the flux in the annulus using the same growth curve used for the aperture correction. In section 4.2.5, we shall discuss the aperture corrections we have adopted.

This second technique too proved to be quite effective. The Local Standard star **S2** in Walker and Suntzeff (1990) is the only standard that is marginally saturated in our frames. Using an inner radius of 3 pixels, we have measured its magnitude to be $m(\mathrm{F555W}) = 16.048 \pm 0.004$ which corresponds to $m(\mathrm{V}) = 16.06 \pm 0.005$, again using the transformations in Holtzman et al. (1995a). The error quoted here is just the *internal error* on photometry and does not take into account absolute calibration errors. Once again, the agreement with the magnitude measured by Walker and Suntzeff (1990) ($m(\mathrm{V}) = 16.07 \pm 0.02$) is excellent.

4.2.5 Photometry: the final recipe

We are finally ready to perform the photometry on the normal, non saturated stars. Let us review the parameters we have chosen to use in the final photometry.

Parameters for Aperture Photometry

The first thing to do is to choose the radius of the photometry aperture (r_i) and the inner and outer radii of the annulus for sky evaluation (r_j and r_k, respectively) shown in Figure 4.3.

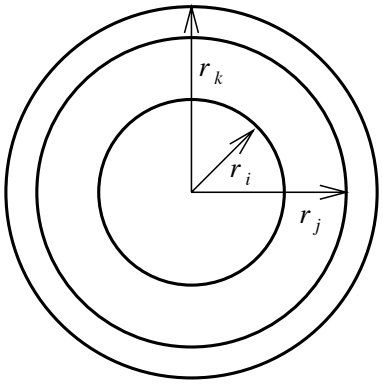

Figure 4.3: *Illustration of the source and sky evaluation in aperture photometry*

As we have repeatedly stated, the WFPC2 PSF is undersampled, especially in the WF chips. As a consequence, most of the light falls in the very central pixels and there is no need to take a big aperture in which to measure the flux. Increasing the aperture size would only enhance the probability, which grows as the area of the aperture, of enclosing a bad pixel or significant flux from a neighbor in it, without any significant increase of the encircled energy. Hence, we have chosen the smallest sensible aperture: $r_i = 2$ pixels. A smaller aperture is not advisable, since the enclosed flux would then strongly depend on where the star's centre actually falls in the pixel.

Since the background is rather clumpy, we want to make sure that we are measuring it as close as possible to the star. For this reason, we have set $r_j = 3$ and $r_k = 5$ pixels which also minimizes the influence of nearby stars on the determination of the background. With this choice of the sky annulus, a non negligible fraction of the stellar PSF falls in it and this has to be properly taken into account.

The ***phot*** task writes its output in an `IRAF` table containing various fields. Besides the newly computed centres of the stars, the ones we are interested in to compute the magnitudes and their errors are listed in Table 4.4 on the next page.

In terms of the quantities in Table 4.4 on the facing page, after a little of simple algebra, the *total* flux from the source in Data Numbers (DN_{source}) is given by:

Quantity	Symbol	`IRAF` table field name
Flux in the aperture	DN_{r_i}	`sum`
Sky flux per pixel	dn_{jk}	`msky`
Sky rms	σ	`stdev`
Area of the aperture	A_i	`area`
Area of the annulus	A_{jk}	`nsky`

Table 4.4: *Selected fields from the output of the* ***phot*** *task.*

$$\mathrm{DN}_{\mathrm{source}} = \left(\mathrm{DN}_{r_i} - A_i \cdot \mathrm{dn}_{jk}\right) \cdot \left[a_i - \left(a_k - a_j\right) \cdot \frac{A_i}{A_{jk}}\right]^{-1} \tag{4.6}$$

where a_l is the fraction of the total flux that falls inside a radius l ($l = i, j, k$), *i.e.* the aperture correction as a function of radius. We will come back to this in the next section. The first term is the flux from the source in the aperture and the second is the correction for the flux falling outside the aperture. The corresponding error *in electrons* is given by:

$$\sigma^2_{\mathrm{source}} = \left[a_i \cdot A_{jk} - \left(a_k - a_j\right) \cdot A_i\right]^{-2} \cdot \left\{A^2_{jk} \cdot \left(\delta\mathrm{sum}\right)^2 + A^2_i \cdot A_{jk} \cdot \left(gain \cdot \sigma\right)^2\right\} \tag{4.7}$$

where δsum is the error on the electrons counted in the aperture r_i due to the Poissonian statistics of the source and of the sky and the noise due to the electronics of the detector:

$$\left(\delta\mathrm{sum}\right)^2 = gain \cdot \left[a_i - \left(a_k - a_j\right) \cdot \frac{A_i}{A_{jk}}\right] \cdot \mathrm{DN}_{\mathrm{source}} + A_i \cdot \left(gain \cdot \sigma\right)^2$$

The magnitude and its error are then computed as:

$$\begin{cases} m &= -2.5 \cdot \log\left(\mathrm{DN}_{\mathrm{source}}\right) + ZP \\ \delta\left(m\right) &= 2.5 \cdot \log\left(1 + \frac{\sigma_{\mathrm{source}}}{gain \cdot \mathrm{DN}_{\mathrm{source}}}\right) \end{cases} \tag{4.8}$$

We will come back to the zeropoint (ZP) in the next section.

Possibly, the only advantage of the bizarre definition of magnitude is that:

$$2.5 \cdot \log\left(1 + x\right) \overset{x \to 0}{\to} x$$

so that is very easy to readily compute the signal-to-noise ratio from the magnitude error and vice-versa.

As we have already said in section 4.2.1, when describing the ***daofind*** algorithm, we look for and identify stars once and for all in the deepest frame and perform photometry on the objects in this list in all of the filters. As a consequence, an object might not be detectable in all the filters, because of the combination of intrinsic faint emission and low detector sensitivity in a certain wavelength range. We have adopted a detection threshold of "three sigmas", in the sense that, whenever the measured signal-to-noise ratio of a given star in a filter is lower than three, we flag it and assign to it *only an upper limit* to its flux, set equal to three standard deviations of the background.

Aperture corrections and zeropoints

Since in our images there are very few well exposed, but not saturated stars, we have computed the aperture corrections from stars retrieved from the WFPC2 PSF Library that can be accessed from the WWW at the following address:

`http://www.stsci.edu/ftp/instrument_news/WFPC2/Wfpc2_psf/wfpc2-psf-form.html`

This is a library of *observed*, well-exposed and isolated stars for almost all of the WFPC2 filter in different positions on the chips.

Following Holtzman et al. (1995b), we have normalized the aperture corrections to $1''$, *i.e.* 20 PC or 10 WF pixels. For every aperture, we have averaged the fraction of the flux in it of several stars (exactly how many basically depended on the availability in the archive). Then, we have clipped the data at the 1.5σ level to get rid of any possible bad pixel or badly removed cosmic ray that could have effected the flux measure in a certain aperture. The resulting aperture corrections for the PC chip we have used throughout our analysis are reported in Table 4.5:

Radius	F255W	F336W	F439W
2	0.70±0.12	0.67±0.063	0.70±0.040
3	0.79±0.11	0.77±0.074	0.80±0.043
5	0.87±0.10	0.84±0.077	0.87±0.044
Radius	F555W	F675W	F814W
2	0.68±0.016	0.62±0.020	0.58±0.027
3	0.83±0.024	0.80±0.023	0.77±0.033
5	0.90±0.029	0.88±0.023	0.89±0.035

Table 4.5: *Aperture corrections for the PC chip in the filter we have used the most. The quoted errors are the rms deviation of the aperture corrections of the different stars used.*

and the ones for the WF chips in Table 4.6:

Radius	F255W	F336W	F439W
2	0.76±0.012	0.78±0.044	0.80±0.037
3	0.84±0.010	0.86±0.039	0.89±0.031
5	0.91±0.012	0.91±0.034	0.94±0.027
Radius	F555W	F675W	F814W
2	0.83±0.014	0.79±0.007	0.80±0.029
3	0.90±0.011	0.88±0.012	0.89±0.029
5	0.95±0.003	0.95±0.011	0.94±0.017

Table 4.6: *Same as Table 4.5 on the facing page, but for the WF chips.*

The comparison between the aperture correction we have computed and the ones of Holtzman et al. (1995b) for the F555W filter is shown in Figure 4.4. These latter ones are determined by averaging eight separate observations of a single flux standard. The agreement if very good, despite the fact that a different set of stars were used to compute them, clearly indicating that the encircled energy is remarkably constant.

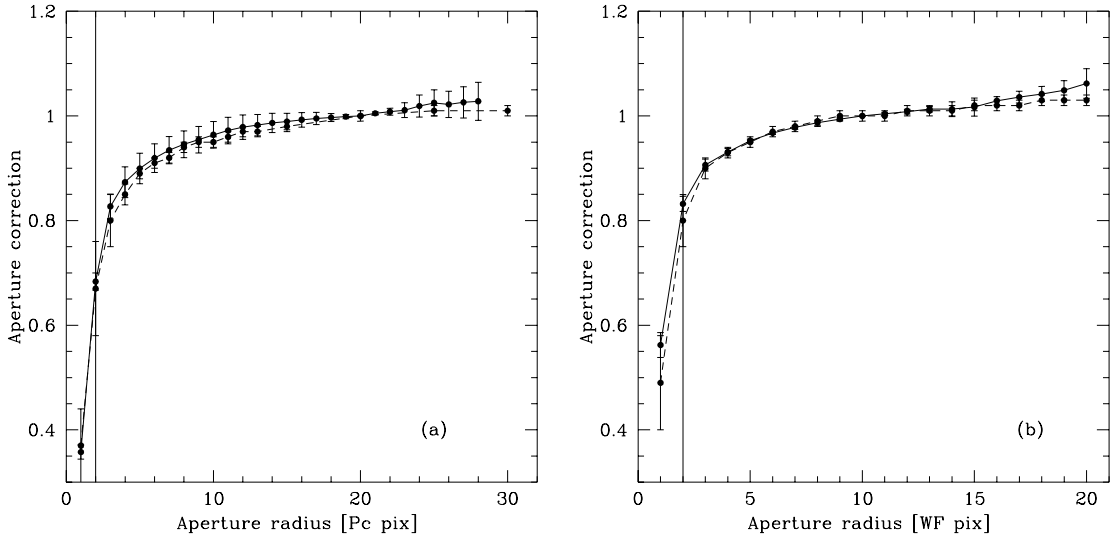

Figure 4.4: *Aperture correction as function of radius for (a) the PC and (b) the WF4 chip. Both our determination (full line) and the values from Holtzman et al. (1995b) (dashed line) are shown. The scale is 0″.0455 per pixel in the PC and 0″.0996 in the WF. All of the curves are normalized at 1″ and the radius of the aperture in which the flux is measured is shown as vertical line.*

The aperture correction in Tables 4.5 on the facing page and 4.6 are referred to a 1″ aperture and, hence, another factor has to be applied to include the flux up to infinity. Since we did not have stars isolated enough in our fields, we have used the value for the biggest aperture in Holtzman et al. (1995b) (130 pixels for the PC and 60 pixels for the WF) to

estimate it. This further correction amounts to a factor of 1.08 for the PC and 1.06 for the WF chips.

The last thing we have to set are the *zeropoints* (ZP) in the various filters. Coming back to equation (4.8), the zeropoint in a certain filter is the magnitude of a star that produces 1 DN per second in that filter. It is simply determined by observing a set of *standard stars*, *i.e.* stars of known magnitude.

We have used the zeropoints, in the VEGAMAG scale, from Whitmore (1995). However, let us stress here that the ZP has no influence whatsoever on the final results that we want to achieve, *i.e.* luminosity and temperature for the individual stars. As we shall see in greater detail, we will compare the observed Data Numbers directly to the Data Numbers that the models would produce when observed with WFPC2, without any need to compare magnitudes.

Aperture photometry vs. PSF fitting

As we have already mentioned, after a few trials we have opted for aperture photometry as the way to measure fluxes, claiming that the crowding in our fields is very modest and PSF fitting is not really necessary. To justify this choice, let us compare the photometry with the two methods in one of most crowded of our chips: the WF3 chip of the July 1997 observations around Supernova 1987A. The F555W image of this field is displayed in the left panel of Figure 4.5 on the facing page. Running ***daofind*** on it with a 5σ threshold results in 3481 stars detected.

In order to carry out the comparison, we have measured the fluxes with PSF fitting in the F555W and F814W filters. The PSF was built interactively as explained in section 4.2.3, starting from 40 PSF candidates selected with ***pstselect***. We have iterated the PSF construction process three times in both filters and 10 and 9 stars were actually used for the final PSF in the F555W and F814W images, respectively. No saturated stars were used in the process.

After the stars are identified, the first thing to do to set up the fitting procedure is to perform a preliminary aperture photometry. We have used the same parameters we normally use in aperture photometry. However, the PSF fitting task ***allstar*** implicitly assumes that only a negligible fraction of the star falls in the sky annulus and, hence, setting $a_j = a_k = 0$ in equation (4.6) on page 81, the flux from the source in the aperture is:

$$\mathrm{DN}_{\mathrm{source}} = \frac{1}{a_i} \cdot (\mathrm{DN}_{\mathrm{r}_i} - A_i \cdot \mathrm{dn}_{jk})$$

As we have pointed out, given the choice of the sky annulus that we make, this is not the case. As a result, the sky is over-subtracted and, hence, the source flux is underestimated. While it is straightforward to account for this as far as the output magnitudes are concerned (see equation (4.6)), it will lead to an incorrect PSF subtraction from the input image. So,

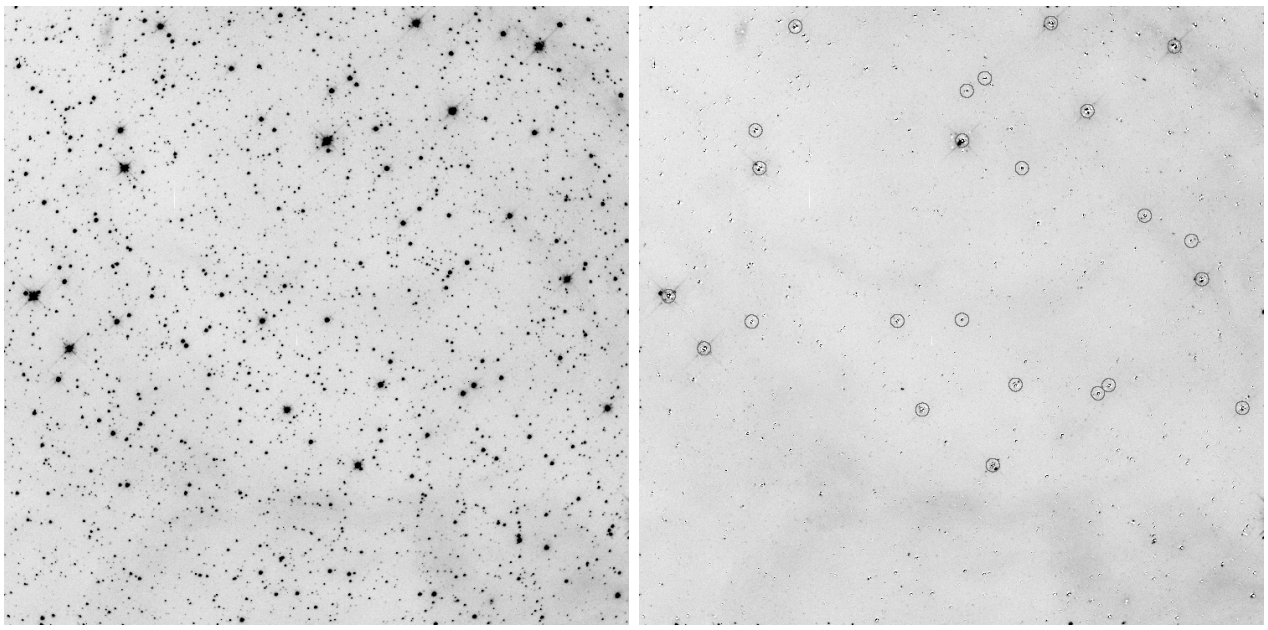

Figure 4.5: *The WF3 chip of the July 1997 observations around Supernova 1987A. The original frame is shown in the* left panel *and the one resulting from PSF subtraction in the* right panel *(see text). The circles in the right panel mark the saturated stars.*

for illustration purposes only, we have also computed a subtracted image starting from a preliminary photometry with the sky annulus much farther out than we usually use: $r_j = 10$ and $r_k = 12$. By doing so, the subtraction is performed in the proper way. The resulting image is shown in the right panel of Figure 4.5, where the circles mark the saturated stars for which, obviously, the core is over subtracted (white colour).

As it can be seen, we did quite a good job, as the vast majority of stars are gone from the image. A few stars were not subtracted perfectly, but let us not forget how hard it is to characterize the WFPC2 PSF, especially in the three WF chips where it is badly undersampled. It is also apparent by looking at the subtracted image in Figure 4.5 (right panel), and even more by running ***daofind*** on it, that there were no faint stars hidden under bright ones and, hence, not visible in the original image (left panel). This confirms that there is no compelling need for star subtraction in order not to loose any of them.

The comparison of the two photometric techniques is made in Figure 4.6 on the next page for stars with photometry more accurate than 0.1 *mag* which are not saturated. The two different techniques lead to comparable results for the vast majority of stars, even though a somewhat large scatter, independent of the magnitude (see panel (*b*)) is present. As an example, we have highlighted two stars that appear much brighter with aperture photometry than with PSF fitting. An inspection of the image reveals that they have a close projected companion that contributes to the flux in the photometry aperture (see the right side of

Figure 4.6). In these cases, PSF fitting is likely to do a better job.

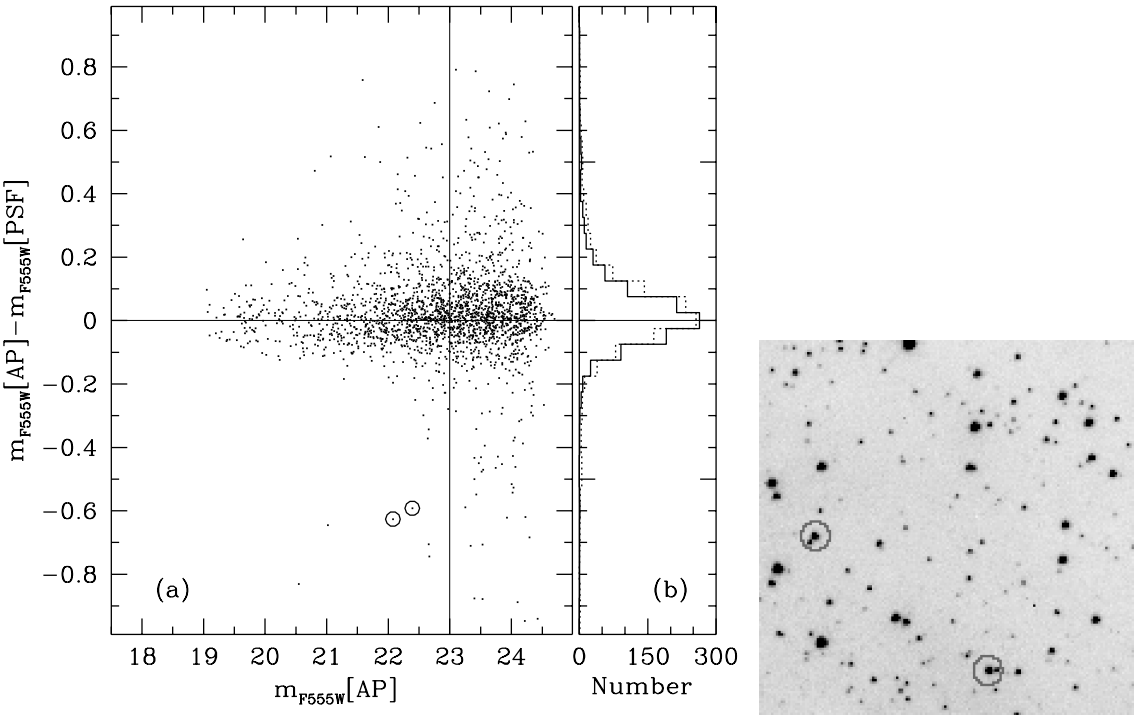

Figure 4.6: *Comparison of aperture photometry and PSF fitting for stars with a photometric error smaller than 0.1 mag. In panel (a), the magnitude difference in the F555W filter is plotted as a function of magnitude. In panel (b), we show the histograms of the magnitude difference for stars brighter than (solid line) or fainter than (dotted line) 23rd mag. The two stars circled in panel (a) are also shown in the image on the right (see text).*

The question arises as what is the origin of the scatter in Figure 4.6 and, above all, what is the best photometry technique to use. The analysis of Colour-Magnitude Diagram (CMD) of Figure 4.7 on the facing page is of some help. We will discuss the properties and stellar content of diagrams like this in the next chapter, but, for the moment, let us concentrate on the colour distribution as a function of magnitude in the interval $20 < m_{\rm F555W} < 26$, where the majority of stars are.

The histograms of the slices in 1 *mag* intervals are shown in Figure 4.8 on page 88. The Main Sequence becomes bluer (*i.e.* smaller colour) as the magnitude becomes brighter. In the last two magnitude intervals, between $m_{\rm F555W} = 22$ and $m_{\rm F555W} = 20$, the Red Giant Branch appears, producing the red peak located at $m_{\rm F555W} - m_{\rm F814W} > 1$.

As apparent from Figure 4.8, the Main Sequence is narrower when the photometry is performed with the PSF fitting and there is not an obvious systematic difference between

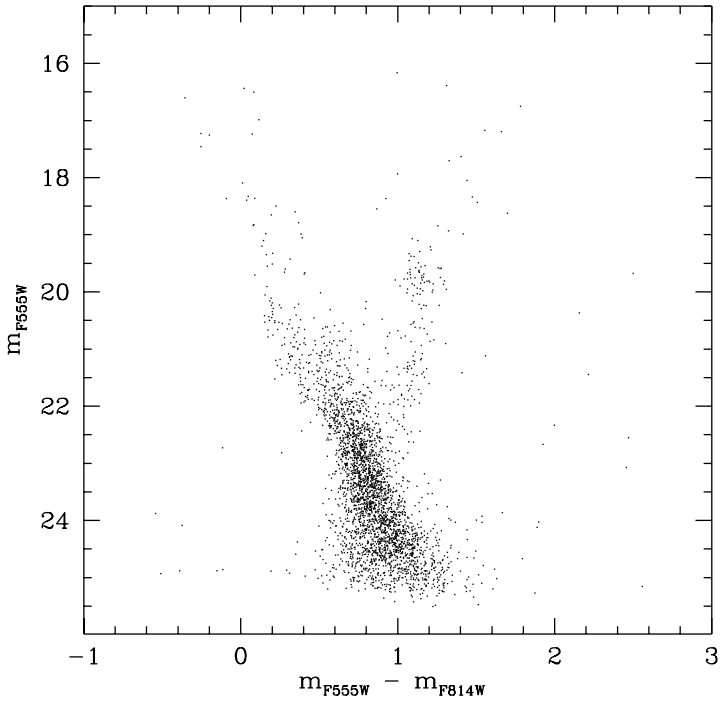

Figure 4.7: *Colour-Magnitude Diagram of the WF3 chip of the July 1997 observations of SN1987A. The magnitudes were measured with aperture photometry.*

the distributions. By taking the average width of the histograms in the $25 > m_{\mathrm{F555W}} > 22$ range, we estimate the widening to be of the order of 17%. So, *not only PSF fitting does not provide better results, but it actually introduces more scatter in the data than the simpler aperture photometry.* In fact, a similar result is found by Elson et al. (1997). Again in a WFPC2 study of a field in the LMC, they find that the Main Sequence is 25% narrower in Colour-Magnitude Diagrams constructed from aperture photometry.

The intrinsic width of the main-Sequence of a Globular cluster is expected to be extremely small, one or two hundredths of a magnitude, since only a single generation of stars is present. For this reason, Globular clusters offer an excellent opportunity to test the accuracy of photometry techniques. In studying the Galactic Globular cluster NGC 6397, Cool and King (1995) find that, indeed, PSF fitting produces a larger scatter than aperture photometry on the intrinsically narrow Main-Sequence of the cluster. However, they also find that the simple weighting of the pixels values by the inverse of the pixel variance gives even better results, again as judged by the width of the resulting Main-Sequence. For all practical purposes, this corresponds to setting to zero all of the additional weights in `DAOPHOT`, leaving only the the intrinsic variance of the pixels.

We have tried this prescription on our data and the resulting histograms of the colour distribution as a function of magnitude along the Main-Sequence is shown in Figure 4.9. As it can be seen, this choice of weights results in a narrower Main-Sequence compared to the

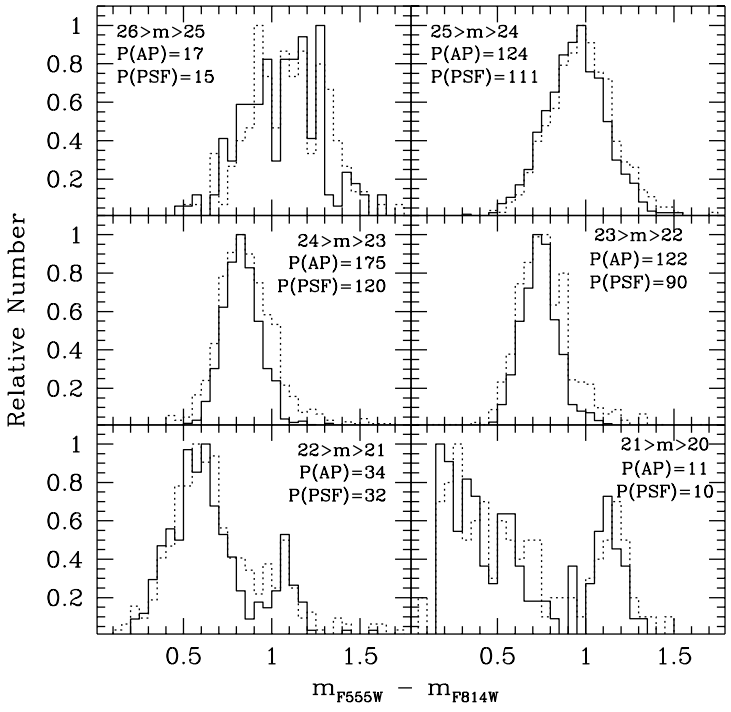

Figure 4.8: *Colour distribution along the Main Sequence of Figure 4.7 on the previous page. The aperture photometry results are shown as a full line and the PSF fitting ones as a dotted line. In every panel, the magnitude range and the peak value for the aperture photometry (P[AP]) and PSF fitting (P[PSF]) are indicated.*

standard PSF fitting. The resulting distribution is now almost indistinguishable from the one derived with aperture photometry and we have definitively adopted the simple aperture photometry as our final recipe.

In general terms, it is difficult to assess once and for all what is the best technique to use in performing photometry on such an undersampled PSF like the one of WFPC2. Probably a universal recipe just does not exist. Different authors have their own preferences and, when it is the case, even change the prescription according to the scientific goal. For example, Gallagher et al. (1996) use aperture photometry with a 2 pixel aperture for a field in the Large Magellanic Cloud, but prefer PSF fitting when they want to push the photometry as deep as possible (Holtzman et al., 1997). In any case, the PSF used in this latter study is not built from stars in the field in the standard way we have described, but it comes from a complex modelling of the optics of the telescope. This includes variations of the pupil function across the field of view as determined from phase retrieval[a] of a number of bright stars in a separate field and medium-scale structure on the *HST* mirrors as determined from out-of-focus images taken with WFPC2 (Krist and Burrows, 1994). Spacecraft jitter information were included in the model for each filter in each exposure. In addition, phase

[a] *Phase retrieval* is a reconstruction technique based on the fact that almost all 2-dimensional sequences with finite support are uniquely defined *just by the magnitude* of their Fourier transform (see, for example, Hayes, 1987). This is not true for 1-dimensional sequences.

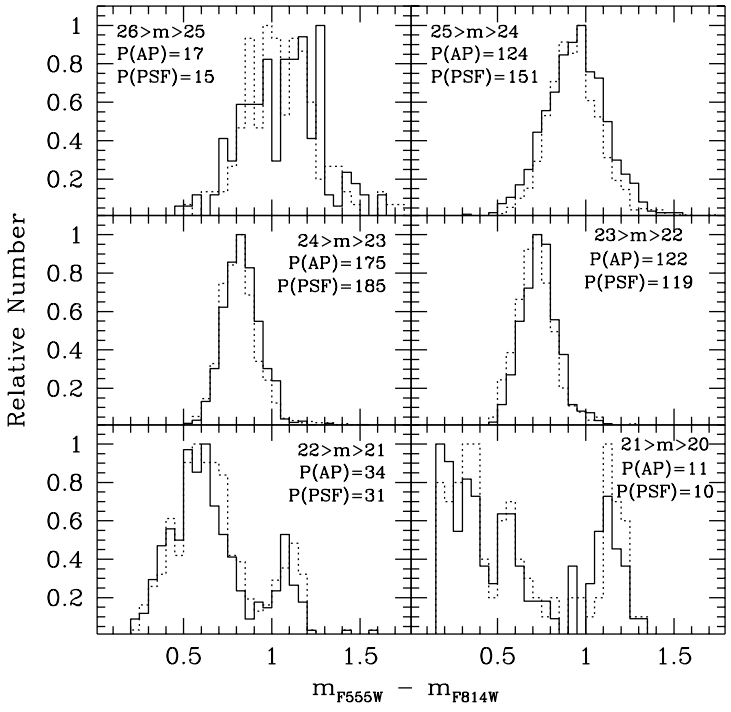

Figure 4.9: *Same as Figure 4.8 on the preceding page, but this time, following Cool and King (1995), the weights for the PSF fitting are just proportional to the inverse pixel variance (dotted line). The results of aperture photometry are also shown (full line).*

retrieval was performed for several stars in each exposure to determine a separate focus value for each exposure.

Bibliography

Biretta, J.A., Burrows, C., Holtzman, J., Heyer, I., Stevens, M., Bagget, S., Casertano, S., Clampin, M., Fruchter, A., Ferguson, H., Griffiths, R., Krist, J., Noll, K., O'Dea, C., Stiavelli, M., Suchkov, A., Surdej, J., and Whitmore, B. *WFPC2 Instrument Handbook Version 4.0*. STScI, Baltimore, 1996.

Cool, A.M. and King, I.R. 1995, In *Calibrating HST: Post Servicing Mission*, A. Koratkar and C. Leitherer (Eds.), Baltimore. STScI, p. 290.

Elson, R.A.W., Gilmore, G.F., and Santiago, B.X. 1997, *MNRAS*, **289**, 157.

Gallagher, J.S. III, Mould, J.R., De Feijter, E., Holtzman, J., Stappers, B., Watson, A., Trauger, J., Ballester, G. E., Burrows, C.J., Casertano, S., Clarke, J.T., Crisp, D., Griffiths, R.E., Hester, J.J., Hoessel, J., Krist, J., Matthews, L.D., Scowen, P.A., Stapelfeld, K.R., and Westphal, J.A. 1996, *ApJ*, **466**, 732.

Gilliland, R.L. 1994, *ApJ*, **435**, L63.

Hayes, M.H. 1987, In *Image Recovery: Theory and Application*, H. Stark (Ed.), Orlando. Academic Press, Inc., p. 195.

Holtzman, J.A., Burrows, C.J., Casertano, S., Hester, J.J., Trauger, J.T., Watson, A.M., and Worthey, G. 1995a, *PASP*, **107**, 1065.

Holtzman, J.A., Hester, J.J., Casertano, S., Trauger, J.T., Watson, A.M., Ballester, G.E., Burrows, C.J., Clarke, J.T., Crisp, D., Evans, R.W., Gallagher, J.S. III, Griffiths, R.E., Hoessel, J.G., Matthews, L.D., Mould, J.R., Scowen, P.A., Stapelfeldt, K.R., and Westphal, J.A. 1995b, *PASP*, **107**, 156.

Holtzman, J.A., Mould, J.R., Gallagher, J.S. III, Watson, A.M., Grillmair, C.J., Ballester, G.E., Burrows, C.J., Clarke, J.T., Crisp, D., Evans, R.W., Griffiths, R.E., Hester, J.J., Hoessel, J.G, Scowen, P.A., Stapelfeldt, K.R., Trauger, J.T., and Westphal, J.A. 1997, *AJ*, **113**, 656.

Krist, J.E. and Burrows, C.J. 1994, *Appl. Opt*, **34**, 4951.

Scuderi, S., Panagia, N., Gilmozzi, R., Challis, P.M., and Kirshner, R.P. 1996, *ApJ*, **465**, 956.

Sonneborn, G., Fransson, C., Lundqvist, P., Cassatella, A., Gilmozzi, R., Kirshner, R.P., Panagia, N., and Wamsteker, W. 1997, *ApJ*, **477**, 848.

Stetson, P.B. 1987, *PASP*, **99**, 191.

Bibliography for chapter 4

Stetson, P.B. 1992, In *Astronomical Data Analysis Software and Systems I*, D.M. Worrall, C. Biemesderfer, and J. Barnes (Eds.), volume 25, San Francisco. A.S.P. Conference Series, p. 297.

Voit, M. *HST Data Handbook, Volume I.* STScI, Baltimore, 3^{rd} edition, 1997.

Walborn, N.R., Phillips, M.M., Walker, A.R., and Elias, J.H. 1993, *PASP*, **105**, 1240.

Walker, A.R. and Suntzeff, N.B. 1990, *PASP*, **102**, 131.

Whitmore, B. 1995, In *Calibrating HST: Post Servicing Mission*, A. Koratkar and C. Leitherer (Eds.), Baltimore. STScI, p. 269.

Chapter 5

A new procedure to measure the intrinsic properties of the stars

Until now, we have described how to measure fluxes from point-like sources. The next step is to recover as much information as possible from the photometry. In order to do this, we have devised a method that uses the fluxes at different wavelengths to determine the intrinsic properties of the stars. In this chapter we shall describe this method and in the next ones we will apply it to the study of stellar populations in different environments.

In this chapter, we will use the stars in the WF3 chip of the July 1997 observations to illustrate the various problems we have encountered and how we have solved them.

5.1 The Colour-Magnitude diagrams

The classical way to study resolved stellar populations is to use *Colour-Magnitude Diagrams* (CMD). As we have briefly explained in section 2.1.1, the colour of a star is the difference in

magnitudes between the fluxes in two bands (see equation (2.6) on page 10). Moreover, as we have discussed in section 2.1.4, interstellar dust attenuates radiation at short wavelengths more than at longer ones, thus causing the light to be reddened. Hence, the observed colour of a star is its intrinsic colour, which is a function of its temperature, gravity and chemical composition, as seen through the amount of dust along that particular line of sight.

Our ultimate goal is to compare the observations to stellar evolutionary models to infer the properties of the different populations in our fields, such as mass function and the star formation history. In order perform this comparison, we have to evaluate and eliminate the influence of the interstellar dust, which has nothing to do with the evolutionary status of the stars.

As we shall seen in section 5.2.3, in order to determine the temperature and the reddening for individual stars, it is at least necessary to have good photometry over a wavelength range from the U band to the I band. In order to select stars with overall good photometry, we have often used the average error in 5 bands ($\overline{\delta}_5$), excluding the UV, defined as:

$$\overline{\delta}_5 \equiv \sqrt{\frac{\delta^2_{\rm F336W} + \delta^2_{\rm F439W} + \delta^2_{\rm F555W} + \delta^2_{\rm F675W} + \delta^2_{\rm F814W}}{5}} \tag{5.1}$$

Typically, among the bands in the definition of $\overline{\delta}_5$, the error in the F336W magnitude is biggest one, due to the combined effect of the lower CCD sensitivity (see Figure 3.5 on page 54) and filter throughput (see Figure 3.6 on page 55) at short wavelengths. We have not included the UV in the definition of the mean error because, unfortunately, given our typical exposure times (see Table 6.1, for example), only roughly 7% of the stars are well exposed in these images. For the rest of them, we only have upper limits to the UV fluxes.

The CMDs of the stars in the WF3 chip of the July 1997 epoch for four independent combinations of bands are shown in Figure 5.1 on the facing page, where the the black dots are the stars with $\overline{\delta}_5 < 0.1$. The error threshold of $\overline{\delta}_5 < 0.1$ reflects itself as a magnitude threshold at $m_{\rm F555W} \simeq 23$. Out of a total of 3139 stars, 1043 of them have $\overline{\delta}_5 < 0.1$. For the stars with $\overline{\delta}_5 > 0.1$, *i.e.* the grey dots in Figure 5.1, only upper limits to the fluxes are available in the blue filters. This explains why the lower Main Sequence extends asymmetrically to the blue.

It is apparent that, despite the high quality of the measurements (average internal uncertainties less than 0.1 *mag*), the various features of the CMDs, such as the Zero Age Main Sequence (ZAMS), for the early (*i.e.* hot) stars, and the Red Giant clump for the more evolved populations, are rather "fuzzy" and not sharply defined. Although this is due in part to the presence of several stellar populations projected on each other, most of the problem resides in the fact that reddening is not quite uniform over the field, thus causing the points of otherwise identical stars to fall in appreciably different locations of the diagrams. Let us see how we dealt with the differential reddening.

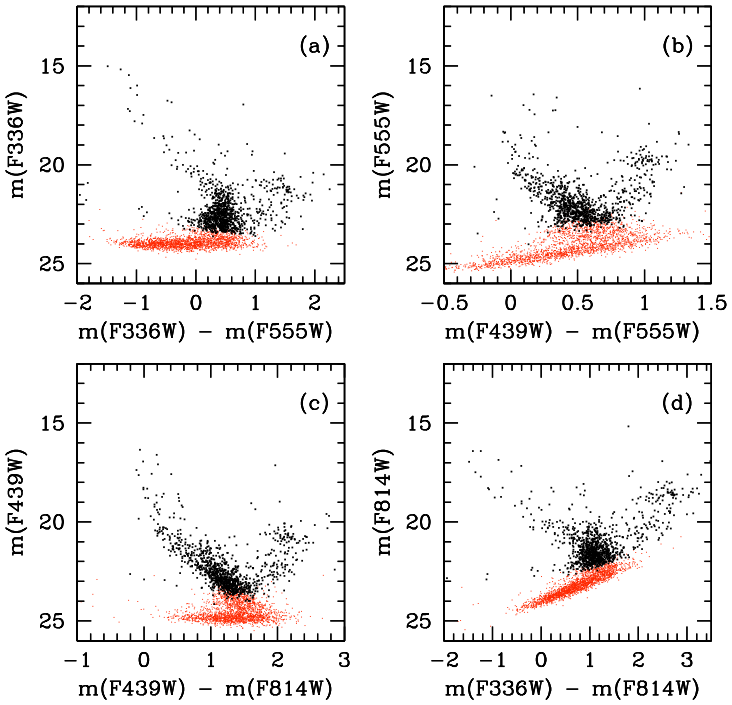

Figure 5.1: *Colour-Magnitude Diagrams of the stars in the WF3 chip of the July 1997 observations around SN1987A for four combination of filters. The grey dots are stars with* $\overline{\delta}_5 > 0.1$ *(see equation (5.1)), whereas the black dots are the 1043 stars with* $\overline{\delta}_5 < 0.1$.

5.2 The method

The large number of bands available (6 broad band filters) which cover a wide baseline (more than a factor of 4 in wavelength, extending from 2200 to 9200 Å) provide us with a sort of *wide-band spectroscopy* which defines the continuum spectral distribution of each star quite well. Of course, the resolution is very low, of the order of $\lambda/\Delta\lambda \simeq 7$, but, still, important features, such as the Balmer jump between the U and B bands, are clearly visible. Four examples of "wide band spectra" are shown in Figure 5.2. The flux (F_λ) is in units of erg cm^{-2} s^{-1} Å^{-1}.

As we shall see in great detail shortly, we fit theoretical predictions to photometric points to recover the reddening and the intrinsic properties of the stars. As an illustration, the best-fit parameters for the stars of Figure 5.2 are given in Table 5.1 on the next page. The corresponding model atmosphere curves are also shown in Figure 5.2.

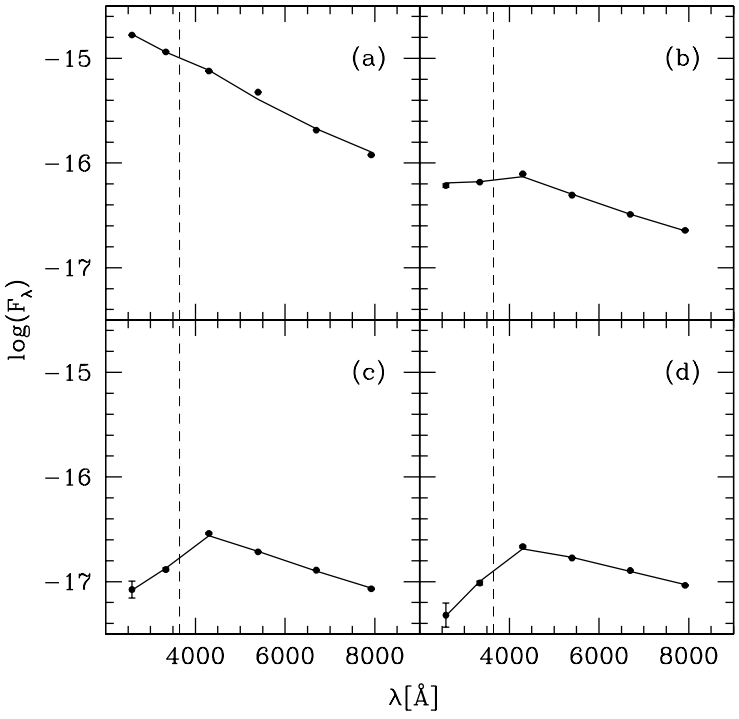

Figure 5.2: *Four examples of the spectral resolution of the "Wide Band spectroscopy". The spectra are shown in decreasing order of temperature. The best-fitting model is shown as full line ad the fit parameters are given in Table 5.1 (see text). The position of the Balmer jump at 3646 Å is indicated with a dashed line.*

Panel	T_{eff}(K)	$E(B-V)$	$L/L_\odot$	$R/R_\odot$
(a)	$25,350 \pm 5,700$	0.202 ± 0.080	$4,590 \pm 4,244$	3.444 ± 0.090
(b)	$18,160 \pm 2,100$	0.431 ± 0.051	495 ± 230	2.265 ± 0.050
(c)	$8,000 \pm 350$	0.117 ± 0.050	15 ± 3	2.070 ± 0.042
(d)	$7,480 \pm 300$	0.209 ± 0.047	18 ± 3	2.548 ± 0.052

Table 5.1: *Best-fit parameters for the spectra of Figure 5.2. The reddening quoted is the sum of Galactic and LMC extinction. The star in panel (a) is saturated and this causes the large quoted errors on the quantities derived for it.*

5.2.1 The naive fitting procedure

Having all these bands, we can do better than just comparing theoretical isochrones to the observed points for different combinations of filters to infer the global properties of the stellar populations in the field. Our aim is to *determine the reddening, the intrinsic temperature and the radius* (and, hence, the intrinsic luminosity) of *individual stars*. It is very important to correct every star individually whenever the Interstellar Medium is clumpy and, hence, the reddening is very likely to vary on short distance scales. This is certainly to be expected in regions of recent star formation, in which the Interstellar Medium from which stars were

formed did not have time to be blown away and/or stirred up by Supernovæ and stellar winds.

A fundamental ingredient in our analysis are the *model atmospheres* used to compute the theoretical colours to be compared to the observed photometric points. We have used the model atmospheres by Castelli (1998, see also Bessel et al. 1998). They are computed with an updated version of the `ATLAS9` code used for the Kurucz (1993) models and without convective overshooting (see Castelli et al., 1997a,b). These models cover a temperature interval between 3,500 and 50,000 K with a variable temperature spacing. Typically, 60-70 temperatures are computed, depending on metallicity, which spans from solar abundance to $3 \cdot 10^{-3}$ $Z_\odot$. Given a temperature, various models are computed for different surface gravities between $\log(g) = 0$ and $\log(g) = 5$ in cgs units, in steps of $\delta \log(g) = 0.5$. The spectra are not computed for every combination of gravity and temperature, but only the larger gravities are available for the larger temperatures. The models cover a wavelength range between 90 and 1,600,000 Å.

We have convolved the *m*odel *s*pectra with the WFPC2 response in our filters to obtain the theoretical magnitudes at the surface of the star ($M^0_{ms,ij}$) for the grid of temperatures provided by Castelli (1998). Here the index i indicates the filter and the index j the spectrum. The convolution was performed with the `STSDAS` ***calcphot*** task. In order to faithfully model the data, we have computed separately the expected *Data Numbers* (see section 3.1.2) that a given spectrum would produce on *each* of the four WFPC2 detectors. The throughput variation between decontaminations of the camera was taken into account by specifying the Julian date of the observation. The fit is made by comparing the DNs from the model to the observed ones. Once the convolution was performed, we have used a spline interpolation to get a temperature grid with a logarithmic step of 0.005, *i.e.* 1%.

We have kept the gravity to a fixed value of $\log(g) = 4.5$ in cgs units, which is the typical value for Main Sequence stars. Also, we have used model atmospheres for a metallicity of Z= $0.3 \cdot Z_\odot$, the expected value for the LMC. In section 5.3 we will describe the effects of these two parameters on the fit and we will see that neither of them influences the result in any appreciable manner.

The other input ingredient is the *reddening law*. This is a combination of foreground extinction due to dust in the Milky Way and internal extinction in the LMC. We have taken the first component to be the same for all of the stars, with $E(\mathrm{B-V})_{\mathrm{MW}} = 0.05$ (see, for example, Schwering and Israel, 1991). We have used the Galactic reddening law as compiled by Savage and Mathis (1979). On the other hand, the amount of extinction from the LMC dust is one of the parameters of the fit. We have taken the LMC reddening law in the direction of our field to be the one determined by Scuderi et al. (1996) from a study of an HST-FOS UV-optical spectrum of Star 2, one of the companions to SN1987A. For every input model spectrum, filter and value of $E(\mathrm{B-V})$, we have computed the absorption coefficients R_i according to equation (2.20) on page 18. We have, then, used these coefficients to redden the theoretical models before comparing them to the actual data.

Among the three parameters we want to determine, only two change the *shape* of the spectrum, *i.e.* $E(\mathrm{B}-\mathrm{V})$ and effective temperature (T_{eff}). The third one, *i.e.* the radius $\mathcal{R}$, causes just a rigid shift of the flux on a logarithmic scale. So, we first determine the shape of the spectrum by solving simultaneously for $E(\mathrm{B}-\mathrm{V})$ and T_{eff}, then we compute the radius of the star. For every star, the following steps are performed:

1. The input spectrum is normalized to the band with the highest photometric accuracy, usually the F555W, to eliminate the overall normalization, which depends an the star's radius. Obviously, the theoretical spectra are normalized in the same way. Let $m_{obs,i}$ be the normalized observed magnitude in filter i and $m^0_{ms,ij}$ the normalized model magnitude for temperature $j-th$ in the same filter;

2. The theoretical magnitudes are reddened, for various values of $E(\mathrm{B}-\mathrm{V})$. If R_i is the extinction coefficient in the band i due to the LMC dust and $R_{i,\mathrm{MW}}$ is the one due to our Galaxy:

$$m_{ms,ij}\left[E(\mathrm{B}-\mathrm{V})\right] = m^0_{ms,ij} + \left[R_i \cdot E(\mathrm{B}-\mathrm{V})\right] + \left[R_{i,\mathrm{MW}} \cdot E(\mathrm{B}-\mathrm{V})_{\mathrm{MW}}\right]$$

   with $E(\mathrm{B}-\mathrm{V})_{\mathrm{MW}} = 0.05$, as already discussed. We have defined the extinction coefficients in equation (2.15) in section 2.1.4;

3. For any given temperature and reddening, we have computed the χ^2 as:

$$\chi^2_j\left[E(\mathrm{B}-\mathrm{V})\right] = \sum_{i=1}^{N-1}\left[\frac{m_{ms,ij}\left[E(\mathrm{B}-\mathrm{V})\right] - m_{obs,i}}{\delta m_{obs,i}}\right]^2$$

   where N is the number of photometric points and $\delta m_{obs,i}$ is the error on the observed magnitude $m_{obs,i}$. The quantity $\delta m_{obs,i}$, of course, is the sum in quadrature of the photometric error on the magnitude in band i plus the one on the magnitude in the band to which the spectrum was normalized. The index i in the sum runs on all bands, but the one that was used to normalize the spectrum.

   Of course, the best-fit model corresponds to the combination temperature, and $E(\mathrm{B}-\mathrm{V})$ that minimizes $\chi^2_j\left[E(\mathrm{B}-\mathrm{V})\right]$;

4. Once the minimum χ^2_j is found, the errors in temperature ($\delta\mathrm{T}_{eff}$) and reddening ($\delta E(\mathrm{B}-\mathrm{V})$) are computed from the χ^2 map;

5. Now that the shape of the spectrum is determined, we compute the *radius* of the star as the error-weighted mean of the logarithmic shifts required to match the model to the observed flux in every band. Since the theoretical fluxes are flux densities at the *surface of the star*, the angular radius ρ derived from band i is:

$$\log(\rho_i) = -0.2 \cdot \left(m^0_{obs,i} - m^{fit}_{ms,i}\right)$$

where $m^{fit}_{ms,i}$ is the magnitude in filter i of the best-fitting theoretical spectrum and $m^0_{obs,i}$ is the observed magnitude, dereddened with the the best-fitting value of $E(\mathrm{B-V})$. The best estimate of the angular radius ρ, then, is:

$$\rho = \frac{\sum_{i=1}^{n} \rho_i / \delta\left(m_{obs,i}\right)^2}{\sum_{i=1}^{n} 1/\delta\left(m_{obs,i}\right)^2}$$

where n is the number of bands with actual flux measurements and not just an upper limit to it. The associated error $\delta\rho$, then, is:

$$(\delta\rho)^2 = \frac{\sum_{i=1}^{n} \left(\rho_i - \rho\right)^2 / \delta\left(m_{obs,i}\right)^2}{(n-1) \cdot \sum_{i=1}^{n} 1/\delta\left(m_{obs,i}\right)^2}$$

To convert the angular radius of a star to the linear one ($\mathcal{R}$), it is necessary to know its distance D:

$$\mathcal{R} = \rho \cdot \frac{D}{\mathrm{R}_\odot}$$

in this case, $\mathcal{R}$ is expressed in units of the solar radius $\mathrm{R}_\odot$ (see Table 2.1 on page 11). Given the uncertainty on the distance, the error on the linear radius ($\delta\mathcal{R}$) is:

$$\frac{\delta\mathcal{R}}{\mathcal{R}} = \sqrt{\left(\frac{\delta\rho}{\rho}\right)^2 + \left(\frac{\delta D}{D}\right)^2}$$

This error does not take into account any intrinsic dispersion in the distance of individual stars, which may introduce additional scattering in the HR diagram.

For example, in the case of the LMC, we have adopted the value originally measured purely geometrically by Panagia et al. (1991) and later improved by Panagia (1998). Using the rings around SN1987A, they found $D = 51.4 \pm 1.2$ kpc;

6. Finally, the intrinsic luminosity (L) can be computed according to the black body law:

$$\frac{\mathrm{L}}{\mathrm{L}_\odot} = \left(\frac{\mathcal{R}}{\mathrm{R}_\odot}\right)^2 \cdot \left(\frac{\mathrm{T}_{eff}}{\mathrm{T}_{eff,\odot}}\right)^4$$

where $\mathrm{T}_{eff,\odot}$ is the temperature of the Sun, again listed in Table 2.1.

Since the errors in temperature and radius are correlated, the error on the luminosity cannot be computed in a straightforward way from the previous equation. It is more convenient to write the luminosity in another, completely equivalent form. Let us first define the quantities:

$$l_{obs,i} \equiv 10^{-0.4\cdot\left(m^0_{obs,i}-ZP_i\right)}$$

i.e. the observed flux in filter i, and:

$$b \equiv \frac{\sigma\,{\rm T}_{eff}{}^4}{\sum_{i=1}^{n} l^{fit}_{ms,i}}$$

where $l^{fit}_{ms,i}$ is the flux in filter i of the best-fitting model. The quantity b is the equivalent of the bolometric correction, relating the total flux in n bands to the bolometric luminosity per unit surface $\sigma{\rm T}_{eff}{}^4$. We can now write the luminosity as:

$$L = 4\pi D^2\, l_{obs}\, b$$

where $l_{obs} = \sum_i l_{obs,i}$. All the quantities in this last equation are independent from each other and, hence, it is straightforward to compute the error on the luminosity:

$$\frac{\delta L}{L} = \sqrt{\left(2\,\frac{\delta D}{D}\right)^2 + \left(\frac{\delta l_{obs}}{l_{obs}}\right)^2 + \left(\frac{\delta b}{b}\right)^2}$$

where

$$\frac{\delta l_{obs}}{l_{obs}} = \frac{1}{l_{obs}}\sqrt{\sum_{i=1}^{n}\left[(10^{0.4\delta m_{obs,i}}-1)\cdot l_{i,obs}\right]^2}$$

and:

$$\frac{\delta b}{b} = \frac{db}{d{\rm T}_{eff}}\,\delta{\rm T}_{eff}$$

In this last equation, it is clear that the first term is completely determined by the models, whereas the second one is the error on the temperature from the fit computed in step 4.

In the case of the LMC, $\delta D/D = 0.02$ (Panagia, 1998).

Let us stress once again that the stars may not be all at the same distance and that this may introduce additional scattering in luminosity. From photometry alone, distances can be measured only in a statistical sense for an entire population and not for individual stars. However, since the intrinsic depth the LMC is estimated to be smaller than 600 pc (Crotts et al., 1995), this uncertainty is negligible.

The temperature-luminosity plane (HR diagram) resulting from this fitting procedure for the stars in the WF3 chip of the July 1997 observations is shown in Figure 5.3. The theoretical locus of the *Zero Age Main Sequence* (ZAMS) for Z= 0.3·Z$_\odot$ the expected mean metallicity of the LMC, is also shown (solid line).

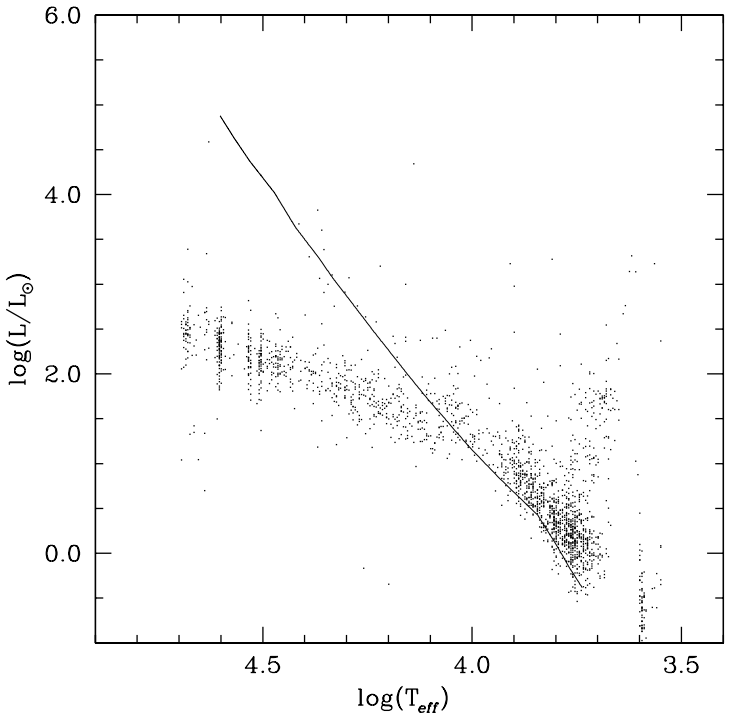

Figure 5.3: *HR diagram for the July 1997 WF3 chip obtained with the "naive" fitting procedure. The solid line is the theoretical locus of the Zero Age Main Sequence for* $Z = 0.3 \cdot Z_\odot$.

Unfortunately, as apparent, the inspection of Figure 5.3 is quite disappointing. While some stars fall in plausible areas of the HR diagram, *i.e.* colder and more luminous than the ZAMS, roughly one star out of two populates the "spur" clearly visible under the Main Sequence locus. The fact of a star being in the spur does not correlate with its photometric error, thus indicating that the problem is intrinsic to the fit. On the other hand, though, we must not be to far from truth, because the main features of the HR diagram are where they are expected to be. The lower envelope of the Main Sequence, for example, falls beautifully on the theoretical locus for Z= 0.3·Z$_\odot$, *i.e.* the expected metallicity for the LMC.

The stars in the spur are obviously too hot. If the temperature is too high, the reddening must also be too high, since they are coupled in determining the shape of the spectrum. Indeed, the fitted value of $E(\mathrm{B-V})$ for the stars in the spur is generally very high. Obviously, then, the solution of the problem lies in finding a better way to disentangle the effects of reddening and temperature. Let us further notice here that photometry in the F255W filter is not available for any of the stars in the spur, since they are too red and faint. As a consequence, we have to limit our analysis to the U band and longer wavelengths.

5.2.2 Reddening-free colours

Let us introduce a special combination of the U, B and I band magnitude (see, for example, Mihalas and Binney, 1981, page 186):

$$Q_{\rm UBI} \equiv ({\rm U}-{\rm B}) - \frac{R_{\rm U}-R_{\rm B}}{R_{\rm B}-R_{\rm I}} \cdot ({\rm B}-{\rm I}) \tag{5.2}$$

where, as usual, R_i is the extinction coefficient in the filter i. This colour is *reddening-free*, in the sense that, with the usual notation $R_i - R_j = E(i-j)$:

$$Q_{\rm UBI} = ({\rm U}-{\rm B})^0 + E({\rm U}-{\rm B}) - \frac{R_{\rm U}-R_{\rm B}}{R_{\rm B}-R_{\rm I}} \cdot \left[({\rm B}-{\rm I})^0 + E({\rm B}-{\rm I})\right] = Q^0_{\rm UBI} \tag{5.3}$$

where the superscript "0" indicates the unreddened quantity.

Equation (5.3) holds true only under the approximation that the extinction coefficients are constant. As we have seen in section 2.1.4, though, this is not strictly true, since they depend upon the spectrum of the star and the amount of dust along the line of sight. However, the dependence upon these two quantities is mild and $Q_{\rm UBI}$ is in first approximation really reddening-free. Clearly, given three bands, it is always possible to define a reddening-free colour according to the prescription of equation (5.2).

The reddening-free colour $Q_{\rm UBI}$ is plotted in Figure 5.4 on the facing page versus (U−I). The colours were computed using Castelli (1998) model atmospheres. The parameter that identifies the points along the theoretical curve is the model temperature and models correspond to higher temperatures moving away from the lower-right corner. The temperature interval spanned in Figure 5.4 is 3,500 (lower-right corner) to 50,000 K (upper-left corner).

The effect of extinction is to move the points from the zero-reddening locus *horizontally*, since $Q_{\rm UBI} = Q^0_{\rm UBI}$, to the *right* (*i.e.* greater U−I colours), as indicated by the arrow in Figure 5.4. So, Δ(U-I), the horizontal distance of an observed point from the theoretical zero-reddening curve, is proportional to $E({\rm B}-{\rm V})$:

$$\Delta\,({\rm U}-{\rm I}) = E({\rm U}-{\rm I}) = [R_{\rm U}-R_{\rm I}] \cdot E({\rm B}-{\rm V}) \simeq 3.3 \cdot E({\rm B}-{\rm V}) \tag{5.4}$$

whereas the observed $Q_{\rm UBI}$ is a function only of the star's temperature.

In principle, then, this is a way to decouple the effects of reddening and temperature and, hence, measure both of them. As apparent from Figure 5.6, though, $Q_{\rm UBI}$ is not monotonic with ${\rm U}-{\rm I}$, *i.e.* temperature, but it is W-shaped. The additional hook at ${\rm U}-{\rm I} \gtrsim 3.5$ is caused by the U filter red leak[a].

[a] Ultraviolet filters often show a residual transmission at optical wavelengths. This phenomenon is called *red leak*. Of course, its effect is larger for cold stars for which the intrinsic blue flux is small compared to the optical one.

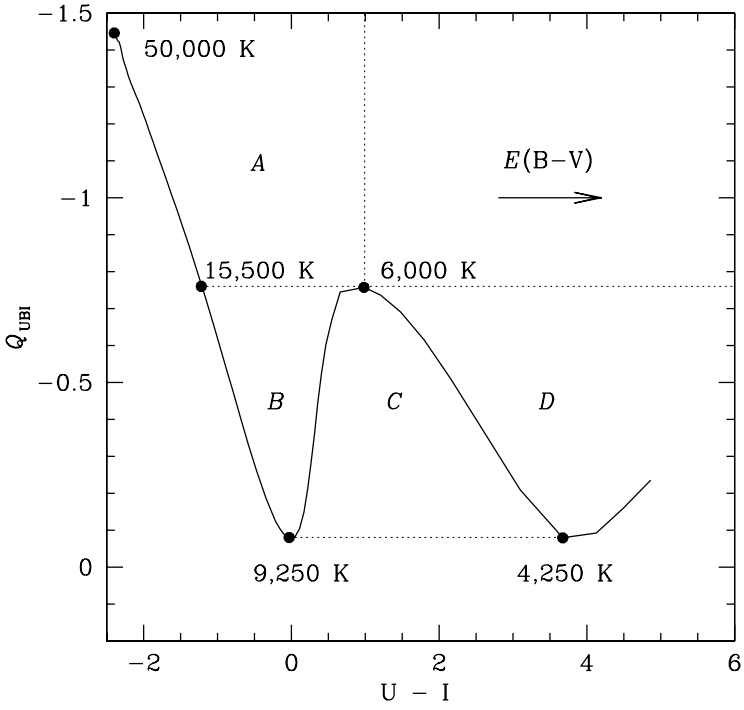

Figure 5.4: *Reddening-free colour* $Q_{\rm UBI}$ *as a function of* $U-I$ *from the theoretical models by Castelli (1998) for* $Z = 0.3 \cdot Z_{\odot}$ *and* $\log(g) = 4.5$. *The horizontal arrow indicates the reddening vector and a few important temperatures along the sequence are also marked. Stars in the four regions* $A \rightarrow D$ *have a different number of solutions (see text).*

As shown in Figure 5.5, $Q_{\rm UBI}$ is not monotonic because of the non-monotonicity of the Balmer jump with temperature and, as a consequence, a similar behaviour will occur every time that filters on both of its sides are used. The W-shape is most pronounced for the $\rm U-B$ (full line) colour, diluted because of the greater wavelength baseline in the case of the $\rm U-I$ colour (dashed line) and completely absent in the $\rm B-I$ one (dotted line), since both filters are on the same side of the Balmer jump.

Reddening moves stars horizontally to their right in the $Q_{\rm UBI}$ vs. $\rm U-I$ plane. So, stars in region A in Figure 5.4 have only one possible intersection with the zero reddening curve and for them the solution is unique. In the case of stars in region B, there are three intersections with the reddening curve, but the two on the right are easily rejected by noticing they correspond to negative values of $E(\rm B-V)$ (see equation (5.4)). The solution, therefore, even if not unique, is unambiguous.

For all stars redder than $\rm U-I \simeq\ 0$, *i.e.* with $\rm T_{\mathit{eff}} \lesssim 9,000$ K, instead, the solution is not only non-unique, but also ambiguous. As a matter of fact, there are two (region C) or three (region D) combinations of $\rm T_{\mathit{eff}}$ and $E(\rm B-V)$ that are absolutely equivalent. All of these solutions are physical and there is not an a priori criterion the decide which one is the right one. This, then, explains what was happening during the "blind" fit described above. In case of multiple solutions, there is more than one minimum in the χ^2 map and the fitting procedure would just pick the one that happened to have the smallest value, even though it

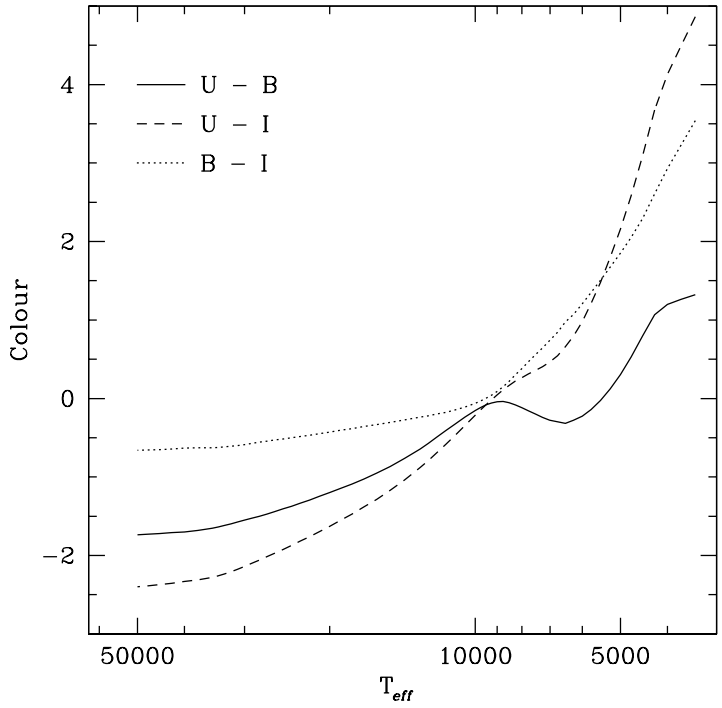

Figure 5.5: *The three colours used in Figure 5.4, computed with the Castelli (1998) models for Z=* $0.3{\cdot}Z_{\odot}$ *and* $\log(g) = 4.5$*, plotted as a function of* T_{eff}.

was not necessarily statistically more significant as compared to the others. Obviously, this is just a consequence of photometric errors, that distort the spectrum non-rigidly, and of using a finite grid in the parameter space. Actually, which of the different values is chosen by the procedure depends on such things as the grid step, clearly corroborating this last hypothesis.

In Figure 5.6 on the facing page we plot the observed stars in the July 1997 WF3 chip with $\overline{\delta}_5 < 0.1$, corrected for $E(\mathrm{B-V})_{\mathrm{MW}} = 0.05$ Galactic reddening, in the Q_{UBI} versus (U−I) plane. The zero-reddening theoretical curve from Figure 5.4 is also shown as a full line. As it can be seen, the observed points are systematically displaced with respect to the theoretical line. Of course, this is the effect of the reddening in the LMC.

The dashed line in Figure 5.6 highlights a "plume" of stars with $Q_{\mathrm{UBI}} \lesssim -0.7$, $\mathrm{U-I} \lesssim 1$. These stars lie on a line of slope roughly 1, thus indicating that they are displaced from the expected locus because the U magnitude is too bright compared to the other ones with respect to the predictions of the model atmospheres. This can either be due to a large error in the U band, or to to the fact that these objects have a real ultraviolet excess compared to normal stars. In the next chapter, we shall discuss the nature of these objects that are not well fitted by models of single stars.

As we have explained, the solution is not unique for all of the stars, depending on their location in the Q_{UBI} vs. $\mathrm{U-I}$ plane. Let us now investigate the problem by considering

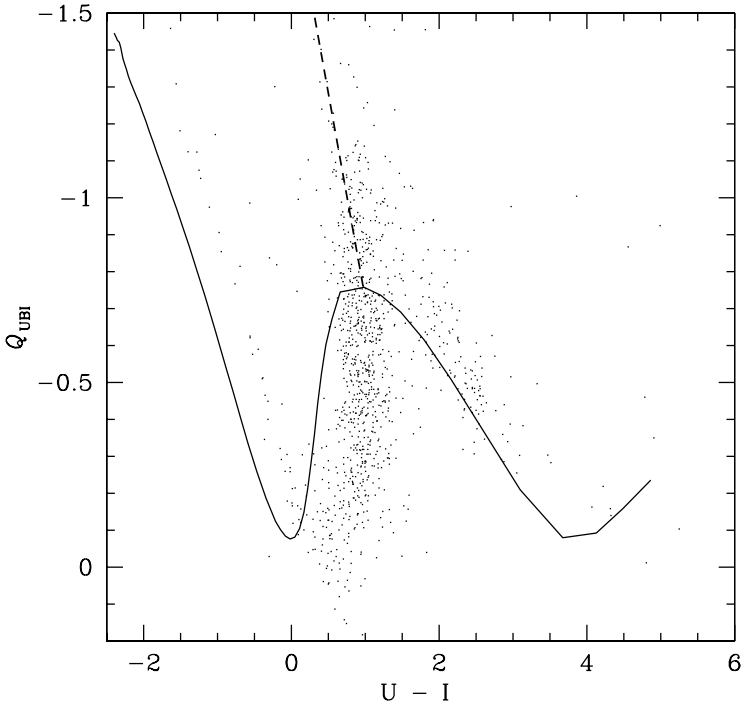

Figure 5.6: *Reddening-free colour* $Q_{\rm UBI}$ *as a function of U−I. The full line comes from the theoretical models by Castelli (1998). The dots are the observed points with* $\overline{\delta}_5 < 0.1$, *corrected only for the Galactic reddening. The dashed line indicates the slope, roughly 1, of the "plume" of stars discussed in the text.*

χ^2 maps. In Figure 5.7 on the next page we show the contour plots for four stars with unambiguous solution. As we have already noticed, unambiguous does not necessarily mean unique. Stars in panel (a) and (b) are in region A of the $Q_{\rm UBI}$ vs. U − I plane and, hence, the χ^2 has only one minimum. On the other hand, the χ^2 for the stars in panel (c) and (d) has two minima and a third one is way outside the limits of Figure 5.7. As it can be expected from the an inspection of the $Q_{\rm UBI}$ vs. U − I plane, these stars are in the B region of the $Q_{\rm UBI}$ vs. U − I plane. Among these three solutions, only the one with $E({\rm B-V}) > 0$ is physically meaningful.

In Figure 5.8 on page 107 we show the contour plots of four stars in the C region of the $Q_{\rm UBI}$ vs. U − I plane. As expected, all of them have two physically acceptable minima and the higher reddening is coupled with a higher value of temperature.

A confirmation of this scenario comes from the inspection of the reddening distribution resulting from the fit, shown in panel (a) in Figure 5.9 on page 108. This distribution is essentially bimodal, the additional peak at $E({\rm B-V}) = -0.025$ being caused by stars with poor photometry. As expected, the peak at lower reddening corresponds the mean value of this region of the LMC, *i.e.* $E({\rm B-V})_{\rm LMC} \simeq 0.1$ (see, for example, Walker and Suntzeff, 1990). Moreover, the stars in the spur in the HR diagram of Figure 5.3 on page 101 all have high reddening, as shown by the hatched histogram in Figure 5.9. Let us further notice that none of them belongs to region A or B in the $Q_{\rm UBI}$ vs. U − I plane. Both these things

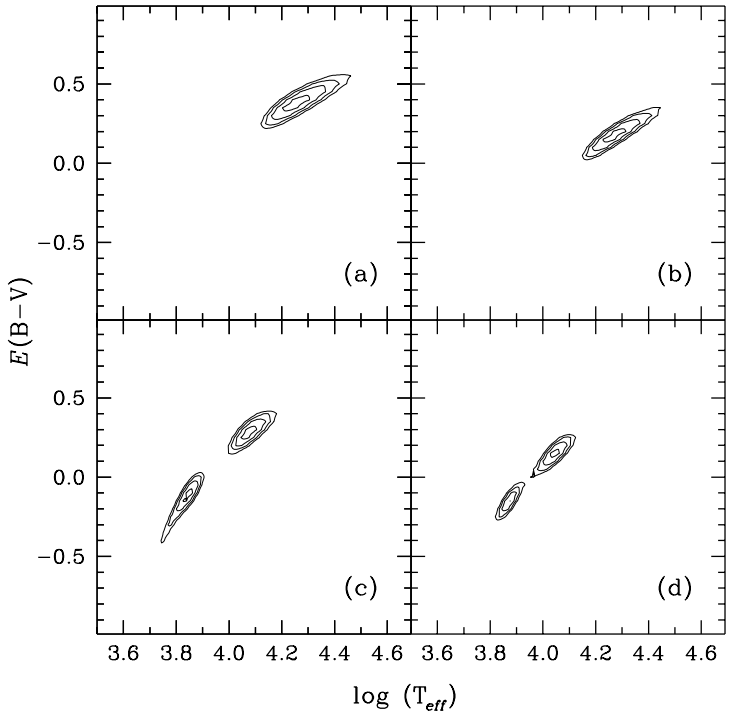

Figure 5.7: *Contour plots in the* T_{eff}-$E(\mathrm{B}-\mathrm{V})$ *space for four stars with unambiguous solution (see text). The contours are for* $\delta\chi^2 = 2$ *from the minimum.*

support our interpretation of the results of the fit given above. As already mentioned, the stars in the plume do not seem to be well fitted by the spectrum of normal stars. We will come back to them later.

5.2.3 The bands needed

As we have fully demonstrated, the cause of the problem highlighted in the HR diagram in Figure 5.3 on page 101 lies in the non monotonicity of Q_{UBI} with temperature or, from an observational point of view, colour. As we have already anticipated, this behaviour is caused by the presence of the Balmer jump. Indeed, in the case of black body atmospheres, the relation is absolutely monotonic, as shown in Figure 5.10 on page 109. However, the relation is much shallower in the case of black bodies, thus making the simultaneous determination of temperature and reddening much more uncertain.

It is interesting to notice that a reddened black-body is almost indistinguishable from an unreddened one of appropriate temperature. In fact, for typical stellar conditions at visible wavelengths $\exp(h\nu/k\mathrm{T}_{eff}) \gg 1$ and, hence, the flux of a black body spectrum can be approximated with Wien's law:

$$f_{bb}^0 \sim \nu^3 \cdot \exp\left(-\frac{h\nu}{k\mathrm{T}_{eff}}\right)$$

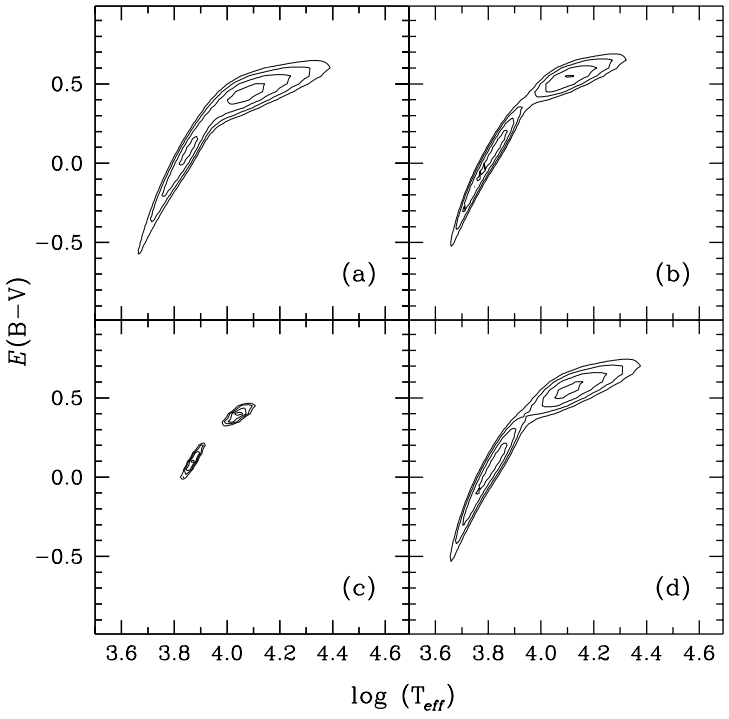

Figure 5.8: *Same as Figure 5.7, but for stars with multiple and ambiguous solutions.*

where, once again, the superscript "0" indicates the intrinsic, unreddened emission. If the optical depth of extinction (τ) were exactly proportional to ν, *i.e.* λ^{-1} (see equation (2.17) on page 17), then:

$$f_{bb} = e^{-\tau} \cdot f^0_{bb} = e^{-a\nu} \cdot f^0_{bb} \sim \nu^3 \cdot \exp\left[-\left(a + \frac{h}{k\mathrm{T}_{eff}}\right)\nu\right]$$

where a depends on the amount of dust along the line of sight. As a consequence, the reddened spectrum would be absolutely indistinguishable from an unreddened one with temperature T'_{eff}:

$$\mathrm{T}'_{eff} = \frac{h}{k}\left(a + \frac{h}{k\mathrm{T}_{eff}}\right)^{-1} < \mathrm{T}_{eff}$$

Both Wien's law and τ being exactly proportional to ν are only approximations, and, in reality, it is possible to disentangle the effects of temperature and reddening also for black bodies, as shown by the dashed line in Figure 5.10.

Since we have established that the problem is the Balmer jump, one may be tempted to avoid it by using only filters redward of it. By analogy with equation 5.2 on page 102, we can define another reddening-free colour using the B, V and I bands:

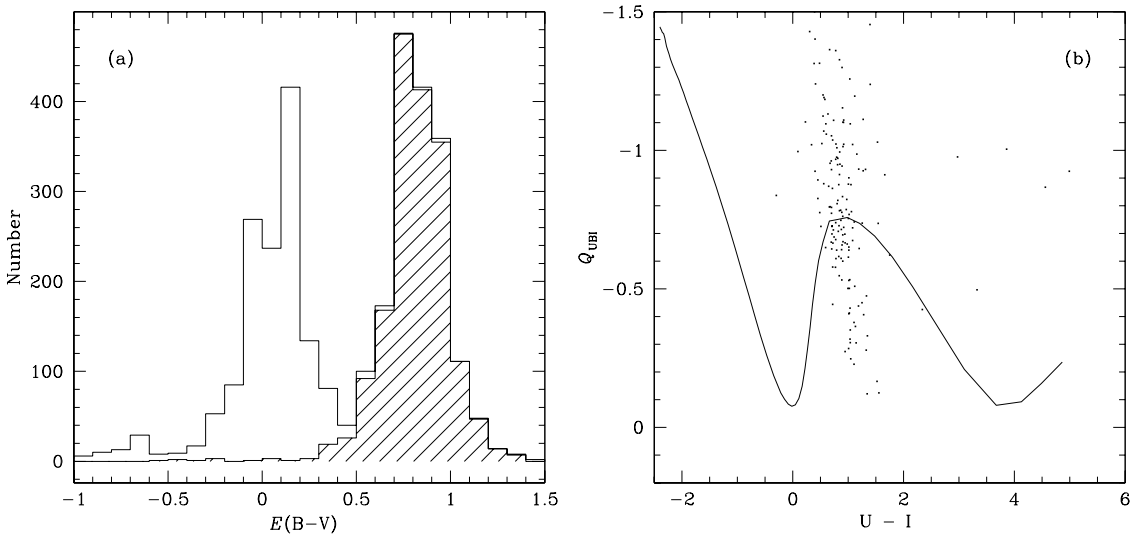

Figure 5.9: *Panel (a): reddening distribution from the "naive" fit. The hatched histogram contains only the stars in the "spur" in the HR diagram in Figure 5.3. As it can be seen, the peak at higher* $E(\mathrm{B}-\mathrm{V})$ *is made entirely of them. Panel (b): location in the* Q_{UBI} *vs.* $\mathrm{U}-\mathrm{I}$ *plane of the stars in the spur with* $\overline{\delta}_5 < 0.1$.

$$Q_{\mathrm{BVI}} \equiv (\mathrm{B}-\mathrm{V}) - \frac{R_{\mathrm{B}} - R_{\mathrm{V}}}{R_{\mathrm{V}} - R_{\mathrm{I}}} \cdot (\mathrm{V}-\mathrm{I}) \tag{5.5}$$

Q_{BVI} is shown in Figure 5.11 on the facing page as a function of $\mathrm{B}-\mathrm{I}$ in panel (a) and T_{eff} in panel (b).

As expected, apart for the hook at very low temperatures due to the B filter red leak, the relation is indeed monotonic, thus solving the problem of ambiguities in the solution. However, one immediately notices that the slope of the curve is much shallower than in the Q_{UBI} case. In fact, the total excursion of Q_{BVI} between 3,500 and 50,000 K is only 0.4 *mag* and it is almost totally insensitive to temperatures higher than 6,000 K, *i.e.* $\mathrm{B}-\mathrm{I} \lesssim 1$. Thus, in order to avoid the Balmer jump, we had to reduce the wavelength baseline and this has greatly reduced the sensitivity of the reddening-free colour to temperature.

In principle, if there were no measurements errors, it would be possible to use Q_{BVI} to determine both reddening and temperature temperature. But, of course, this is not the case, nor it will ever be. The combined effect of the mild dependence of Q_{BVI} on temperature and of photometric errors, that distort the spectra non-rigidly, is to make every combination $E(\mathrm{B}-\mathrm{V})$-T_{eff} along the reddening vector essentially equivalent. As an illustration of this, in Figure 5.12 on page 110 we show the χ^2 map of the fit using only four bands (B, V, R, and I) for the same stars of Figure 5.8 on the preceding page. As it can be seen, the χ^2 has no distinct minima, and, hence, it is not possible to determine both the reddening and the

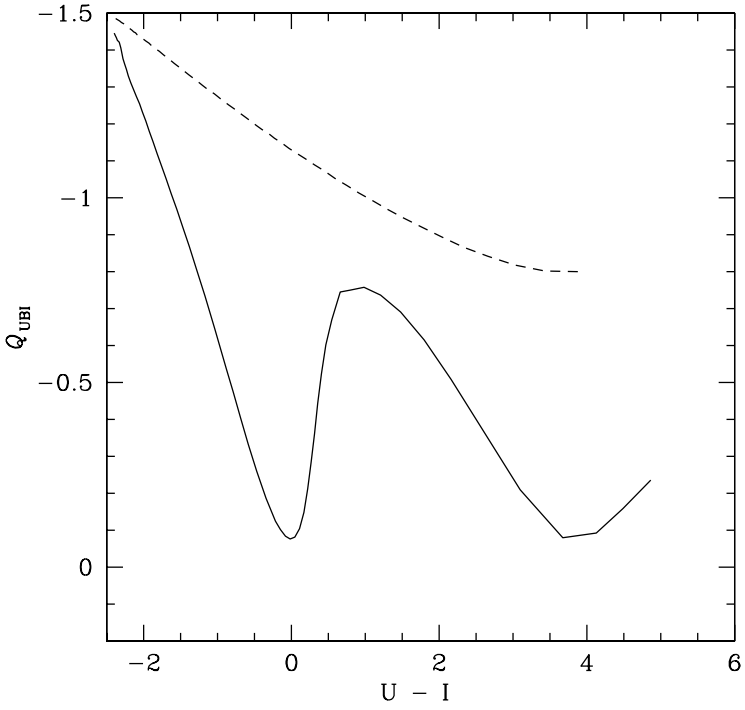

Figure 5.10: *The $Q_{\rm UBI}$ reddening-free colour as a function of* U − I *for the Castelli (1998) model atmospheres (solid line) and for black bodies (dashed line).*

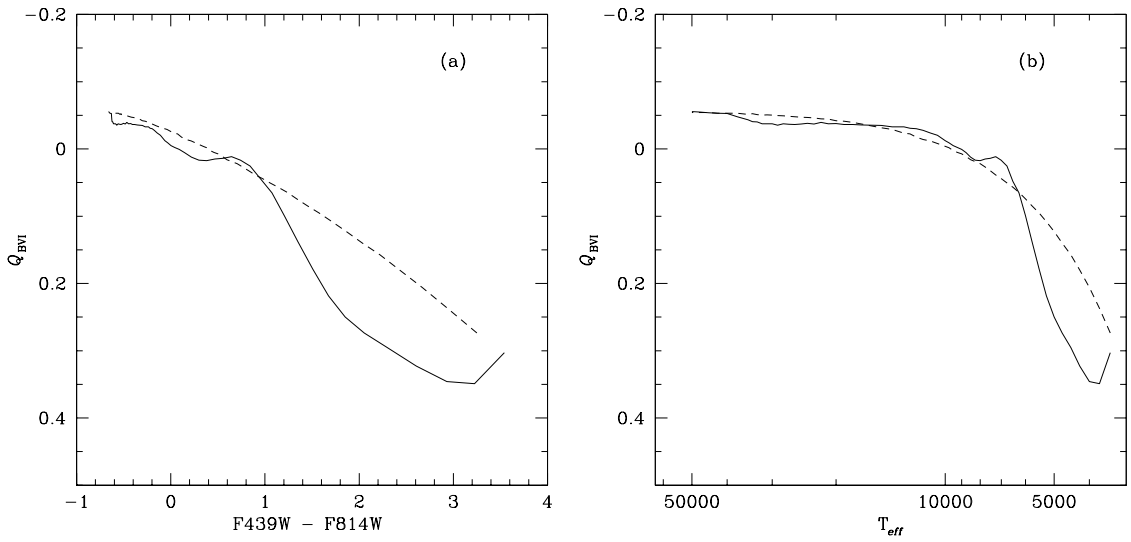

Figure 5.11: *The $Q_{\rm BVI}$ reddening-free colour as a function of* B − I *(panel (a)) and* T_{eff} *(panel (b)) for the Castelli (1998) model atmospheres for Z= 0.3·$Z_\odot$ and $log(g) = 4.5$. The case of black body spectra is shown in both panels as a dashed line.*

temperature using only four bands.

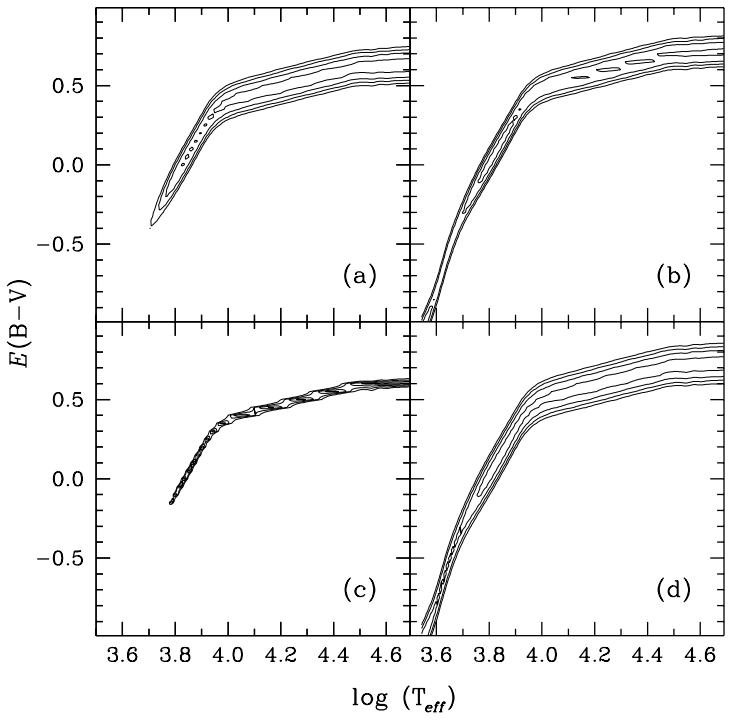

Figure 5.12: *Same as Figure 5.8, but this time the fit uses only 4 bands.*

As it can be expected, using only bands redward of the Balmer jump makes the solution ill defined also for stars in regions A and B in the $Q_{\rm UBI}$ vs. U−I plane, as shown in Figure 5.13 on the next page.

In conclusion, **in order to recover both the the temperature and the reddening, at least three bands are needed, since there are three unknowns, *i.e.*** T_{eff}**,** $\mathcal{R}$ **and** $E(\mathrm{B-V})$**. Moreover, one needs as a long wavelength baseline as possible, including UV and optical filters**. The three-band requirement is the minimum one in order for the problem to be mathematically well defined. Of course, photometric errors introduce scatter in the data and at least another band is advisable to better constrain the fit. In general terms, these are minimal requirements and the more well-exposed bands are available, the better the final results will be.

In fact, yet another band blue-ward of the Balmer jump would completely break the degeneracy and would make the solution unique even for stars with $\mathrm{T}_{eff} \lesssim 9,000$ K. To illustrate this point, we have generated a "synthetic" star with $\mathrm{T}_{eff} = 7,000$ K and $E(\mathrm{B-V}) = 0.15$ (from the LMC alone) by reddening the Castelli (1998) model for that temperature. A random noise was also added to the magnitudes. The χ^2 contours are shown in Figure 5.14. Panel (a) shows the situation if the star were well exposed also in the F255W filter, whereas in panel (b) the more realistic case of a much bigger error in this filter

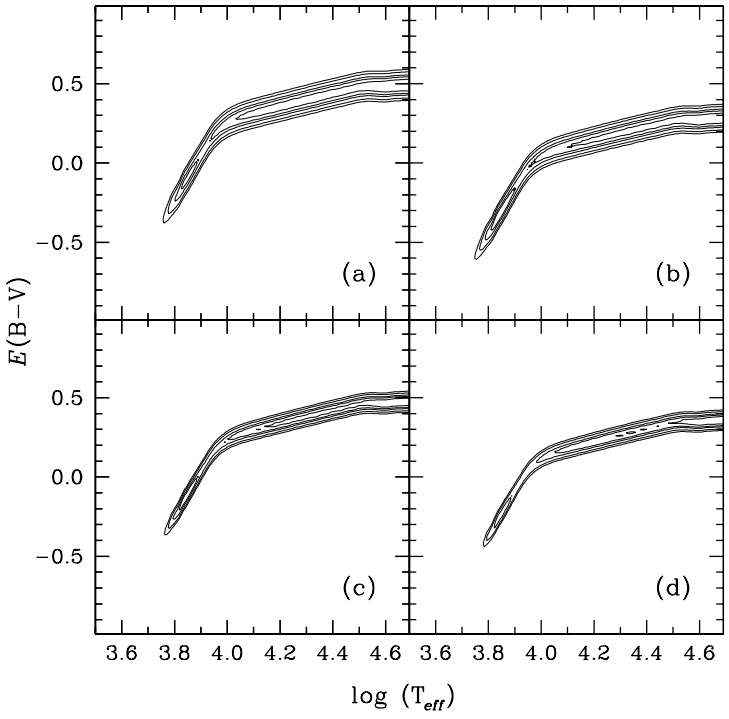

Figure 5.13: *Same as Figure 5.7, but this time the fit uses only 4 bands.*

compared to the other ones is reported. As it can be seen, if cold stars were well exposed also in the F255W filter, there would not be any problem and the "naive" fit would always give the correct result. However, given the lower detector sensitivity in the UV, the exposure times would be much longer than the typical ones of our observations (see Table 6.1). For example, roughly 4,700 seconds are required to reach a signal to noise ratio of 5 for a star with $T_{eff} \simeq 7,000$ K, *i.e.* spectral type F0, and $E(B-V) = 0.2$ (total) with the F255W filter in one of the WF chips of the WFPC2. The exposure time is even longer in the PC chip, roughly 6,200 seconds, because of the smaller pixel size.

5.2.4 The final recipe

Now that we have understood all the facets of the problem, we are ready to devise a way to recover as much information as possible from the data. Basically, we will use the reddening-free colour $Q_{\rm UBI}$ to determine which stars can be used to measure the reddening. Once this is done, we will use the full information from the 6 bands to fit all of the stars.

The final procedure consists of two iterations. In the first one, we perform the following steps:

1. Obviously, if a star, for whatever reason, has poor photometry there is no hope to gain any meaningful information from it. Also, for all of the reasons explained above, the

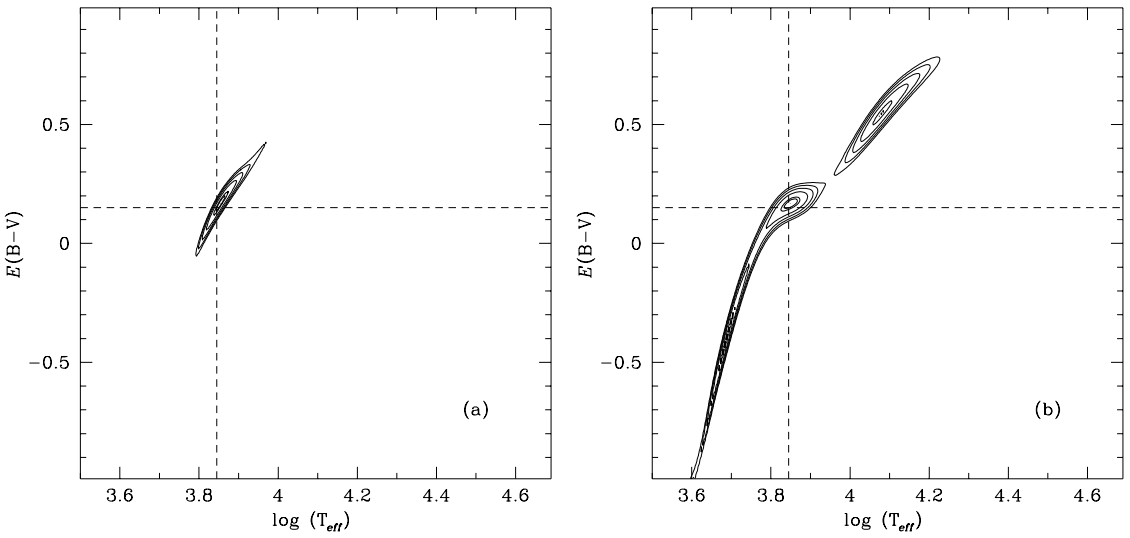

Figure 5.14: χ^2 *contour map for a artificial star with* $\mathrm{T}_{eff} = 7,000$ *K and* $E(\mathrm{B}-\mathrm{V}) = 0.15$ *(see text). In panel (a) we show the case in which the photometric accuracy in the F255W filter is comparable to that in the other filters. In panel (b) the more realistic case of a UV error much bigger than the one in the other bands is shown. The dashed lines indicate the input values of* T_{eff} *and* $E(\mathrm{B}-\mathrm{V})$.

photometric accuracy has to be good at least up to the U band. This is the reason why we have introduced the $\overline{\delta}_5$ mean error (see equation (5.1) on page 94). The first step, then, is to select the stars with $\overline{\delta}_5 < 0.1$. In the case of the WF3 chip of the July 1997 observations, their location in the Q_{UBI} vs. $\mathrm{U}-\mathrm{I}$ plane is shown in Figure 5.6 on page 105. For reasons that will soon be clear, we call the stars that do not match this criterion, *i.e.* those with $\overline{\delta}_5 > 0.1$, **class IV** stars.

2. We, then, divide the well measured stars in three classes, according to the number of intersections that they have *to their left*, *i.e.* bluer $\mathrm{U}-\mathrm{I}$ colour, with the theoretical zero-reddening curve in the Q_{UBI} vs. $\mathrm{U}-\mathrm{I}$ plane.

   In order to account for the photometric errors, we project the measured value $\pm 2 \cdot \delta$, where δ is the photometric error. A star belongs to a certain class if the measured point *and* the $\pm 2 \cdot \delta$ values have the *same* number of intersections. The classes are defined as:

   class I: stars that have only one intersection to their left. They are the stars in region A and B in Figure 5.4 on page 103 and for them there is no ambiguity;

   class II: stars in region C in Figure 5.4. They have two intersections to their left. The solution is not unique and we shall see shortly how we choose between the

different possibilities;

class III: stars that, in spite of their good photometry ($\overline{\delta}_5 < 0.1$), have a "problematic" location in the $Q_{\rm UBI}$ vs. U − I plane. These are:

- stars whose horizontal projection never intersects the zero-reddening curve to their left;
- stars that belong to region D Figure 5.4 and, hence, have three intersections to their left. As we shall discuss in section 5.3, in this region the particular combination of colours we have chosen becomes sensitive to metallicity;
- stars in the "plume" highlighted in Figure 5.6 on page 105. As we have pointed out, their U flux is too strong as compared to the one in the other bands. This can either be a consequence of a large U error, or could also be that their spectrum is not well represented by the one of a normal star. We will come back to this point in the next chapter. They are part of the "spur" in the HR diagram of Figure 5.3 on page 101 because, taken at face value, their position in the $Q_{\rm UBI}$ vs. U − I plane would require a very high value of reddening and effective temperature.

3. Clearly, the intersections with the zero-reddening curve also provide an estimate of $E(\mathrm{B}-\mathrm{V})$, see equation (5.4), and of temperature.

As we have already mentioned, stars with $\overline{\delta}_5 > 0.1$ are assigned to **class IV**.

The result of the division in classes is shown in Figure 5.15 on the following page for the WF3 chip of the July 1997 observations. Class I stars are hotter than about 10,000 K, whereas class II stars are between 6,750 and 8,500 K. In this particular case, out of a total number of 3139 stars, 40 belong to class I, 388 to class II and 615 to class III. The rest of them belong to class IV.

Once the stars are divided into classes, we fit the entire spectrum for every one of them. At this stage, it is useful to have even only upper limits to the fluxes in the ultraviolet filters to tell apart a cold, unreddened star from a hot, heavily reddened one. The information gathered in the selection process is used as a starting point for the actual fit:

class I: The fit is performed in a neighbourhood of the $E(\mathrm{B}-\mathrm{V})$ value deducted from the projection in the $Q_{\rm UBI}$ vs. U − I plane;

class II: We choose the smallest of the two $E(\mathrm{B}-\mathrm{V})$ values from the projection described above as the starting point and perform the fit in a neighbourhood around it. This is somewhat arbitrary, but an inspection of Figure 5.15, for example, does not indicate any compelling evidence for a large number of stars with extinction much larger than the mean value. Let us stress here that the reddening is still computed individually for each star;

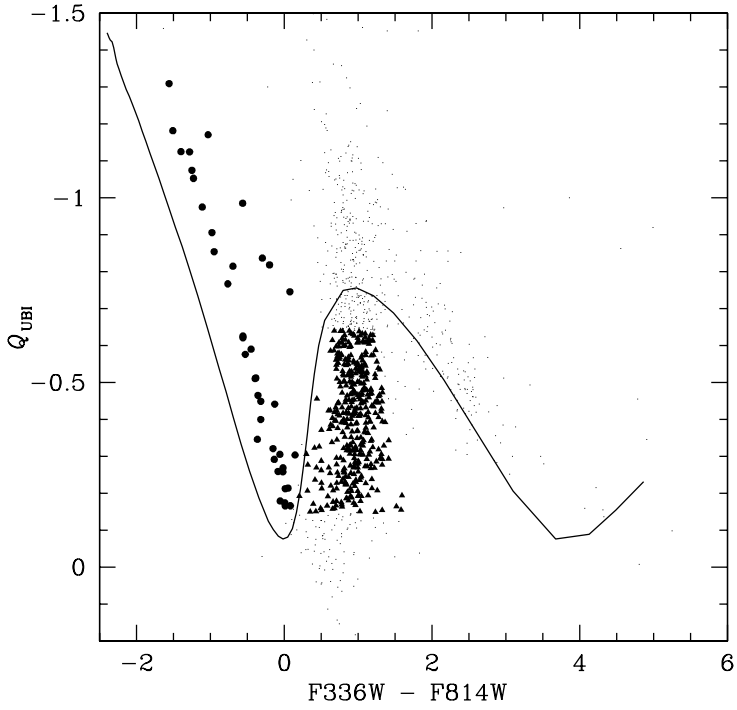

Figure 5.15: *Stars of different classes in the* $Q_{\rm UBI}$ *vs.* U − I *plane. Filled circles are class I stars, filled triangles class II stars and small dots identify class III stars (see text).*

class III and IV: photometry is not reliable enough to allow to solve for all of the three unknowns. For them, we impose the mean reddening of the neighbouring stars of class I and II and find the best temperature that fits the spectrum.

This procedure, at first sight, may seem complicated and redundant, but it assures total control over the fitting process. In fact, even in the case of multiple intersections, it gives a criterion to pick up the most reasonable solution. The 6 band fit uses all the information that we have and, thus, gives the best possible answer. Moreover, the whole procedure is very time-saving, since it limits the grid in the 6 band fitting, which is the most time-consuming part of it all, only to a small region in the parameter space.

The HR diagram for the WF3 chip of the July 1997 observations is shown in Figure 5.16 on the next page. A comparison with Figure 5.3 on page 101 clearly shows that we have done a good job: the spur is completely removed. There still are roughly 50 stars under the Zero Age Main Sequence locus, but they are mostly class IV objects, *i.e.* stars with very poor photometry. In addition, they can also be objects that are not well represented by a single star atmosphere, such as binaries or Pre-Main Sequence stars. We will come back to this point in the next chapter.

As we have repeatedly stated, the effect of differential reddening is to introduce additional scattering in the Colour-Magnitude Diagrams. In Figure 5.17 on page 116 we report the m(F439W) vs. m(F439W)−m(F814) diagram of the stars in the July 1997 WF3 chip with

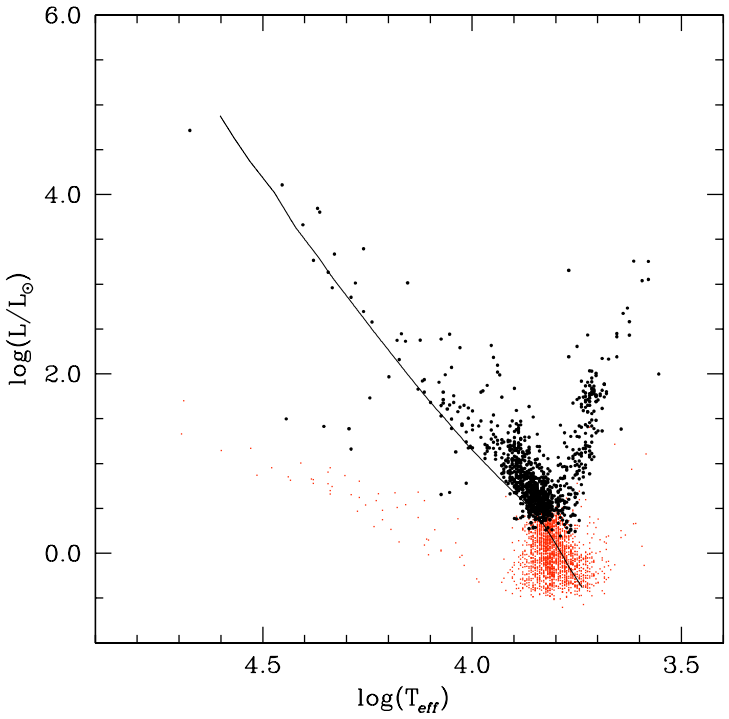

Figure 5.16: *HR diagram for the WF3 chip of the July 1997 observations resulting from the final fitting procedure. The small grey dots are class IV stars. The Zero Age Main Sequence for* $Z = 0.3 \cdot Z_{\odot}$ *is shown as a full line.*

$\overline{\delta}_5 < 0.1$. In panel (a) we show the observed Colour-Magnitude Diagram and in panel (b) the one corrected for extinction with the $E(\mathrm{B}-\mathrm{V})$ values found in the fitting procedure described above. The black dots are class I and II stars, *i.e.* stars for which the reddening was determined individually and the grey dots are the stars that were corrected with the mean value from class I and II stars. It is apparent that the scatter among the stars for which the reddening was determined individually is very much reduced and the Main Sequence is much better defined. This occurrence further confirms that we did a good job with the fitting procedure.

Class III and IV stars were all corrected for the same value of $E(\mathrm{B}-\mathrm{V})$ and, as a consequence, are just shifted rigidly to brighter magnitudes and bluer colours. It is important to realize that the mean reddening used to deredden them is computed from hundreds of stars and, hence, it is on average very accurate. Of course, it is still possible that a few class III and IV stars have, in reality, extinction values significantly different from the mean, but the global effect is absolutely negligible.

5.3 The role of gravity and temperature

Until now we have used model atmospheres with only one single surface gravity and metallicity. The surface gravity of a star changes during its evolution and it is reasonable to expect

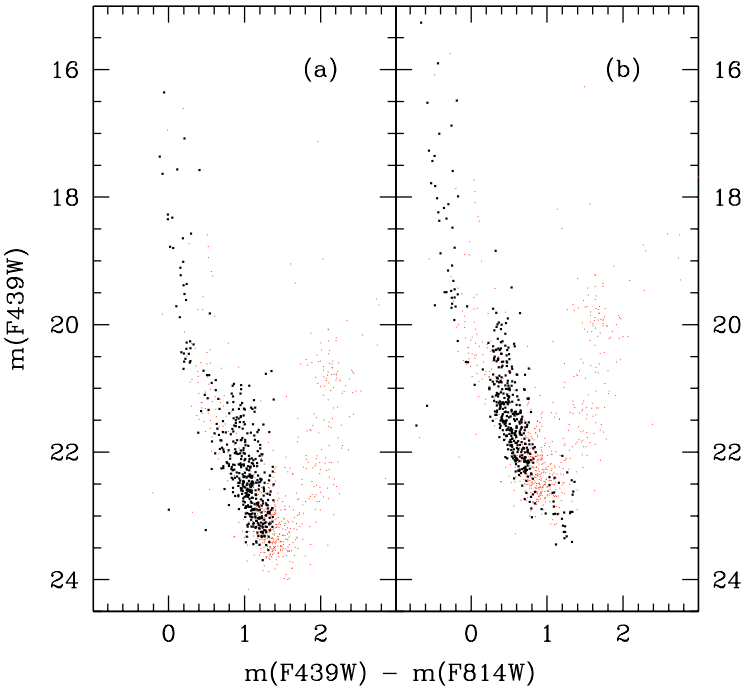

Figure 5.17: *B vs. B−I diagram before (panel (a)) and after (panel (b)) the correction for reddening. The stars are those in the WF3 chip of the July 1997 observations around SN1987A with* $\overline{\delta}_5 < 0.1$. *Black dots are stars for which* $E(\mathrm{B-V})$ *was determined individually (class I and II), whereas the grey dots were corrected using the average* $E(\mathrm{B-V})$ *value.*

that, given an evolutionary phase, the Main Sequence for example, stars of different mass have different gravities. Moreover, even though Z= 0.3·Z$_\odot$ certainly is a sensible assumption for the metallicity of the Large Magellanic Cloud, we want to check its influence on the results of the procedure described above.

The *surface gravity* (g) of a star is defined as:

$$g = G \cdot \frac{\mathrm{M}_*}{\mathcal{R}_*^2}$$

where G is the Gravitational constant and M_* and $\mathcal{R}_*$ are the star's mass and radius, respectively. In a static atmosphere, the weight of the overlying layers is supported by the total pressure (p) and this balance determines the density structure of the medium (see, for example, Mihalas, 1978) :

$$\nabla p = \rho \mathbf{g}$$

where ρ is the mass density.

The zero-reddening locus in the Q_{UBI} vs. U−I plane is shown in Figure 5.18 on the facing page for three values of surface gravity, namely $\log(g) = 4, 4.5$ and 5. As it can be seen, the three curves overlap perfectly for $\mathrm{U-I} \lesssim -0.5$, *i.e.* $\mathrm{T}_{eff} \gtrsim 11,000$ K and $\mathrm{U-I} \gtrsim 1.5$, *i.e.*

$T_{eff} \lesssim 5,500$ K. Elsewhere, however, different surface gravities lead to different expected loci. In particular, this influences the division in classes that is the foundation of the method described above. As we have seen, we use only stars on or near the Main Sequence to determine the reddening, so that we can use models of Main Sequence stars to estimate the gravity in the relevant range of U − I colour, *i.e.* $-0.5 \lesssim$ U − I $\lesssim 1$. Adopting the models by Brocato and Castellani (1993) and Cassisi et al. (1994), we see that for Z= 0.3·$Z_\odot$ the gravity is nearly constant along the Main Sequence and that its value is $\log(g) = 4.5$. This is the value we have used.

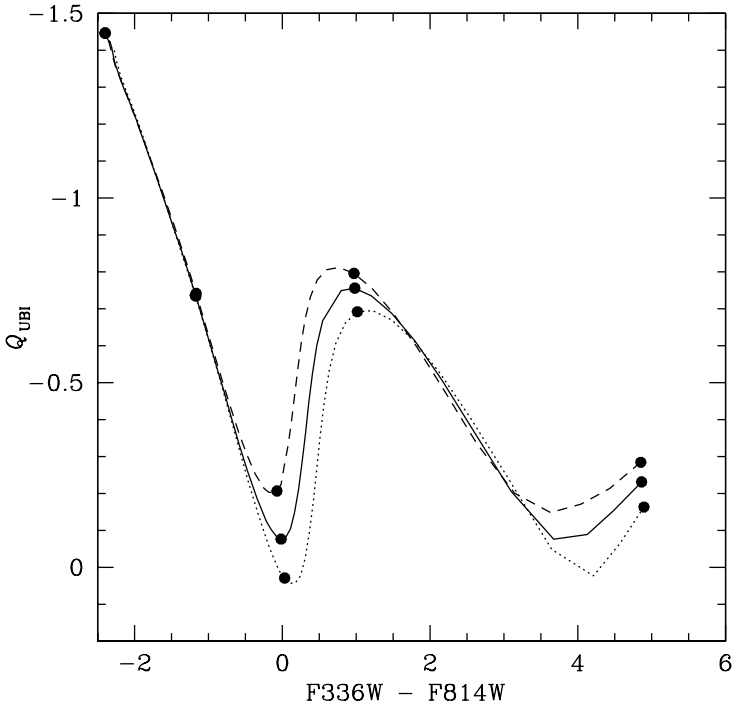

Figure 5.18: *Zero-reddening* $Q_{\rm UBI}$ *vs.* U − I *relation for three values of surface gravity:* $\log(g) = 5$ *(dashed line),* $\log(g) = 4.5$ *(solid line) and* $\log(g) = 4$ *(dotted line). The model atmospheres are those of Castelli (1998) for* Z= 0.3·$Z_\odot$*. The points for* T_{eff}*=50,000, 15,000, 9,250, 6,000 and 3,500 K are marked on each curve.*

The surface gravity of a Main Sequence star may depend on its chemical composition. Given a temperature, the lower the metallicity the lower the luminosity and, hence, the higher the surface gravity. In practice, however, for every metallicity the gravity is almost constant along the Main Sequence and the variations with chemical composition are small. For example, at U − I = 0 the surface gravity ranges from $\log(g) \simeq 4.4$ for a solar metallicity star to $\log(g) \simeq 4.6$ for Z=$Z_\odot$/20. We can, then, safely adopt the value of $\log(g) = 4.5$, as described above.

Once a star evolves off the Main Sequence its surface gravity changes appreciably because its radius increases by as much as a factor of 100. For example, $\log(g) \simeq 3$ is a typical value for the stars in the Red Giant clump, *i.e.* the stars at $\log(T_{eff}) \simeq 3.7$ and $\log(L/L_\odot) \simeq 1.75$ in Figure 5.16. Even though the $Q_{\rm UBI}$ vs. U − I relation is, indeed, sensitive to gravity, the

result of our global fit is not. This is because, as we have seen, we do not fit simultaneously temperature and reddening for stars off the Main Sequence, but rather we assign to them the mean $E(\mathrm{B}-\mathrm{V})$ value of their class I and II neighbours, which are on the Main Sequence and, hence, have $\log(g) \simeq 4.5$. For stars that are off the Main Sequence, we just perform the fit to solve for the radius and effective temperature. Once the reddening is correctly determined, the result of the multi-band fit is no longer sensitive to the surface gravity adopted in computing the theoretical colours. We have checked this by dividing the stars into classes using the Q_{UBI} vs. U − I relation for $\log(g) = 4.5$, *i.e.* the appropriate value, as we have seen, and then fitting the stars with colours computed for various values of the gravity. The maximum variations in temperature for the stars on the Red Giant branch are of 3%, *i.e.* much smaller than the error deriving from the fit itself, and with no systematic trend with gravity. Given this result, we have decided to use $\log(g) = 4.5$ throughout our analysis.

In addition to influencing a star's structure, the chemical composition also plays a role in determining the star's spectrum, through the atmospheric opacity. As a consequence, the colours also depend on this parameter. The Q_{UBI} vs. U − I relation for different values of Z is shown in Figure 5.19. As it can be seen, the variations are negligible for the stars for which we leave the reddening as a free parameter in the fit of the entire spectrum.

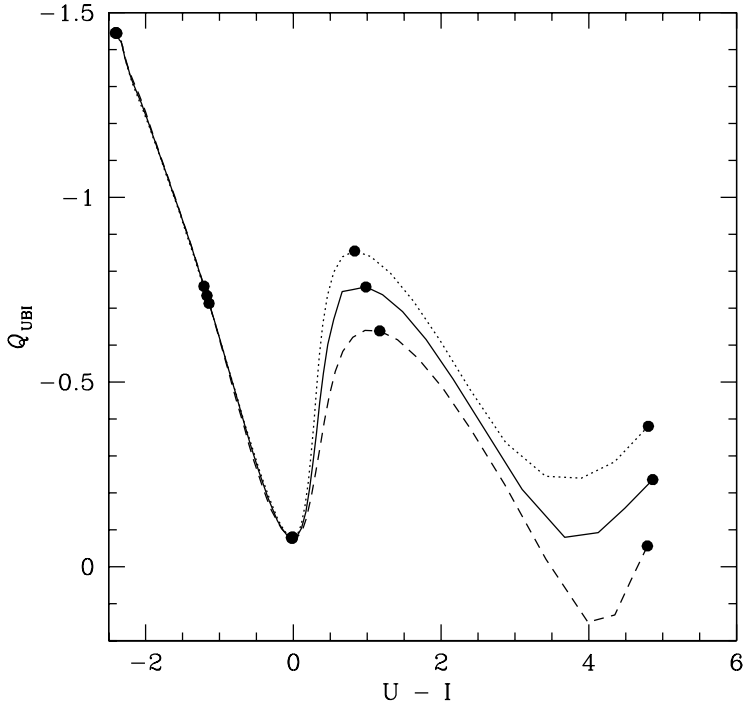

Figure 5.19: *Zero-reddening* Q_{UBI} *vs.* U − I *relation for three values of metallicity:* $Z=Z_{\odot}$ *(dashed line),* $Z= 0.3 \cdot Z_{\odot}$ *(solid line) and* $Z=Z_{\odot}/10$ *(dotted line). The model atmospheres are those of Castelli (1998) for* $\log(g) = 4.5$. *The points for* T_{eff}*=50,000, 15,000, 9,250, 6,000 and 3,500 K are marked on each curve.*

Also in this case, once the division into classes is made and the mean reddening is determined from class I and II stars, the result of the multi-band fit is insensitive to the

details of the stellar atmospheres. The comparison of fits performed with colours computed for different metallicities shows that the results are insensitive to this parameter.

In conclusion, in applying the fitting procedure described in section 5.2.4, we have used colours computed with models by Castelli (1998) for Z= $0.3 \cdot Z_{\odot}$ and $\log(g) = 4.5$.

Bibliography

Bessel, M.S., Castelli, F., and Plez, B. 1998, *AA*. in press.

Brocato, E. and Castellani, V. 1993, *ApJ*, **410**, 99.

Cassisi, S., Castellani, V., and Straniero, O. 1994, *AA*, **282**, 753.

Castelli, F. 1998, In *Views on Distance Indicators*, F. Caputo (Ed.). Società Astronomica Italiana. in press.

Castelli, F., Gratton, R.G., and Kurucz, R.L. 1997a, *AA*, **318**, 841.

Castelli, F., Gratton, R.G., and Kurucz, R.L. 1997b, *AA*, **324**, 432.

Crotts, A.P.S., Kunkel, W.E., and Heathcote, S.R. 1995, *ApJ*, **438**, 724.

Kurucz, R.L. 1993, In *ATLAS9 Stellar Atmosphere Programs and 2 km s^{-1} grid.* (Kurucz CD-ROM No. 13).

Mihalas, D. *Stellar Atmospheres*. W.H. Freeman and Co., San Francisco, 2^{nd} edition, 1978.

Mihalas, D. and Binney, J. *Galactic Astronomy: Structure and Kinematics*. W.H. Freeman and Co., San Francisco, 2^{nd} edition, 1981.

Panagia, N. 1998, In *Views on Distance Indicators*, F. Caputo (Ed.). Società Astronomica Italiana. in press.

Panagia, N., Gilmozzi, R., Macchetto, F., Adorf, H.M., and Kirshner, R.P. 1991, *ApJ*, **380**, L23.

Savage, B.D. and Mathis, J.S. 1979, *ARAA*, **17**, 73.

Schwering, P.B.W. and Israel, F.P. 1991, *AA*, **246**, 231.

Scuderi, S., Panagia, N., Gilmozzi, R., Challis, P.M., and Kirshner, R.P. 1996, *ApJ*, **465**, 956.

Walker, A.R. and Suntzeff, N.B. 1990, *PASP*, **102**, 131.

Chapter 6

The field of Supernova 1987A†

†Based on observations with the NASA/ESA Hubble Space Telescope, obtained at the Space Telescope Science Institute, which is operated by AURA, Inc., under NASA contract NAS 5-26555.

In this chapter, we will present the analysis of the stellar population within 30 parsecs of Supernova 1987A. As an introduction to our results, let us briefly describe Supernova 1987A and review the reasons why the Large Magellanic Cloud is an excellent place in which to study stellar populations.

6.1 Supernova 1987A

Supernova 1987A (SN1987A, a Type II, see section 2.1.3) exploded on February, 23^{rd} 1987 in the **L**arge **M**agellanic **C**loud (**LMC**). It is located at the south-west edge of the Tarantula Nebula, some $20'$ away from its centre. The whole area contains a large number of early type stars interspersed with HII regions and Supernova Remnant shells. The OB association closest to SN1987A is LH 90 (Lucke and Hodge, 1970), which is located about $5'$ to the north-east of the Supernova and whose age is about 4 Myr (Van Dyk et al., 1998).

At the time of writing, then, SN1987A is more than 11 years old and, by now, is probably one of the best studied objects in the Universe. In fact, being the brightest Supernova to be observed since the one observed by Kepler in 1604, it has produced a huge number of scientific papers on all the possible facets of the evolution of the progenitor star, the explosion mechanism, the interaction of its ejecta with the interstellar material (rings etc), its neutrino emission[a] and every other conceivable topic. The study of the Supernova itself is beyond the purposes of this work, but see, for example, McCray (1993) for an excellent and detailed review of this subject.

The progenitor of SN1987A is the star Sk -69 202 (Sanduleak, 1969), a B3I supergiant with V= 12.4 and B−V= 0.04 (Rousseau et al., 1978). From its location in the HR diagram ($L\simeq 10^5$ $L_\odot$, $T_{eff}\simeq 16,000$ K), theoretical models of massive stars make it possible to infer that the initial Main Sequence mass of the progenitor, before mass-loss, was in the range 16-22 $M_\odot$ and its helium core before explosion was between 5 and 7 $M_\odot$(Arnett et al., 1989). The pre-Supernova evolution is believed to have lasted 10-12 Myr (see, for example, Van Dyk et al., 1998).

Here, we will focus our attention on the **stellar populations around SN1987A**, using *HST*-WFPC2 observations taken as a part of the long-term General Observer **S**upernova **IN**tensive **S**tudy (**SINS**) project led by Robert Kirshner of the Harvard-Smithsonian Center for Astrophysics. SN1987A has been observed by SINS at least once a year to monitor its spectro-photometric evolution. Because all of these observations were taken always centering the supernova in the PC chip, but with different positions angles (PA, see Figure 3.1 on page 46), we have the almost complete coverage of a circular region with a radius of more than $2'$ around SN1987A. At the distance of the Supernova, 51.4±1.2 kpc, corresponding to

[a]SN1987A is the only astronomical object, together with the Sun, whose neutrinos have ever been detected.

a distance modulus of 18.55±0.05 *mag* (Panagia, 1998), this translates into a linear distance of roughly 30 pc.

6.2 Stellar populations in the Large Magellanic Cloud

The LMC is fairly close to the Sun and, thus, it very easy to do good photometry of stars of about 1 $M_\odot$, or even slightly less, with the *Hubble Space Telescope*. Its unprecedented spatial resolution allows *HST* to achieve the same resolution in the LMC as, for example, one can reach from the ground in η Carinæ, that is only a few kpc away. In a study like ours, it is crucial to have the best possible spatial resolution in order to minimize the effects of stellar crowding and the possibility of two or more stars blending into one apparent source.

Furthermore, the distance of the LMC from the Sun is very well measured, with a variety of different methods either based on the stellar evolution theory (photometric parallax), stellar pulsations (Cepheid stars) and pure geometry (the rings around Supernova 1987A). Even taking into account the uncertainty in the distance itself and the physical depth of the LMC, all of the stars can be taken to be at the same distance to within 5%.

Moreover, the Large Magellanic Cloud has had a star formation history that is interesting in itself. For example, there seem to be indications that there are no star clusters with an age ranging from 4 to 10 Gyr (Jensen et al., 1988), while the star formation history of the field population, as measured, for example by the width of the Main Sequence Turn Off[a] seems to have been more uniform (see, for example, Gallagher et al., 1996). By comparing different locations in the LMC, it will be possible to address the question as to whether the star formation is spatially uniform, or if, instead, different fields show different epochs of star formation activity.

Also, the LMC has a low metallicity, *i.e.* 2-5 times lower than in the Solar Neighbourhood, and this makes it more similar to the primordial star formation environment. A metallicity of Z= $0.3 \cdot Z_\odot$ corresponds to the inferred mean metallicity of the Interstellar Medium at a redshift of $z \simeq 1.3$ (Pei and Fall, 1995), at which the star formation rate reaches its peak during cosmic evolution (Madau et al., 1996). This can give at least an idea of how the star formation process was like in the early Universe, but in a nearby environment, where the stars can be clearly and easily resolved and accurately studied.

Last, but not least, the extinction in in the direction of the Large Magellanic Cloud due to dust in our Galaxy is very low, about $E(B-V) \simeq 0.05$ (Bessel, 1991; Schwering and Israel, 1991). Hence, our view of the LMC is not severely obstructed.

[a]The Main Sequence Turn Off is the point in the HR diagram at which the stars leave the Main Sequence and begin to burn hydrogen in a shell surrounding the exhausted core. Its location is a powerful age indicator in the sense that, as a population becomes older, the Turn Off becomes less luminous and redder.

6.2.1 The 30 Doradus region

The Wide Field and Planetary Camera 2, despite its name, has a rather small field of view: $35'' \times 35''$ for the PC and $80'' \times 80''$ for each of the 3 WF chips (see section 3.1). Therefore, while its unprecedented spatial resolution is invaluable in resolving stellar populations, WFPC2 only provides coverage of small regions of the sky. Before proceeding any further in describing our findings let us set the stage for our observations by taking a quick look at the region in which our WFPC2 observations are located. The relevant portion of the Large Magellanic Cloud, $40'$ on a side, is shown in Figure 6.1 on the next page. The plate used is part of the Digitized Sky Survey[†].

Several associations of stars are visible in Figure 6.1. Most noticeable is NGC 2070 in the 30 Doradus region. We have discussed R136, its central part, in section 2.2.4 as an example of young cluster in the LMC: 30 Doradus is the prototypical example of a massive nearby starburst region, the Rosetta Stone for starbursts according to Nolan Walborn (see, for example, Walborn, 1991).

In addition to the presence of 30 Doradus, there are signs of recent star formation throughout the entire region. For example, NGC 2060 (also known as 30 Doradus B or LH 99) and NGC 2044 (30 Doradus C, LH 90) both contain young Supernova remnants whose progenitors are inferred to have been very massive. Recently, a pulsar was discovered in the Supernova remnant N157B in NGC 2060 (Marshall et al., 1998; Cusumano et al., 1998). Their young age and active star formation history are confirmed by Walborn et al. (1995) who have imaged both clusters with the Wide Field/Planetary Camera[a].

NGC 2074, also known as LH 101 from the Lucke and Hodge (1970) catalog, is also a young association, as inferred from the presence of early B stars (Wilcots et al., 1993), for which the Main Sequence lifetimes are of the order of 10 Myr.

The integrated UBV photometry of all of the clusters highlighted in Figure 6.1, and 619 more, is presented in Bica et al. (1996), further confirming their young age. Scattered throughout the whole region there are numerous stars from the Sanduleak (1969) catalog. They were selected for being brighter than 14^{th} magnitude and, hence, they are all massive, *i.e.* short-lived, stars.

Massive stars have a profound impact on the interstellar medium, first through their powerful winds and, at the end of their evolution, with the shock fronts created by Supernova explosions. The ejected material can compress the gas in adjacent regions and trigger new episodes of star formation there. This scenario is called *Self Propagating Star Formation*

[†]The Digitized Sky Surveys were produced at the Space Telescope Science Institute under U.S. Government grant NAG W-2166. The images of these surveys are based on photographic data obtained using the Oschin Schmidt Telescope on Palomar Mountain and the UK Schmidt Telescope. The plates were processed into the present compressed digital form with the permission of these institutions.

[a]The Wide Field/Planetary Camera was one of the first-generation instruments on board *HST*. It was removed during the first servicing mission in December 1993 and replaced with WFPC2.

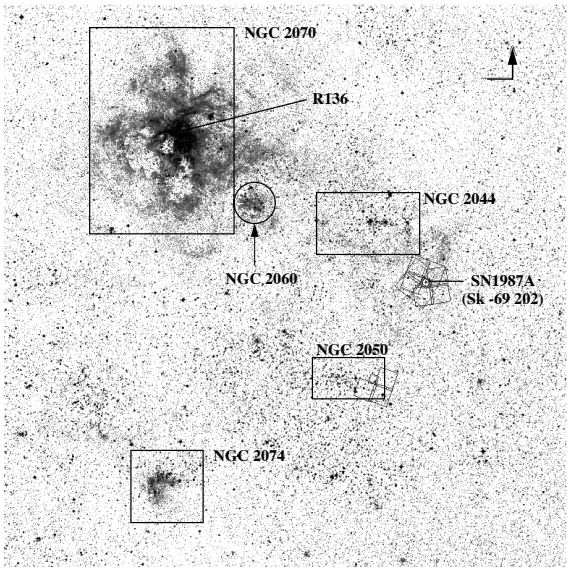

Figure 6.1: *Digitized Sky Survey plate of a* $40' \times 40'$ *region including SN1987A. With the usual convention, north is up and east to the left, as indicated by the arrow in the top-right corner. The fields of view of our WFPC2 observations are shown together with several associations (see Hodge and Wright, 1967). The location of SN1987A and its progenitor Sk -69 202 is also marked.*

(see, for example, Elmegreen, 1992). The typical large scale propagation velocities range from several to a few tens of kilometers per second. As we have seen, there are numerous indications of populations of 10-20 Myrs of age in the region. As an illustration of the time and length scales involved, let us notice that a speed of 8 km s^{-1} is required for a compression front to travel 120 pc, the distance between SN1987A and NGC 2050, in 15 Myr. Thus, it is possible that different parts of this very active region may have interacted with each other.

In conclusion, **Supernova 1987A is located in a region in which star formation was, and still is, very active**. The *Advanced Camera for Surveys*, which is scheduled to be installed on board *HST* in May 2000, will have enhanced detector sensitivity with respect to WFPC2 over a larger field of view ($3' \times 3'$) and with the same pixel size of the PC chip. It

will be an extraordinary tool to perform this type of studies that require both high spatial resolution and large areas to be covered, just like WFPC2 is now.

6.3 Observations and Data Reduction

Since 1994, Supernova 1987A was imaged every year as a part of the SINS project. The log of the observation we have used is reported in Table 6.1. We did not use the observations of March, 3^{rd} 1995 since only 4 bands were taken, all redward of the Balmer jump: F439W, F555W, F675W and F814W because, as we have seen in section 5.2.3, a filter blueward of the Balmer jump is required to recover both temperature *and* reddening. Moreover, these exposures did not provide any significant addition to the portion of sky covered by the other ones. Since the SINS images in Hα were taken only for one epoch (July 1997), we have also retrieved from the *HST* archive the only other observations available for this region in the F656N filter. Shortly, we will see how crucial Hα is in studying young populations. These images were taken by John Trauger on February, 3^{rd} 1994, less than two months after WFPC2 was installed on *HST*. This was the only case in which we had to recalibrate an observation after the standard pipeline procedure described in section 4.1.1 had been applied.

Filter Name	Exposure Time (seconds)			Comments
	September 1994[a]	February 1996[b]	July 1997[c]	
F255W	2×900	$1100 + 1400$	2×1300	UV filter
F336W	2×600	2×600	2×800	U filter
F439W	2×400	$350 + 600$	2×400	B filter
F555W	2×300	2×300	2×300	V filter
F675W	2×300	2×300	2×300	R filter
F814W	2×300	2×300	2×400	I filter
F502N	4×1200	$1100 + 1500$	$2 \times 1300 + 4 \times 1400$	[OIII] λ5007 Å
F656N	—	$1100 + 1300$[d]	4×1400	Hα
F658N	4×1200	$1100 + 1500$	—	[NII] λ 6584 Å[e]

[a]September, 24^{th} 1994, proposal number 5753.
[b]February, 6^{th} 1996, proposal number 6020.
[c]July, 10^{th} 1997, except for F502N taken on July, 12^{th} 1997. Proposal number 6437.
[d]Not from SINS. The PI is John Trauger and the data were taken on February, 3^{rd} 1994.
[e]With a little of contamination from Hα.

Table 6.1: *Log of the observations centered on Supernova 1987A.*

As we have already pointed out, the F336W, F439W, F555W, F675W and F814W filters roughly match the ground based UBVRI Johnson-Cousin system. Their throughput curves

are shown in Figure 3.6 on page 55. For the sake of brevity, we will occasionally substitute the actual filter names with their standard name and F255W with "UV".

The WFPC2 footprints of the observations in Table 6.1, together with the one of a parallel observation 8′ to the south-east of the Supernova, are shown in Figure 6.2, superimposed on a Digitized Sky Survey plate 20′ on a side. North is up and east to the left. The progenitor of SN1987A is clearly visible well centered in the PC chip of all the epochs. As it can be seen, our observations cover virtually an entire circle centered on the Supernova. The OB association LH 90 is also visible north-east of the Supernova location.

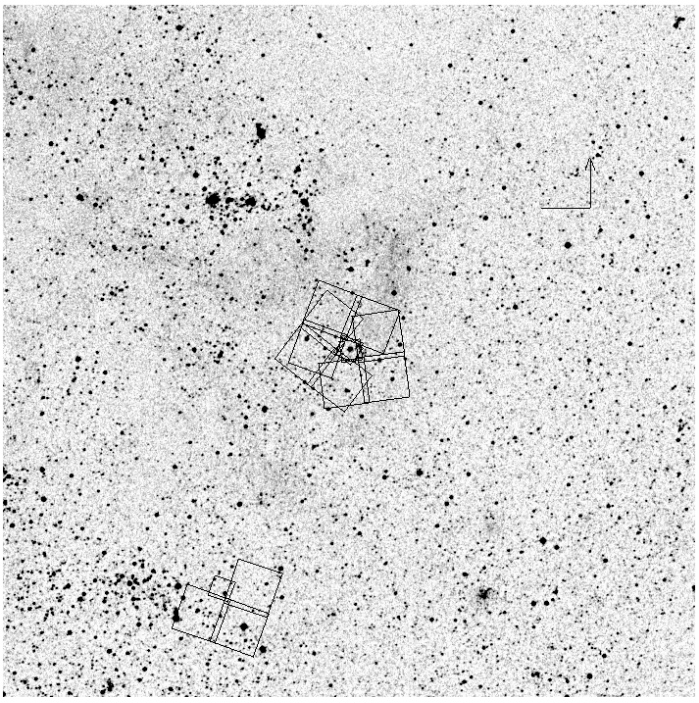

Figure 6.2: *WFPC2 footprints superimposed on a Digitized Sky Survey plate 20′ on a side. North is up and east to the left. The three pointings centered on SN1987A, as well as a parallel field 8′ to the south-east of the Supernova are shown.*

The data were reduced as described in chapter 4 for each chip of the three epochs.

The Hα images retrieved from the archive have almost the same roll angle as the February 1996 ones, since they were taken only three days apart from each other (modulus one year). They had to be carefully aligned so that the stars could be properly matched. Doing so directly on the images (with a task like ***geotran*** in `IRAF`, for example) would lead to a broadening of the Point Spread Function as a consequence of the inevitable interpolations involved. In order to avoid to degrade the quality of the data, we opted for transforming the *coordinates* of the stars identified in the February 1996 frames to the Hα images coordinate system. We then performed the photometry on this list on the Hα image. For each chip, a few bright stars were matched by eye in the two epochs and the `IRAF` task ***geomap*** was used to map the coordinate system of the reference image (February 1996) to the one of the February 1994 frame. The task ***geoxytran*** was, then, used to actually perform the

coordinate transformation.

Also the July 1997 F502N images, which measure the [OIII] 5007 Å line, have a slightly different orientation than the rest of the images of the same epoch, because they were taken two days later. We have used the same procedure described above to align them too.

Figure 6.3 on the facing page shows a composite of all available B, V and R broad band plus the [OIII] and Hα narrow band images. The Supernova and its rings are located right at the centre of the field.

6.3.1 The final list of stars

As it can be seen in Figure 6.2 on the previous page, the fields of view of the three observations centered on SN1987A partially overlap. Since some of the stars were detected in more than one chip, duplications had to be recognized and rejected. In order to do this, we had to consider the problem of both absolute and relative pointing of *HST*.

The *HST* pointing is achieved through its three Fine Guidance Sensors (FGS) (see, for example, Voit, 1997). Each FGS is an optical-mechanical white-light interferometer that can sense 1-2 milliarcseconds displacements in two dimensions of a point-like source in the $3 < V < 15$ brightness range. In principle, the FGSs could detect targets as faint as $V = 17$, but the pointing accuracy would be considerably worse.

A set of *guiding stars* from the **Guide Star Catalogue** are used to point *HST*. The catalogue currently in use is Version 1.1. A description of the different versions and related topics can be found at the following URL:

`http://www-gsss.stsci.edu/gsc/gsc.html`

Since pointing requires two-dimensional control (translation ad roll), two FGSs are usually used simultaneously to track the guide stars. The FGS that controls the translation is called the *dominant guider* and the one that controls the roll is the *roll* or *subdominant guider*.

The Hubble Deep Field campaign (Williams et al., 1996), with its ten days worth of observations of the *same field*, provided an excellent opportunity to study the accuracy and stability of *HST* pointing. It appears that it was stable to better than 5 milliarcseconds while taking many images of the same field without interruption over several orbits. The accuracy for re-acquisition of the same field after slewing to other targets appeared to be roughly 10 milliarcseconds, with occasional errors as large as 20 milliarcseconds. For comparison, let us recall here that the pixel size of the PC chip is roughly 50 milliarcseconds and the one of the three WF cameras is roughly 100 milliarcseconds (see section 3.1).

The high sensitivity and angular resolution of the WFPC2, together with the excellent pointing stability provided by the FGSs, make it possible to precisely measure the *relative* position of an object with respect to other reference points in its field of view. However, the *absolute astrometry* attainable with the instrument is limited by two factors: the precision

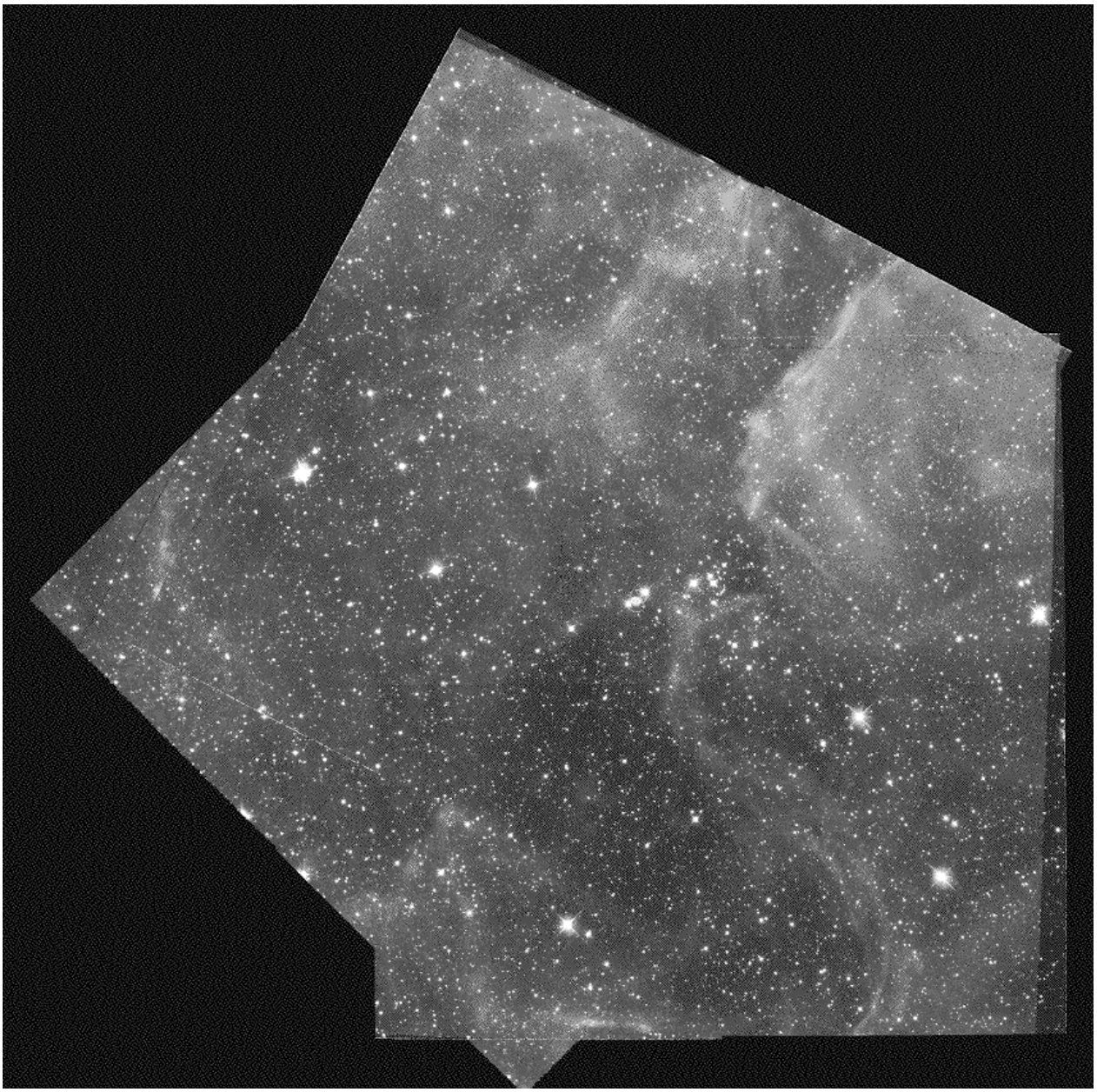

Figure 6.3: *The field centered on SN1987A as observed in the combination of the B, V and R broad bands plus the [OIII] and Hα narrow band images. North is roughly up and east to the left.*

with which the guide star positions are known, which is of the order of $0''.5$ in each coordinate, and the transformation between the FGS and WFPC2 fields of view, which introduces an additional error of the order of $0''.1$. As it can be seen, the absolute pointing is not reliable

enough for our goal of identifying stars that were observed in more than one epoch.

Since the WFPC2 consists of four physically independent detectors, it is necessary to define a system that includes all of them. In order to do so, the relative positions on the sky of the four chips need to be known. This information is obtained as part of the calibration duties by imaging the same set of stars in different positions on a chip (to determine the geometric distortion of the cameras) and in different chips (to determine their relative positions on the sky). The `STSDAS` task ***metric*** is designed to bring the four chips into a *meta-coordinate* system, defined such as to have the same orientation and pixel size as the WF2 chip at its centre. Once this is done, the coordinates are transformed into right ascension and declination using the absolute position and orientation of the WF2 chip. The task ***invmetric*** can be used to perform the inverse transformation, *i.e.* from right ascension and declination to chip and pixel position. The ***metric*** and ***invmetric*** tasks are constantly updated to include the best current estimates of the WFPC2 location on the sky. The final *relative* positions are accurate to better than $0''.005$ for objects in the same chip and $0''.1$ for targets in different chips. Obviously, the *absolute* accuracy is only as good as that of the guide stars used in the observation, *i.e.* $0''.5$ in each direction.

Early WFPC2 images contain header information regarding plate scales and chip-to-chip rotation that are less accurate than that available now. The `STSDAS` task ***uchoord*** updates the relevant parameters and should be run on all observations taken before March 1995. Another useful task, as we shall see, is ***mosaic***. Using the same information as ***metric***, it creates a *mosaic image* from the four chips that constitute a WFPC2 observation.

In order to obtain a single list of stars from the 12 input lists (4 chips for each of the 3 epochs), in principle, we could compute right ascension and declination for all of the stars with ***metric*** and merge the different lists rejecting the duplicate stars. Unfortunately, though, this simple approach does not work in our case. Since different guide stars were used for the different observations, the uncertainty on the relative positions of stars in different epochs is going to be as large as the uncertainty on the absolute position of the guide stars themselves. So, we had to manually align the images obtained at different epochs to a common orientation. We did this by performing the following steps:

1. Transform the coordinates of every epoch to the *meta-coordinate* system of that epoch with ***metric***. This also corrects for the geometric distortion of the camera.

2. For every epoch, transform the meta-coordinates to the *reference system of the mosaic image*:

$$\begin{cases} x_{\rm mos} &= 809 - x_{\rm meta} \\ y_{\rm mos} &= 810 - y_{\rm meta} \end{cases}$$

   The transformation equations were derived by comparing the coordinates of a few stars in the two reference frames.

3. Create the mosaic images for each epoch with ***mosaic*** and compute the transformation to a common orientation with ***geotran***. Since it is almost north-east oriented, we have used the February 1996 image as the reference one.

4. For every epoch, transform the coordinates from the mosaic system of that epoch to the common orientation using the transformation computed in step 3.

   At this point, all of the stars are in the *same reference frame* and all it is left to do is to reject the ones that are in more than one exposure.

5. We chose July 1997 as the *reference epoch*, in the sense that all of the stars identified in this epoch are included in the final list. We have written a simple **S**uper**M**ongo macro to perform the comparison of all the chips of all the epochs with the chips of the reference epoch. As a first approximation, a star is considered a duplicate if it is closer than 5 pixels to a star of the reference epoch.

6. Some iteration is necessary. We used the centroids of the the differences of coordinates along x and y of the "duplicate" stars (in the sense of step 5) to improve the alignment resulting from steps 1 through 4. The shift required is of the order of a pixel or less.

7. Repeat step 5 with the improved coordinate match from step 6. At this stage, we have decreased the matching radius to 2 pixels to minimize the possibility of false duplications. We have used the July 1997 observation as reference (all of the stars identified here are included in the final list) and the February 1996 epoch as secondary (only the stars not in common with the July 1997 list will be included). Among the stars identified in the September 1994 image, only those that are neither in the July 1997 nor in the February 1996 lists are included in the final list.

An eye inspection of the results confirms that the identification and rejection of the duplicate stars was done properly. Among the 32,857 input stars identified in at least one of the the 12 chips, 21,955 are found to be unique. They constitute the *final list of stars* we are going to study.

6.3.2 Photometric accuracy

Before proceeding to analyze the data, let us now check the quality of the photometry. In Figure 6.4 on the following page we show the photometric error as a function of magnitude for each of the 6 broad band filters. The errors are computed according to equation 4.8 on page 81. The sharp cuts in the various panels are consequences of the way we have selected the objects. Let us recall here that an object detected by ***daofind*** needs to have a photometric error in the F555W filter smaller then 0.2 *mag* in order to be included in the final list of stars on which the photometry is, then, performed for all of the other filters (see

section 4.2.1). Moreover, the flux of a star in a given filter is measured only if the signal-to-noise ratio is greater than 3 (see section 4.2.5). This is the reason why the maximum error in Figure 6.4 is $2.5 \cdot \log(1 + 1/3) \simeq 0.31$ *mag*.

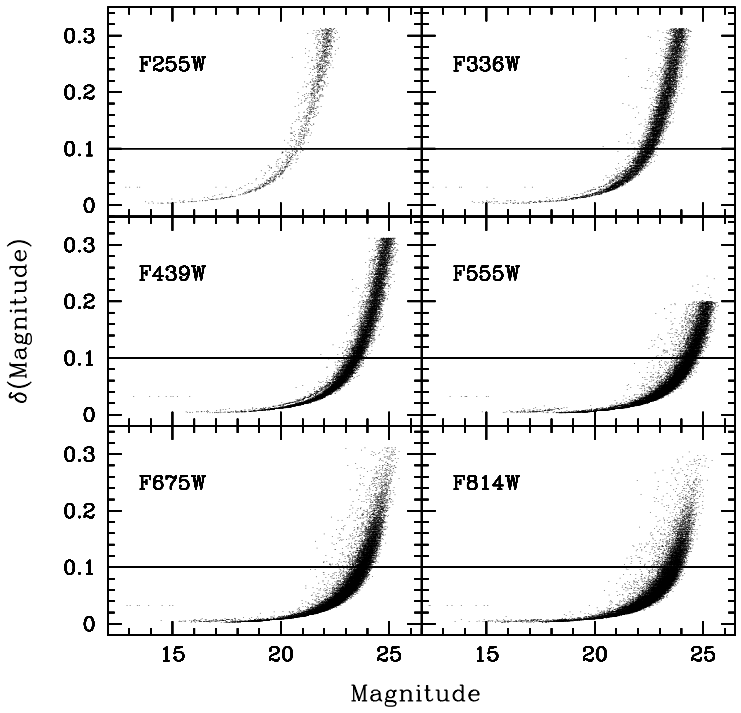

Figure 6.4: *Photometric error as a function of magnitude for the 6 broad band filters around SN1987A. The 0.1 mag error level is indicated.*

As we have mentioned in section 4.2.4, the flux of heavily saturated stars was recovered using the method developed by Gilliland (1994). The error on these stars was arbitrarily set to 0.032 *mag*. This is much bigger than the error that they would actually have, given their brightness, were they not saturated. This causes the discontinuities which can be seen at bright magnitudes in all the panels in Figure 6.4. For marginally saturated stars, for which the flux was recovered using an annulus that excludes the saturated pixels, the error is the appropriate combination of Poissonian and the other sources of noise.

The total number of stars detected according to our criteria is 21,955. More than 15,000 of them have a photometric accuracy better than 0.1 *mag* in the V, R and I filters. This number drops to 6,825 in the B band and only 786 stars have a UV filter uncertainty smaller than 0.2 *mag*. Finally, 6,695 stars have $\overline{\delta}_5 < 0.1$ *mag*, where $\overline{\delta}_5$ is the mean error in 5 bands, excluding the UV, defined in equation (5.1):

$$\overline{\delta}_5 \equiv \sqrt{\frac{\delta^2_{\mathrm{F336W}} + \delta^2_{\mathrm{F439W}} + \delta^2_{\mathrm{F555W}} + \delta^2_{\mathrm{F675W}} + \delta^2_{\mathrm{F814W}}}{5}}$$

6.4 The Colour-Magnitude diagrams

Now that we have discussed how to calibrate the data and how to reduce them, we are finally ready to analyze them. The first step to do is to plot Colour-Magnitude diagrams (CMD) to have a first insight into the stellar content of the region. We recall that the observed magnitude and colour of a star are the intrinsic values, which are a function of its chemical composition and evolutionary status, as seen through the "sheet" of dust along that particular line of sight. The CMDs for all the stars in the field for four combinations of bands are shown in Figure 6.5.

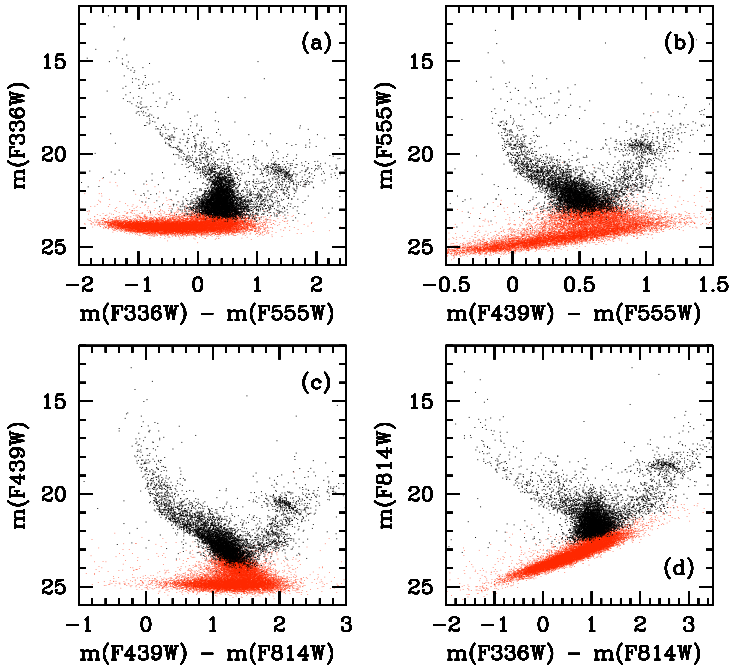

Figure 6.5: *Colour-Magnitude diagrams of the stars around SN1987A for four combination of filters. The grey dots are stars with* $\overline{\delta}_5 > 0.1$*, whereas the black ones are the 6,695 stars with* $\overline{\delta}_5 < 0.1$.

As we have already noticed when discussing Figure 5.1, the error threshold of $\overline{\delta}_5 < 0.1$ corresponds to a magnitude threshold at $m_{\mathrm{F555W}} \simeq 23$.

At least two very different population are clearly visible in Figure 6.5. The first one is associated with the feature extending up to $m_{\mathrm{F439W}} \simeq 15$ and $m_{\mathrm{F439W}} - m_{\mathrm{F814W}} \simeq 0$ (see panel (c)). This is a young generation of stars still on or just outside the Zero Age Main-Sequence (ZAMS), *i.e.* burning hydrogen into helium in their cores. The other population

is identified by the presence of a clump of stars at $m_{\mathrm{F439W}} \simeq 20.5$, $m_{\mathrm{F439W}} - m_{\mathrm{F814W}} \simeq 2$. This is the *red clump*, *i.e.* stars of intermediate mass between half and a few billion years old that are burning helium into carbon and oxygen in their cores (see, for example, Castellani et al., 1992).

As we have already noticed and discussed in section 5.1 on page 93, despite the high quality of the measurements, the various features of the CMDs are rather "fuzzy" and not sharply defined. Although this is due in part to the presence of several stellar populations projected on each other, most of the problem resides in the fact that reddening is not quite uniform over the field. Also, there is not a combination of two bands suited to characterize properly both the hot *and* the cold stars. What we need to do, then, is to determine the extinction and the intrinsic temperature with the method described in chapter 5. As an illustration of the results of the process, in Figure 6.6 we show the m(F439W) vs. m(F439W)−m(F814) Colur-Magnitude diagram of the stars around SN1987A with $\overline{\delta}_5 < 0.1$. In panel (a) we show the observed Colour-Magnitude Diagram and in panel (b) the one corrected for extinction with the $E(\mathrm{B}-\mathrm{V})$ values found in the fitting procedure described above. The black dots are class I and II stars, *i.e.* stars for which the reddening was determined individually and the grey dots are the stars that were corrected with the mean value from class I and II stars.

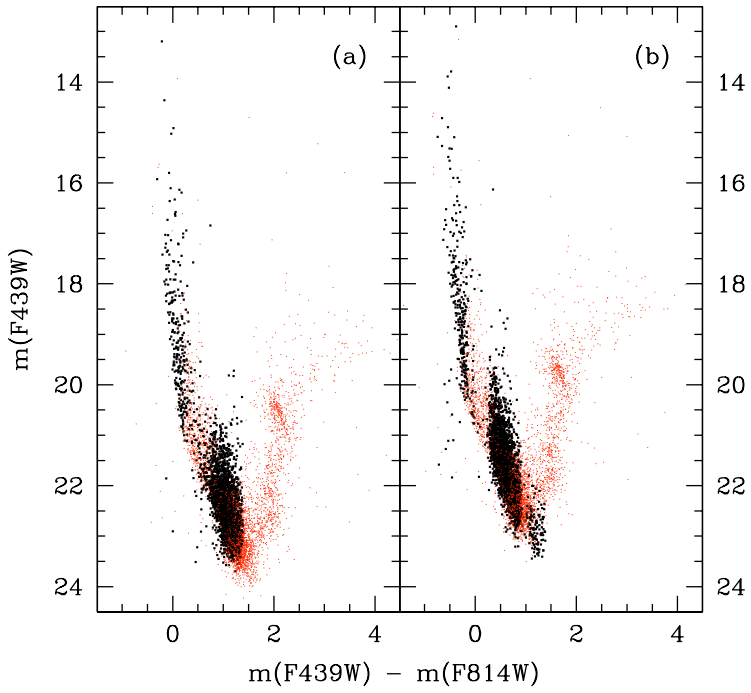

Figure 6.6: *B vs. B−I diagram before (panel (a)) and after (panel (b)) the correction for reddening for the stars around SN1987A with* $\overline{\delta}_5 < 0.1$. *Black dots are stars for which* $E(\mathrm{B}-\mathrm{V})$ *was determined individually (class I and II), whereas the grey dots were corrected using the average* $E(\mathrm{B}-\mathrm{V})$ *value.*

As we have discussed when commenting Figure 5.17 on page 116, the scatter among the stars for which the reddening was determined individually is very much reduced and the

Main Sequence is much better defined. Let us notice again that all of the Main Sequence stars brighter than m(F439W)$\simeq$ 20 *mag* have essentially the same m(F439W)−m(F814) colour, thus making the temperature determination highly uncertain. A larger baseline, like the one we have used, is needed to fully characterize their properties.

6.5 Reddening distribution

As previously pointed out, stars are seen through the interstellar medium present along the line of sight to them. The fitting procedure we have described in chapter 5 and will applied here to the stars around SN1987A was devised precisely to measure the extinction due to the intervening material and correct for it. Out of a total of 21,955 stars, a sample of 2,510, *i.e.* the ones belonging to classes I and II defined in section 5.2.4, have individual reddening determinations.

The number of stars as a function of the reddening is shown in panel (a) of Figure 6.7. Here, the reddening is only the one caused by the dust in the Large Magellanic Cloud. The contribution of our Galaxy is taken to be the same for all of the stars: $E(\mathrm{B-V})_{\mathrm{MW}} = 0.05$ (Bessel, 1991; Schwering and Israel, 1991).

The reddening distribution peaks at $E(\mathrm{B-V}) = 0.15$ which, incidentally, is virtually identical to the value of $E(\mathrm{B-V}) = 0.14 \pm 0.02$ found by Scuderi et al. (1996) from *HST*-FOS spectroscopy of Star 2, one of the two bright stars projected within a few arcseconds from SN1987A. The rms width of the distribution is quite large and roughly equal to half the mean value: $\sigma(E(\mathrm{B-V})) = 0.072$. Also, the histogram is skewed towards high values of $E(\mathrm{B-V})$. In conclusion, *an inspection at the histogram in Figure 6.7 further confirms the necessity for a careful determination of individual reddenings in regions where the interstellar medium is clumpy.*

In panel (b) of Figure 6.7, we show the spatial distribution of stars with extreme reddening values. The stars with *high reddenings* ($E(\mathrm{B-V}) > 0.25$) are plotted as black dots and those with *low reddenings* ($E(\mathrm{B-V}) < 0.05$) as open circles. As it can be seen, the two categories of stars are distributed rather smoothly over the field. It is also worth noticing that the reddening is very patchy and heavily reddened stars are projected within few arcseconds from relatively unobscured ones.

As a general remark, let us stress here that we can only measure the total optical depth of the interstellar medium in front of a star (see equation 2.13 on page 16). We have no way of knowing if the star is deeply embedded in a low density cloud, or, rather, it is just under the skin of a high density one. That is to say that we cannot distinguish between optical depth and physical depth within the Large Magellanic Cloud. *In order to measure the total optical depth through a galaxy, one should use objects that are definitely in the background, such as distant galaxies* (Olsen and Hodge, 1996; Gonzalez et al., 1998).

Finally, if the extinction towards a given line of sight is high enough, we would not

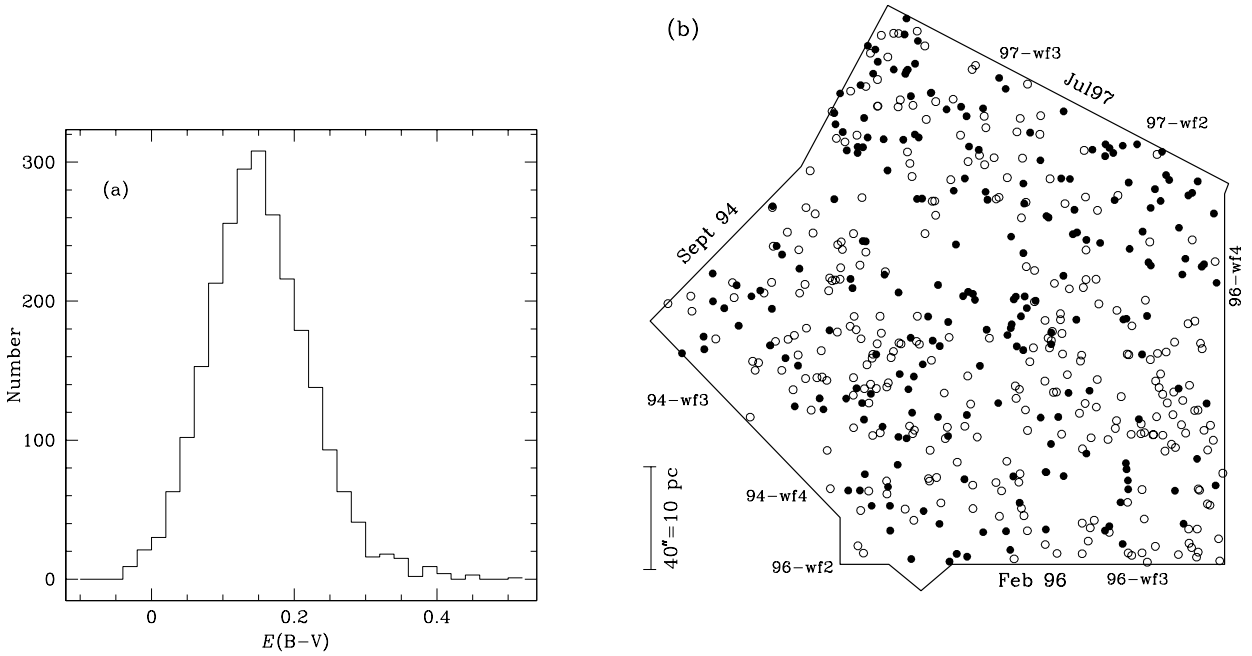

Figure 6.7: *Panel (a): reddening histogram from the stars in the field of Supernova 1987A. Only stars for which* $E(\mathrm{B-V})$ *was measured individually (class I and II, see section 5.2.4) are used here. Panel (b): spatial distribution of stars with high* ($E(\mathrm{B-V}) > 0.25$, *filled circles) and low* ($E(\mathrm{B-V}) < 0.05$, *open circles) reddening. In both panels, the reddening is only due to the dust within the LMC. The contribution from the Milky Way is* $E(\mathrm{B-V})_{\mathrm{MW}} = 0.05$ *for all of the stars.*

detect the stars in that direction and, of course, intrinsically faint stars are preferentially lost. Once again, though, it is impossible to disentangle this effect from a real hole in the spatial distribution of the stars.

6.6 The HR diagram

We can now apply the method described in the previous chapter and recover the luminosity and effective temperature for the 21,955 stars around SN1987A. Let us stress here that we have no free parameters, since the reddening is measured directly as described in chapter 5 and the distance is the one measured from the study of the inner circumstellar ring around SN1987A (51.4 ± 1.2 kpc, Panagia, 1998). The resulting HR diagram, *i.e.* $\log(\mathrm{L/L_\odot})$ vs. $\log(\mathrm{T}_{eff})$ plot, is shown in Figure 6.8 on the next page.

More than 40% (9,474 out of 21,955) of the stars have an excellent temperature determination, *i.e.* $\delta \log(\mathrm{T}_{eff}) < 0.05$, which corresponds to 12%. The gap in the stars with accurate

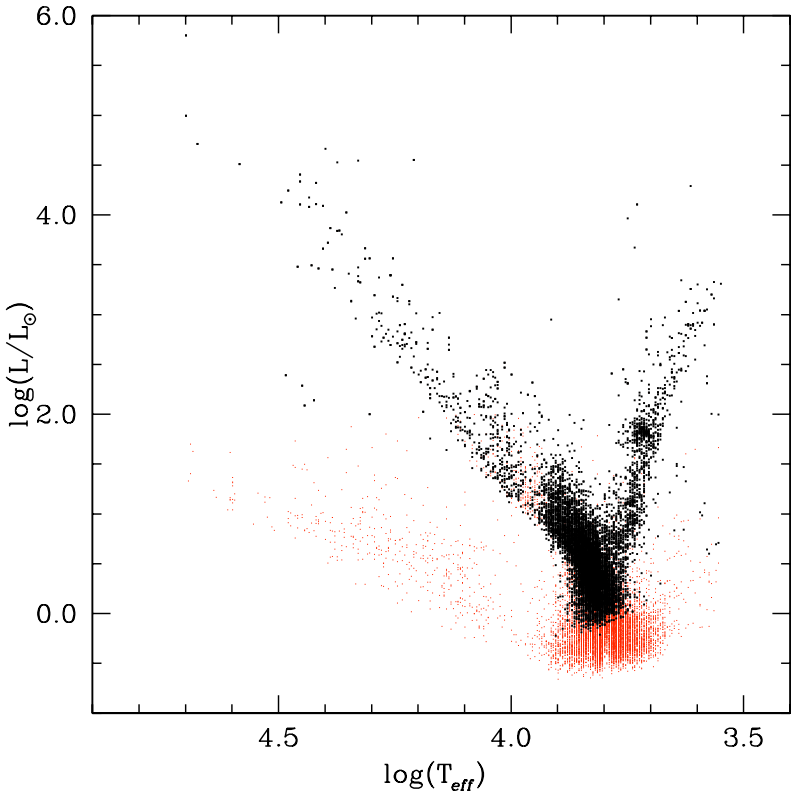

Figure 6.8: *HR diagram for the stars in the field around SN1987A. The black dots are the 9,474 stars with* $\delta \log(\mathrm{T}_{eff}) < 0.05$.

temperature determination in the interval $3.9 \lesssim \log(\mathrm{T}_{eff}) \lesssim 3.95$, corresponds to the "elbow" in the Q_{UBI} vs. U−I plane at U−I $\simeq 0$ (see, for example, Figure 5.4 on page 103). This is because, as we have seen in the previous chapter, in that region the stellar atmospheres are the most sensitive to the detailed input parameters, such as the surface gravity of the star. A difference between the actual values for a star and the ones we have used in the fit can result in a less precise fit.

About 600 stars, less than 3% of the total, fall under the Zero Age Main Sequence locus, *i.e.* the 6-band fit results in an unreasonably high temperature. Most of them belong to class IV and their photometric accuracy is quite poor, especially at short wavelengths. These stars were assigned the mean value of $E(\mathrm{B}-\mathrm{V})$ of their neighbours and the only fitted parameter was the temperature. So, it could be that, in reality, these stars would require a much smaller $E(\mathrm{B}-\mathrm{V})$ than the mean value and, hence, when the fit is forced to have a too big extinction, it yields a temperature which is also too large. It could also be, however, that the spectra of these stars are not well represented by the model atmospheres.

In particular, if they had a UV excess with respect to the models, the fit would lead to a higher temperature than the one indicated by their optical colours. In fact, if we fit these stars excluding the UV and U bands, the majority of them, roughly 400, has a location in the HR diagram consistent with the lower Main Sequence and this is how we have fitted them. As we shall see, some Pre-Main Sequence stars are observed to have an ultraviolet excess and, hence, these stars are excellent Pre-main Sequence candidates.

Another case in which the observed spectrum can differ significantly from that of a "normal" star is the occurrence of *unresolved binary* or multiple stars. The various components can either be gravitationally bound, or just projected within the angular resolution of WFPC2 ($0''.1$ at the distance of the LMC correspond to roughly 5,000 Astronomical Units). In any case, the resulting spectrum is different from the one of a single star. Exactly how much different depends on the relative fluxes of the components of the system as a function of wavelength, *i.e.* it ultimately depends their temperatures and luminosities. If the deviation from a single star's spectrum is significant, one can expect the quality of the fit to be worse and, consequently, the error on the temperature to be bigger than the average one of stars with comparable photometric accuracy.

In order to estimate a *lower limit to the binary fraction of Main Sequence stars*, we have selected the objects in the $4 \leq \log(T_{eff}) \leq 4.2$ range, corresponding to $1 \lesssim \log(L/L_{\odot}) \lesssim 2.3$. The interval was chosen to avoid the faint, poorly measured stars and the bright ones affected by saturation. Among these stars, we consider the ones with $\delta \log(T_{eff}) > 0.05$ as binary candidates. Of course, some of them are single stars that have a large error simply because of statistical fluctuations. After rejecting their appropriate number, as expected from a Gaussian distribution, we estimate that at least 12% of the stars are in binary, or indeed, multiple systems. This is clearly a lower limit and, for comparison, the fraction of binaries among local Main Sequence solar-type stars is estimated to be roughly 60% (Duquennoy and Mayor, 1991). Let us further notice that an unresolved Main Sequence binary would appear brighter than any of its components, but with an intermediate temperature. It would, then, look evolved. As a consequence, it is very difficult to recognize the effects of binarity when there is a superposition of various generation of stars (see, for example, Serra-Ricart et al., 1996).

Finally, as a check of our fitting procedure, we can compare our results for Star 2, one of the stars projected near SN1987A, with those obtained by Scuderi et al. (1996) by fitting the whole optical and UV spectrum in the range from 1200 to 8000 Å. Our fit gives $T_{eff} = 25,000 \pm 3,000$ K, as compared to $T_{eff} = 22,000 \pm 2,000$ K. The agreement is very good, particularly considering that Star 2 is heavily saturated in the optical filters and moderately so in the UV ones, thus making the relative photometry extremely difficult.

Let us now describe in some detail the global properties of the stellar populations in the field as derived from the HR diagram.

6.6.1 The mean metallicity

As we have explained in section 5.3, even if we fit the observed colours to models with a particular metallicity, *i.e.* Z= 0.3·$Z_\odot$, the result of the fit does not depend on it. As a consequence, we can infer the metallicity, at least the mean one, of the stars in the field by comparing their location in the HR diagram to stellar models computed with different chemical compositions. Unless otherwise noted, in the following discussion we will use the models by Brocato and Castellani (1993) and Cassisi et al. (1994) as Main Sequence and Post-Main Sequence evolutionary tracks. We would like to stress that the position of the ZAMS is essentially the same for all the sets of evolutionary calculations available in the literature because the physics involved is well known and there are no ambiguous free parameters that can affect the results.

In Figure 6.9 we show the HR diagram of Figure 6.8 (the stars in the spur under the Main Sequence were omitted for clarity), together with the theoretical loci of the ZAMS for three different values of the metallicity: Z=$Z_\odot$ (dashed line), Z= 0.3·$Z_\odot$ (full line) and Z=$Z_\odot$/20 (dotted line).

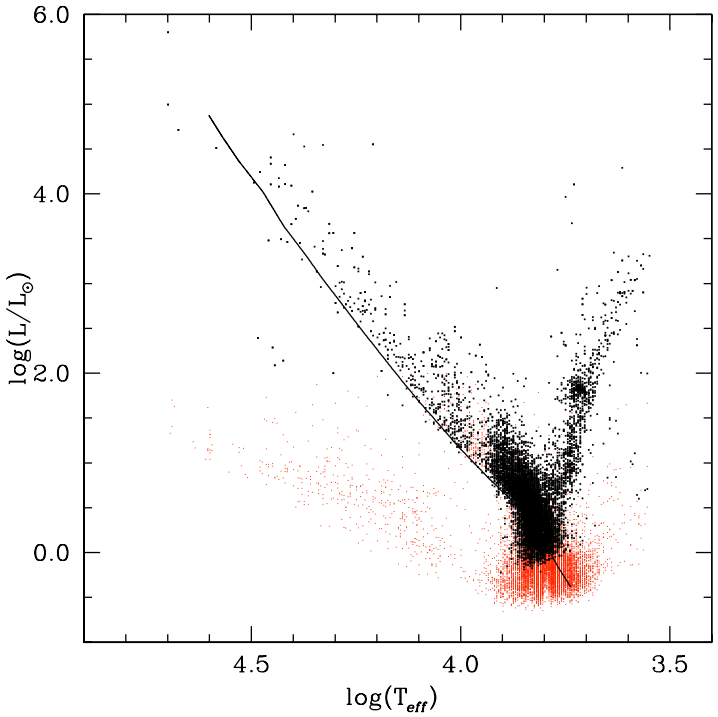

Figure 6.9: *HR diagram for the stars in the field around SN1987A. Black dots are stars with* $\delta \log(T_{eff}) < 0.05$. *The locus of the ZAMS is shown for three values of the metallicity:* Z=$Z_\odot$ *(dashed line),* Z= 0.3·$Z_\odot$ *(full line) and* Z=$Z_\odot$/20 *(dotted line).*

As it can be seen, the ZAMS computed for Z= 0.3·$Z_\odot$ nicely defines the lower envelope of the observed stellar distribution. On the contrary, the solar metallicity sequence is, at any given temperature, definitely too luminous and the very metal poor one is, on the other hand, underluminous. The agreement of the data with the models is satisfactorily good and

we have not attempted to interpolate between the sequences for different metallicities to refine this estimate.

The metallicity value we infer is essentially in agreement with what is found in the literature, often with large quoted uncertainties. For example, Geha et al. (1998) find $Z \simeq Z_{\odot}/2.5$ from photometry of the upper Main Sequence of three fields in the LMC and Olszewski et al. (1991) find a mean value of $Z \simeq Z_{\odot}/2$ from the spectroscopy of stars in 31 LMC clusters. The scatter they found, however, is quite large: 0.2 dex.

6.6.2 Masses and ages

We can assign masses and ages to the stars in the field by comparing their position in the HR diagram to theoretical evolutionary tracks and isochrones, respectively. We have used the models by Brocato and Castellani (1993) and Cassisi et al. (1994) for $Z = 0.3 \cdot Z_{\odot}$. The highest mass computed in this set of tracks is 25 $M_{\odot}$ and we have extended them to higher masses with the models by Schaerer et al. (1993). These models are computed for a slightly higher metallicity ($Z = 0.4 \cdot Z_{\odot}$) and we have shifted them in order to match the ZAMS location of the 20 $M_{\odot}$ model. The shift required is of $+0.019$ in the logarithm of temperature and -0.008 in the logarithm of luminosity.

Different assumptions on poorly known parameters, such as the convective mixing length and overshooting, or on the appropriate treatment of the convection itself and of the mass-loss lead to different theoretical evolutionary tracks. However, it is important to notice that the detailed conclusion of our analysis may be model dependent, but the general picture is not.

In Figure 6.10 on the facing page we plot the observed stars together with selected evolutionary tracks in the relevant mass range.

The brightest star in the field is indicated with an open circle in Figure 6.10. For it, the fit yields $T_{eff} \simeq 50,000$ K and $\log(L/L_{\odot}) \simeq 6.3 \cdot 10^5$. It may be even be hotter, since 50,000 K is the temperature of the hottest atmosphere model by Castelli (1998). A comparison to the models by Schaerer et al. (1993) gives a mass well in excess of 60 $M_{\odot}$. The Main Sequence lifetime of a stars this massive is shorter than 3.7 Myr. This star is easily recognizable in Figure 6.3 on page 129: it is the bright one to the north-east of SN1987A.

Selected isochrones computed from the set of tracks by Brocato and Castellani (1993) and Cassisi et al. (1994) are shown in Figure 6.11 on page 142. The upper Main Sequence by Schaerer et al. (1993) is shown as a dashed line.

An inspection of Figure 6.11 reveals that:

- Excluding the extremely bright and massive star at $\log(T_{eff}) \simeq 4.7$ and $\log(L/L_{\odot}) \simeq 5.8$, the positions of the most luminous blue stars fall on isochrones corresponding to ages around 10-12 Myrs, *i.e.* they are coeval with Sk -69 202, the progenitor of SN1987A, and Star 2 (Scuderi et al., 1996). The evolutionary tracks used to compute the

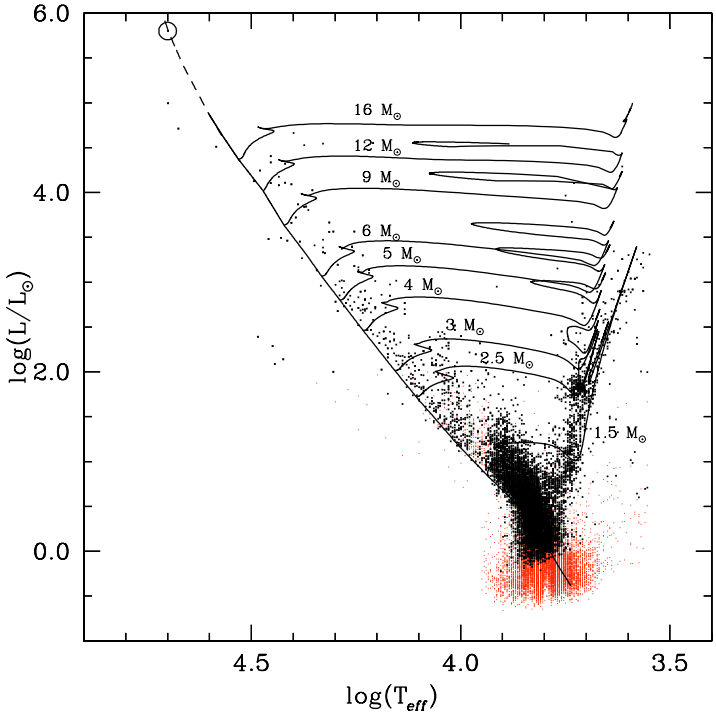

Figure 6.10: *HR diagram for the stars in the field around SN1987A. Black dots are stars with* $\delta \log(T_{eff}) < 0.05$ *and the open circle highlights the most massive star in the field. The Zero Age Main Sequence and evolutionary tracks for the quoted masses and* $Z = 0.3 \cdot Z_{\odot}$ *computed by Brocato and Castellani (1993) and Cassisi et al. (1994) are shown. The dashed line is the high mass ZAMS from Schaerer et al. (1993) (sse text).*

isochrones indicate masses of 12-13 $M_{\odot}$ for these hot and luminous stars (see Figure 6.10).

- There are a number of stars at intermediate luminosities and temperatures, *i.e.* with $\log(L/L_{\odot}) \simeq$ 2-4 and $\log(T_{eff}) \simeq$ 3.65-3.7, that indicate distinct stellar generations with ages in the range 40-150 Myrs.

- The lower Main Sequence and the Red Giants are mostly old populations, consistent with a metallicity either identical to, or slightly lower than the one of the young components. No single age can explain the distribution of the old population, and stellar generations between 600 Myrs and 6 Gyrs are required to account for the observations. This is the LMC field population.

A better evaluation of masses and ages will be given in chapter 8 when we will discuss Star Formation History of this region.

Our results, broadly speaking, confirm the early findings of the ground-based studies by Walker and Suntzeff (1990) and Walborn et al. (1993), but, at the same time, are much more detailed and, by reaching fainter magnitudes with high spatial resolution, also more statistically valid and accurate.

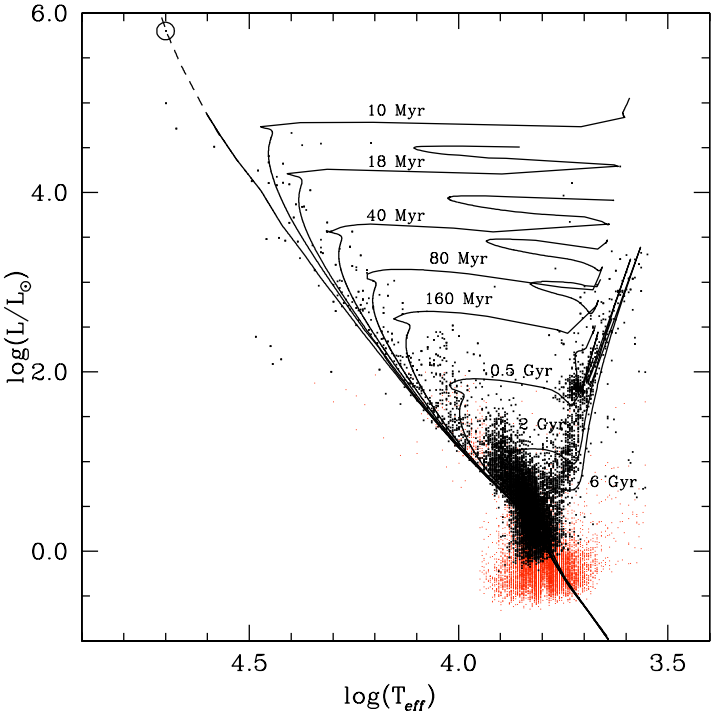

Figure 6.11: *Same as Figure 6.10 on the preceding page, but this time selected isochrones are displayed.*

6.7 Pre-Main Sequence stars

As we have seen, there is a population of hot, massive (M≃12-13 $M_\odot$) stars of about 12 Myrs of age in the neighbourhood of SN1987A. Since they are the brightest objects in the field, they are easily identified in the HR diagram. Do they have a counterpart at low luminosities? In other words, is there a population of low mass stars with the same young age?

At the age of the youngest massive stars in our field, low mass stars are expected to be still in the *Pre-Main Sequence* (PMS) phase. This is the transition stage during which newly formed stars reach for the first time an equilibrium configuration with the onset of hydrogen burning nuclear reactions in their cores. During Pre-Main Sequence evolution, the star shines primarily through the release of gravitational energy produced in the quasi-static contraction towards the Main Sequence. Throughout the PMS phase, nuclear burning is limited to the lighter elements (deuterium, ^{6}Li, ^{7}Li, ^{9}Be, ^{11}B and ^{10}B) at temperatures of a few million degrees. Among these, the deuterium burning is the only one that releases a non negligible amount of energy, capable of influencing the star's evolution (see, for example, Forestini, 1994; D'Antona and Mazzitelli, 1994).

Evolutionary models of Pre-Main Sequence stars, such as those computed by Siess et al. (1997), for example, indicate that stars less massive than about 2 $M_\odot$ have not yet reached the Main Sequence after 10 Myrs of evolution (see Figure 6.12 on the next page). These

stars are usually called T Tauri stars, because they were first discovered in 1945 in the Taurus-Auriga dark cloud by Alfred H. Joy, who named the class after its brightest member (see Hearnshaw, 1986, for the history of the discovery). We refer the reader to the paper by Bertout (1989) for an thorough review of the subject.

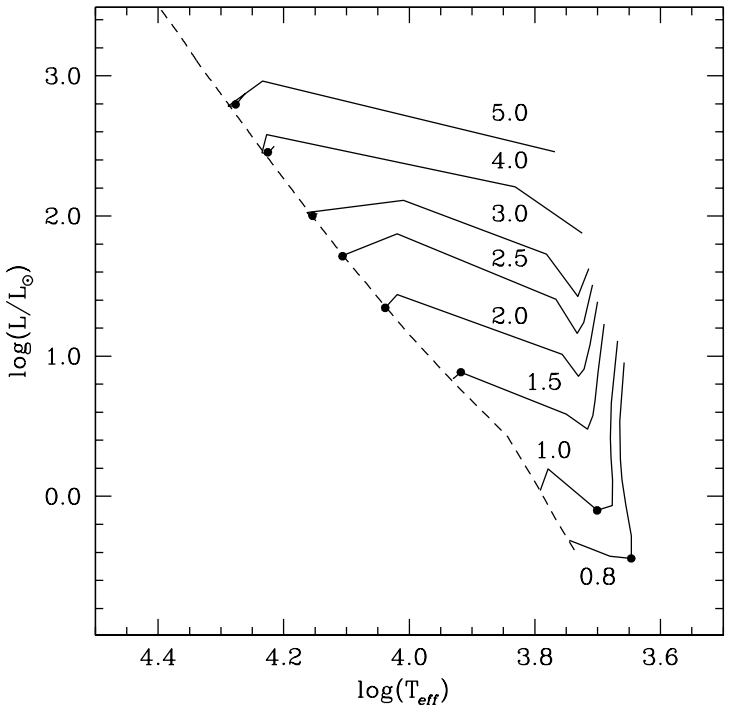

Figure 6.12: *Evolutionary tracks for T Tauri stars computed by Siess et al. (1997) for Z= 0.3·$Z_\odot$. Stellar masses, in units of $M_\odot$, are indicated for each track. The dots mark the position of the stars at 10 Myrs. The Zero Age Main Sequence for the same metallicity, computed from the models of Brocato and Castellani (1993) and Cassisi et al. (1994), is shown as dotted line.*

As a general fact, the mass function increases at low masses, that is to say that less massive stars are much more numerous than more massive ones. In particular, there are many more T Tauri stars than massive stars of the same age. As a consequence, PMS stars are an extremely powerful tool to study young populations because their large number may provide more significant results. Moreover, they make it possible to study the star formation process in a different mass range than the one sampled by the stars in the upper Main Sequence.

The problem, however, is that T Tauri stars occupy the same area of the HR diagram of the old population, the one that also populates the Red Giant clump. How can we distinguish these two components, so different in age and evolutionary status, but so similar on the HR diagram?

6.7.1 Spectral properties of T Tauri stars

From an observational point of view, it has been known for a long time that T Tauri stars are spectroscopically peculiar when compared to Main Sequence stars of the same spectral type. The most striking anomaly is the presence of Hα and/or Ca II H and K lines[a] in the spectrum of a cool star, as early recognized by Herbig (1962). In addition, emission in the high Balmer lines, iron, helium and other elements can also be present. The continuum emission can also be peculiar, showing excesses in the ultraviolet and infrared. Low mass Pre-Main Sequence stars are usually divided in two broad categories depending on the strength of the emission lines. In order to quantify the strength of a line, let us introduce the *equivalent width* W_λ, which gives a measure of the line's flux compared to the one of the continuum:

$$EW\left(\overline{\lambda}\right) \equiv \left| \int_{line} \left(1 - \frac{f_\lambda}{f_c}\right) d\lambda \right| \tag{6.1}$$

where f_λ is the flux in the line at wavelength $\overline{\lambda}$ and f_c is the continuum flux in its neighbourhood. With the definition of equation (6.1) the equivalent width, which was originally introduced for absorption lines, is always a positive quantity. Also, it follows from its definition that $EW\left(\overline{\lambda}\right)$ dimensionally is a wavelength and it corresponds to the width of a rectangular line that encloses all the flux of the actual line.

Classical T Tauri stars (CTTs) are defined as T Tauri stars that have Hα emission with an equivalent width in excess of 10 Å, whereas T Tauri star with Hα emission weaker than this value are classified as **Weak T Tauri stars** (WTTs) (Fernandez et al., 1995). As we shall see, Classical T Tauri stars are interpreted as Pre-Main sequence stars surrounded by a disk, responsible for the emission lines. As an example, in Figure 6.13 we show typical Hα *residual* line profiles for Classical T Tauri stars from Edwards et al. (1994). An appropriate stellar template was subtracted from each observed spectrum to eliminate the photospheric contribution. The emission line profiles present a variety of shapes: single peak (second panel in the top row, for example), double peak with central absorption (third panel in the top row) and P Cygni profile[b] (first panel in the last row from the top).

The presence of emission lines is related to excess emission in the continuum: Weak T Tauri stars, which do not show near-infrared excess emission, also show no hot continuum emission at UV and optical wavelengths. Classical T Tauri stars, on the other hand, show both infrared and ultraviolet continuum excesses.

As an illustration, 12 spectra between 3200 and 5400 Å of T Tauri stars from Gullbring et al. (1998) are shown in Figure 6.14 on page 146. All of them are Classical T Tauri stars

[a]The Ca II H and K lines have a wavelength of 3968 and 3934 Å, respectively. They owe their name to Joseph Fraunhofer who observed them among the 10 strongest lines in the spectrum of the Sun in the early 19^{th} century.

[b]The P Cygni profile is characterized by a blue-shifted absorption component and a red-shifted emission component. They are interpreted as a signature of outflows (see, for example, Mihalas, 1978).

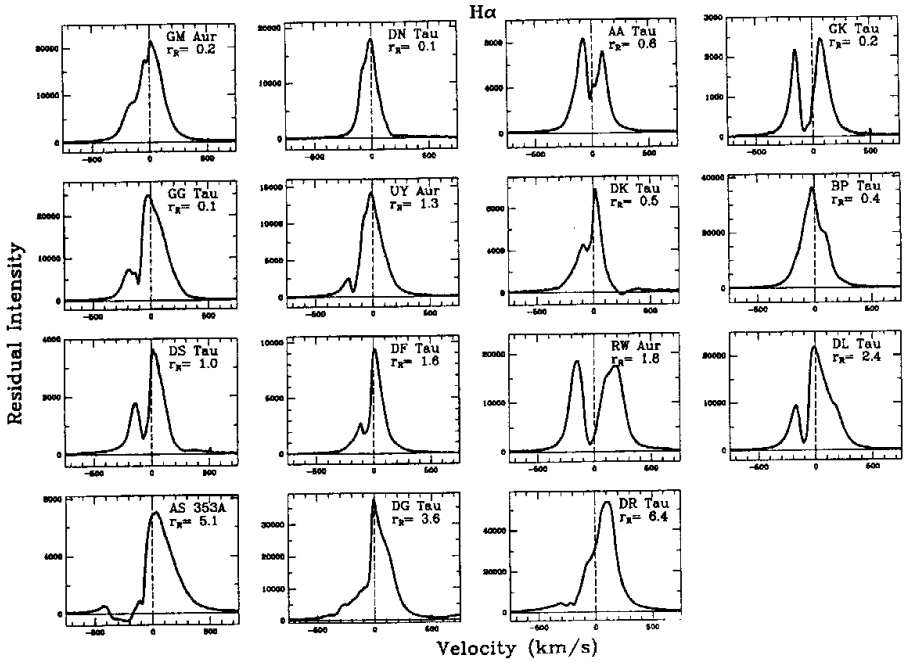

Figure 6.13: *Residual* Hα *profiles in Classical T Tauri stars from Edwards et al. (1994). An appropriate stellar template was subtracted from each observed spectrum to eliminate the photospheric contribution (see text). Velocities are referred to the stellar photospheric velocity.*

with the exception of HBC 351, LkCa7, V819 Tau and V836 Tau that are classified as Weak T Tauri stars.

From a theoretical point of view, the excess continuum emission from Classical T Tauri stars was first interpreted as originating in a dusty accretion disk surrounding the Pre-Main Sequence star itself (Lynden-Bell and Pringle, 1974). In this model, the infrared excess luminosity is generated in the disk, in part by viscous energy dissipation and in part by re-processing of light coming from the central star (Bertout et al., 1988). The UV excess was attributed to energy released in a boundary layer interface where the the material accreting from the disk, which is rotating with a Keplerian velocity of the order of 250 km s^{-1}, is slowed down to the photospheric rotation velocity, which is typically of the order of a few tens of km s^{-1} (see, for example, Basri and Bertout, 1989, and reference therein). This model nicely relates the infrared and ultraviolet excesses to each other through a common physical agent, *i.e.* the presence of an accretion disk interacting with the star. In this framework, therefore, Weak T Tauri stars are naturally interpreted as "naked" Pre-Main Sequence stars, in the sense that they are not surrounded by an appreciable accretion disk.

In order to fully model the system, one has to include the photospheric emission from the

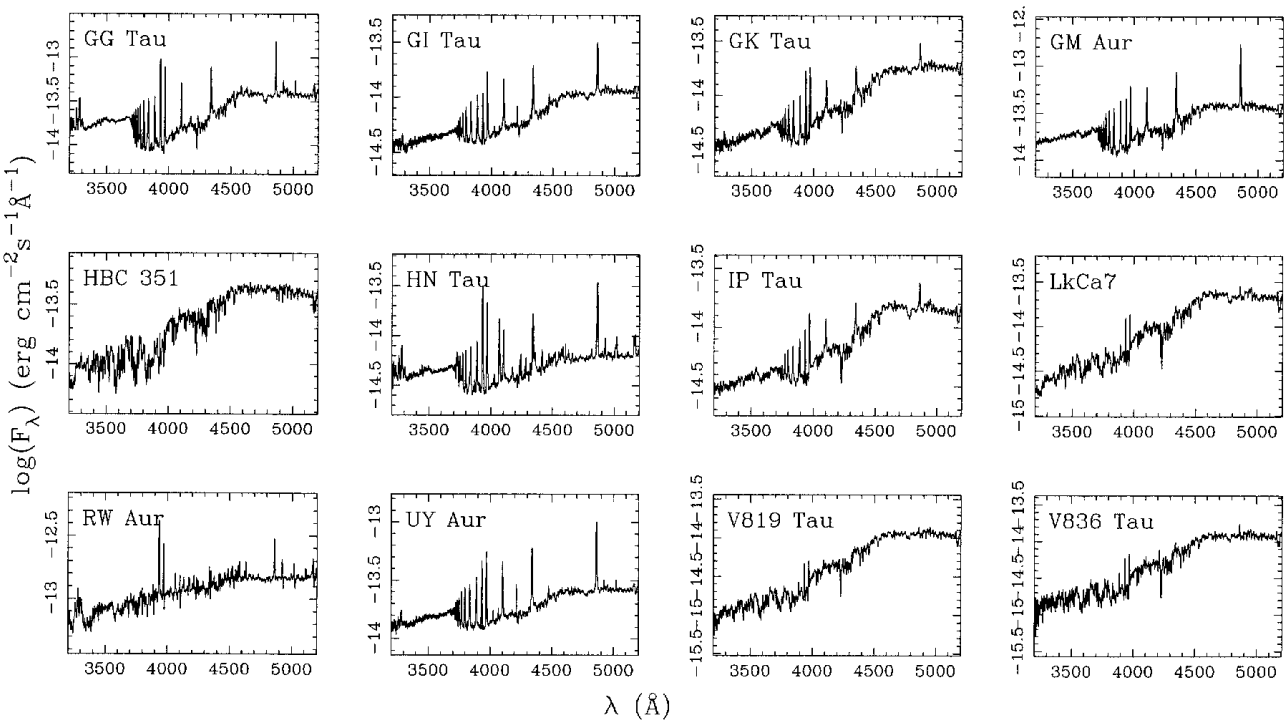

Figure 6.14: *Examples of T Tauri spectra in the 3200-5400 Å wavelength range from Gullbring et al. (1998). All of the stars are classified as Classical T Tauri except HBC 351, LkCa7, V819 Tau and V836 Tau that are Weak T Tauri stars.*

central star. In this picture, the interaction between the star and the circumstellar disk is confined to the equatorial boundary layer and, therefore, is likely to have little effect on the stellar spectrum. As a consequence, the photospheric emission is assumed to be the same as the one in a non-accreting star of the same spectral type. In principle, the best template for the star's emission is the spectrum of a Weak T Tauri star, but the disk parameters do not change significantly if a late-type star subgiant of the same spectral type is used instead (Bertout et al., 1988).

Even though the boundary layer model can successfully explain the excess emission in the ultraviolet and in the optical, it cannot produce the high *infall* velocities necessary to account for the observed *inverse P Cygni profile*, *i.e.* red-shifted absorption, often observed Classic T Tauri stars. For example, Edwards et al. (1994) find evidence for inverse P Cygni profiles in 13 out of the 15 stars in their program, in at least one of the six spectral lines monitored. The red-shifted absorption features indicate infall velocities of 200-300 km s^{-1}. Among the stars in Figure 6.13 on the previous page, DN Tau and DK Tau show this feature in the Hα line, although barely visible with the naked eye.

To explain the emission line profiles, recent theoretical work on accretion in Classical T Tauri has moved away from the boundary layer model described above in favor of *magnetospheric accretion* (see, for example, Muzerolle et al., 1998, and references therein). The presence of magnetic fields in T Tauri stars is confirmed by the X-ray emission observed in Pre-Main Sequence stars (see, for example, Carkner et al., 1996). The X-ray spectrum can be interpreted as due to bremsstrahlung emission from an optically thin plasma trapped in closed magnetic structures and heated to temperatures of the order of a few 10^7 K, *i.e.* energies of the order of thousands of eV (see Palla, 1996, and references therein). As a matter of fact, Weak T Tauri stars are discovered only in the X-rays, because of their lack of optical signatures.

In the this scenario, the stellar magnetic field disrupts the disk at several stellar radii and accreting material is channelled along magnetic field lines. The infalling gas is at free-fall velocity when it reaches the photosphere, forming a shock where most of the kinetic energy is dissipated by X-ray and far-ultraviolet emission. There, the gas is very optically thick and the radiation is immediately absorbed and re-emitted at longer wavelength and this accounts for the optical and ultraviolet excess continuum emission. Moreover, it is assumed that the stellar magnetic field channels the accretion flow onto a small area of the star's surface, so that the photospheric emission is almost unaffected by the interaction. Also in this kind of models, then, the central star spectrum is modelled with the one of a non-accreting PMS star or with a subgiant star of the same spectral type.

In conclusion, even though the phenomenon is not fully understood yet, it is a well established observational fact that T Tauri stars have a UV excess and emission lines and we can use these spectral peculiarities to distinguish them from the much older field population.

6.7.2 U-band excess

As can be seen in Figure 6.14 on the facing page, not only Classical T Tauri stars do not have the Balmer jump in absorption, but sometimes they even have it in emission. The star in the first panel of the first row, GG Tau, is an excellent example of this: the flux at 3600 Å, *i.e.* blueward of the jump, is 1.6 times that at 4000 Å, *i.e.* redward of it (Gullbring et al., 1998).

As we have already explained, the (U − B) colour is an excellent diagnostic tool to measure the strength of the Balmer jump. In Figure 6.15 on the next page we show the $(U_0 - B_0)$ vs. $(B_0 - I_0)$ plane for the stars with $\overline{\delta}_5 < 0.1$ *mag*. The magnitudes are corrected for extinction, hence the subscript "0", according to the value of $E(B - V)$ derived in the fitting procedure. The colours computed with the model atmospheres of Castelli (1998) are shown as a full line. Its width reflects the change in the WFPC2 filter throughput between decontaminations (see section 4.1.1).

As can be seen in Figure 6.15 the models and the data are in general excellent agreement. Let us notice that it has to be so, since the $E(B-V)$ value was derived by fitting the observed

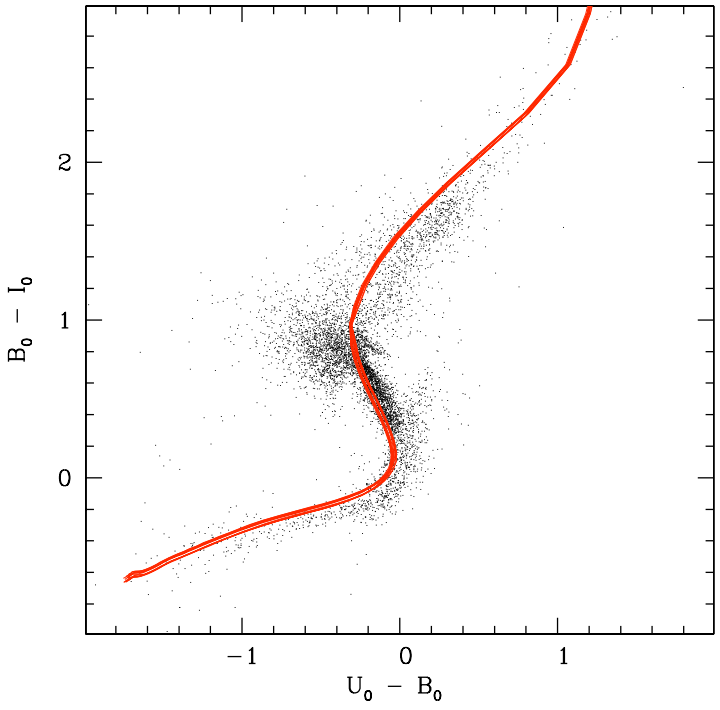

Figure 6.15: $(U_0 - B_0)$ *vs.* $(B_0 - I_0)$ *colour-colour diagram of the stars in the field of SN1987A with* $\overline{\delta}_5 < 0.1$ *mag. The stars were dereddened for the* $E(B-V)$ *value from the 6-band fit. The full line represents the expected locus from the Castelli (1998) model atmospheres.*

magnitudes to these same models. On the other hand, though, a prominent group of stars with $(U_0 - B_0) \lesssim 0.2$ and $(B_0 - I_0) \simeq 0.8$ is clearly offset from the models. They have too blue a $(U_0 - B_0)$ colour given their $(B_0 - I_0)$. Their magnitudes are in the right range for Pre-Main Sequence stars: $23 \gtrsim m_{F555W} \gtrsim 21.5$.

The broadening at $(B_0 - I_0) \simeq 0.8$ cannot be due primarily to photometric errors for two reasons. First of all, the stars in Figure 6.15 are selected to have good photometric accuracy: $\overline{\delta}_5 < 0.1$ *mag*. This threshold corresponds to $\delta(U) \lesssim 0.2$, which is much smaller than the dispersion seen in the colour-colour plane. Secondly, the stars are not scattered symmetrically. This fact, which is clearly visible in Figure 6.15, is even more clearly shown by the histogram in Figure 6.16 on the facing page.

The $(U_0 - B_0)$ distribution of stars with $0.7 \leq (B_0 - I_0) \leq 1.2$ and $\overline{\delta}_5 < 0.1$ is shown as full line in Figure 6.16. If the distribution were due only to photometric errors, one would expect it to be symmetrical with respect to its peak value, which, in turn, should roughly coincide with the theoretical colour. As shown in Figure 6.16, the observed distribution peaks at $(U_0 - B_0) = -0.275$. For comparison, the elbow in the $(U_0 - B_0)$ vs. $(B_0 - I_0)$ plane in the same $(B_0 - I_0)$ range is located at $(U_0 - B_0) = -0.315$. However, the observed distribution is definitely not symmetrical with respect to the peak, but there are many more stars to its left than there are to its right. To quantify the asymmetry, the dashed line shows the reflection about the peak of the histogram of the points redward of it. The hatched area,

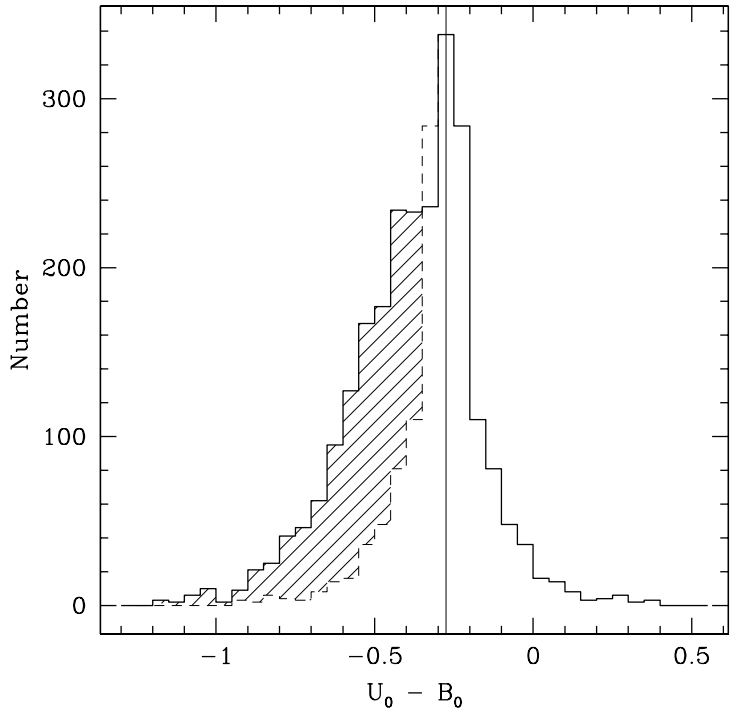

Figure 6.16: $(U_0 - B_0)$ *distribution of the stars with* $0.7 \leq (B_0 - I_0) \leq 1.2$ *and* $\overline{\delta}_5 < 0.1$. *The dashed histogram is the reflection of the portion redder than the peak with respect to the peak itself and the hatched area highlights the asymmetry of the histogram, which is skewed towards blue colours.*

then, highlights the roughly 850 stars with $\overline{\delta}_5 < 0.1$ and U-band excess.

As a final remark, let us notice here that the stars in Figure 6.15 on the preceding page are not the ones we have discussed on page 138 as possible T Tauri candidates. As the reader recalls, those were class IV stars, *i.e.* with $\overline{\delta}_5 > 0.1$, whereas the ones discussed here have $\overline{\delta}_5 < 0.1$.

6.7.3 Hα emission

We can compare the magnitude in the **F675W** [$\overline{\lambda}$=6696 Å, $\Delta\lambda$=866 Å] filter (R) to the one in the **F656N** [$\overline{\lambda}$=6563.7 Å, $\Delta\lambda$=21.4 Å] (Hα) filter to measure the strength of the Hα line for the stars in our field. Normal stars should have the Hα in absorption, as opposed to T Tauri and Be stars[a].

The computation of the equivalent width according to equation (6.1) requires the knowledge of the spectrum in the neighbourhood of the line, but we only have images in a narrow band filter centered on the line and in a wide band one that encompasses it. Since the line is narrow, however, we can substitute the flux $f_c(\lambda)$ of the continuum across it by its mean

[a]A Be star is a star of spectral type B, *i.e.* $10,000 \lesssim T_{eff} \lesssim 30,000$, that shows emission lines. They are interpreted as originating in the extended atmosphere of the star rotating at near break-up speed. For example, Star 3 (Walborn et al., 1993) and, possibly, Star 2 (Scuderi et al., 1996) are Be stars.

value measured in the broad-band (BB) filter:

$$f_c(\lambda) \simeq \overline{f}_c = \frac{\int_{BB} P(\lambda) f(\lambda)\, d\lambda}{\int_{BB} P(\lambda)\, d\lambda}$$

Here, we have implicitly assumed that the flux in the line is negligible compared to the one in the broad band filter. It is trivial to extend the computation to the case in which this is not true.

The equivalent width defined in equation (6.1), thus, becomes:

$$EW\left(\overline{\lambda}\right) \simeq \frac{\int_{BB} P(\lambda)\, d\lambda}{\int_{BB} P(\lambda) f(\lambda)\, d\lambda} \cdot \int_{NB} f(\lambda)\, d\lambda - \int_{NB} d\lambda$$

where the subscript NB indicates the integration over the bandpass of the narrow-band filter. So, using the definition of magnitude of equation (2.1), we can write:

$$EW\left(\overline{\lambda}\right) \simeq 10^{0.4(m_{BB}-m_{NB})} \cdot \frac{\int_{NB} P(\lambda)\, d\lambda}{\int_{NB} P(\lambda) f(\lambda)\, d\lambda} \cdot \int_{NB} f(\lambda)\, d\lambda - \int_{NB} d\lambda$$

where m_{BB} and m_{NB} are the magnitudes in the broad and narrow-band, respectively. Finally, again because the line is narrow:

$$\frac{\int_{NB} P(\lambda) f(\lambda)\, d\lambda}{\int_{NB} P(\lambda)\, d\lambda} \simeq \frac{\int_{NB} f(\lambda)\, d\lambda}{\int_{NB} d\lambda}$$

and so:

$$EW\left(\overline{\lambda}\right) \simeq \left(10^{0.4(m_{BB}-m_{NB})} - 1\right) \cdot \int_{NB} d\lambda \tag{6.2}$$

where the last term is the width of the narrow-band filter. This is the formula we were looking for, linking the magnitudes in the broad and narrow band filters to the equivalent width of the line.

We identify the objects with a statistically meaningful Hα excess by requiring that all of the following conditions are met:

- $\mathbf{H\alpha_{exc} \equiv m_{F675W} - m_{F656N} > 0.3\ mag}$. According to equation (6.2), this corresponds to an Hα emission with equivalent width in excess of 7 Å. This cutoff excludes any contamination by normal stars with chromospheric activity, because they have equivalent widths of less than 3 Å (Frasca and Catalano, 1994);

- $\boldsymbol{m_{\mathrm{F675W}} - m_{\mathrm{F656N}} > 4 \cdot \delta_{exc}}$, where δ_{exc} is the error on the Hα excess:

$$\delta_{exc} = \sqrt{\delta^2_{\mathrm{F675W}} + \delta^2_{\mathrm{F656N}}}$$

  This requirement ensures that the measured excess is statistically significant compared to its photometric error;

- $\mathbf{\log(L/L_\odot) < 2}$ to exclude Be stars.

The most stringent requirement is the second one and it turns out that the minimum excess we consider meaningful is $m_{\mathrm{F675W}} - m_{\mathrm{F656N}} \simeq 0.34$, *i.e.* $EW(\mathrm{H}\alpha) \simeq 8$ Å. With these criteria, we find 499 T Tauri star candidates.

A last word of caution is necessary before we proceed. As can be seen in Figure 6.3 on page 129, the nebular emission is very structured and there are narrow filaments scattered over the entire field. The interstellar medium has line emission, but does not emit in the continuum. As a consequence, the fact that a star is projected on top of one of these structures could mimic a line emission. This is because, as explained in section 4.2.2, for every star the background is measured as the mode of the brightness distribution in an annulus close to it. In the narrow-band image, the filament is much brighter than the surroundings, but it affects a small number of pixels of the annulus. The mode, then, will not be influence by it[a]. On the other hand, the filament emission will contribute significantly to the flux measured in the aperture in which the star's flux is evaluated. In conclusion, the filament contribution to the flux in the photometry aperture is not subtracted properly and the star will appear to have an emission in the line considered. This will happen for all the nebular emission lines, such as Hα and [OIII].

T Tauri stars are observed to have weak [OIII] 5007 Å emission (see, for example, the spectra in Figure 6.14 on page 146). In order to recognize a false T Tauri detection among the stars that appear to have Hα emission, we have rejected those with a strong [OIII] emission, *i.e.* whose $m_{\mathrm{F555W}} - m_{\mathrm{F502N}}$ colour is redder than the mean value at a given m_{F555W} magnitude. The stars with Hα excess are show as round black dots in the left panel of Figure 6.17 on the following page. The rejected stars are the ones above and to the right of the lines. There are 11 of them.

Four of the objects rejected as false T Tauri stars are shown in the right panel in Figure 6.17. As it can be seen, they are really projected on narrow filaments and most of them are barely visible as point-like objects in the Hα image.

At this stage, we are sure that the objects that satisfy the criteria given above have a significant Hα excess an can, thus, be safely regarded as real T Tauri stars. After excluding the stars projected on filaments, we detect 488 of them.

[a] As a matter of fact, this is the reason why we have used the mode, *i.e.* the most probable value, to evaluate the sky level: it is not influenced by a few out-lier points.

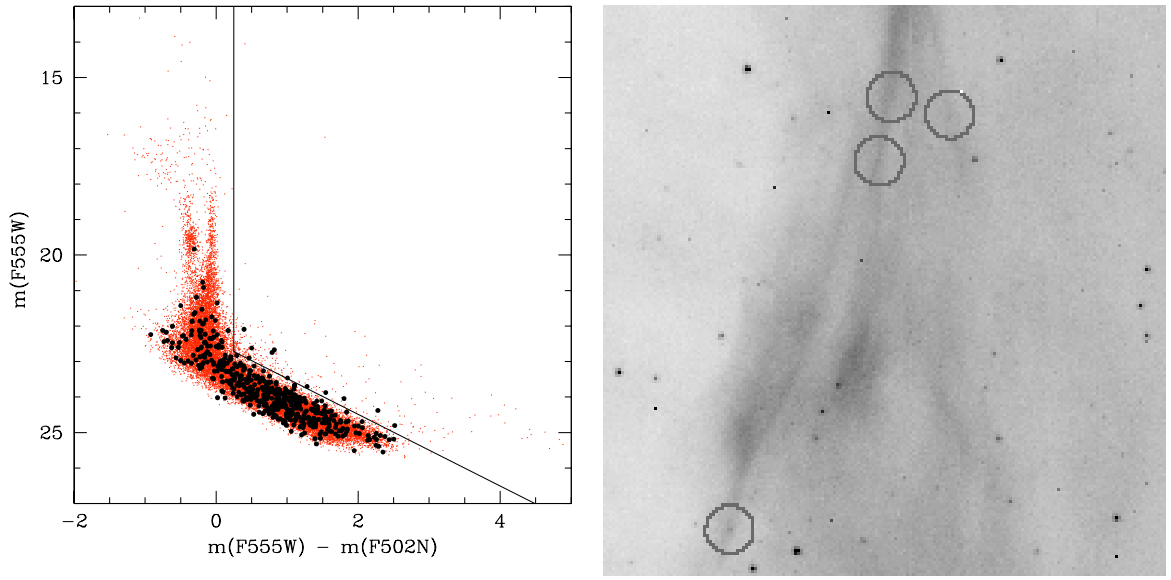

Figure 6.17: *Left panel: observed locus of the stars around SN1987A in the m(F555W) vs. m(F555W)−m(F502N) plane. The objects with* Hα *emission are plotted as black round dots. The lines mark the envelope above and to the right of which stars with* Hα *excess are rejected (see text). Right panel: positions of four of these fake detections on a F656N image.*

We like to stress that our search for T Tauri stars is not complete because of a number of facts. Firstly, we are certainly missing the Weak T Tauri stars, *i.e.* the ones with little or no Hα emission and U-band excess. Moreover, T Tauri stars are known to vary with time and, in particular, the Hα equivalent width is observed to change up to a factor of three or more (see, for example, Fernandez et al., 1995). As a consequence, we may be missing Classical T Tauri stars just because, at the time of a particular observation, the emission was at a low point in its cycle.

Most of the stars selected according to their Hα emission also have U-band excess, as shown in Figure 6.18 on the next page, where we plot in the $(U_0 - B_0)$ vs. $(B_0 - I_0)$ plane the stars with Hα excess according to the criteria of page 150. The stars with Hα emission *and* $\overline{\delta}_5 < 0.1$ are shown as empty squares. The number of stars with U-band excess (roughly 850 with $\overline{\delta}_5 < 0.1$) may be a better approximation to the real number of T Tauri stars, since the selection criterion is less stringent than the one on Hα emission. In any case, it is still a lower limits because we would still miss the Weak T Tauri stars and the time variability may "hide" some of the strong ones.

In the following we will use Hα emission to identify T Tauri stars because, as we have explained earlier, the stars selected in this way can be regarded as positive identifications.

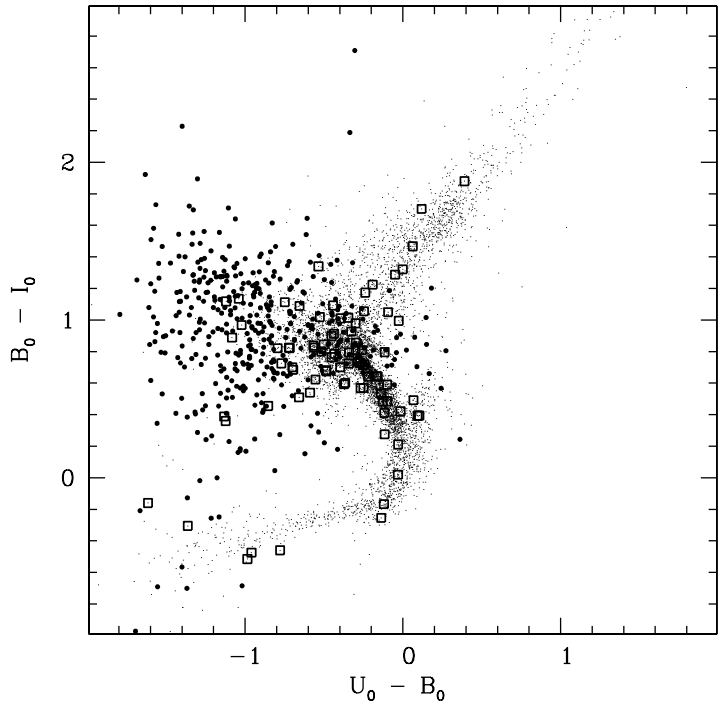

Figure 6.18: *Location in the* $(U_0 - B_0)$ *vs.* $(B_0 - I_0)$ *plane of the stars with* Hα *excess (filled circles). Open squares are stars with* Hα *excess and* $\overline{\delta}_5 < 0.1$. *The dots are all the stars with* $\overline{\delta}_5 < 0.1$.

6.7.4 HR diagram location, masses and ages

The location in the HR diagram of the T Tauri stars identified through their Hα emission as described in the previous section is shown in Figure 6.19 on the following page. As we have seen, the Hα emission is accompanied by a continuum excess shortward of the Balmer jump when compared to the spectrum of "normal" star. In order to determine the temperature and luminosity more reliably, then, we have excluded the F255W and F336W filters when fitting the stars with Hα emission. This reduces their scatter in the HR diagram, thus corroborating the choice.

The comparison of the HR diagram location of the T Tauri stars with the Pre-Main Sequence evolutionary tracks and isochrones computed by Siess et al. (1997), panel (a) and (b) in Figure 6.19, respectively, allows us to estimate the masses and ages of these stars. As it can be seen, the position of the 275 well measured Pre-Main Sequence stars indicates that stars as massive as 2 $M_\odot$ are still in the T Tauri phase and their ages range between 1-2 and 10-20 Myrs.

With an age somewhat in excess of 10 Myrs, the majority of the T Tauri stars in the region surrounding SN1987A are coeval with the most massive stars still present in the field and with the Supernova progenitor. The fact that they do not fall all onto one isochrone further confirms that *the star formation process was not instantaneous, not even for this young generation of stars.* In fact the brightest ones, *i.e.* the ones with smaller photometric errors,

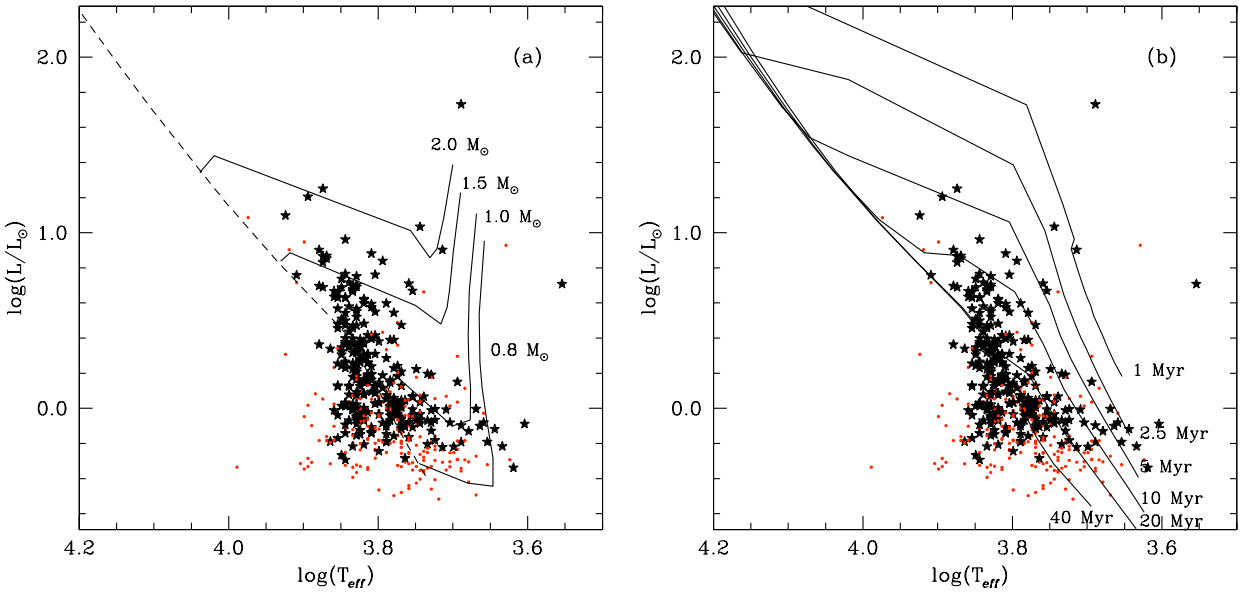

Figure 6.19: *HR diagram for the stars with* Hα *emission in the SN1987A field. Black dots are the 275 stars with* $\delta \log(T_{eff}) < 0.06$. *In Panel (a) we show the Pre-Main Sequence evolutionary tracks of Siess et al. (1997) for the quoted masses, while in panel (b) we show isochrones computed from them. The dashed line in panel (a) is the ZAMS locus computed from the models by Brocato and Castellani (1993) and Cassisi et al. (1994).*

are also the youngest and the age spread cannot be mimicked by the effects of errors. Their ages are compatible with the young age inferred from the presence of the Main Sequence star at $\log(T_{eff}) \simeq 4.7$ and $\log(L/L_{\odot}) \simeq 5.8$ (see Figure 6.11 on page 142).

It is clear, then, that a determination of the IMF is very hard and requires a proper separation of the various stellar generations to avoid systematic biases and errors.

6.8 Spatial distribution

Next point to investigate is what is the *spatial distribution* of the stars of different ages and masses present in the region.

Let us now define three classes, which will be used as tracers of different types of stars:

Young and massive: these are the massive stars coeval with the Supernova progenitor and Star 2. They are selected by requiring $\log(T_{eff}) > 4$ and $\log(L/L_{\odot}) > 3$, corresponding to $\boldsymbol{M \gtrsim 6\ M_{\odot}}$.

Young, not so massive: the low mass stars of the same generation as the Supernova pro-

genitor. As explained in section 6.7, they are still in the Pre-Main Sequence phase and we identify them through their Hα emission according to the criteria described above. For them, $\boldsymbol{M \lesssim 2\ M_\odot}$. Their number is just a lower limit to the real number of T Tauri stars, but their spatial distribution reflects the actual one.

Old Red Giants: we use the members of the Red Giant clump as a tracer of the LMC field population, with ages older than roughly half a billion years. The clump is defined by:

$$3.65 < \log(T_{eff}) < 3.9 \quad \text{and} \quad 1.5 < \log L/L_\odot < 2.1$$

The spatial distributions of massive and Pre-Main Sequence stars belonging to the same generation are shown in Figure 6.20 on the following page. We see that massive stars are strongly concentrated around SN1987A, forming a cluster. It has a diameter of roughly 10 pc, a typical value for LMC clusters (Hodge, 1980, 1988).

The Pre-Main Sequence stars, on the other hand, do not show any strong concentration, but are clearly more numerous west of the Supernova, especially south-west of it, *i.e.* in the lower-right corner in Figure 6.20.

To quantify these statements, we have divided the field in 9 regions, as shown in Figure 6.21 on page 157. The regions are defined as:

Region C (for cluster) is a circle of 20″ of radius centered on the cluster of young stars. At the distance of Supernova 1987A (51.4 kpc, Panagia, 1998), this corresponds to a radius of 5 pc. It includes Star 2 and 3 and the location of the Supernova progenitor;

Regions 1-8 are slices each subtending an angle of 45 degrees from the centre of the central circle. They are numbered counterclockwise.

In order to make meaningful comparisons, we have to refer the observed numbers to some standard area. We have chosen Region C as a reference. It has an effective surface of 1207 square arcseconds, *i.e.* slightly less than the one of a circle of the same radius because the different WFPC2 chips do not overlap perfectly. The areas of the other regions, in units of that of Region C, are listed in Table 6.2 on page 158. The portions of the field not covered with Hα observations were not included in the analysis, since we cannot identify T Tauri stars there.

The number and density of stars, together with their associated Poissonian errors, are given in Table 6.2 on page 158.

An inspection at the star number densities reported in Table 6.2 reveals that there are enormous variations of the proportion of low mass relative to massive stars. For example, their ratio is of the order of unity (1.43) in the central area, while elsewhere it varies between roughly 7 in region 3 and 28 in region 5. There is even a region, the one we have labelled

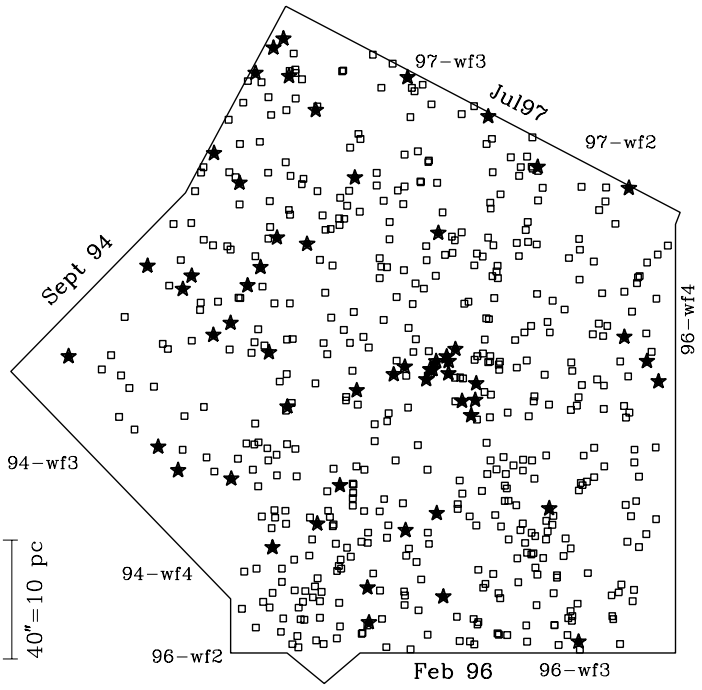

Figure 6.20: *The spatial distributions of massive ($M \gtrsim 6\ M_\odot$; star symbol) and Pre-Main Sequence ($M \lesssim 2\ M_\odot$; open squares) stars belonging to the same young generation are shown. North is up and east to the left. It is clear that the two distributions are remarkably different. The PMS stars are identified through their* Hα *excess as explained in the text. No* Hα *images were taken in the September 1994 observations and the area not covered has been excluded from the analysis.*

with the number 6, which contains a number of T Tauri stars consistent with the average one, but no massive stars at all. In general, there is a lack of massive stars in the south-west corner, where the T Tauri stars are most numerous. Let us further notice that the most massive stars in the field is in region 2, where the density of Pre-Main Sequence stars is well below average.

These differences are highly significant because they greatly exceed the simple Poissonian fluctuations. An experimental check of this fact is provided by similar statistics on the number of stars belonging to the Red Giant clump. They are part of a much older population which, therefore, should be uniformly distributed over the field. And indeed, as seen in Table 6.2, the observed number densities for these stars show fluctuations perfectly in agreement with Poisson statistics.

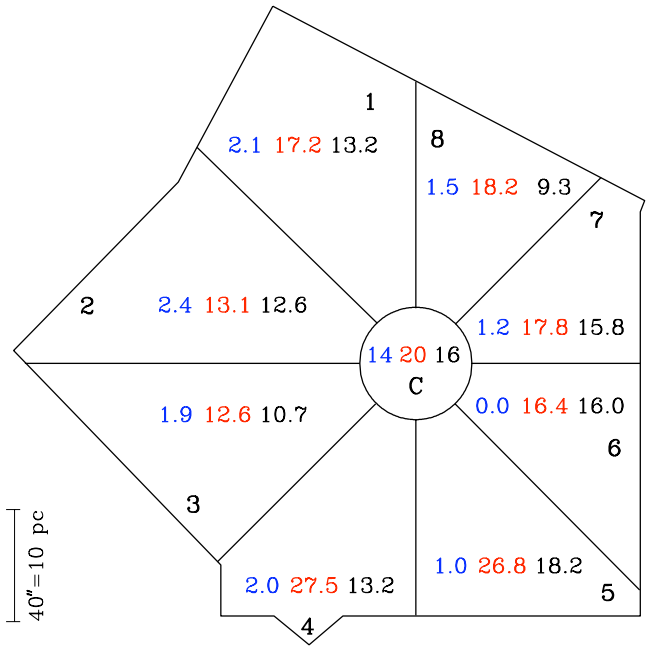

Figure 6.21: *Density of stars in different parts of the field around SN1987A. For every slice the number densities of massive, T Tauri and field Red Giants are given (see text). The numbers are normalized to the area of region "C"*, i.e. *1207 square arcseconds. Full details are given in Table 6.2.*

The almost anti-correlation of spatial distributions of high and low mass stars of a coeval generation indicates that star formation processes for different ranges of stellar masses are rather different and/or require different initial conditions. An important corollary of this result is that the very concept of an Initial Mass Function seems not to have validity in detail, but may rather be the result of a random process, so that it could make sense to talk about an average IMF over a suitably large area, *i.e.* bigger than the central cluster, in which all different star formation processes are concurrently operating.

Let us conclude the discussion on the spatial distribution of stars with a word of caution. Low mass stars in the disk of the Galaxy are observed to have a higher velocity dispersion than the high mass ones (see, for example, Gilmore et al., 1989). A similar occurence in our fields could partly account for the observations.

Region	Area[a]	Massive stars[b]		T Tauri stars[c]		Red Giants[d]	
		Number	Density	Number	Density	Number	Density
C	1.00	14 ± 3.7	14 ± 3.7	20 ± 4.5	20 ± 4.5	16 ± 4	16 ± 4
1	4.70	10 ± 3.2	2.1 ± 0.7	81 ± 9	17.2 ± 1.9	62 ± 7.9	13.2 ± 1.7
2	3.80	9 ± 3	2.4 ± 0.8	50 ± 7.1	13.2 ± 1.9	48 ± 6.9	12.6 ± 1.8
3	3.16	6 ± 2.5	1.9 ± 0.8	40 ± 6.3	12.6 ± 2.0	34 ± 5.8	10.7 ± 1.8
4	3.02	6 ± 2.5	2.0 ± 0.8	83 ± 9.1	27.5 ± 3.0	40 ± 6.3	13.2 ± 2.1
5	3.14	3 ± 1.7	1.0 ± 0.6	84 ± 9.2	26.8 ± 2.9	57 ± 7.6	18.2 ± 2.4
6	2.31	0	0	38 ± 6.2	16.4 ± 2.7	37 ± 6.1	16.0 ± 2.6
7	2.41	3 ± 1.7	1.2 ± 0.7	43 ± 6.6	17.8 ± 2.7	38 ± 6.1	15.8 ± 2.6
8	2.69	4 ± 2	1.5 ± 0.7	49 ± 7	18.2 ± 2.6	25 ± 5	9.3 ± 1.9
Total	26.23	55 ± 7.4	2.1 ± 0.3	488 ± 22.1	18.6 ± 0.8	357 ± 18.9	13.6 ± 0.7

[a] In units of the area of Region C (1207 square arcseconds).
[b] $\log(L/L_\odot) > 3$, $M > 6$ $M_\odot$.
[c] $EW(H\alpha) \gtrsim 8$ Å, $M < 2$ $M_\odot$.
[d] $3.65 < \log(T_{eff}) < 3.9$ and $1.5 < \log L/L_\odot < 2.1$, LMC field population.

Table 6.2: *Actual numbers and densities per unit area of region C (1207 square arcseconds) of the various types of stars in the regions illustrated in Figure 6.21. The quoted errors are the fluctuations due to Poissonian statistics.*

Bibliography

Arnett, W.D., Bahcall, J.N., Kirshner, R.P., and Woosley, S.E. 1989, *ARAA*, **27**, 629.

Basri, G. and Bertout, C. 1989, *ApJ*, **341**, 340.

Bertout, C. 1989, *ARAA*, **27**, 351.

Bertout, C., Basri, G., and Bouvier, J. 1988, *ApJ*, **330**, 350.

Bessel, M.S. 1991, *AA*, **242**, L17.

Bica, E., Claria, J.J., Dottori, H., Santos, J.F.C., and Piatti, A.E. 1996, *ApJS*, **102**, 57.

Brocato, E. and Castellani, V. 1993, *ApJ*, **410**, 99.

Carkner, L., Feigelson, E.D., Koyama, K., Montmerle, T., and Reid, I.N. 1996, *ApJ*, **464**, 286.

Cassisi, S., Castellani, V., and Straniero, O. 1994, *AA*, **282**, 753.

Castellani, V., Chieffi, A., and Straniero, O. 1992, *ApJS*, **78**, 517.

Castelli, F. 1998, In *Views on Distance Indicators*, F. Caputo (Ed.). Società Astronomica Italiana. in press.

Cusumano, G., Maccarone, M.C., Mineo, T., Sacco, B., Massaro, E., Bandiera, R., and Salvati, M. 1998, *AA*, **333**, L55.

D'Antona, F. and Mazzitelli, I. 1994, *ApJS*, **90**, 467.

Duquennoy, A. and Mayor, M. 1991, *AA*, **248**, 485.

Edwards, S., Hartigan, P., Ghandour, L., and Andrulis, C. 1994, *AJ*, **108**, 1056.

Elmegreen, B.G. 1992, In *Star Formation in Stellar Systems*, G. Tenorio-Tagle, M. Prieto, and F. Sánchez (Eds.), III Canary Islands Winter School of Astrophysics, Cambridge. Cambridge University Press, p. 381.

Fernandez, M., Ortiz, E., Eiroa, C., and Miranda, L.F. 1995, *AASS*, **114**, 439.

Forestini, M. 1994, *AA*, **285**, 473.

Frasca, A. and Catalano, S. 1994, *AA*, **284**, 883.

Bibliography for chapter 6

Gallagher, J.S. III, Mould, J.R., De Feijter, E., Holtzman, J., Stappers, B., Watson, A., Trauger, J., Ballester, G. E., Burrows, C.J., Casertano, S., Clarke, J.T., Crisp, D., Griffiths, R.E., Hester, J.J., Hoessel, J., Krist, J., Matthews, L.D., Scowen, P.A., Stapelfeld, K.R., and Westphal, J.A. 1996, *ApJ*, **466**, 732.

Geha, M.C., Holtzman, J.A., Mould, J.R., Gallagher, J.S. III, Watson, A.M., Cole, A.A., Grillmair, C.J., Stapelfeldt, K.R., Ballester, G.E., Burrows, C.J., Clarke, J.T., Crisp, D., Evans, R.W., Griffiths, R.E., Hester, J., Scowen, P.A., Trauger, J.T., and Westphal, J.A. 1998, *AJ*, **115**, 1045.

Gilliland, R.L. 1994, *ApJ*, **435**, L63.

Gilmore, G., Wyse, Rosemary F.G., and Kuijken, K. 1989, *ARAA*, **27**, 555.

Gonzalez, R.A., Allen, R.J., Dirsch, B., Ferguson, H.C., Calzetti, D., and Panagia, N. 1998, *ApJ.* in press.

Gullbring, E., Hartmann, L., Briceno, C., and Calvet, N. 1998, *ApJ*, **492**, 323.

Hearnshaw, J.B. *The analysis of starlight: One hundred and fifty years of astronomical spectroscopy.* Cambridge University Press, Cambridge and New York, 1986.

Herbig, G.H. 1962, *Adv. Astr. Ap*, **1**, 47.

Hodge, P.W. 1980, *AJ*, **85**, 423.

Hodge, P.W. 1988, *PASP*, **100**, 1051.

Hodge, P.W. and Wright, F.W. *The Large Magellanic Cloud.* Smithsonian Press, Washington, 1967.

Jensen, J., Mould, J., and Reid, N. 1988, *ApJS*, **67**, 77.

Lucke, P.B. and Hodge, P.W. 1970, *AJ*, **75**, 171.

Lynden-Bell, D. and Pringle, J. E. 1974, *MNRAS*, **168**, 603.

Madau, P., Ferguson, H.C., Dickinson, M.E., Giavalisco, M., Steidel, C.C., and Fruchter, A. 1996, *MNRAS*, **283**, 1388.

Marshall, F.E., Gotthelf, E.V., Zhang, W., Middleditch, J., and Wang, Q.D. 1998, *ApJ*, **499**, L179.

McCray, R. 1993, *ARAA*, **31**, 175.

Mihalas, D. *Stellar Atmospheres.* W.H. Freeman and Co., San Francisco, 2^{nd} edition, 1978.

Muzerolle, J., Calvet, N., and Hartmann, L. 1998, *ApJ*, **492**, 743.

Olsen, K. and Hodge, P.W. 1996, *Bull. American Astronomical Society*, **188**, abstract 61.13.

Olszewski, E.W., Schommer, R.A., Suntzeff, N.B., and Harris, H.C. 1991, *AJ*, **101**, 515.

Palla, F. 1996, In *The Transparent Universe*, B. Kaldeich-Schürmann (Ed.), ESTEC, Noordwijk. ESA Publications Division, p. 25.

Panagia, N. 1998, In *Views on Distance Indicators*, F. Caputo (Ed.). Società Astronomica Italiana. in press.

Pei, Y.C. and Fall, S.M. 1995, *ApJ*, **454**, 69.

Rousseau, J., Martin, N., Prevot, L., Rebeirot, E., Robin, A., and Brunet, J.P. 1978, *AASS*, **31**, 243.

Sanduleak, N. *Contr. Cerro Tololo Interam. Obs.*, No. 89, 1969.

Schaerer, D., Meynet, G., Maeder, A., and Schaller, G. 1993, *AASS*, **98**, 523.

Schwering, P.B.W. and Israel, F.P. 1991, *AA*, **246**, 231.

Scuderi, S., Panagia, N., Gilmozzi, R., Challis, P.M., and Kirshner, R.P. 1996, *ApJ*, **465**, 956.

Serra-Ricart, M., Aparicio, A., Garrido, L., and Gaitan, V. 1996, *ApJ*, **462**, 221.

Siess, L., Forestini, M., and Dougados, C. 1997, *AA*, **324**, 556.

Van Dyk, S., Hamuy, M., and Mateo, M. 1998, In *SN1987A: Ten Years Later*, M.M. Phillips and N.B. Suntzeff (Eds.). ASP Conference Series. in press.

Voit, M. *HST Data Handbook, Volume I.* STScI, Baltimore, 3^{rd} edition, 1997.

Walborn, N.R. 1991, In *Massive Stars in Starbursts*, C. Leitherer, N.R. Walborn, T.M. Heckman, and C.A. Norman (Eds.), STScI Symposium 5, Cambridge. Cambridge University Press, p. 145.

Walborn, N.R., Mackenty, J.W., Saha, A., White, R.L., and Parker, J.Wn. 1995, *ApJ*, **439**, L47.

Walborn, N.R., Phillips, M.M., Walker, A.R., and Elias, J.H. 1993, *PASP*, **105**, 1240.

Walker, A.R. and Suntzeff, N.B. 1990, *PASP*, **102**, 131.

Bibliography for chapter 6

Wilcots, E., Hodge, P.W., and King, N. 1993, *Bull. American Astronomical Society*, **182**, abstract 49.07.

Williams, R.E., Blacker, B., Dickinson, M., Dixon, W.V.D., Ferguson, H.C., Fruchter, A.S., Giavalisco, M., Gilliland, R.L., Heyer, I., Katsanis, R., Levay, Z., Lucas, R.A., McElroy, D.B., Petro, L., and Postman, M. 1996, *AJ*, **112**, 1335.

Chapter 7

The "parallel" field†

Observing time with *HST* is very valuable and every effort is made to optimize its use. One way to maximize the scientific return of the observatory is to take *parallel observations* with the instruments on board whenever they are not the prime one. Of course, the primary instrument is pointed at a specific object, whereas the other ones fall on random patches of sky: the angular distance from the primary target is fixed by the projection on the plane of the sky of the fields of view of the different instruments, but the position on that circle is determined by the roll angle of the telescope at the time of the observations. This latter quantity is primarily determined by the day of the year in which the observations are made: it increases roughly 1 degree every day. It can only be changed at most by ±15 degrees in case of special requirements on the primary observation, such as the placement of a slit for spectroscopy.

†Based on observations with the NASA/ESA Hubble Space Telescope, obtained at the Space Telescope Science Institute, which is operated by AURA, Inc., under NASA contract NAS 5-26555.

We have taken advantage of this opportunity by observing with WFPC2 while the *Faint Object Spectrograph* (FOS) was being used by the SINS collaboration to take spectra of Supernova 1987A and its rings. The angular separation between FOS and WFPC2 is $8'$ which, at the distance of the Large Magellanic Cloud, correspond to roughly 120 pc. The field of view of these parallel observations, located to the south-east of SN1987A, is shown in Figure 6.2 on page 127.

7.1 Observations and Data Reduction

As it can be seen in Figure 6.1 on page 125, the parallel field is located at the periphery of a group of bright stars (NGC 2050) and a few of them actually fall inside the WFPC2 field of view. The true colour image of the parallel field is shown in Figure 7.1. Its inspection reveals that, indeed, there are bright stars in the field, mainly concentrated in a linear structure across the WF2 and WF3 chips, *i.e.* the bottom of the Figure. A prominent diffuse Hα emission is also visible, thus indicating the presence of ionized interstellar gas.

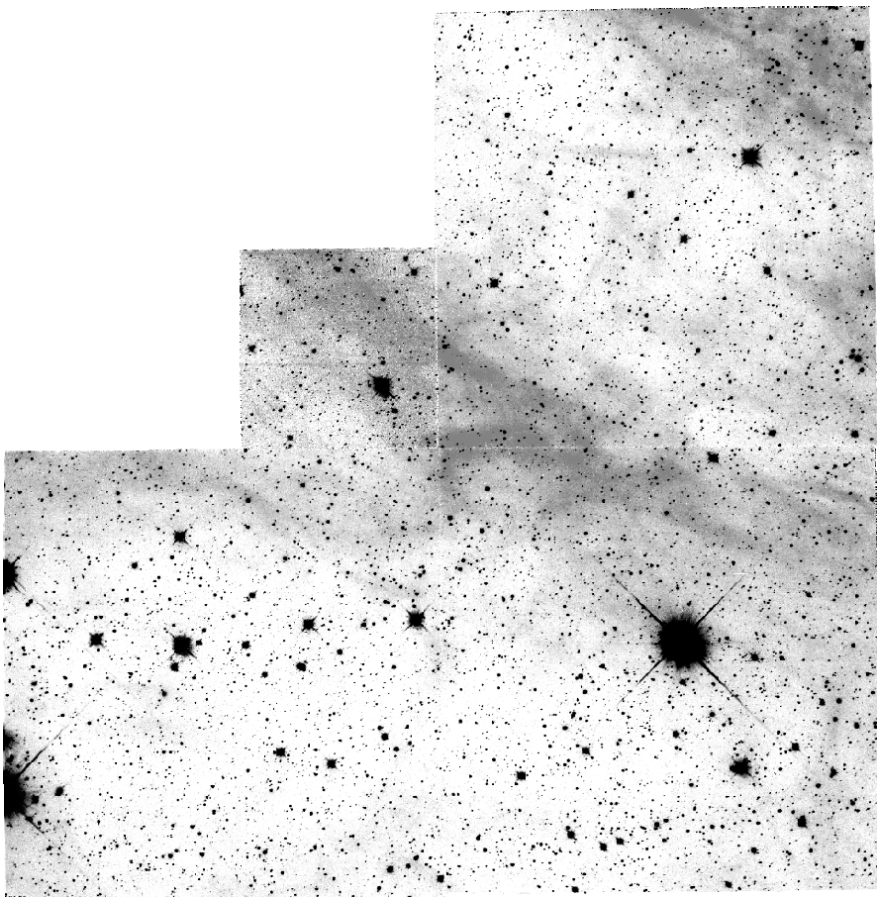

Figure 7.1: *The parallel field for SN1987A as observed in the combination of the B, V and R broad band plus Hα narrow band images. The V band was mimicked as (B+R)/2.*

The log of the parallel observations, taken on January, 1st 1997, is reported in Table 7.1.

Filter Name	Exposure Time (s)	Comments
F300W	600 + 1200	Wide U filter
F450W	50 + 200	Wide B filter
F675W	50 + 200	R filter
F814W	140 + 400	I filter
F656N	1200 + 1200 + 1300	Hα

Table 7.1: *Log of the observations of the control field for SN1987A. They were taken on January, 1st 1997 and the proposal number is 6437.*

The total exposure time available was set by the duration of the primary FOS observations and by the fact that the number of WFPC2 exposure had to be the same, or less, than that of FOS ones, since WFPC2 could not be read while FOS was still acquiring data. In order to improve the signal to noise, we have opted for blue/ultraviolet filters with a wider wavelength width than the ones we have used around SN1987A. The throughput curves of the **F300W** [$\overline{\lambda}$=2943 Å, $\Delta\lambda$=736 Å] and **F450W** [$\overline{\lambda}$=4519 Å, $\Delta\lambda$=957 Å] filters are shown in Figure 3.6 on page 55. The F675W filter was preferred to the F555W in order to compute the Hα equivalent width according to equation 6.2 on page 150.

Short exposures were taken in all the broad band filters to minimize the effect of saturation. If a star is saturated in the long exposure and, hence, in the combined one, we use the short one to measure its flux. There are a few stars belonging to the upper Main Sequence that are saturated in both F300W exposures and, for them, we have used the recipe by Gilliland (1994) on the combined image, as explained in section 4.2.4.

The data were reduced for each chip as described in chapter 4. The only complication was that the long and short exposures in the F300W and F450W filters were shifted by a fraction of a pixel with respect to one another. As a consequence, the two exposures had to be carefully aligned by hand before coadding them to remove the cosmic rays as described in section 4.1.3.

The stars were searched with the ***daofind*** `IRAF` task in the deepest image, in this case the one in the F814W filter. As usual, only the stars with an error in this reference filter smaller than 0.2 *mag* were included in the final list. The errors in the four wide band filters as a function of magnitude are shown in Figure 7.2 on the following page.

Following equation (5.1), we have defined the mean photometric error in four bands ($\overline{\delta}_4$):

$$\overline{\delta}_4 \equiv \sqrt{\frac{\delta^2_{\rm F300W} + \delta^2_{\rm F450W} + \delta^2_{\rm F675W} + \delta^2_{\rm F814W}}{4}} \tag{7.1}$$

As usual, we have used it as an indicator of the general photometric quality of a star on the whole spectrum. Out of a total of 13,098 stars in the final list, 4,108 have $\overline{\delta}_4 < 0.1$ *mag*.

The bright star right at the centre of the WF3 chip is, in fact, so bright that it has hundreds of saturated pixels, even in the short exposures, thus making the photometry

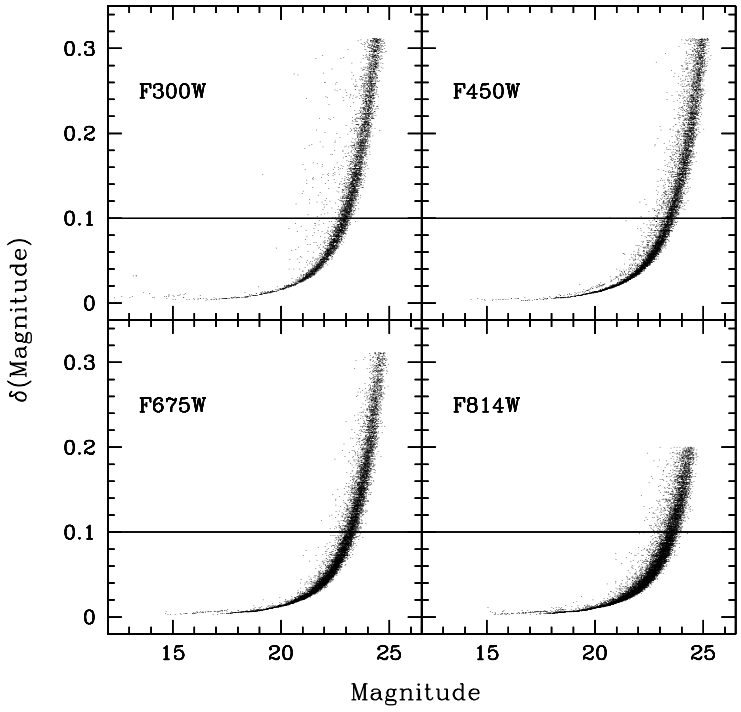

Figure 7.2: *Photometric error as a function of magnitude for the 4 broad band filters in the control field for SN1987A. The 0.1 mag error level is indicated.*

extremely hard and uncertain. By the same token, it is a well known star, Sk -69 211 (Sanduleak, 1969), also known as HDE 269832. Its photometry is available from ground-based studies. Fitzpatrick (1988) classify it as B9Ia supergiant with V= 10.36 and B−V= 0.09. According to Schmidt-Kaler (1982), the intrinsic colour for stars of this spectral type is $(B-V)_0 \simeq 0$ and the temperature is roughly 10,000 K. Once dereddened, the measured V magnitude leads to a luminosity of roughly $3 \cdot 10^5$ $L_\odot$, adopting a bolometric correction of -0.52 *mag*, again taken from Schmidt-Kaler (1982). We can anticipate that, being so bright, it has to be extremely massive and young.

7.2 The Colour-Magnitude diagrams

The Colour-Magnitude diagrams for four combination of filters are shown in Figure 7.3 on the next page. There are 4,108 stars with an overall photometric accuracy better than 10% and the error threshold of $\overline{\delta}_4 < 0.1$ reflects itself as a magnitude threshold at $m_{\rm F814W} \simeq 22.5$ *mag*.

Also in this field, we can identify at least two very different populations in Figure 7.3. The first one is associated with the feature extending up to $m_{\rm F450W} \simeq 15$ and with a colour $m_{\rm F450W} - m_{\rm F814W} \simeq -0.6$ (see panel (c)). Of course, this is a young generation of stars still on or just off the Zero Age Main-Sequence. The other population is identified by the presence of the clump of stars at $m_{\rm F450W} \simeq 20$, $m_{\rm F450W} - m_{\rm F814W} \simeq 1.8$. As repeatedly stated, these

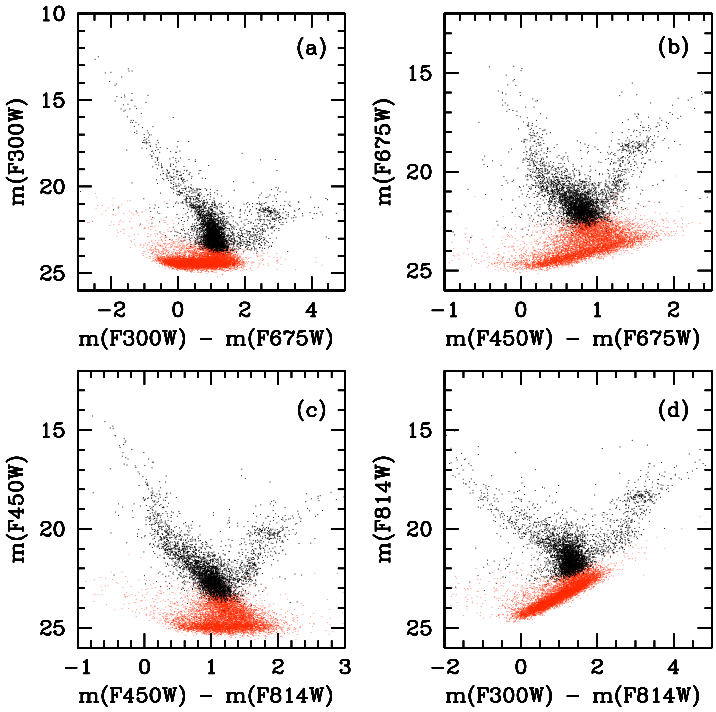

Figure 7.3: *Colour-Magnitude diagrams of the stars in the parallel for four combination of filters. The grey dots are stars with* $\overline{\delta}_4 > 0.1$*, whereas the black ones are the 4,108 stars with* $\overline{\delta}_4 < 0.1$*. Sk -69 211 is not shown.*

stars belong to the Red Giant clump and have ages between half and about two billion years.

Before studying the stellar populations present in the field in full detail, let us evaluate the extinction to them with the fitting technique described in chapter 5.

7.3 Reddening distribution

The *reddening distribution*, as obtained from the fit to the photometric data following the procedures illustrated in section 5.2.4, is shown in Figure 7.4 on the following page. It peaks at $E(\mathrm{B-V})_{\mathrm{LMC}} = 0.13$. For comparison, the value found for the field around SN1987A (see section 6.5) was $E(\mathrm{B-V})_{\mathrm{LMC}} = 0.15$: they are almost identical to one another and also their Full Widths at Half Maximum are comparable.

The mean reddening in the WF3 and WF4 chips is significantly lower than the one in the other two chips, as it can be easily judged from the distribution of points in panel (b) of Figure 7.4. In fact, the narrow peak at $E(\mathrm{B-V}) = 0.07$ is composed mainly of stars in these two chips. Incidentally, the WF2 chip is the closest to the young cluster NGC 2050

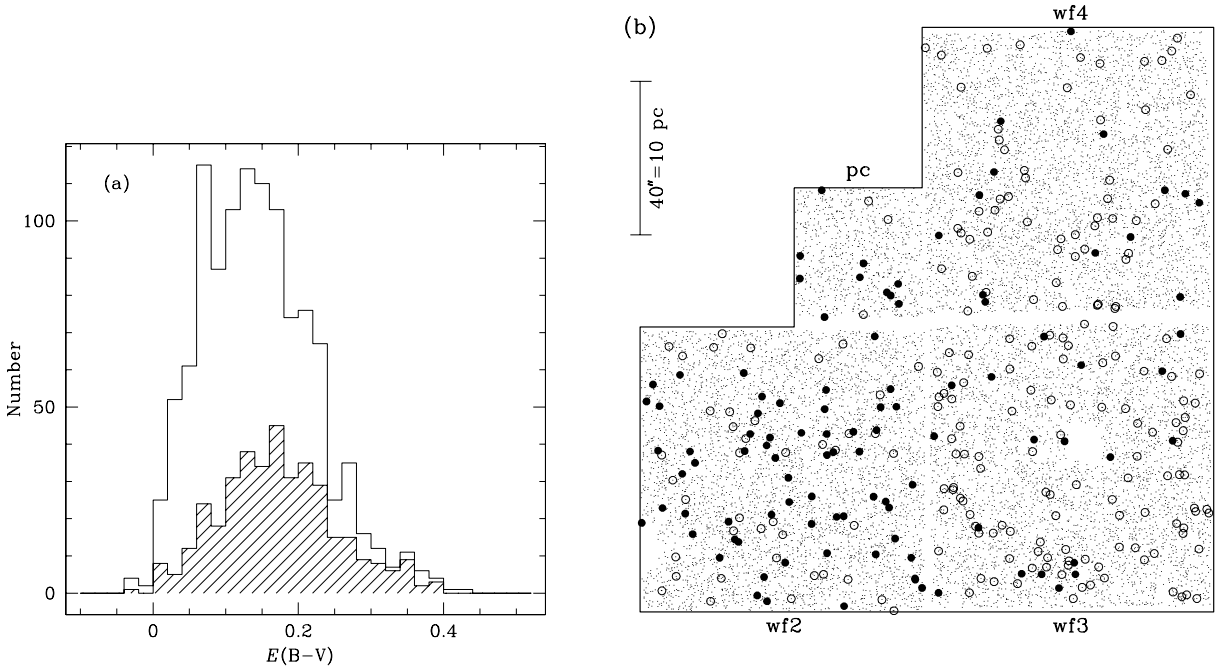

Figure 7.4: *Panel (a): reddening histogram from the stars in the parallel field. Only stars for which* $E(\mathrm{B}-\mathrm{V})$ *was measured individually (class I and II, see section 5.2.4) are used here. The shaded histogram is the reddening distribution in the WF2 chip, almost entirely responsible for the high* $E(\mathrm{B}-\mathrm{V})$ *tail. Panel (b): spatial distribution of stars with high (*$E(\mathrm{B}-\mathrm{V})_{\mathrm{LMC}} > 0.25$*, filled circles) and low (*$E(\mathrm{B}-\mathrm{V})_{\mathrm{LMC}} < 0.05$*, open circles) reddening. In both panels, the reddening is only due to the dust within the LMC. The contribution from the Milky Way is* $E(\mathrm{B}-\mathrm{V})_{\mathrm{MW}} = 0.05$ *for all of the stars.*

(see Figure 6.1 on page 125) and the stars in it are almost entirely responsible for the high $E(\mathrm{B}-\mathrm{V})$ tail visible in panel (a) of Figure 7.4.

7.4 The HR diagram

Once the photometry was performed on the stars in the parallel field, we have applied the fitting procedure described in chapter 5 to recover their intrinsic temperatures and luminosities. A distance of 51.4 kpc (Panagia, 1998) was also used here. The resulting HR diagram is shown in Figure 7.5 on the facing page. The theoretical locus of the Zero Age main Sequence computed by Brocato and Castellani (1993) and Cassisi et al. (1994) is indicated as a full line, while its high mass portion by Schaerer et al. (1993) is shown as a dashed line. This latter one was shifted by 0.019 in the logarithm of the temperature and -0.008 in the logarithm of the luminosity to take into account the different metallicity

with respect to the lower mass models. We have discussed the caveats linked to theoretical evolutionary computations in section 6.6.2.

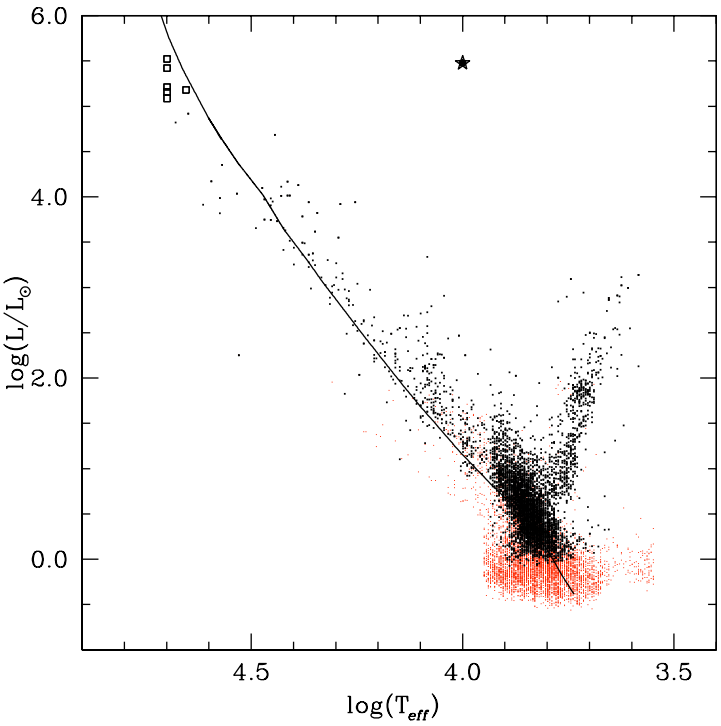

Figure 7.5: *HR diagram for the 13,098 stars in the control field for SN1987A. Black dots are the 4,912 stars with* $\delta \log(T_{eff}) < 0.05$. *The open squares indicate stars for which the F300W magnitude is ill determined because of saturation and, hence, the fit was performed excluding this filter. All of them, but one, require a temperature equal to or larger than 50,000 K, the highest available for the model atmospheres by Castelli (1998). The location of Sk -69 211 according to the photometry by Fitzpatrick (1988) is shown with a star symbol. The theoretical ZAMS by Brocato and Castellani (1993) and Cassisi et al. (1994) is indicated with a full line and its high mass end by Schaerer et al. (1993) as a dashed line.*

As it can be seen, the observed Main Sequence, although still in very good agreement with the theoretical one, is less sharply defined than the one in the field of SN1987A (see Figure 6.8 on page 137). In particular, there are more stars under the theoretical ZAMS. This is mainly due to the different filters we have chosen. Firstly, the F300W filter does not reach wavelengths as short as the F255W one. This causes the flux in the F300W filter to be less sensitive to temperature for hot stars and, hence, for them, the fit is less accurate. Secondly, we did not have enough observing time to obtain both the F555W, or a similar band like F606W, and the F675W filter. We have opted for this latter one to identify stars with Hα emission more accurately. Unfortunately, though, the photometric points are not

spaced in wavelength widely enough. As a consequence, the fit to the cooler stars, the ones that are not well exposed in F300W and F450W bands, has to rely on a short wavelength baseline and, thus, is less precise than it would have been if observations at roughly 5000 Å had been available. This also results in more stars below the Main Sequence (roughly 600 out of a total of nearly 13,100) when compared to the main field (roughly 200 out of almost 22,000). As we have discussed in section 6.6 on page 136, these red and faint stars were fitted excluding the flux in the F300W filter. *In general, however, the data are of excellent quality.*

There is a group of bright stars ($\log(T_{eff}) \gtrsim 4$ and $\log(L/L_{\odot}) \gtrsim 1$) that lie below the $Z = 0.3 \cdot Z_{\odot}$ Main Sequence. They could indicate the presence of a generation of stars with slightly lower metallicity, of the order of $Z_{\odot}/5$, than the majority of stars. The problems linked to the filters we have used and that we have just discussed, however, do not allow any stronger conclusion.

In section 6.6 we have examined the presence and influence of *binary and multiple systems* in the field around SN1987A. By repeating the crude computation outlined there, we find that these system constitute at least 10% of the Main Sequence stars also in the parallel field. Again, this is only a lower limits because we only identify the objects whose spectra are significantly different from those of single stars.

7.4.1 Masses and ages

The comparison of the observed stars with selected evolutionary tracks and isochrones by Brocato and Castellani (1993) and Cassisi et al. (1994) (full line) and Schaerer et al. (1993) (dashed line) is shown in Figure 7.6 on the next page. As discussed previously, these latter ones are shifted to match the metallicity of $Z = 0.3 \cdot Z_{\odot}$.

As it can be seen in Figure 7.6, not only there are *young* and *massive* stars also in the control field, but quite a few of them are brighter than most of the ones in the SN1987A surroundings. In particular, according to the models by Schaerer et al. (1993), the most massive stars in the field, shown as open squares in Figure 7.6, have masses well in excess of 40 $M_{\odot}$ and, as a consequence, are definitely younger than 5 Myr. Unfortunately, though, they are severely affected by saturation in both F300W exposure and they were fitted excluding the flux in this filter. As we have seen in chapter 5, lacking the UV information, the fit is quite uncertain. In any case, all of them, but one, seem to require temperatures higher than 50,000 K, the highest available for the Castelli (1998) models. In conclusion, they are certainly very massive and, hence, young, even more so than indicated by their position in the HR diagrams of Figure 7.6.

Again using the evolutionary computations by Schaerer et al. (1993), we can infer the mass and age of Sk -69 211. Its mass is of roughly 27 $M_{\odot}$, almost twice as much than the most massive stars belonging to the SN1987A cluster. It falls perfectly on a 7 Myr isochrone, as indicated by the dashed line in Figure 7.6. One may suspect it to be a foreground star,

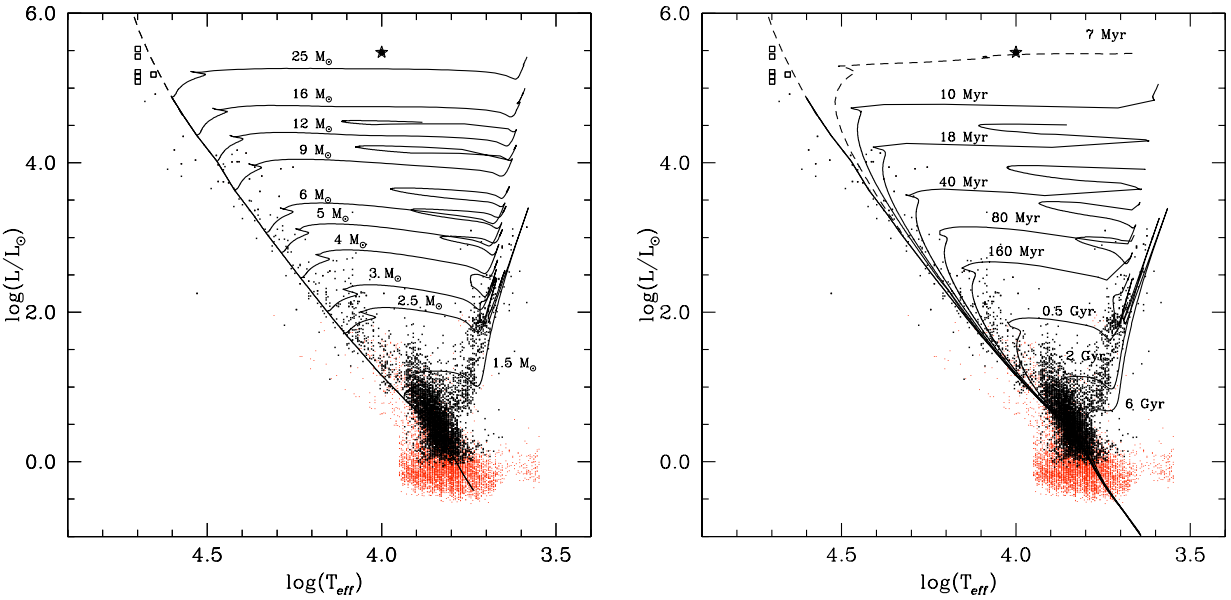

Figure 7.6: *Same as Figure 7.5, except that the stars in the spur under the Main Sequence were omitted for clarity. Selected evolutionary tracks and isochrones for Z= 0.3·Z⊙ by Brocato and Castellani (1993) and Cassisi et al. (1994) are overlaid to the data in the left and rigth panel, respectively (full line). The ZAMS computed from these same models is also indicated as a full line. The 7 Myr isochrone in the right panel and the dashed ZAMS in both panels were computed by Schaerer et al. (1993).*

but the possibility is ruled out by noticing that its radial velocity[a] is of +272 km s^{-1}, *i.e.* an appropriate value for that region of the LMC (Ardeberg et al., 1972).

Also in the case of the parallel field, there is no single age that can explain all of the observations. On the contrary, many generations of stars with age ranging from a few million to a few billion years are required. Again, the stars at intermediate luminosities and temperatures ($\log(L/L_\odot) \simeq 3$ and $\log(T_{eff}) \simeq 3.7$) imply ages of 80-160 Myr. It is interesting to notice that, while the age of Sk -69 211 is certainly younger than that of any of the stars still present close to SN1987A, massive stars *coeval* with the Supernova progenitor seem to be absent from the parallel field.

[a]The radial velocity is the velocity along the line of sight to an object. With the usual sign convention, a positive velocity indicates that the object is receding from, *i.e.* its spectrum is redshifted.

7.5 Pre-Main Sequence stars

Let us now consider the low-mass stars belonging to the young generation identified by the presence of the most massive stars in the field. By applying the selection criteria on Hα emission as described on page 150, we identify 175 stars with significant excess. Also, we fit the observed magnitudes with the model spectra by Castelli (1998) excluding the F300W filter, which may be appreciably affected by excess UV emission. The location in the HR diagram of the stars in the parallel field with Hα excess is shown in Figure 7.7. As it was the case with the PMS stars in the field of SN1987A, the fit excluding the filter blueward of the Balmer jump results in smaller scatter in the temperature-luminosity plane.

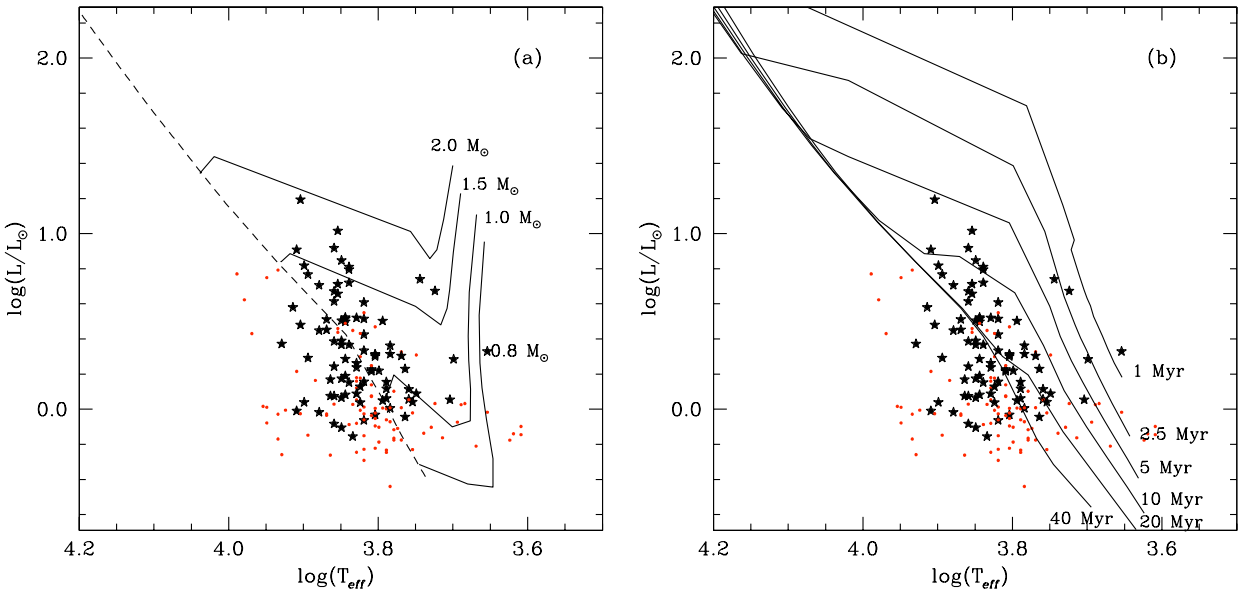

Figure 7.7: *HR diagram for the stars with* Hα *emission in the SN1987A parallel field. Black dots are the 85 stars with* $\delta \log(T_{eff}) < 0.06$. *In Panel (a) we show the Pre-Main Sequence evolutionary tracks of Siess et al. (1997) for the quoted masses, while in panel (b) we show isochrones computed from them. The dashed line in panel (a) is the ZAMS locus computed from the models by Brocato and Castellani (1993) and Cassisi et al. (1994).*

The comparison with Pre-Main Sequence isochrones by Siess et al. (1997) shown in panel (b) of Figure 7.7 confirms the presence of a generation of young stars, mainly with ages in excess of 10 Myr. However, a considerable age spread is also evident from the location of T Tauri stars in the HR diagram, in agreement with what the upper Main Sequence indicates. Their masses can be roughly inferred from the comparison to the evolutionary tracks, as shown in panel (a) of the same Figure, and full discussion will be given in chapter 8.

7.6 Spatial distribution

Let us now investigate the spatial distribution of the stars in the parallel field, as we did in section 6.8 for the ones in neighbourhood of Supernova 1987A. As in the case of the "main" field, we will consider the three classes of stars as defined on page 154. This time the geometry of the portion of sky covered by the observations is much simpler. Its shape is just the field of view of WFPC2 (see Figure 3.1 on page 46). Moreover, there is no obvious association of stars like the cluster of young stars close to the Supernova. For these reasons, we have divided the field in just four regions, coinciding with the four chips of the camera.

The spatial distributions of massive and Pre-Main Sequence stars belonging to the same generation are shown in Figure 7.8 superimposed on all measured stars. The hole in the middle of the WF3 chip is the area affected by the bleeding of electrons caused by the extremely high flux of Sk -69 211. The non-perfect overlap of the chips is also evident.

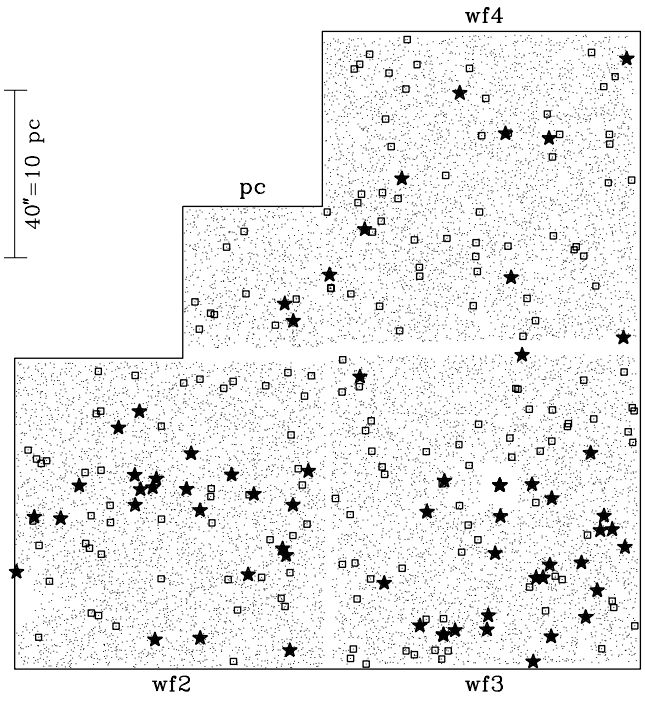

Figure 7.8: *The spatial distributions of massive ($M \gtrsim 6\ M_\odot$; star symbol) and Pre-Main Sequence ($M \lesssim 2\ M_\odot$; open squares) stars belonging to the same young generation are shown superimposed on all measured stars (dots). It is clear that the density of hot, massive stars is higher in WF2 and WF3 than elsewhere.*

The number and densities of the young stars highlighted in Figure 7.8, together with the ones of the stars belonging to the Red Giant clump, are reported in Table 7.2.

There is a clear deficiency of *massive stars* in the PC and WF4 chips, while most of the massive stars are confined to the WF2 and WF3 chips, *i.e.* in the direction of the bright stars we have already noticed in Figure 6.2. It is certainly worth noting that *total* number of these stars is higher in this field than it is in the one around SN1987A. Since the area covered

Chip	Area[a]	Massive stars[b]		T Tauri stars[c]		Red Giants[d]	
		Number	Density	Number	Density	Number	Density
PC	0.93	2 ± 1.4	2.2 ± 1.5	9 ± 3	9.7 ± 3.2	25 ± 5	26.9 ± 5.4
WF2	4.48	24 ± 4.9	5.4 ± 1.1	51 ± 7.1	11.4 ± 1.6	63 ± 7.9	14.1 ± 1.8
WF3	4.49	29 ± 5.4	6.5 ± 1.2	61 ± 7.8	13.6 ± 1.8	61 ± 7.8	13.6 ± 1.7
WF4	4.54	9 ± 3	2.0 ± 0.7	54 ± 7.4	11.9 ± 1.6	51 ± 7.1	11.2 ± 1.6
Total	14.44	64 ± 8	4.4 ± 0.6	175 ± 13.2	12.1 ± 0.9	200 ± 14.1	13.9 ± 1.0

[a] In units of the area of Region C defined on page 154 (1207 square arcseconds).
[b] $\log(L/L_\odot) > 3$, $M > 6\ M_\odot$.
[c] $EW(H\alpha) \gtrsim 8$ Å, $M < 2\ M_\odot$.
[d] $3.65 < \log(T_{eff}) < 3.9$ and $1.5 < \log L/L_\odot < 2.1$, LMC field population.

Table 7.2: *Actual numbers and densities per unit area of region C defined on page 154 (1207 square arcseconds) of the various types of stars in the four chips of the parallel observations. The quoted errors are the fluctuations due to Poissonian statistics.*

here is 1.8 time smaller than the other one, the *overall density* of massive stars is more than twice as high here than in the vicinities of the Supernova. An inspection of Figure 6.2 shows that the distribution of stars is, indeed, very patchy throughout the entire region and that the parallel field happens to be in one of the densest spots. Had the SINS FOS observations be taken a few days later, the WFPC2 field of view would have fallen right on top of group of bright stars just east of the WF2 chip and the number of massive stars would have been even higher.

The distribution of *young low mass stars* belonging to the same generation as the massive ones is remarkably constant throughout the field. As a consequence, the ratio of T Tauri to massive stars is higher where the density of massive stars is lower. This is the same trend we have found in the field of SN1987A. Moreover, the overall density of low mass PMS stars in the parallel field is significantly smaller (roughly two thirds) than the one in the "main" field. This confirms the existence of a sort of anti-correlation between high and low mass young stars. Let us stress once again that the number of T Tauri stars we identify is only a lower limit to their total number. The trends in the two fields, however, are preserved.

The density of *Red Giant stars* is perfectly constant in the three WF chips. It is higher in the PC chip, but this is consistent with a 2σ fluctuation. The density of Red Clump Giants in the parallel field is virtually identical to the value measured around SN1987A. This further confirms that the older LMC population is uniformly distributed, at least on the scales probed by our observations.

Bibliography

Ardeberg, A., Brunet, J.P., Maurice, E., and Prevot, L. 1972, *AASS*, **6**, 249.

Brocato, E. and Castellani, V. 1993, *ApJ*, **410**, 99.

Cassisi, S., Castellani, V., and Straniero, O. 1994, *AA*, **282**, 753.

Castelli, F. 1998, In *Views on Distance Indicators*, F. Caputo (Ed.). Società Astronomica Italiana. in press.

Fitzpatrick, E.L. 1988, *ApJ*, **335**, 703.

Gilliland, R.L. 1994, *ApJ*, **435**, L63.

Panagia, N. 1998, In *Views on Distance Indicators*, F. Caputo (Ed.). Società Astronomica Italiana. in press.

Sanduleak, N. *Contr. Cerro Tololo Interam. Obs.*, No. 89, 1969.

Schaerer, D., Meynet, G., Maeder, A., and Schaller, G. 1993, *AASS*, **98**, 523.

Schmidt-Kaler, T. 1982, In *Landolt-Bornstein: Numerical Data and Functional Relationships in Science and Technology*, volume 2b, Berlin. Springer-Verlag, p. 297.

Siess, L., Forestini, M., and Dougados, C. 1997, *AA*, **324**, 556.

Chapter 8

The resulting Star Formation History and constraints on the Initial Mass Function

As we have seen in the last two chapters, the observations both in the neighbourhood of SN1987A and in the parallel field cannot be explained in terms of a single generation of stars. Many episodes of star formation must have followed one another resulting in a complicated superposition of stars of different ages. We are now ready to undertake the final step and determine the *star formation history* of our fields. Let us recall here that the star formation history, besides being interesting in itself, is also a key ingredient in computing the Initial Mass Function (IMF) (see section 2.2.1 and, in particular, equation (2.34) on page 24).

The problem of interpreting the complex interplay of the effects that determine the appearance of the HR diagram in regions in which the star formation process is extended in time is often addressed in the literature through Monte Carlo simulations. The basic idea is to create a model HR diagram[a] by randomly extracting luminosity and temperature (magnitude and colour) from theoretical evolutionary tracks using an assumed IMF and a star formation history. The random extraction of stars along the evolutionary tracks is meant to mimic the stochastic nature of the star formation process. The simulations attempt to fully recreate the circumstances of the observed data by including the spread due to photometric errors and incompleteness of the data as a function of magnitude. This basic idea was first applied to galaxies by Ferraro et al. (1989) and a full description of the method can be found in Tosi et al. (1991).

Once a synthetic model is constructed, it has to be compared to the actual observed data to assess its validity. The comparison between models and observations is done by counting the stars in selected regions of the Colour-Magnitude diagram. Mighell and Butcher (1992), for example, use the luminosity function of Main Sequence stars, whereas Bertelli et al. (1992) define three stellar number ratios, each sensitive to different parameters in the star formation history. Both these approaches select a sub-sample of the data and, hence, do not use the whole information available. Tolstoy and Saha (1996) have recently developed a method in which all of the stars in the Colour-Magnitude diagram are used in computing the likelihood that a given model will result in the observational set. Usually, various models are constructed and tested as explained above and the one providing the best match to the data is taken as the one representing the actual star formation history that took place in the region considered.

The problem, however, is that in such experiments it is virtually impossible to construct the set of *all* possible models, since, if nothing else, it would be prohibitively large. In practice, then, only a small fraction of the parameter space and/or subsample of the family of models can ever be considered. Therefore, we have opted for a different approach, dubbed **the sieve**, in which the star's position in the HR diagram is used directly to infer its evolutionary status, *i.e.* age and mass. This method is described in the next section.

8.1 The sieve

The basic idea is to compare the position of an individual star in the HR diagram with evolutionary tracks to infer its mass and age, *i.e.* the time it took to reach that location in the diagram. The advantage of this approach is that we do not impose any preconceived ideas on the data, such as, for example, that the mass function should have a certain functional

[a] In fact, Colour-Magnitude diagrams are more commonly used, since very often the available data are limited only to two photometric bands. See chapter 5 for a discussion on the bands needed to recover the whole luminosity and temperature information.

form.

As customary in this Thesis, we have adopted the post Main Sequence theoretical evolutionary models by Brocato and Castellani (1993) and Cassisi et al. (1994) for masses up to 25 $M_\odot$ and those by Schaerer et al. (1993) above this limit. We model the Pre-Main Sequence evolution with the tracks by Siess et al. (1997).

To enhance the mass coverage, we interpolate among the input tracks to build a grid with a logarithmic step of 0.025. A word of caution is necessary here. The time steps used to compute evolutionary tracks depend on the evolutionary phase the star is in. For example, during the Main Sequence phase the evolution is very slow and a long time step can be used. On the contrary, along the giant branch the evolution is fast and, accordingly, the time step has to be short. As a consequence, the output of evolutionary computations for different masses cannot be directly interpolated to compute the evolution of an intermediate mass. Instead, the interpolation is done by first identifying, on each track, a few important evolutionary phases. These usually include, for example, the exhaustion of hydrogen in the star's core, the beginning of the giant branch, the onset of the central helium burning etc. Each track, as computed by the evolutionary code is, then, interpolated in time to contain the same number of time steps between these marks. Once this is done, the interpolation in mass is trivial because the n^{th} point along the track of a given mass corresponds to the same evolutionary phase as the n^{th} point along any other track.

Once we have assigned an age to every star, we can compute the number of stars $n(t)dt$ that were born in the time interval $(t, t + dt)$ and that are *still present in the field*. In the following, we will set the origin of times at the present epoch and, hence, the time t is the *look-back time*. The maximum look-back time (T) one can reach is determined by the longest-lived stars, *i.e.* the ones with the smallest masses, one can detect. Our observations allow us to safely reach $T = 5$ Gyr, beyond which the data begin to be heavily affected by incompleteness.

In general, $n(t)dt$ does not represent the number of all the stars that were formed in the interval $(t, t + dt)$ because a star of mass M has a finite lifetime $\tau(M)$. So, among the stars born at a time t, the only ones we can observe now are the ones for which $\tau(M) \geq t$. Since we are going to use stars in every region of the HR diagram, $\tau(M)$ is the *total* lifetime of a star of mass M and not only the Main Sequence one. In order to estimate the number of stars that have evolved, we would have to know the IMF, which, of course, is not given *a priori*. Therefore, we will estimate their number by initially assuming a Salpeter (1955) IMF, *i.e.* a power-law function with an logarithmic slope $\Gamma = -1.35$. We can, then, compute the *birthrate* $B(t)$, so that $B(t)dt$ is the *total number* of stars formed between t and $t + dt$. Finally, we can determine an improved estimate of the IMF using equation (8.1). We will, then, iterate the process by using this latter quantity to estimate the number of stars that have already evolved, compute the new birthrate and so on until convergence is reached. At that point, *we will have determined both the star formation history and the Initial Mass Function in a self consistent way.*

Before describing the sieve in full detail, let us rewrite here equation (2.34) that links Present Day Mass Function $\xi_{PD}(\log M)$, Initial Mass Function $\xi(\log M)$ and birthrate $B(t)$. This equation was derived in section 2.2.1 and let us just recall here that it is only valid if the IMF is time independent, *i.e.* if the Creation Function is separable.

$$\xi(\log M) = \begin{cases} \xi_{PD}(\log M) \cdot \frac{\int_0^T B(t)\,dt}{\int_0^{\tau(M)} B(t)\,dt} & \text{if} \quad \tau(M) < T \\ \\ \xi_{PD}(\log M) & \text{if} \quad \tau(M) \geqslant T \end{cases} \tag{8.1}$$

The notation is the same as in chapter 2: ξ is the Initial Mass Function, ξ_{PD} is the Present Day Mass Function (PDMF), which is *observable*, $B(t)$ is the birthrate at time t, T is the maximum look-back time and $\tau(M)$ is the total lifetime of a star of mass M.

8.1.1 The grid

First of all, we have to assign masses and ages to every location of the HR diagram. The procedure is as follows:

1. We define a grid in luminosity and temperature in the HR diagram. The cells are evenly spaced in the HR diagram, *i.e.* the step is logarithmic both in temperature and luminosity. The sizes of the cells are chosen to be comparable to the typical observational errors. Taking them bigger than the errors would degrade the information and, obviously, taking them smaller would not increase the resolution.

2. Given the evolutionary model of a star of a certain mass, we identify all the cells that the star crosses throughout its evolution. For each of these cells, we compute the crossing time (difference between the times of exit and entrance) and its characteristic age (the average of exit and entrance times). In general, the evolutionary path is not monotonic in luminosity and temperature, and a track may cross a given cell more than once at different times.

3. Step 2 is repeated for all the tracks resulting from the interpolation mentioned above. Of course, stars of different masses can cross the same cell.

The results of the process are four matrices containing all the relevant information: mass ($\boldsymbol{M[i,j,k]}$), age ($\boldsymbol{t[i,j,k]}$), time of permanence in a given cell ($\boldsymbol{\delta t[i,j,k]}$) and multiplicity, *i.e.* number of possible solutions, $\boldsymbol{N[i,j]}$. The two indices $[i,j]$ identify the cell in the HR diagram in temperature and luminosity, respectively. As we have explained, a given cell $[i,j]$ may not contain a single mass at a single age, but the same mass may cross it more than once and, also, it may contain different masses. The index k in the matrices introduced above keeps track of the multiplicity of the solutions. If cell $[i,j]$ does not intersect any track then $N[i,j] = 0$, otherwise k runs from 1 to $N[i,j]$.

All the information from the evolutionary tracks is now contained in the four matrices $M[i,j,k]$, $t[i,j,k]$, $\delta t[i,j,k]$ and $N[i,j]$. The step of the grid and of the interpolation in mass among evolutionary tracks were chosen so that the entire allowed portion of the HR diagram is covered.

Given the k-th solution for a star that occupies the cell with indices $[i_\star, j_\star]$, the shorter $\delta t[i_\star, j_\star, k]$, the more precise is our knowledge of its age $t[i_\star, j_\star, k]$. In general terms, we have no information as to which is the *real* age in the $t[i_\star, j_\star, k] \pm \delta t[i_\star, j_\star, k]/2$ interval of any given star that falls in the box. Whenever δt is larger than some value δt_{max}, then, instead of computing the age as the mean of the entrance and exit times in the cell, we assign to the star all possible ages, within the allowed interval, with the same probability. We have set $\delta t_{max} = 30$ Myr and varying it within a reasonable interval does not affect the results at all.

The Main Sequence is by far the longest evolutionary phase, occupying roughly 90% of the entire life of a star and the Main Sequence lifetime of a star is roughly proportional to the -2.5 power of its mass (see Table 2.2 on page 13 for the Main Sequence lifetimes as a function of mass from the evolutionary computations by Schaller et al. (1992)). As a consequence, we can expect the occurrence mentioned above to be more important for low mass stars. Moreover, since they did not have time to evolve off the Main Sequence, low mass stars of all the generations which have one and the same mass will occupy the same cell in the grid.

8.1.2 The weights

Given an observed star, we compute the cell $[i_\star, j_\star]$ of the grid to which it belongs and, consequently, we know all the possible masses and ages it may have. There are three possible cases:

- $N[i_\star, j_\star] = 0$, *i.e.* no solutions: the star falls in an "impossible" location of the HR diagram, in the sense that no evolutionary track ever reaches it. If the star is in the lower part of the HR diagram, $\log(\mathrm{L}/\mathrm{L}_\odot) \lesssim 0$ (see, for example, Figure 6.10 on page 141), the error is too big to allow us to draw any conclusion. For this reason, we will limit our analysis to luminosities higher than this value, corresponding to a mass greater than roughly 1.2 $\mathrm{M}_\odot$.

  There are a few *bright* stars to the left of the upper Main Sequence for which we can estimate the mass. Since the error in temperature is always much larger than the one in radius, they are displaced along a line of constant radius from their real location. As a consequence, we move them back to the Main Sequence along this vector. We disregard those for which the intersection is more than $2 \cdot \sigma$ away from the measured value.

- $N[i_\star, j_\star] = 1$: the solution is unique and there is no ambiguity: the mass of the star is $M[i_\star, j_\star, 1]$ and its age $t[i_\star, j_\star, 1]$.

- $N[i_\star, j_\star] > 1$: more than one track crosses the cell to which the star belongs and/or a certain mass crosses it at different times. All the different solutions are *a priori* acceptable and there is no reason to disregard any of them. As zero-th order approximation, we assign to the k-th solution a *weight* $W_\star(k)$ proportional to the time $\delta t[i_\star, j_\star, k]$ it spends in the cell:

$$W_{\star,0}(k) = \frac{\delta t[i_\star, j_\star, k]}{\sum_{i=1}^{N[i_\star, j_\star]} \delta t[i_\star, j_\star, i]} \tag{8.2}$$

the normalization in equation (8.2) is chosen so that:

$$\sum_{k=1}^{N[i_\star, j_\star]} W_{\star,0}(k) = 1$$

The weight hereby defined gives the probability that the star we are considering has mass $M[i_\star, j_\star, k]$ and age $t[i_\star, j_\star, k]$ as opposed to the other possible solutions that populate the cell $[i_\star, j_\star]$. Of course, if the solution for a give star is unique, *i.e.* $N[i_\star, j_\star] = 1$, k can only be 1 and $W_{\star,1}(k) = 1$.

It is very important to realize that this *choice of the weights corresponds to assuming a constant birthrate*. This is only the zero-th order approximation and from here it is necessary to iterate, to take into account a more realistic star formation history.

8.1.3 Refining the weights

At this stage, we have assigned ages to all the stars and, in case of multiple solutions, also a weight to each possibility so that each of them can be accounted for properly. Let us introduce $n_0(t)$, so that $n_0(t)dt$ is the number of stars whose age is in the interval $(t, t + dt)$ and that are still present in the field. $n_0(t)$ is computed by counting the stars in each time bin, each solution being weighed with the appropriate weight from equation (8.2). The location in the HR diagram of stars in the field of SN1987A in four ranges of ages is shown in Figure 8.1 on the facing page. As expected, as the age of the population increases going from panel (a) to panel (d), the brightest stars present become fainter and the Red Giant Branch is more and more populated.

Given $n_0(t)$, we can estimate the rate of stars formed at time t by assuming, for the moment, that the IMF is the Salpeter (1955) one, *i.e.* a power law of index -2.35:

$$B_0(t) = n_0(t) \cdot \frac{M_i^{-1.35}}{M_i^{-1.35} - M_m^{-1.35}} \tag{8.3}$$

where M_i is the observational lower mass cutoff and M_m is such that $\tau(M_m) = t$.

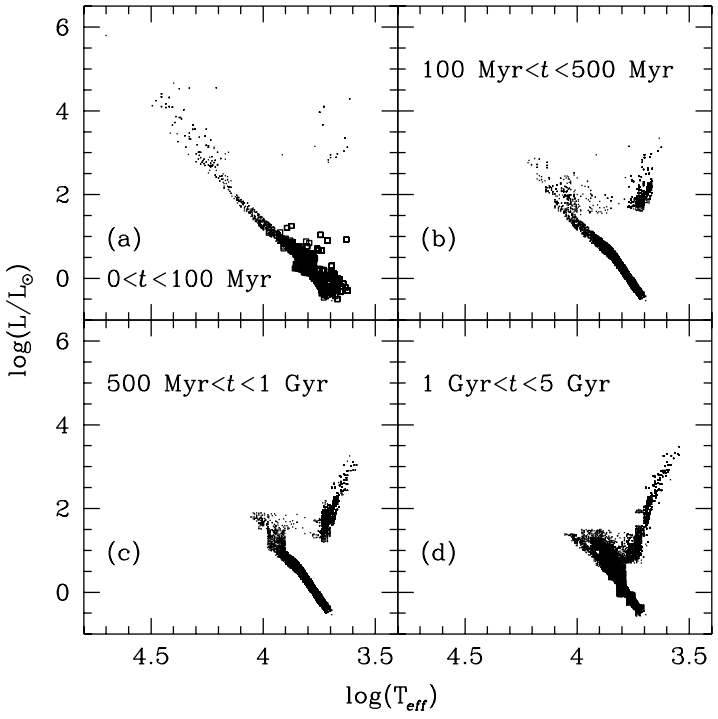

Figure 8.1: *Location in the HR diagram of stars in the field of SN1987A in the quoted ranges of age. The lower Main Sequence has been trimmed to show the T Tauri stars in panel (a) (open squares). The effects of the finite size of the grid are clearly visible.*

The next step is to realize that the number of stars expected in a certain cell is not only proportional to the time spent in it, but also to the birthrate *at the epoch at which the star was formed*. We can use the time distribution of the stars weighed as described above as the input to compute new weights:

$$W_{\star,1}(k) = \frac{\delta t[i_\star, j_\star, k] \cdot B_0(t[i_\star, j_\star, k])}{\sum_{i=1}^{N[i_\star, j_\star]} \delta t[i_\star, j_\star, i] \cdot B_0(t[i_\star, j_\star, i])} \tag{8.4}$$

Again, the normalization is such that:

$$\sum_{k=1}^{N[i_\star, j_\star]} W_{\star,1}(k) = 1$$

We can now iterate the process and compute $n_1(t)$ using the appropriate weights $W_{\star,1}(k)$ from equation (8.4) and the first-order birthrate $B_1(t)$ according to equation (8.3), again assuming a Salpeter (1955) mass function to correct for the stars that have already evolved.

This iterative process converges rapidly and the differences between successive iterations become negligible after the third one.

8.1.4 The Initial Mass Function

Until now we have corrected for the stars that at the present time are not any more in the HR diagram by assuming a Salpeter (1955) Initial Mass Function. Now that we have a well established birthrate, we can compute the IMF according to equation (8.1) and use it to refine our estimate. Of course, we have to repeat the iterations to compute the weights $W_\star$ until convergence is reached. This time, though, the process is even faster than before, since we can begin from the last birthrate computed, without having to start from the hypothesis of $B(t) = const.$

According to equation (8.1), the birthrate enters in the determination of the IMF at mass M only through its integral from $t = 0$ to $t = \tau(M)$, the look-back time for the mass considered. On the other hand, the correction for the evolved stars is important only for large values of the look-back time t. As we shall see, the birthrate was much lower in the past than it is at the present epoch and, hence, this correction is almost negligible and convergence is very rapid .

8.1.5 Testing the sieve

In order to test the procedure described in the previous sections we have simulated a stellar population born in an instantaneous burst at a time $t = 100$ Myr ago. The synthetic stars were placed in the HR diagram along the 100 Myr isochrone and a Gaussian random error in temperature and radius is assigned to every star and the corresponding error in luminosity is computed. The magnitude of the errors are chosen such as to match the observed behaviour.

Once the stars have been placed in the HR diagram, we apply the sieve described above to recover their age distribution. The results are shown in Figure 8.2 on the next page, where we compare the zero-th order solution with the final one after three iterations.

As it can be seen in Figure 8.2 three iterations are enough to recover almost entirely the input information. The full width at half maximum of the final result after three iterations is roughly 20 Myr, *i.e.* $\delta t/t \simeq 0.2$. The broadening is mainly due to the broadening of the lower Main Sequence due to the photometric errors we have introduced to faithfully mimic the observations.

The secondary peaks clearly visible in the dashed histogram at $t \simeq 40, 70, 120$ and 150 Myr are artifacts of the temporal grid of the zero-th order iteration. They are made of Main Sequence stars with a very long time of permanence in their cell. They are initially assigned a discrete age, instead of a uniform probability of having any age among the allowed ones within the cell. This is fixed in the successive iterations and the peaks tend to vanish.

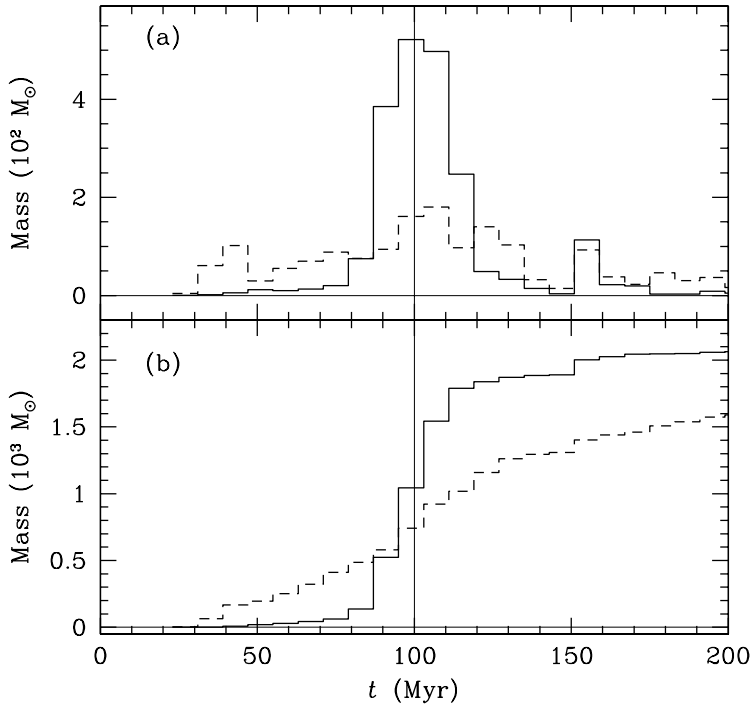

Figure 8.2: *Results of the sieve on a simulated stellar population of 100 Myr. In panel (a) we show the zero-th order temporal distribution (dashed line) and the final one after three iterations (full line). As it can be seen, almost all of the spurious peaks have disappeared. In panel (b) we show the corresponding cumulative distributions. The vertical line in both panels marks the age of the input population.*

8.2 Results

Let us now apply the "sieve" described above to the stars observed in the field around SN1987A and in the parallel field.

It is worth stressing once again that the spatial distributions of stars of the same young generations, but with different masses appear to be remarkably different. High mass stars tend to be concentrated in clusters, whereas the low mass ones are almost uniformly distributed. This trend is evident both in the field surrounding SN1987A (see section 6.8 on page 154) and in the control field located 8′ south-west of it (see section 7.6 on page 173). As a consequence, **the idea itself of an Initial Mass Function is not valid on small spatial scales**.

In the case of the surroundings of SN1987A, for example, the massive young stars are mainly concentrated in a circle of 20″ (5 pc) of radius, while the low mass stars of the same generation are more uniformly distributed over the entire area of roughly 30 pc of radius covered by our observations (see Figure 6.21 on page 157 and Table 6.2 on page 158). In the following, we will consider the whole field together, thus effectively averaging over the spatial inhomogeneities present. One has to bear in mind, then, that *all the results for the young generations of stars, including the high mass end of the IMF, are only valid as a spatial average over the entire region.* On the other hand, the old population is spatially uniform

over the field (again, see Figure 6.21 and Table 6.2).

As we have discussed in section 2.2.1, the assumption that the IMF is constant in time implicitly also implies that, on average, it should be spatially constant. If this were not the case, we would not be entitled to compare the young stars, that did not have time to be displaced from where they were born, with the older one, that have had plenty of time to do so.

8.2.1 Star Formation History

The results for the field around SN1987A are shown in Figure 8.3, where we plot the *Star Formation Rate* (SFR)[a], normalized to the area sampled, as a function of time from the present epoch to the maximum look-back time allowed by the data. Because of the incompleteness of the data at the low mass end, only stars with masses greater than 1 $M_\odot$ are included in the determination of the Star Formation Rate. The corresponding maximum look-back time, according to the models by Brocato and Castellani (1993) and Cassisi et al. (1994) for Z= 0.3·$Z_\odot$, is roughly 8 Gyr. The dashed line indicates the interval of ages that may also be affected by incompleteness.

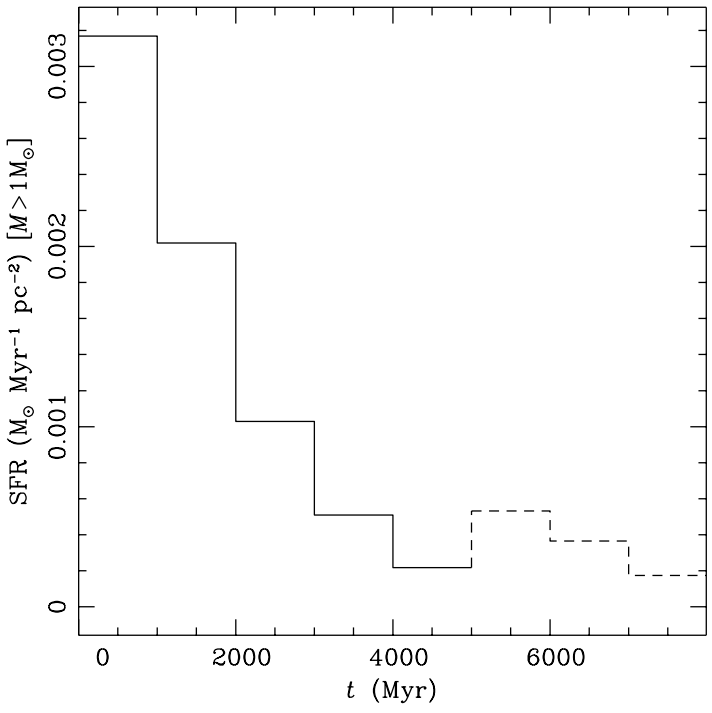

Figure 8.3: *Star Formation Rate (SFR) as a function of time for the field around SN1987A. The area covered is 1973 pc^2 and only stars with $M > 1\ M_\odot$ are considered. For ages greater than about 5 Gyr,* i.e. *masses smaller than approximately 1.2 $M_\odot$, observational errors do not allow to draw any firm conclusion (dashed histogram).*

[a]Let us recall from section 2.2.1 that the Star Formation Rate is the mass of stars formed per unit time.

An inspection of Figure 8.3 clearly shows that the Star Formation Rate has been increasing in the past 5 Gyr by a factor of 15 if the value of the bin centred at 4.5 Gyr is taken as representative of the star formation activity in the remote past. However, this bin too may be affected by incompleteness problems and, thus, this could be an overestimate of the real value. In a more conservative way, we can take the SFR value at 3.5 Gyr as representative, in which case the enhancement is a factor of 6. Applying the same method to the parallel field yields to practically the same results. A similar trend with the star formation activity increasing in recent times is seen in various other spots in the LMC (see, for example, Elson et al., 1997; Geha et al., 1998).

The star formation history plotted in Figure 8.3 is the global one of the field. Let us now zoom in and consider in detail the recent past of the neighbourhood of SN1987A. The star formation history for this region in the last 100 Myr is shown in Figure 8.4.

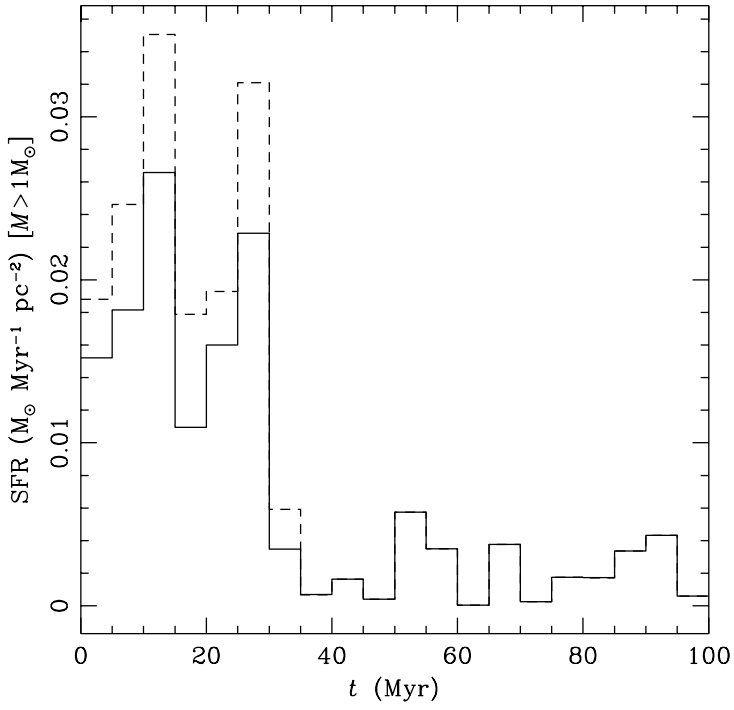

Figure 8.4: *Star Formation Rate in the last 100 Myr for the field around SN1987A for stars with* $M > 1\ M_\odot$. *The full line shows the conservative case in which only the stars with strong* Hα *excess are considered as* bona fide *T Tauri stars (see section 6.7.3), whereas the dashed histogram also includes the stars with U-band excess (see section 6.7.2).*

Let us notice that the features in the HR diagram are more sensitive to age the younger the stellar population is and this makes it possible to follow the recent Star Formation History in great detail, as shown in Figure 8.4.

As we have discussed in section 6.7 on page 142, the low mass stars belonging to the younger generations are still in the Pre-Main Sequence phase. They occupy the same region of the HR diagram of stars of comparable mass, but with ages in excess of a few hundred million years. Also in section 6.7, we have described two methods to recognize the T Tauri

stars and to estimate their number and evolutionary status: through their Hα and/or U-band excesses. The former method provides unambiguous identification whereas the latter one can identify PMS stars only in a statistical sense. Both methods lead to underestimates of the real number of T Tauri stars, but the U-band excess is more likely to be closer to the truth. In Figure 8.4 on the preceding page we show the star formation rates derived including only the 488 stars with Hα excess (full line histogram) or the 850 stars that have a U-band excess.

Of course, including all the objects with U-band excess as T Tauri stars leads to a higher star formation activity in the recent past, but the *shape* of the SFR is the same in both cases. There have been two distinct episodes in the last 30 Myr before which little or no activity was present. The peak at $t \simeq 12$ Myr is coeval to the estimated age of the progenitor of SN1987A (see, for example, Van Dyk et al., 1998). The intensity of these two last episodes of star formation is, for each of them, roughly 10 times higher than the average one in the last billion years (see Figure 8.3 on page 186).

It is interesting to note that almost half of the mass ascribed to the first bin in Figure 8.4 is due to one single star: it is the star with a mass in excess of 60 $M_\odot$ which we have discussed in section 6.6.2 when describing the various features in the HR diagram. High mass stars are much less numerous than the lower mass ones (the exact proportions depend, of course, upon the IMF). When dealing with the high mass end of the stellar spectrum, then, one has to bear in mind that the fluctuations on the small number of objects expected dominate the statistics. Even if the IMF existed, then, different realizations of the same statistical ensemble could lead to huge differences in the population of high mass stars. For example, this effect could mimic an upper mass cutoff just because, in a given realization, no stars with masses higher than a certain value happened to be formed.

8.2.2 Initial Mass Function

We can now take the final step and estimate the Initial Mass Function. Let us stress once again that what we are going to measure here is the *spatial and temporal average* resulting from the superposition of different generations of stars. The IMFs we are going to estimate, then, need not be valid for any one of them individually, but only be meaningful on average. Moreover, as we have discussed in section 2.2.1, it may very well be possible that the concept itself of an Initial Mass Function is not valid. Once again, though, if this is the case, there is no way to disentangle the effects of the time and mass dependences in the *Creation Function* introduced in section 2.2.1. If this is, indeed, the case, it would only make sense to estimate the IMF for Simple Stellar populations in which the stars formation activity is confined to a single burst with a short time duration compared to its age.

After these words of caution, let us proceed assuming that there exists an IMF. We shall further discuss its validity and meaning once we will have estimated its shape and slope. Equation 8.1 on page 180 states that, under the assumption that the Creation Function is

separable, the correction required to transform the observed Present Day Mass Function into the Initial Mass Function depends on the birthrate integrated from the present epoch all the way back to the look-back time of a given mass M. So, all the stars of different masses formed during this period of time contribute to the correction to the PDF for mass M. Once again, then, the uncertainty in the number of T Tauri stars causes a range of possible values. Let us notice here that the more numerous the low mass young stars, the steeper the resulting IMF will be, because more stars will contribute to the integral over the lifetime of massive stars.

The IMF computed including as T Tauri stars only the stars with Hα excess is shown as a full line in Figure 8.5, the one computed including also the stars with U-band excess as a dashed line. Let us note that the biggest effect that T Tauri stars have is to lower the mass function at the the high mass end, as opposed to increasing it in the mass range to which they belong. The turnover at $\log(M/\mathrm{M}_\odot) \simeq 0$ is caused by the incompleteness of the data at faint magnitudes. It does not represent a real feature of the IMF.

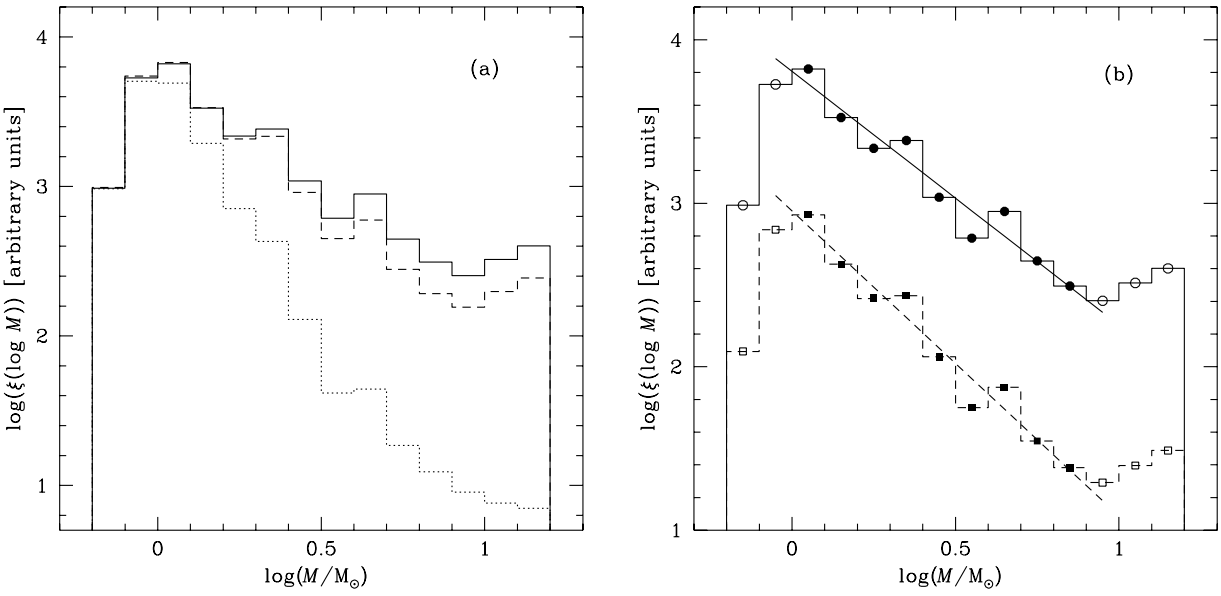

Figure 8.5: *Initial Mass Function for the neighbourhood of SN1987A. Panel (a): the IMF computed including as T Tauri stars only the stars with* Hα *excess is shown as a full line, the one computed including also the stars with U-band excess as a dashed line. The Present Day Mass Function is also shown with a dotted histogram. Panel (b): power-law fit to the IMFs of panel (a) including only the stars with* Hα *excess (full lines and circles,* $\Gamma = -1.55$*) and also those with U-band excess (dashed lines and square symbols,* $\Gamma = -1.87$*). The bins used for the fit are marked with dots. An arbitrary shift was applied to better show the data. The Poissonian fluctuations are smaller than the symbols in panel (b).*

The dotted line in Figure 8.5 shows the Present Day Mass Function. As it can be seen, the correction required to recover the IMF from it is quite large and, as we did, *every caution needs to be taken in computing the birthrate as accurately as possible to reliably determine the IMF using equation (8.1).*

Both the IMF estimates in Figure 8.5 are well represented by power-law functions. Let us stress again that we did not impose this in any way and this too has to be regarded as a meaningful result. A least-square fit in the $1 \leq M/\mathrm{M}_{\odot} \leq 7$ interval, where the sample is not affected by incompleteness, yields a slope of $\Gamma = \alpha + 1 = -1.55$ if only the stars with Hα excesses are included in the young population and a value of $\Gamma = -1.87$ if also the stars with U-band excesses are added. The slope can be as steep as $\Gamma = -2.2$, should the number of Pre-Main Sequence stars be still underestimated by a factor of 2.

Since the T Tauri stars present in the field are *at least* those we identify through their Hα excess, the value of $\Gamma = -1.55$ has to be regarded as an upper limit to the real slope in this mass range. In fact, the excess of massive stars visible in both panels of Figure 8.5 indicates that both estimates of the number of T Tauri stars are likely to be lower limits. However, there are only a few stars in these mass bins and, consequently, the mass function here is not as reliable as it is for lower masses.

The formal error on these fits does not have a strong meaning because, as we have seen, the error budget is dominated by intrinsic uncertainties on the number of young, low mass stars present in the field.

Also in this case, the analysis of the parallel field leads to essentially the same results.

For comparison, the classical Salpeter (1955) value is $\Gamma = -1.35$ in the mass range from 1 to 10 $\mathrm{M}_{\odot}$. More recently, Scalo (1998) quotes a value of $\Gamma = -1.7 \pm 0.5$ for the same range of masses (see equation 2.38 on page 33). This latter result comes from a compilation of values found in the literature for 61 clusters in the Galaxy and the Large Magellanic Cloud. The quoted uncertainty reflects the scatter among them and it is not the formal error on the slope. All of these results are independent of each other and, in turn, ours, both the "main" and parallel field, are independent of any of them. Moreover, different environments were probed and, still, the derived slopes are perfectly compatible with one another. Both the uncertainties in our determination and the scatter among the values used by Scalo (1998) are quite large, but their coincidence seems to indicate that, when suitably averaged over time *and* space, the star formation process in the $1 \leq M/\mathrm{M}_{\odot} \leq 7$ mass range leads to a *power-law mass function with a slope of* $\Gamma \simeq -1.7$. It is important to stress once again that, as we have demonstrated throughout this Thesis, this average result may not hold true for any particular star formation episode.

Bibliography

Bertelli, G., Mateo, M., Chiosi, C., and Bressan, A. 1992, *ApJ*, **388**, 400.

Brocato, E. and Castellani, V. 1993, *ApJ*, **410**, 99.

Cassisi, S., Castellani, V., and Straniero, O. 1994, *AA*, **282**, 753.

Elson, R.A.W., Gilmore, G.F., and Santiago, B.X. 1997, *MNRAS*, **289**, 157.

Ferraro, F.R., Fusi Pecci, F., Tosi, M., and Buonanno, R. 1989, *MNRAS*, **241**, 433.

Geha, M.C., Holtzman, J.A., Mould, J.R., Gallagher, J.S. III, Watson, A.M., Cole, A.A., Grillmair, C.J., Stapelfeldt, K.R., Ballester, G.E., Burrows, C.J., Clarke, J.T., Crisp, D., Evans, R.W., Griffiths, R.E., Hester, J., Scowen, P.A., Trauger, J.T., and Westphal, J.A. 1998, *AJ*, **115**, 1045.

Mighell, K.J. and Butcher, H.R. 1992, *AA*, **255**, 26.

Salpeter, E.E. 1955, *ApJ*, **121**, 161.

Scalo, J. 1998, In *The Stellar Initial Mass Function*, G. Gilmore and D. Howell (Eds.), volume 142 of *38th Herstmonceux Conference*, San Francisco. ASP Conference Series, p. 201.

Schaerer, D., Meynet, G., Maeder, A., and Schaller, G. 1993, *AASS*, **98**, 523.

Schaller, G., Schaerer, D., Meynet, G., and Maeder, A. 1992, *AASS*, **96**, 269.

Siess, L., Forestini, M., and Dougados, C. 1997, *AA*, **324**, 556.

Tolstoy, E. and Saha, A. 1996, *ApJ*, **462**, 672.

Tosi, M., Greggio, L., Marconi, G., and Focardi, P. 1991, *AJ*, **102**, 951.

Van Dyk, S., Hamuy, M., and Mateo, M. 1998, In *SN1987A: Ten Years Later*, M.M. Phillips and N.B. Suntzeff (Eds.). ASP Conference Series. in press.

Future developments

In the course of this Thesis we have developed advanced techniques to study stellar populations with complex star formation histories. We have applied them to analyze fields in one very interesting astrophysical environment and, obviously, much more work needs to be done along the same lines of research.

Our group has already access to multi-band WFPC2 observations of additional fields in the Large Magellanic Cloud. These are located in the outskirts of R136, in the vicinity of SN1987A, and centered on NGC 1850, a young double cluster. Such very diverse environments will, hopefully, provide precious insights on how the star formation process takes place under different physical conditions. Eventually one might be able to map a representative number of fields so as to get a global picture of the star formation history in the LMC. The analysis discussed in this Thesis is based on multi-band observations. However, even if the set of filters used is limited to two or three and the complete analysis performed here cannot be done, many interesting questions can still be addressed. For example, if two wide-bands and the Hα filters are available one can identify with very little effort the T Tauri stars using the diagnostic tools described here, providing a census of the young, low-mass stellar population. This would allow us to compare the two different environments of the LMC and of the Milky Way, where the young, low-mass populations are born under different conditions.

Another interesting object is the Small Magellanic Cloud (SMC), which, so far, has been studied in much lower detail than the LMC. It is only slightly more distant from the Sun and, hence, the spatial resolution attainable there is comparable to the one in the LMC itself. The SMC has a metallicity less than one tenth of the solar value. In this respect, then, it is even more similar to the primordial environment where the first generations of stars were formed. Extensive investigations of the characteristics of the relevant stellar populations in it would, thus, provide invaluable information that might find applications in clarifying spectral properties of high redshift galaxies.

As we have seen in this Thesis, *resolved* populations can be studied in great detail. These results can be used to interpret the data from more distant galaxies, where point-like objects may, in fact, be groups of stars that are closer to each other than the spatial resolution of the instrument used to observe them. At 5 Mpc, for example, a cluster with a diameter of 10 pc, like the one surrounding SN1987A, would subtend an angle of $0''.4$. From the ground,

in typical seeing conditions, the cluster would appear as a point-like source. It could be resolved with *HST*, but, even at this superb spatial resolution, the point-like objects would be, in effect, the superposition of more than one star. By degrading the images of a nearby object to reproduce the crowding conditions of a more distant galaxy, one can easily and faithfully mimic the effects of confusion and take them into account properly. We have tested this "empirical population synthesis" in the case of the point-like sources identified in WFPC2 exposures of M81 and M51, two spiral galaxies a few Mpc away. The results are very encouraging and will appear in a forthcoming paper.

The use of HST has certainly opened new and unprecedented possibilities in astronomy. However, high quality ground-based data provide an excellent complementary counterpart to those taken from space. For example, 10 meter class telescopes, such as the VLT at ESO or the Keck telescopes at Mauna Kea, can provide spectroscopic data that are the ideal complement to space-based observations. In the context of this thesis, once the T Tauri stars are identified using *HST*, as we have done here, ground-based follow-up spectroscopy can be used to study them in detail. In general terms, the unprecedented image quality of *HST* can be used to identify interesting objects in external galaxies (T Tauri stars, massive stars, recently formed star clusters, etc) the spectra of which can, then, be taken from the ground.

Two last remarks on future instruments before concluding. Over the years the Wide Field and Planetary Camera 2 has proven to be an invaluable tool to observe stellar populations. However, a limitation is that its field of view is rather small and only small portions of nearby galaxies, like the Large Magellanic Cloud, can be covered with one exposure. The *Advanced Camera for Surveys*, once installed on board *HST* in the year 2000, will make it easier to cover large portions of the sky with its field of view of $3' \times 3'$ and its enhanced sensitivity.

Possibly, the most important contribution from *HST* to stellar studies has come from its unprecedented spatial resolution. This has enabled its users to actually *clearly see* objects in regions that appeared extremely crowded from the ground. This has led to important results such as the determination of the mass function down to the hydrogen burning limit in galactic Globular Clusters or of the star formation history back to very early times in dwarf galaxies of the Local Group, just to mention two striking cases. Obviously, the problem of crowding becomes more severe for more distant galaxies and, in fact, it is the confusion, and not the exposure time, that currently sets the limit to the depth attainable with *HST*. Numerous examples of this can be found in the *HST* archive. In order to reach fainter magnitudes, *i.e.* smaller masses, a better spatial resolving power is required. This can only be done from space, because ground-based observations are fatally plagued by atmospheric turbulence and adaptive optics techniques provide excellent spatial resolution only for extremely small fields of view. Space-based observatories can be, in principle, diffraction limited, so that the angular resolution attainable is of the order of λ/D, where λ is the wavelength at which the observations are made and D is the diameter of the telescope. As a consequence, the spatial resolution can be increased by observing through bigger telescopes and/or at

shorter wavelengths. The concept of a space-based 8 m telescope, the *Next Generation Space Telescope* (NGST), is currently being studied. The current focus is to optimize it for the infrared for cosmological purposes, *i.e.* to study very high redshift galaxies. If its sensitivity could be extended at least to optical wavelengths and its optical elements could be designed with a high enough accuracy to reach the diffraction limit in this range, the NGST could also bring new and more exciting surprises in the study of young stellar populations.

Bibliography

Adams, F.C. and Fatuzzo, M. 1996, *ApJ*, **464**, 256.

Ardeberg, A., Brunet, J.P., Maurice, E., and Prevot, L. 1972, *AASS*, **6**, 249.

Arnett, W.D., Bahcall, J.N., Kirshner, R.P., and Woosley, S.E. 1989, *ARAA*, **27**, 629.

Basri, G. and Bertout, C. 1989, *ApJ*, **341**, 340.

Bertelli, G., Mateo, M., Chiosi, C., and Bressan, A. 1992, *ApJ*, **388**, 400.

Bertout, C. 1989, *ARAA*, **27**, 351.

Bertout, C., Basri, G., and Bouvier, J. 1988, *ApJ*, **330**, 350.

Bessel, M.S. 1991, *AA*, **242**, L17.

Bessel, M.S., Castelli, F., and Plez, B. 1998, *AA*. in press.

Bica, E., Claria, J.J., Dottori, H., Santos, J.F.C., and Piatti, A.E. 1996, *ApJS*, **102**, 57.

Biretta, J.A., Burrows, C., Holtzman, J., Heyer, I., Stevens, M., Bagget, S., Casertano, S., Clampin, M., Fruchter, A., Ferguson, H., Griffiths, R., Krist, J., Noll, K., O'Dea, C., Stiavelli, M., Suchkov, A., Surdej, J., and Whitmore, B. *WFPC2 Instrument Handbook Version 4.0*. STScI, Baltimore, 1996.

Brocato, E. and Castellani, V. 1993, *ApJ*, **410**, 99.

Brocato, E., Castellani, V., and Romaniello, M. 1998, *AA*. submitted to.

Carkner, L., Feigelson, E.D., Koyama, K., Montmerle, T., and Reid, I.N. 1996, *ApJ*, **464**, 286.

Cassisi, S., Castellani, V., and Straniero, O. 1994, *AA*, **282**, 753.

Castellani, V. *Astrofisica Stellare*. Zanichelli, Bologna, 1^{st} edition, 1985.

Castellani, V., Chieffi, A., and Straniero, O. 1992, *ApJS*, **78**, 517.

Castelli, F. 1998, In *Views on Distance Indicators*, F. Caputo (Ed.). Società Astronomica Italiana. in press.

Castelli, F., Gratton, R.G., and Kurucz, R.L. 1997a, *AA*, **318**, 841.

Castelli, F., Gratton, R.G., and Kurucz, R.L. 1997b, *AA*, **324**, 432.

Chiosi, C., Bertelli, G., and Bressan, A. 1992, *ARAA*, **30**, 235.

Cool, A.M. and King, I.R. 1995, In *Calibrating HST: Post Servicing Mission*, A. Koratkar and C. Leitherer (Eds.), Baltimore. STScI, p. 290.

Cool, A.M., Piotto, G., and King, I.R. 1996, *ApJ*, **468**, 655.

Crotts, A.P.S., Kunkel, W.E., and Heathcote, S.R. 1995, *ApJ*, **438**, 724.

Cusumano, G., Maccarone, M.C., Mineo, T., Sacco, B., Massaro, E., Bandiera, R., and Salvati, M. 1998, *AA*, **333**, L55.

D'Antona, F. and Mazzitelli, I. 1994, *ApJS*, **90**, 467.

D'Antona, F. and Mazzitelli, I. 1996, *ApJ*, **456**, 329.

De Marchi, G., Clampin, M., Greggio, L., Leitherer, C., Nota, A., and Tosi, M. 1997, *ApJ*, **479**, L27.

De Marchi, G. and Paresce, F. 1995a, *AA*, **304**, 202.

De Marchi, G. and Paresce, F. 1995b, *AA*, **304**, 211.

Duquennoy, A. and Mayor, M. 1991, *AA*, **248**, 485.

Edwards, S., Hartigan, P., Ghandour, L., and Andrulis, C. 1994, *AJ*, **108**, 1056.

Elmegreen, B.G. 1992, In *Star Formation in Stellar Systems*, G. Tenorio-Tagle, M. Prieto, and F. Sánchez (Eds.), III Canary Islands Winter School of Astrophysics, Cambridge. Cambridge University Press, p. 381.

Elmegreen, B.G. 1997, *ApJ*, **486**, 944.

Elson, R.A.W., Gilmore, G.F., and Santiago, B.X. 1997, *MNRAS*, **289**, 157.

Elson, R.A.W., Gilmore, G.F., Santiago, B.X., and Casertano, S. 1995, *AJ*, **110**, 682.

Fabian, A.C., Pringle, J.E., and Rees, M.J. 1974, *MNRAS*, **172**, 15.

Fernandez, M., Ortiz, E., Eiroa, C., and Miranda, L.F. 1995, *AASS*, **114**, 439.

Ferraro, F.R., Fusi Pecci, F., Tosi, M., and Buonanno, R. 1989, *MNRAS*, **241**, 433.

Fitzpatrick, E.L. 1988, *ApJ*, **335**, 703.

Forestini, M. 1994, *AA*, **285**, 473.

Frasca, A. and Catalano, S. 1994, *AA*, **284**, 883.

Gallagher, J.S. III, Mould, J.R., De Feijter, E., Holtzman, J., Stappers, B., Watson, A., Trauger, J., Ballester, G. E., Burrows, C.J., Casertano, S., Clarke, J.T., Crisp, D., Griffiths, R.E., Hester, J.J., Hoessel, J., Krist, J., Matthews, L.D., Scowen, P.A., Stapelfeld, K.R., and Westphal, J.A. 1996, *ApJ*, **466**, 732.

Geha, M.C., Holtzman, J.A., Mould, J.R., Gallagher, J.S. III, Watson, A.M., Cole, A.A., Grillmair, C.J., Stapelfeldt, K.R., Ballester, G.E., Burrows, C.J., Clarke, J.T., Crisp, D., Evans, R.W., Griffiths, R.E., Hester, J., Scowen, P.A., Trauger, J.T., and Westphal, J.A. 1998, *AJ*, **115**, 1045.

Gilliland, R.L. 1994, *ApJ*, **435**, L63.

Gilmore, G., Wyse, Rosemary F.G., and Kuijken, K. 1989, *ARAA*, **27**, 555.

Gonzalez, R.A., Allen, R.J., Dirsch, B., Ferguson, H.C., Calzetti, D., and Panagia, N. 1998, *ApJ.* in press.

Gullbring, E., Hartmann, L., Briceno, C., and Calvet, N. 1998, *ApJ*, **492**, 323.

Hartwick, F.D.A., Cowley, A.P., and Mould, J.R. 1984, *ApJ*, **286**, 269.

Hayes, M.H. 1987, In *Image Recovery: Theory and Application*, H. Stark (Ed.), Orlando. Academic Press, Inc., p. 195.

Hearnshaw, J.B. *The analysis of starlight: One hundred and fifty years of astronomical spectroscopy.* Cambridge University Press, Cambridge and New York, 1986.

Herbig, G.H. 1962, *Adv. Astr. Ap*, **1**, 47.

Hodge, P.W. 1980, *AJ*, **85**, 423.

Hodge, P.W. 1988, *PASP*, **100**, 1051.

Hodge, P.W. and Wright, F.W. *The Large Magellanic Cloud.* Smithsonian Press, Washington, 1967.

Holtzman, J.A., Burrows, C.J., Casertano, S., Hester, J.J., Trauger, J.T., Watson, A.M., and Worthey, G. 1995a, *PASP*, **107**, 1065.

Holtzman, J.A., Hester, J.J., Casertano, S., Trauger, J.T., Watson, A.M., Ballester, G.E., Burrows, C.J., Clarke, J.T., Crisp, D., Evans, R.W., Gallagher, J.S. III, Griffiths, R.E., Hoessel, J.G., Matthews, L.D., Mould, J.R., Scowen, P.A., Stapelfeldt, K.R., and Westphal, J.A. 1995b, *PASP*, **107**, 156.

Holtzman, J.A., Mould, J.R., Gallagher, J.S. III, Watson, A.M., Grillmair, C.J., Ballester, G.E., Burrows, C.J., Clarke, J.T., Crisp, D., Evans, R.W., Griffiths, R.E., Hester, J.J., Hoessel, J.G, Scowen, P.A., Stapelfeldt, K.R., Trauger, J.T., and Westphal, J.A. 1997, *AJ*, **113**, 656.

Hunter, D.A., Gillett, F.C., Gallagher, J.S. III, Rice, W.L., and Low, F.J. 1986, *ApJ*, **303**, 171.

Hunter, D.A., O'Neil, E.J., Lynds, R., Shaya, E.J., Groth, E.J., and Holtzman, J.A. 1996, *ApJ*, **459**, L27.

Hunter, D.A., Shaya, E.J., Holtzman, J.A., Light, R.M., O'Neil, E.J., and Lynds, R. 1995, *ApJ*, **448**, 179.

Jensen, J., Mould, J., and Reid, N. 1988, *ApJS*, **67**, 77.

Jones, B.F. and Stauffer, J.R. 1991, *AJ*, **102**, 1080.

Krist, J. and Hook, R. *The Tiny Tim User's Guide Version 4.4*, 1997. http://scivax.stsci.edu/~krist/tinytim.html.

Krist, J.E. and Burrows, C.J. 1994, *Appl. Opt*, **34**, 4951.

Kurucz, R.L. 1993, In *ATLAS9 Stellar Atmosphere Programs and 2 km s^{-1} grid.* (Kurucz CD-ROM No. 13).

Lada, C.J. 1987, In *Star-Forming Regions*, M. Peimbert and J. Jugaku (Eds.), volume 115, Dordrecht. Reidel Pub. Co., p. 1.

Lada, E.A., Strom, K.M., and Myers, P.C. 1993, In *Protostars and planets III*, E. Levy and J. Lunine (Eds.), Tucson. University of Arizona Press, p. 245.

Lamers, H.J.G.L.M. and Leitherer, C. 1993, *ApJ*, **412**, 771.

Leitherer, C. 1998, In *The Stellar Initial Mass Function*, G. Gilmore and D. Howell (Eds.), volume 142 of *38th Herstmonceux Conference*, San Francisco. ASP Conference Series, p. 61.

Lenzuni, P and Panagia, N., 1998. in preparation.

Lucke, P.B. and Hodge, P.W. 1970, *AJ*, **75**, 171.

Lynden-Bell, D. and Pringle, J. E. 1974, *MNRAS*, **168**, 603.

Madau, P., Ferguson, H.C., Dickinson, M.E., Giavalisco, M., Steidel, C.C., and Fruchter, A. 1996, *MNRAS*, **283**, 1388.

Marshall, F.E., Gotthelf, E.V., Zhang, W., Middleditch, J., and Wang, Q.D. 1998, *ApJ*, **499**, L179.

Massey, P., Lang, C.C., Degioia-Eastwood, K., and Garmany, C.D. 1995, *ApJ*, **438**, 188.

McCray, R. 1993, *ARAA*, **31**, 175.

Mighell, K.J. and Butcher, H.R. 1992, *AA*, **255**, 26.

Mihalas, D. *Stellar Atmospheres*. W.H. Freeman and Co., San Francisco, 2^{nd} edition, 1978.

Mihalas, D. and Binney, J. *Galactic Astronomy: Structure and Kinematics*. W.H. Freeman and Co., San Francisco, 2^{nd} edition, 1981.

Miller, G.E. and Scalo, J.M. 1979, *ApJS*, **41**, 513.

Mould, J.R., Watson, A.M., Gallagher, J.S. III, Ballester, G.E., Burrows, C.J., Casertano, S., Clarke, J.T., Crisp, D., Griffiths, R.E., Hester, J.J., Hoessel, J.G., Holtzman, J.A., Scowen, P.A., Stapelfeldt, K.R., Trauger, J.T., and Westphal, J.A. 1996, *PASP*, **108**, 682.

Murray, S.D. and Lin, D.N.C. 1996, *ApJ*, **467**, 728.

Muzerolle, J., Calvet, N., and Hartmann, L. 1998, *ApJ*, **492**, 743.

Olsen, K. and Hodge, P.W. 1996, *Bull. American Astronomical Society*, **188**, abstract 61.13.

Olszewski, E.W., Schommer, R.A., Suntzeff, N.B., and Harris, H.C. 1991, *AJ*, **101**, 515.

Palla, F. 1996, In *The Transparent Universe*, B. Kaldeich-Schürmann (Ed.), ESTEC, Noordwijk. ESA Publications Division, p. 25.

Palla, F. and Stahler, S.W. 1990, *ApJ*, **360**, L47.

Panagia, N. 1980, In *Radio Recombination Lines*, P. A. Shaver (Ed.), Dordrecht. D. Reidel Pub. Co, p. 99.

Panagia, N. 1998, In *Views on Distance Indicators*, F. Caputo (Ed.). Società Astronomica Italiana. in press.

Panagia, N., Gilmozzi, R., Macchetto, F., Adorf, H.M., and Kirshner, R.P. 1991, *ApJ*, **380**, L23.

Paresce, F., De Marchi, G., and Romaniello, M. 1995, *ApJ*, **440**, 216.

Pei, Y.C. and Fall, S.M. 1995, *ApJ*, **454**, 69.

Pfenniger, D. 1996, In *New Extragalactic Perspectives in the New South Africa*, D.L. Block and J.M. Greenberg (Eds.), Dordrecht. Kluver, p. 439.

Piotto, G., Cool, A.M., and King, I.R. 1997, *AJ*, **113**, 1345.

Pryor, C., Smith, G.H., and McClure, R.D. 1986, *AJ*, **92**, 1358.

Puls, J., Kudritzki, R.P., Herrero, A., Pauldrach, A.W.A., Haser, S.M., Lennon, D.J., Gabler, R., Voels, S.A., Vilchez, J.M., Wachter, S., and Feldmeier, A. 1996, *AA*, **305**, 171.

Rana, N.C. 1991, *ARAA*, **29**, 129.

Richer, H.B. and Fahlman, G.G. 1991, In *The Formation and Evolution of Star Clusters*, K. Janes (Ed.), volume 13, Boston. ASP Conference Series, p. 120.

Richer, H.B., Fahlman, G.G., Buonanno, R., Fusi Pecci, F., Searle, L., and Thompson, I.B. 1991, *ApJ*, **381**, 147.

Rousseau, J., Martin, N., Prevot, L., Rebeirot, E., Robin, A., and Brunet, J.P. 1978, *AASS*, **31**, 243.

Salpeter, E.E. 1955, *ApJ*, **121**, 161.

Sanduleak, N. *Contr. Cerro Tololo Interam. Obs.*, No. 89, 1969.

Savage, B.D. and Mathis, J.S. 1979, *ARAA*, **17**, 73.

Scalo, J. 1998, In *The Stellar Initial Mass Function*, G. Gilmore and D. Howell (Eds.), volume 142 of *38th Herstmonceux Conference*, San Francisco. ASP Conference Series, p. 201.

Scalo, J.M. 1986, *Fundamentals of Cosmic Physics*, **11**, 1.

Schaerer, D., Meynet, G., Maeder, A., and Schaller, G. 1993, *AASS*, **98**, 523.

Schaller, G., Schaerer, D., Meynet, G., and Maeder, A. 1992, *AASS*, **96**, 269.

Schmidt-Kaler, T. 1982, In *Landolt-Bornstein: Numerical Data and Functional Relationships in Science and Technology*, volume 2b, Berlin. Springer-Verlag, p. 297.

Schroeder, D.J. *Astronomical Optics*. Academic Press, Inc., San Diego, 1987.

Schwering, P.B.W. and Israel, F.P. 1991, *AA*, **246**, 231.

Scuderi, S., Panagia, N., Gilmozzi, R., Challis, P.M., and Kirshner, R.P. 1996, *ApJ*, **465**, 956.

Serra-Ricart, M., Aparicio, A., Garrido, L., and Gaitan, V. 1996, *ApJ*, **462**, 221.

Shu, F.H., Adams, F.C., and Lizano, S. 1987, *ARAA*, **25**, 23.

Siess, L., Forestini, M., and Dougados, C. 1997, *AA*, **324**, 556.

Soifer, B.T., Sanders, D.B., Madore, B.F., Neugebauer, G.E., G. Danielson, Elias, J.H., Lonsdale, C.J., and Rice, W.L. 1987, *ApJ*, **320**, 238.

Sonneborn, G., Fransson, C., Lundqvist, P., Cassatella, A., Gilmozzi, R., Kirshner, R.P., Panagia, N., and Wamsteker, W. 1997, *ApJ*, **477**, 848.

Stetson, P.B. 1987, *PASP*, **99**, 191.

Stetson, P.B. 1992, In *Astronomical Data Analysis Software and Systems I*, D.M. Worrall, C. Biemesderfer, and J. Barnes (Eds.), volume 25, San Francisco. A.S.P. Conference Series, p. 297.

Tolstoy, E. and Saha, A. 1996, *ApJ*, **462**, 672.

Tosi, M., Greggio, L., Marconi, G., and Focardi, P. 1991, *AJ*, **102**, 951.

van den Bergh, S. and Tammann, G.A. 1991, *ARAA*, **29**, 363.

Van Dyk, S., Hamuy, M., and Mateo, M. 1998, In *SN1987A: Ten Years Later*, M.M. Phillips and N.B. Suntzeff (Eds.). ASP Conference Series. in press.

Voit, M. *HST Data Handbook, Volume I.* STScI, Baltimore, 3^{rd} edition, 1997.

Walborn, N.R. 1991, In *Massive Stars in Starbursts*, C. Leitherer, N.R. Walborn, T.M. Heckman, and C.A. Norman (Eds.), STScI Symposium 5, Cambridge. Cambridge University Press, p. 145.

Walborn, N.R., Mackenty, J.W., Saha, A., White, R.L., and Parker, J.Wn. 1995, *ApJ*, **439**, L47.

Walborn, N.R., Phillips, M.M., Walker, A.R., and Elias, J.H. 1993, *PASP*, **105**, 1240.

Walker, A.R. and Suntzeff, N.B. 1990, *PASP*, **102**, 131.

Wheeler, J.C., Sneden, C., and Truran, J.W. 1989, *ARAA*, **27**, 279.

Whitmore, B. 1995, In *Calibrating HST: Post Servicing Mission*, A. Koratkar and C. Leitherer (Eds.), Baltimore. STScI, p. 269.

Whittet, D.C.B. 1992, In *Dust in the galactic environment*, Bristol. Techno House.

Wilcots, E., Hodge, P.W., and King, N. 1993, *Bull. American Astronomical Society*, **182**, abstract 49.07.

Williams, R.E., Blacker, B., Dickinson, M., Dixon, W.V.D., Ferguson, H.C., Fruchter, A.S., Giavalisco, M., Gilliland, R.L., Heyer, I., Katsanis, R., Levay, Z., Lucas, R.A., McElroy, D.B., Petro, L., and Postman, M. 1996, *AJ*, **112**, 1335.

Zombeck, M.V. *Handbook of Space Astronomy and Astrophysics.* Cambridge University Press, Cambridge, New York, 2^{nd} edition, 1990.

Ringraziamenti

Questa tesi ha due relatori: il Professor Giuseppe Bertin e il Professor Nino Panagia, in rigoroso ordine alfabetico. Ho imparato molto da entrambi ed è con grande piacere che li ringrazio per l'aiuto e la guida che non mi hanno mai fatto mancare in questi anni.

Un ringraziamento, sempre doveroso e sentitissimo, va al Professor Vittorio Castellani, con cui ho avuto la fortuna di laurearmi all'Università di Pisa. Il suo contributo al mio bagaglio di cultura astrofisica è stato tanto grande da non poter essere neanche quantificato.

Questa tesi conclude il mio corso di studi. Vorrei qui ringraziare il Professor Piergiorgio Giudici che, durante gli ultimi tre anni di scuola superiore al Liceo Volta, nella nebbiosa Milano, mi ha fatto scoprire lo straordinario fascino della ricerca scientifica, plasmando molte delle mie scelte successive.

La lista delle *persone senza le quali...*, a menzionarle tutte, rischia di essere più lunga della Tesi stessa. Mi limiterò, quindi, a pochi nomi.

Un grazie, dunque, a Stefano Casertano e Massimo Stiavelli, astrofisici di grande classe e profondi conoscitori di WFPC2, che hanno sempre trovato delle risposte, quelle giuste, alle mie mille domande. Con loro rigrazio tutti gli altri *WFPC2 instrument scientists* ed i membri dei vari *help desks* ad STScI a cui mi sono rivolto nell'affannoso tentativo di sfruttare al meglio le osservazioni. Mi auguro solo di essere riuscito ad applicare in modo adeguato i loro consigli.

Come non ringraziare, poi, Nicola Caon per le moltissime, illuminati discussioni sui più svariati temi? Tra le tante altre cose, lo sviluppo della routine di fit multibanda utilizzata in questa tesi deve molto alla sua straordinaria conoscenza di *SuperMongo*.

Un grazie va a Salvo "Turi" Scuderi, mio predecessore come studente del "Professore", per il lavoro svolto in questi anni e che, un giorno o l'altro, auspicabilmente vedrà la luce su qualche rivista.

Non posso certo esimermi dal ringraziare Bob Kirshner e tutti i membri della *SINS collaboration* per avermi fatto accedere agli straordinari dati qui discussi e per la illimitata pazienza con cui hanno sempre accolto i miei sermoni su argomenti, per così dire, non sempre conformi ai loro principali interessi di ricerca.

Ringrazio tutti i miei compagni di studi alla Scuola Normale Superiore di Pisa ed allo

Space Telescope Science Institute di Baltimora. Spesso si impara di più chiaccherando amabilmente tra amici (competenti) che in formalissimi seminari. Non posso che augurarmi di incontrare altre persone così in futuro.

Per concludere, non si può proprio dire che sia stato facile, ma, una volta di più, ne è valsa la pena, eccome se ne è valsa la pena...